THE ANALYSIS OF THERMAL AND FIRE PERFORMANCE OF CEMENTITIOUS BUILDING COMPONENTS

by

Zhaohui Huang

Thesis

Submitted in Partial Fulfilment of the Requirements for the Degree of Doctor of Philosophy

Department of the Built Environment

University of Central Lancashire

Preston, Lancashire

United Kingdom

October 1995

ACKNOWLEDGEMENTS

The author wishes to express his appreciation and gratitude to Dr. Andrew Platten and Professor John Roberts for their guidance, support, and encouragement throughout the course of this research. The author is also grateful to the academic staff and technician in the Department of Built Environment for their help and contribution to the project.

The author wishes to thank the University of Central Lancashire from whom he was in receipt of a studentship. Thanks are also due to from Manchester Computer Centre for allowing the use of their VPX super computer.

The author must express his gratitude to his wife Huiping, for her patience and encouragement during the work.

ABSTRACT

This work is concerned with the thermal and structural behaviour of reinforced concrete members in fire conditions. The numerical analyses of temperature histories and mechanical behaviour of reinforced concrete structural members subjected to fire are the major components of this research.

In this thesis a non-linear finite element procedure is proposed to predict the temperature distribution history in the cross section of structural members, such as beams composed of reinforced concrete, in fire conditions. A theoretical analysis of heat and moisture transfer in concrete was made which incorporated the simplifications that energy transfer by convection and diffusion in concrete could be neglected. However, the effect of water evaporation in concrete was considered. The thermal properties of concrete were considered as temperature and moisture dependent and the thermal properties of steel as temperature dependent only. The fire conditions were described by standard time-temperature fire curves and convection and radiation boundary conditions were used. In order to validate the model a series of verification tests have been carried out through a quantitative comparison of the model predictions against known test results. Fairly good accuracy has been found.

A non-linear finite element procedure for predicting the structural behaviour of the planar reinforced concrete members is also developed. The proposed procedure is based on "plane stress" theory and an iterative, secant stiffness formulation is employed. The complex features of structural behaviour in fire conditions, such as thermal expansion, shrinkage, creep, transient strains, cracking or crushing and change of material properties with temperature are considered in this model. Predictions from the model proposed are compared against experimental results, as well as against the model proposed by previous researchers, and a better correlation to experimental data is found. It is shown that the secant stiffness approach can provide good numerical stability for the analysis of planar reinforced concrete members in fire conditions. The model proposed in this study has the potential to predict the fire resistance of a planar

reinforced concrete members with an accuracy that is adequate for practical purposes if realistic material properties are available.

TABLE OF CONTENTS

ACKNOWLEDGEMENTS i

ABSTRACT ii

TABLE OF CONTENTS iv

NOMENCLATURE 1

1. INTRODUCTION 7

1.1 General Introduction 7

1.2 General Literature Review 9

1.3 Purpose and Scope of the Research 11

2. MATERIAL PROPERTIES AT ELEVATED TEMPERATURES 14

2.1 Introduction 14

2.2 Thermal Properties of Material at Elevated Temperatures 15

2.2.1 Thermal Conductivity of Concrete, k_c 15

2.2.2 Density, ρ_c, and Specific Heat , $C_{p,c}$, of Concrete 20

2.2.3 Thermal Conductivity of Steel, k_s 21

2.2.4 Specific Heat, $C_{p,s}$, and Density, ρ_s, of Steel 22

2.3 Strength and Deformation Properties of Materials

at Elevated Temperatures 24

2.3.1 Constitutive Modelling of Plain Concrete 24

2.3.2 Constitutive Modelling of Steel 55

2.3.3 Constitutive Modelling of Shear Reinforcement

and Reinforced Concrete 60

2.3.4 Free Creep Strain of Concrete 62

2.3.5 Free Shrinkage Strain of Concrete 69

2.3.6 Free Thermal Strain of Concrete 72

2.3.7 Free Transient Strain of Concrete 73

2.3.8 Free Creep Strain of Steel 75

2.3.9 Free Thermal Strain of Steel 80

2.4 Summary 82
3. THERMAL ANALYSIS 84
3.1 Introduction 84
3.2 The Theoretical Background of the Model 86
3.2.1 One-dimensional Energy Equation 88
3.2.2 Two-dimensional Energy Equation 91
3.2.3 Initial and Boundary Conditions 92
3.3 Finite Element Solution Procedure 93
3.3.1 The Basic Equation 94
3.3.2 Conductivity Matrix, $\underline{K}$ 94
3.3.3 Heat Capacity Matrix, $\underline{C}$ 103
3.3.4 External Heat Flow Vector, $\underline{Q}$ 104
3.3.5 Numerical Scheme 107
3.3.6 Fire Boundary Conditions 109
3.3.7 Description of Computer Programme, FPRCBC-T 114
4. STRUCTURAL ANALYSIS 116
4.1 Introduction 116
4.2 Mathematical Background of Plane Stress Problem 117
4.3 Non-linear Finite Element Analysis Procedure 120
4.3.1 Discritization by Finite Element Method 121
4.3.2 Structural Stiffness Matrix, $[K]$ 125
4.3.3 Nominal Nodal Force Vector, $\{F\}$ 135
4.3.4 External Loading Vector, $\{R\}$ 137
4.3.5 Boundary Conditions 140
4.3.6 Numerical Solution Procedure of Non-linear Analysis 140
4.3.7 Description of Computer Programme, FPPRCM-S 147
5. VERIFICATION OF ANALYTICAL METHODS 149
5.1 Introduction 149
5.2 Thermal Analysis 149

5.3 Structural Analysis 162
6. CONCLUSIONS AND RECOMMENDATIONS 175
6.1 Conclusions 175
6.2 Recommendations for Future Studies 179
REFERENCE 181
APPENDIX A THE EXAMPLE OUTPUT OF FPPRCM-S 190
APPENDIX B AUTHOR'S PUBLICATIONS 212

LIST OF FIGURES

Figures Pages

2.1 Thermal Properties of Dry Concrete: The Relationship of the Percentage Change of Ambient Values of the Specific Heat and Thermal Conductivity with Temperature [5, 13] 19

2.2 Thermal Properties of Steel: The Relationship of the Percentage Change of Ambient Values of the Specific Heat and Thermal Conductivity with Temperature [3] 23

2.3 Concrete Biaxial Failure Envelope: Representative Relationship of the Variation of Biaxial Tensile and Compressive Stresses in Concrete at Failure [21] 26

2.4 Determination of Non-linear Index, γ, [21] 31

2.5 Post-failure Behaviour for Tension-compression States of Stress that Result in Crushing of Concrete [21] 35

2.6 Variation of Secant Value of Poisson's Ratio, $\bar{\nu}_c$: The Relationship Presents Calculated Values of $\bar{\nu}_c$ Using Equation (2.23) 36

2.7 Orientation of Cracks in Concrete Elements 40

2.8 Stress-strain Curves for the Concrete Specimen under Uniaxial Tension [21] 43

2.9 Tension Constitutive Relation of Concrete Used in Analysis Procedure 44

2.10 The Relationship of the Percentage Change of Ambient Values of the Material Properties of Concrete with Temperature [10] 49

2.11 The Relationship of the Percentage Change of Ambient Values of the Modulus of Elasticity, E_s, and Yield Strength, f_y, of Steel with Temperature [5] 57

2.12 Idealised Stress-Strain Curve for Steel [4] 59

2.13 i-th Shear Reinforcement Components 61

2.14 Stress History Considered in Determination of Concrete Creep Strain 65

Figures Pages

2.15 Typical Creep Curve of Steel [7] 76

2.16 Harmathy's Formulation of Creep Model [7] 78

3.1 Geometric Idealisation for Two-dimensional Heat Transfer Model 85

3.2 Triangle Natural Co-ordinates and Side Designation 96

3.3 Standard Local Node Numbering and Co-ordinate Axes of Quadrilateral 101

3.4 Heat Capacity and Internal Heat Generation Idealisation 105

3.5 ISO 834 and ASTM-E119 Fire Curves [1, 63] 111

3.6 Flowchart for Programme FPRCBC-T 115

4.1 Normal and Shear Stresses on the x and y Faces of a Differential Solid [97] 118

4.2 Division of Reinforced Concrete Member into Concrete and Main Reinforced Steel Bar Elements 122

4.3 Two-node Bar Element 133

4.4 Distributed Stress Traction on One Side of the Element 139

4.5 Iterative Procedure for the Solution of Non-linear Equilibrium Equation (4.58) 142

4.6 Load and Displacement History for Non-linear Analysis Procedure 145

4.7 The Main Flowchart of FPPRCM-S 148

5.1 Illustration of Testing Arrangement [87] 150

5.2 Schematic Diagram of Cross-section of Column for Thermal Proving Tests (Dimensions in mm) [87] 151

5.3 Finite Element Mesh for Modelled Half Cross-section of Column 153

5.4 Comparison of Predicted and Measured [87] Temperature at Mid-section of the Column Exposed to ISO 834 Fire ($\varepsilon_f = 0.6$) 156

5.5 Comparison of Predicted and Measured [87] Temperature at Mid-section of the Column Exposed to ISO 834 Fire ($\varepsilon_f = 0.75$) 157

5.6 Comparison of Predicted and Measured [87] Temperature at Mid-section of the Column Exposed to ISO 834 Fire ($\varepsilon_f = 0.9$) 158

Figures Pages

5.7 Analysed Beam Specimen Details [100] 163

5.8 Furnace Atmosphere Temperature for ASTM and SDHI Fire Exposures [100] 164

5.9 Measured Cantilever Loads [100]: Plot of Load Against Time 166

5.10 Comparison of Predicted and Measured Maximum Deflection of Beam No.3 (ASTM Fire) 170

5.11 Comparison of Predicted and Measured Maximum Deflection of Beam No.5 (SDHI Fire) 171

5.12 Comparison of Predicted and Measured Maximum Deflection of Beam No.6 (SDHI Fire) 172

A.1 The Location of Reinforced Concrete Layers; Elements; Gauss-point: Main Reinforcing Steel Bars for Reference to Tables A.1-A.8 191

LIST OF TABLES

Tables Pages

2.1 The List of J_i's Values 63

2.2 Empirical Constants, A, B, C, D, E, F, σ^*, Used in Equations (2.83) to (2.84) for Several Reinforcing Steels [8, 42] 81

5.1 Values of the Parameters Used in Figures 5.4-5.6 152

5.2 Predicted Errors of FPRCBC-T in Figure 5.4 ($\varepsilon_f = 0.6$) at the Different Instances of Time 159

5.3 Predicted Errors of FPRCBC-T in Figure 5.5 ($\varepsilon_f = 0.75$) at the Different Instances of Time 160

5.4 Predicted Errors of FPRCBC-T in Figure 5.6 ($\varepsilon_f = 0.9$) at the Different Instances of Time 161

5.5 Detail of Beam Test Conditions [100] 165

5.6 Measured Material Properties at Ambient Condition 167

5.7 Comparison of Predicted and Measured Temperatures in Main Reinforcement 168

5.8 The Predicted Percentage Errors in Deflection between Measured Values and Analytical Models in Figures 5.10-5.12 at the Different Instances of Time 173

A.1 The Example Output of Stresses, Strains, and Degradation at Each Gauss-point of Concrete Layers which are Located at Different Portions of Beam No. 3 (See Figure A.1) at t = 0 (Calculated by FPPRCM-S) 192

A.2 The Example Output of Stresses, Strains, and Degradation at Each Gauss-point of Concrete Layers which are Located at Different Portions of Beam No. 3 (See Figure A.1) at t = 1 hr (Calculated by FPPRCM-S) 196

A.3 The Example Output of Stresses, Strains, and Degradation at Each Gauss-point of Concrete Layers which are Located at Different Portions of Beam No. 3 (See Figure A.1) at t = 2 hr (Calculated by FPPRCM-S) 200

Tables Pages

A.4 The Example Output of Stresses, Strains, and Degradation at Each Gauss-point of Concrete Layers which are Located at Different Portions of Beam No. 3 (See Figure A.1) at t = 3 hr (Calculated by FPPRCM-S) 204

A.5 The Example Output of Stresses, Strains, and Degradation of Main Reinforcing Steel Bar Elements which are Located at Different Portions of Beam No. 3 (See Figure A.1) at t = 0 (Calculated by FPPRCM-S) 208

A.6 The Example Output of Stresses, Strains, and Degradation of Main Reinforcing Steel Bar Elements which are Located at Different Portions of Beam No. 3 (See Figure A.1) at t = 1 hr (Calculated by FPPRCM-S) 209

A.7 The Example Output of Stresses, Strains, and Degradation of Main Reinforcing Steel Bar Elements which are Located at Different Portions of Beam No. 3 (See Figure A.1) at t = 2 hr (Calculated by FPPRCM-S) 210

A.8 The Example Output of Stresses, Strains, and Degradation of Main Reinforcing Steel Bar Elements which are Located at Different Portions of Beam No. 3 (See Figure A.1) at t = 3 hr (Calculated by FPPRCM-S) 211

NOMENCLATURE

a (Chapter 3) = absorption coefficient of surface

A (Chapter 2) = constant, defined by equation (2.18). dimensionless

A (Chapter 3) = convection coefficient of fire $[W\ {}^{0}C^{-N}\ m^{-2}]$

$[B]$ (Chapter 3) = temperature gradient interpolation matrix

$[B]$ (Chapter 4) = strain displacement transformation matrix

$[B_c]$ = strain displacement transformation matrix of concrete element

$[B_s]$ = strain displacement transformation matrix of reinforced steel bar element

C_p = specific heat at constant pressure $[J\ {}^{0}C^{-1}kg^{-1}]$

$C_r = \rho_m C_{p,m} / (\rho C_p)$, heat capacity ratio, moist air/concrete

$\underline{C}$ = heat capacity matrix

$[C]$ = constitutive matrix of plane stress

$[C]_c$ = constitutive matrix of concrete

$[C]_{rc}$ = constitutive matrix of reinforced concrete

$[C']$ = constitutive matrix of cracked concrete in principal axes (1, 2)

D (Chapter 2) = post-crushing parameter of concrete, dimensionless

D (Chapter 3) = diffusion coefficients for Fick's law for air-vapour mixture $[m^2\ s^{-1}]$

E = elastic modulus of material $[MPa]$

E_c = modulus of elasticity of concrete $[MPa]$

E_s = elastic modulus of steel reinforcement $[MPa]$

E_f = secant value of Young's modulus of concrete at failure $[MPa]$

$\overline{E}_c$ = secant value of Young's modulus of concrete $[MPa]$

$\overline{E}_{c1}$ = secant modulus of concrete in principal axis 1 $[MPa]$

$\overline{E}_{c2}$ = secant modulus of concrete in principal axis 2 $[MPa]$

$\overline{E}_{cp}$ = secant modulus of concrete at f_c' $[MPa]$

$\overline{E}_s$ = secant modulus of steel reinforcement $[MPa]$

f_t' = tensile strength of concrete $[MPa]$

f_c' = compressive strength of concrete $[MPa]$

f_y = yield strength of steel reinforcement [MPa]

$F(t)$ = fire curve

$\{F\}$ = nominal structure nodal force vector [N]

$\{F_c\}_m$ = nominal nodal force vector of concrete element [N]

$\{F_s\}_m$ = nominal nodal force vector of reinforced steel bar element [N]

G_c = shear modulus of concrete [MPa]

h (Chapter 3) = linear convection coefficient [$W\ {}^0C^{-1}\ m^{-2}$]

h_{fg}, = heat of evaporation of water [$J\ kg^{-1}$]

J_2 = second invariant of stress deviator tensor

k = thermal conductivity [$W\ {}^0C^{-1}m^{-1}$]

$k_{s'}$ = thermal conductivity of the solid phase of concrete without pores [$W\ {}^0C^{-1}m^{-1}$]

$\underline{k}_m$ = element conductivity matrix

$[k_c]_m$ = concrete element stiffness matrix

$[k_s]_m$ = stiffness matrix of reinforced steel bar element

$\underline{K}$ = heat conductivity matrix

$[K]$ = structure stiffness matrix

L (Chapter 3) = dimension of x-direction of members [m]

L_e = D_0/α_0, modified Lewis number

n_c = number of concrete elements

n_s = number of reinforced steel bar elements

N (Chapter 3) = convection power factor

$\{q\}$ = displacement vector

$\underline{Q}$ = external heat flow vector

$\{Q\}$ = structure internal force vector

R (Chapter 3) = gas constant per unit mass [$J\ {}^0C^{-1}\ kg^{-1}$]

$\{R\}$ = structure external force vector

t = time

T = temperature [^0C]

$\underline{T}$ = temperature vector

$\dot{\underline{T}}$ = temperature time rate of change vector

$[T]$ = transformation matrix

u = displacement in x-direction

u_m = velocity of moist air $[m\ s^{-1}]$

$\overline{u}_m$ = $u_m\ L/\alpha_0$, dimensionless velocity

$\{u_c\}$ = displacement vector of concrete element

$\{u_s\}$ = displacement vector of reinforced steel bar element

$\{U\}$ = structure nodal displacement vector

v (Chapter 3) = radiation view factor (v_1 for horizontal surfaces and v_2 for vertical surfaces)

v (Chapter 4) = displacement in y-direction

V_c = volume of concrete element

V_s = volume of reinforced steel bar element

w = moisture content by weight [%]

w_a = ρ_a/ρ_m, mass fraction of air with respect to the density of air-vapour mixture

X (Chapter 2) = invariant, defined by equation (2.19), dimensionless

x, y, z = global Cartesian co-ordinates

α (Chapter 3) = thermal diffusivity $[m^2\ s^{-1}]$

θ (Chapter 3) = absolute temperature $[K]$

ρ = density $[kg\ m^{-3}]$

$\overline{\rho}_m$ = ρ_m/ρ_0, dimensionless density

ρ_l = mass of liquid water for univolum of concrete $[kg\ m^{-3}]$

ρ_l^* = mass of liquid water per unit volume of liquid water $[kg\ m^{-3}]$

σ (Chapter 3) = Stefan-Boltzmann constant $[J\ s^{-1}\ m^{-2}\ K^{-4}]$

σ (Chapter 4) = normal stress $[MPa]$

σ_c = normal stress of concrete $[MPa]$

σ_{c1} = principal stress in concrete, relative principal axis 1 $[MPa]$

σ_{c2} = principal stress in concrete, relative principal axis 2 $[MPa]$

σ_{ct} = tensile stress of concrete $[MPa]$

σ_s = steel reinforcement stress in bar axes [MPa]

σ_s^F = nominal stress of reinforced steel caused by free strains [MPa]

$\{\sigma\}$ = stress vector

$\{\sigma_c\}$ = stress vector of concrete

$\{\sigma_c\}_{12}$ = stress vector of concrete, relative to principal axes (1,2)

$\{\sigma_c\}_{xy}$ = stress vector of concrete, relative to axes (x,y)

$\{\sigma_c^F\}$ = nominal stress vector of concrete caused by free strains [MPa]

τ = shear stress [MPa]

τ_c = shear stress of concrete [MPa]

τ_{c12} = shear stress of concrete, relative to principal axes (1.2)

ε (Chapter 2) = porosity of concrete

ε (Chapter 4) = normal strain

ε_c = normal strain of concrete

ε_{c0} = concrete compressive strain at $f_c^{'}$

ε_{c1} = principal strain in concrete, relative to principal axis 1

ε_{c2} = principal strain in concrete, relative to principal axis 2

ε_{ct} = tensile strain of concrete

ε_s (Chapter 3) = surface emissivity

ε_s (Chapter 2 and Chapter 4) = steel reinforcement strains in bar axes

ε_f = flame emissivity of fire

ε_y = yield strain of steel reinforcement

ε_c^{creep} = free normal creep strain of concrete

ε_c^{sh} = free normal shrinkage strain of concrete

ε_c^T = free normal thermal strain of concrete

ε_c^{tr} = free normal transient strain of concrete

ε_s^{creep} = free creep strain of steel

ε_s^T = free thermal strain of steel

ε_s^m = mechanical strains of reinforced steel

ε_s^F = free strain of reinforced steel

$\{\varepsilon\}$ = strain vector

$\{\varepsilon_c\}_{12}$ = strain vector of concrete, relative to principal axes (1,2)

$\{\varepsilon_c\}_{xy}$ = strain vector of concrete, relative to axes (x,y)

$\{\varepsilon_c^m\}$ = mechanical strain vector of concrete

$\{\varepsilon_c^F\}$ = free strain vector of concrete

$\{\varepsilon_c^{creep}\}$ = free creep strain vector of concrete

$\{\varepsilon_c^{sh}\}$ = free shrinkage strain vector of concrete

$\{\varepsilon_c^{tr}\}$ = free transient strain vector of concrete

$\{\varepsilon_c^T\}$ = free thermal strain vector of concrete

γ (Chapter 2) = non-linearity index of concrete, dimensionless

γ (Chapter 4) = shear strain

γ_c = shear strain of concrete

γ_{c12} = shear strain of concrete, relative to principal axes (1,2)

γ_f = non-linearity index of concrete at failure, dimensionless

γ_c^{creep} = free creep shear strain of concrete

γ_c^{sh} = free shrinkage shear strain of concrete

γ_c^T = free thermal shear strain of concrete

γ_c^{tr} = free transient shear strain of concrete

ν = elastic Poisson's ratio of material

ν_c = elastic Poisson's ratio of concrete

ν_f = secant value of Poisson's ratio of concrete at the failure of crushing

ν_{cr} = creep Poisson's ratio of concrete

$\bar{\nu}_c$ = secant value of Poisson's ratio of concrete

Γ_m = production rate of moisture vapour per unit total volume $[kg\ m^{-3}s^{-1}]$

Subscripts:

a = air

c = concrete

d = dry concrete

f = fire

l = liquid

m = moist air

s (Chapter 2) = steel

s (Chapter 3) = surface

st (Chapter 3) = steel

v = vapour

x = in x co-ordinate direction

y = in y co-ordinate direction

z = in z co-ordinate direction

xy = in x-y co-ordinates plane

0 = initial condition or datum

∞ = ambient

1. INTRODUCTION

1.1 General Introduction

Fire causes tremendous losses both in lives and property. Many of these fires occur in buildings; combustible materials begin to burn, non combustible materials such as load-carrying members gradually decompose and lose their stiffness and strength, and in some cases collapse. The catastrophic failure of building elements can lead to the consequential loss of further lives and property. If a building is not properly designed for fire resistance, it may fail in a relatively short period of time. Thus, the endurance of a building and it's structural components during a fire is a critical factor in fire protection.

The behaviour of a structural element exposed to fire is described in terms of its **fire endurance** (or **fire resistance**) which is the period of time on exposure to fire at which failure occurs. Currently, the fire resistance of elements of building construction is expressed in terms of fire endurance as determined by standard fire tests. These criteria may vary from code to code but the most widely used is the ISO 834 Standard, "Fire resistance tests on elements of building construction" [1]. The British Standard BS476, "Fire test on building materials and structures: part 20: method of determination of the fire resistance of elements of construction (general principles)", [2] is largely based on the ISO specifications.

Since fire tests can rarely be carried out on complete buildings. The likely behaviour of the building is predicted from the fire test data on single elements and in order to achieve this, simplifications must be made. An important way in which the behaviour of elements in buildings is critically different from the furnace tests concerns the boundary conditions. There are two main reasons. The first is that in the furnace tests the furnace temperature can be controlled to follow the standard fire curves. However, the actual severity of a real fire in a compartment depends upon three main factors: (a) fuel for the fire, or fire load; (b) ventilation (e.g. air supply) to promote its growth: and (c) the geometric and physical characteristics of the compartment. Because of the

complexity of real fires it is difficult to model each of these factors exactly using the standard fire curves. The second is the structural restraint boundary condition. Due to the limitations of experimental conditions some simplified arrangements are employed for the restraint of the tested elements during standard fire tests. For example, there is either no restraint or nearly full restraint. It is still hard to model the real structural restraint for standard fire tests (e.g. restraint provided by structural continuity).

Therefore, the standard tests such as ISO and the British Standard, require the tested specimens to be realistic prototypes of the construction to be used in practice and should be full size. The tested sample should be subjected to a loading that models the natural situation. The standard also requires the specimen to be supported or restrained at the ends as they would be in service. Thus, the standard fire tests require large specialist apparatus and are more expensive and time consuming than computer predictions.

It is, therefore, becoming increasingly important to have analytical methods that can predict the structural capacity of structures when subject to fire conditions. High speed digital computers and modern methods of numerical analysis provide the tools necessary for a reliable analytical solution and such analytical solutions, when verified by a sufficiently wide range of experimental data and observations of behaviour in actual fires, can reduce the necessity for experimental testing, and provide the basis for safer design of elements of buildings.

Computing the fire response of elements of structure has several advantages over physical testing:

(a) In buildings, the expansion of structural elements during a fire is resisted by the surrounding structure, giving rise to restraint forces on the element. Although the structural element support conditions can be accounted for in computer programmes it is difficult to simulate support conditions physically, generally requiring that standard fire tests are carried out under constant load.

(b) The results from a fire test on a structural member are valid only for the particular dimensions, reinforcement, loading, and composition of the specimen

tested. It is hardly conceivable that all forms of structural member could ever be subjected to fire tests, since any variation in construction would required a separate test. However, when using computer programmes, it is relatively easy to vary some structural member's characteristics such as material properties, amount of reinforcement, and loading conditions, and to investigate the sensitivity of member's response to such variations.

(c) In most fire tests, the deterioration mechanisms of members are not visible (e.g. cracking and crushing within the member). Therefore, calculated responses, which predict deterioration resulting from fire, can help in the interpretation of physical test results.

Clearly, the analytical predictions of the structural response in fires can play an important role in the development of judicial structural design for fire safety.

The analytical study of the behaviour of a reinforced concrete element during fire conditions should include an investigation of the effect of temperature on the properties and laws of materials. Therefore, the thermal and structural analyses are two major parts of this research.

1.2 General Literature Review

A brief review of analytical studies made on the fire response of reinforced concrete structures is given here. Detailed reviews on specific topic follow in later Chapters.

1.2.1 Thermal Analysis of Reinforced Concrete

The aim of thermal analysis of reinforced concrete in fire conditions is to predict the temperature distribution histories within the components. Since concrete is a capillary-porous material, the problem is complicated by the presence of moisture. Heat and mass transfer take place simultaneously in concrete during heating conditions and the temperature distributions are affected by the presence of the moisture.

There have been a number of studies undertaken using non-linear finite element procedure to predict the temperature distribution histories in reinforced concrete

subject to fire conditions [3, 4]. Ellingwood and Lin [5] used a two-dimensional finite difference approach to solve the heat flow equation to predict temperature distribution histories of cross-sections of reinforced concrete beams in fire conditions. However. these studies did not consider the effect of moisture in the concrete. Wickström [6] used the concept of enthalpy to consider the effect of moisture subjected to evaporation in concrete. However, it is difficult to modify the enthalpy curve for concrete to allow for varying initial moisture content.

1.2.2 Structural Analysis of Reinforced Concrete

A more well-known computer programme, FIRES-RC, which can be used to analyse the structural response of reinforced concrete frames in a fire has been developed by Becker and Bresler [7]. This programme was an extension of the work done by Bizri [3]. The programme considers non-linearity due to thermal expansion, the change of mechanical properties of the material with temperatures, degradation of the section, and shrinkage and creep. The finite element method was used as the solution technique. In this study geometrical non-linearity and the structural failure procedure has not been considered. Ellingwood and Lin [5] used modified FIRES-RC to take into account the transient strain of concrete at elevated temperatures and to perform the structural analysis of reinforced concrete beams in fire conditions. Weeks [8] developed a computer programme, SAFE-RCC, which made use of a stiffness approach where loads are tested for convergence and the resultant deflections calculated. The geometrical non-linearity, plastic hinge, and interaction of the column with the surrounding structure were taken into account. Lie and Irwin [9] proposed a method to calculate structural behaviour of reinforced concrete columns subjected to fires.

The analyses stated above were based on the "plane sections" theory. The researchers carried out the one-dimensional stresses analysis. Transverse stresses, strains, and shear forces were ignored. However, Nizamuddin [10] developed an analytical

procedure based on, tangent stiffness approach to predict the fire response of reinforced concrete slabs.

1.3 Purpose and Scope of the Research

In this thesis, an analytical procedure and computer programme for predicting temperature distribution histories of cross-sections of structural members, such as beams composed of reinforced concrete, in fire conditions is developed and verified.

Developing a procedure for the thermal analysis of reinforced concrete structural members is complicated by the present of moisture in the concrete. In this study a two-dimensional non-linear finite element procedure is proposed which is based on a one-dimensional heat and mass transfer theoretical model in concrete proposed by Sahota [11] and a computer programme, FPRCBC-T, has been developed to predict the temperature distribution histories of the cross-section of reinforced concrete structural members in fire conditions (see Chapter 3). In this procedure three assumptions were made to evaluate the effect of water evaporation in the concrete. The thermal properties of concrete were considered as temperature and moisture dependent.

The effect of temperature upon the thermal properties (conductivity, density, and specific heat) of concrete and steel was investigated (see Chapter 2). The study showed that thermal properties at temperatures met with in fires differ considerable from those at room temperature.

In this study it was assumed that the temperature distribution histories were not affected by structural response, such as cracking and crushing. Therefore, thermal analysis can be carried out separately from the structural analysis. The temperature distribution histories generated by FPRCBC-T can be used as temperature input for predicting the mechanical response of reinforced concrete structural members.

A non-linear finite element procedure and computer programme for predicting the structural behaviour of planar reinforced concrete members subject to fires is developed and verified in this thesis. The procedure proposed is based on the "plane stress" theory (see Chapter 4). In this procedure the structural members were divided

into concrete and the main reinforcing steel bar elements. The concrete elements were sub-divided into layers to consider temperature distribution on cross-section of the members. A secant stiffness formulation and an iterative analysis approach were employed to model the complex features of structural behaviour in fire conditions, such as, thermal expansion, shrinkage, creep, cracking or crushing. and the change of material properties with temperatures.

The effect of temperature on the strength and deformation properties of concrete and steel was investigated (see Chapter 2). In this study stress and strain normal to the load plane of structure may be neglected so that any point in the concrete elements can be considered to be in a state of plane stress (biaxial state of stress). Hence, the strength and deformation properties of concrete were developed for plane stress.

The effect of high temperature on the non-linear stress-strain relationship and failure criteria of concrete under biaxial loading was reviewed and appropriate mathematical models were developed. From the literature reviewed, it was concluded that the strength and stiffness of concrete generally decrease with a rise in temperature. This decrease can be attributed to either weakening or failure of the bond at the mortar/coarse aggregate interface as a result of stresses accompanying incompatible thermal expansion of these constituents.

The deformation properties of concrete on creep, shrinkage, transient, thermal expansion under biaxial loading at elevated temperature were reviewed and appropriate mathematical models were developed. A similar investigation was made on the effect of temperature on the uniaxial stress-strain relationship, uniaxial creep, and coefficient of thermal expansion of steel, and appropriate models were developed. The study showed that, in general, the strength and deformation properties of concrete and steel at temperatures encountered in fires differ considerably from those at ambient conditions.

The exact nature of the material properties of concrete and steel at elevated temperature is much debated and still in need of further research. Therefore, the

models of material behaviour used in this research can provide only a first order approximation of the relationships.

For verification of the proposed analytical model, a series of proving tests have been carried out using a quantitative verification of the model against known test response data. These indicate that the proposed analytical methods incorporating these material models predict both thermal and structural response with fairly good accuracy at least in certain circumstances.

2. MATERIAL PROPERTIES AT ELEVATED TEMPERATURES

2.1 Introduction

In this chapter the effect of temperature on the properties of concrete and steel are reviewed, and mathematical models describing these properties are established. Detailed discussions on specific properties can be found in the references cited in this chapter.

The behaviour of a reinforced concrete structural member subjected to fires largely depends on the thermal and mechanical properties of the concrete and steel. Most of these properties are temperature dependent, some of them are also stress dependent, and some are time dependent, such as shrinkage and creep. For success in evaluating the response of a reinforced concrete member in fire conditions it is very important to understand the properties of the component materials in the temperature range caused by fires (20 - 1100 ^{0}C).

The properties of concrete are known to depend on a large number of factors including mix proportions, environmental conditions, load level, size and shape of member, age at loading and duration of load. In addition, the properties of concrete generally vary throughout the structure. Therefore, the material properties discussed here can only be considered to represent an average state in the body. Moreover, concrete is a heterogeneous material consisting of mortar and aggregate, for purposes of analysis it is considered as homogeneous in a macroscopic sense. Compared to concrete, the properties of reinforcing steel are generally well defined.

It is well known that concrete is not physiochemical stable at high temperatures which cause physical and chemical change in cement paste and aggregate, and internal stresses are induced due to the difference in coefficients of thermal expansion between cement paste and aggregate. Because of the complexity of concrete, the material properties are affected by many factors and different testing procedures produce different results. This makes direct comparisons between the experimental results

from different sources of research difficult. The range of the reported values for any property at any particular temperature is quite broad. In this study the load cycling on the material properties is not considered.

2.2 Thermal Properties of Materials at Elevated Temperatures

For evaluating the temperature distribution histories of a reinforced concrete structure in fire conditions it is necessary to know the thermal properties of concrete and steel in the temperature ranges associated with fire.

2.2.1 Thermal Conductivity of Concrete, k_c

Bizri [3] made a wide literature search for the determination of the thermal properties of concrete. The principal finding was that in spite of the wide range of values for any one property for different concretes the general trends found by different investigations are quite consistent. It has been shown that conductivity, k_c, decreases with increase in temperature.

2.2.1.1 The Factors Influencing the Conductivity, k_c

(1) Moisture:

Since the conductivity of air is much lower than that of water, the degree of saturation of concrete strongly affects its conductivity. It is to be expected that drying (loss of free water) by replacing moisture with air, and dehydration (e. g. loss of chemically combined water which forming a definite part of the hydrated compounds) would result in a lowering of the conductivity. On the other hand, the simultaneous presence of free moisture with an increase in temperature might lead to an increase in the rate of heat transfer by diffusion of water vapour, thus resulting in higher conductivity. These opposite effects on the conductivity are very clear from the results produced by Harmathy [12] who studied concrete specimens with 0%, 4% and 8% (by volume) initial moisture content. Only the specimen with 0% moisture experiences dehydration, thus k_c decreases steadily. The specimens at 4% and 8% moisture

content exhibit an initial increase in the rate of hydration. thus k_c increases to a maximum value at a temperature of about 100 ^0C. At this point the drying process is more potent than any possible further hydration and, k_c starts decreasing and as this proceeds dehydration also begins and further decreases the conductivity. Finally, the three curves for 0%, 4% and 8% moisture content meet at a temperature of about 125 ^0C and coincide thereafter.

(2) Mix characteristics:

a) Water-cement ratio: The main effect of the water cement ratio is on the initial value of the conductivity, k_c. It has a direct bearing on the amount of hydrated products and on the amount of free moisture available. Because the conductivity of water is less than half that of the cement paste, it can be stated that the lower the water content of the mix, the higher the conductivity of concrete. Except for the influence of moisture, the effect of the water-cement ratio upon the conductivity is negligible.

b) Aggregate-cement ratio: The cement paste has a lower thermal conductivity than normal density aggregate (2000-2700 kg/m^3), so that the leaner the mix, the higher is the conductivity.

c) Aggregate type: Investigations [13] show that the thermal conductivity of the cement paste in concrete does not vary greatly with temperature. However, variations in the thermal conductivity of aggregates are relatively large and responsible for the variation in the thermal conductivity of concrete. Even at room temperature different aggregates have different conductivities. In general, the conductivity of the aggregate decreases with an increase in temperature. The changes in k_c are even more pronounced when an aggregate experiences a change of mineralogical character. From research [14], it could be concluded that k_c might experience sudden drops at about 570 ^0C or 650 ^0C if quartz or biolite are present.

d) Curing and age: Have a slight effect on the initial values of k_c. This effect becomes negligible at high temperature.

(3) Test conditions:

a) Exposure time at high temperature and heating rate: At high temperatures free moisture either combines at an accelerated rate with the still unhydrated products or evaporates. These two processes have opposing effects on k_c. Their relative importance depends on both the exposure time at high temperature and the heating rate.

b) Furnace temperature condition at testing: Zoldners [14] reported that the conductivities of specimens that were cooled after exposure to high temperature, then tested were 10 to 20% higher than the corresponding values of the hot test specimens. The same conclusion could be reached by examination of Crispino's results [15]. In Crispino's investigation the specimens were heated to about 200 ^0C then cooled to room temperature, and measurements of k_c were taken continuously. It was found that k_c increased during the cooling process in agreement with Zoldner's results. Note, however, that the curve representing the values of the conductivity during the cooling process is continuously below the curve representing the values of k_c during the heating process. This is due to the free moisture which cannot be recovered once it is lost.

2.2.1.2 The Mathematical Model of k_c

Because of the complexity of concrete, available data on conductivity from references is subject to wide variation. However, the thermal conductivity of concrete shows a tendency to decrease with increasing temperature over the entire temperature range of interest for fire application. In this study, a two-dimensional non-linear finite element procedure to predict the temperature distribution histories of cross-section of reinforced concrete structural members in fire conditions is developed based on a one-dimensional heat and mass transfer theoretical model in the concrete proposed by Sahota [11] (see Chapter 3). In this model it is assumed that free water boils at 120 ^0C (see Section 3.1). After this point it is assumed that the concrete cannot heat up further until all the free water has evaporated. That is when the temperature is above 120 ^0C

there is no free water in the concrete, the concrete is dry. Two formulas are used to calculate k_c, one for wet concrete, the other for dry concrete.

The thermal conductivity of wet concrete may be calculated using the following empirical equation suggested by Kingery [16]:

$$k_c = \left[\left(\varepsilon - \frac{\rho_l}{\rho_l^*}\right) k_m{}^n + \frac{\rho_l}{\rho_l^*} k_l{}^n + (1-\varepsilon) k_s{}^n\right]^{\frac{1}{n}} \tag{2.1}$$

where, n is a power constant, $-1 \le n \le 1$ and $n \neq 0$. A value of $n = 0.25$ estimated by Harmatly [17] for fire clay brick was assumed to apply for concrete [11].

For dry concrete a model used by Ellingwood and Lin [5] is modified to represent k_d as a function of temperature (see Figure 2.1). This is expressed mathematically as follows:

$$k_d = k_{d,0} \qquad \left(T \le 20\ {}^0C\right) \tag{2.2a}$$

$$k_d = \left[1.0 - 8.9347\times10^{-4}(T-20)\right] k_{d,0} \qquad \left(20 < T \le 300\ {}^0C\right) \tag{2.2b}$$

$$k_d = \left[0.7498 - 4.7166\times10^{-4}(T-300)\right] k_{d,0} \qquad \left(300 < T \le 800\ {}^0C\right) \tag{2.2c}$$

$$k_d = \left[0.5140 - 8.6326\times10^{-5}(T-800)\right] k_{d,0} \qquad \left(800 < T \le 1500\ {}^0C\right) \tag{2.2d}$$

Where, $k_{d,0}$ is thermal conductivity of dry concrete at room temperature for normal weight concrete, a typical value for $k_{d,0}$ is 1.75 $\left(W\ {}^0C^{-1}\ m^{-1}\right)$ [3].

A pseudo k_s for the purposes of using equation (2.1) may be calculated from equation (2.1) by putting $k_d = 1.75\ \left(W\ {}^0C^{-1}\ m^{-1}\right)$, when $\rho_l = 0$. According to Sahota [11], the values of k_l, k_m, and ε to be used are 0.651, 0.026 $\left(W\ {}^0C^{-1}\ m^{-1}\right)$, and 0.21, respectively. Thus pseudo $k_s = 3.31\ \left(W\ {}^0C^{-1}\ m^{-1}\right)$ is obtained. With this value of k_s and for a maximum $\rho_l = 210\ \ (kg\ m^{-3})$, the maximum value of the overall thermal

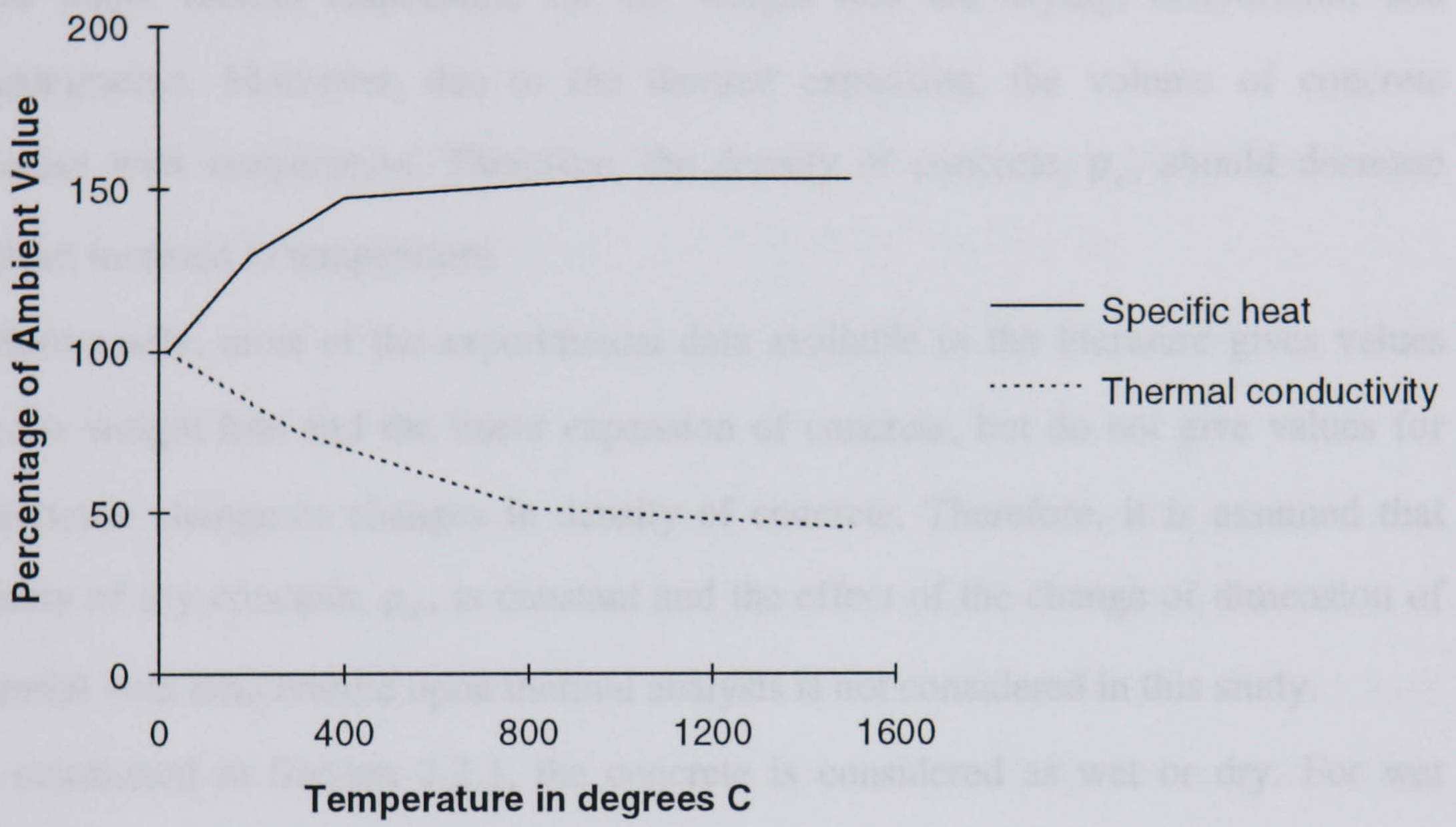

Figure 2.1 Thermal Properties of Dry Concrete: The Relationship of the Percentage Change of Ambient Values of the Specific Heat and Thermal Conductivity with Temperature [5, 13]

conductivity of wet concrete, k_c, is calculated to be 2.48 $\left(W\ {}^0C^{-1}\ m^{-1}\right)$. Thus k_c may vary between 1.75 and 2.48 $\left(W\ {}^0C^{-1}\ m^{-1}\right)$.

2.2.2 Density, ρ_c, and Specific Heat, $C_{p,c}$, of Concrete

When the concrete is subjected to high temperature it experiences a weight loss. The three major factors responsible for the weight loss are drying, dehydration and disintegration. Moreover, due to the thermal expansion, the volume of concrete increase with temperature. Therefore, the density of concrete, ρ_c, should decrease with an increase in temperature.

Unfortunately, most of the experimental data available in the literature gives values for the weight loss and the linear expansion of concrete, but do not give values for volumetric change or changes in density of concrete. Therefore, it is assumed that density of dry concrete, ρ_d, is constant and the effect of the change of dimension of material with temperature upon thermal analysis is not considered in this study.

As mentioned in Section 2.2.1, the concrete is considered as wet or dry. For wet concrete, overall specific heat can be expressed as:

$$C_{p,c} = \frac{\rho_d}{\rho} C_{p,d} + \frac{\rho_l}{\rho} C_{p,l} \tag{2.3}$$

where, $\rho = \rho_d + \rho_l$.

Typical values of normal weight concrete for $C_{p,l}$ and ρ_d at room temperature are 4187 $\left(J\ {}^0C^{-1}\ kg^{-1}\right)$ and 2400 $\left(kg\ m^{-3}\right)$ respectively [3].

A model proposed by Harmathy [13] is modified to represent $C_{p,d}$ as a function of temperature (see Figure 2.1). The model is expressed mathematically as follows:

$$C_{p,d} = C_{p,d,0} \qquad \left(T \le 20\ {}^0C\right) \tag{2.4a}$$

$$C_{p,d} = \left[1.0 + 1.6340 \times 10^{-3}(T - 20)\right] C_{p,d,0} \qquad \left(20 < T \le 200\ {}^0C\right) \tag{2.4b}$$

$$C_{p,d} = \left[1.2941 + 8.8235\times10^{-4}(T-200)\right]C_{p,d,0} \qquad \left(200 < T \leq 400\ ^{0}C\right) \qquad (2.4c)$$

$$C_{p,d} = \left[1.4706 + 9.8039\times10^{-5}(T-400)\right]C_{p,d,0} \qquad \left(400 < T \leq 1000\ ^{0}C\right) \qquad (2.4d)$$

$$C_{p,d} = 1.5294\,C_{p,d,0} \qquad \left(1000\ ^{0}C < T\right) \qquad (2.4e)$$

Where, $C_{p,d,0}$ is the specific heat of dry concrete at room temperature, for normal weight concrete, a typical value for $C_{p,d,0}$ is $850\ \left(J\ ^{0}C^{-1}\,kg^{-1}\right)$ [13].

2.2.3 Thermal Conductivity of Steel, k_s

Steel constitutes only a small percentage in volume of reinforced concrete structures. Therefore, small variations in its thermal properties would have a negligible effect on the distribution of temperatures [3]. However, the thermal properties of steel have been investigated more thoroughly than those of concrete [18], and may be easily described.

Similar to concrete, the thermal conductivity of steel, k_s, decreases with rise in temperature. The amount and rate of this decrease depends mainly upon the composition of the steel, especially the carbon content. A typical model proposed by Bizri [3] is modified to represent k_s as a function of temperature (see Figure 2.2). This model can be expressed mathematically as follows:

$$k_s = k_{s,0} \qquad \left(T \leq 20\ ^{0}C\right) \qquad (2.5a)$$

$$k_s = \left[1.0 - 5.6384\times10^{-4}(T-20)\right]k_{s,0} \qquad \left(20 < T \leq 593\ ^{0}C\right) \qquad (2.5b)$$

$$k_s = 0.6769\,k_{s,0} \qquad \left(593\ ^{0}C < T\right) \qquad (2.5c)$$

Where, $k_{s,0}$ is the thermal conductivity of steel at room temperature, a typical value for $k_{s,0}$ is 50.83 $\left(W\ {}^{0}C^{-1}\ m^{-1}\right)$ [3].

2.2.4 Specific Heat, $C_{p,s}$, and Density, ρ_s, of Steel

Available data in the literature shows that there is no appreciable decrease in density of steel, ρ_s, at high temperatures ($T<600\ {}^{0}C$) [3, 18]. Therefore, ρ_s, may be assumed constant and a typical valve of ρ_s is 7690 $(kg\ m^{-3})$ [3].

However, the available data on the specific heat of steel, $C_{p,s}$, shows that $C_{p,s}$ increases with rise in temperature [18, 3]. A model proposed by Bizri [3] is modified to represent $C_{p,s}$ as a function of temperature (see Figure 2.2). This is expressed mathematically as follows:

$$C_{p,s} = C_{p,s,0} \qquad \left(T \le 20\ {}^{0}C\right) \qquad (2.6a)$$

$$C_{p,s} = \left[1.0+8.1815\times10^{-4}(T-20)\right]C_{p,s,0} \qquad \left(20 < T \le 400\ {}^{0}C\right) \qquad (2.6b)$$

$$C_{p,s} = \left[1.3109+1.3115\times10^{-3}(T-400)\right]C_{p,s,0} \qquad \left(400 < T \le 593\ {}^{0}C\right) \qquad (2.6c)$$

$$C_{p,s} = 1.5640\,C_{p,s,0} \qquad \left(593\ {}^{0}C < T\right) \qquad (2.6d)$$

Where, $C_{p,s,0}$ is the specific heat of steel at room temperature, a typical value of $C_{p,s,0}$ is 460 $\left(J\ {}^{0}C^{-1}\ kg^{-1}\right)$ [3].

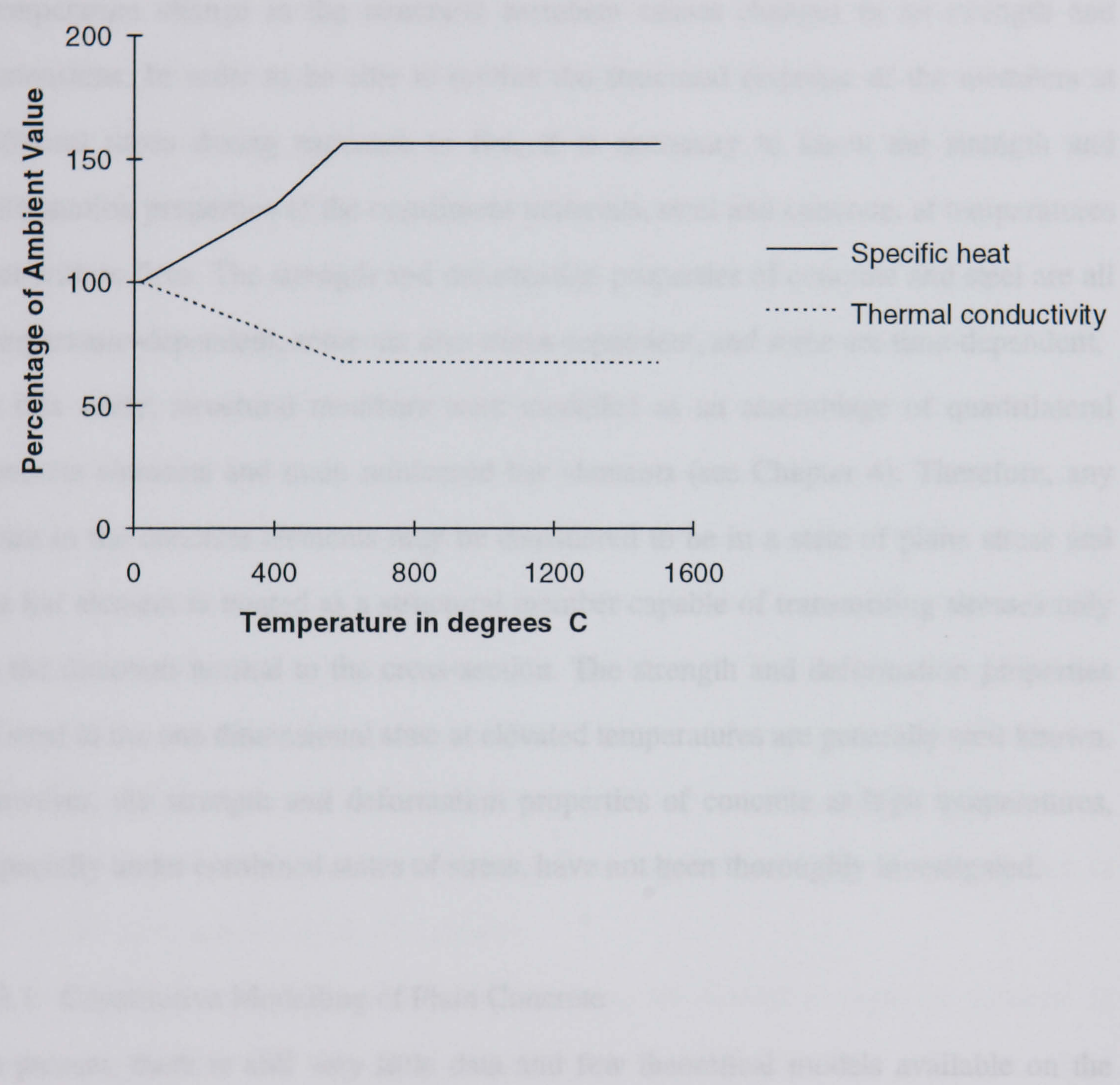

Figure 2.2 Thermal Properties of Steel: The Relationship of the Percentage Change of Ambient Values of the Specific Heat and Thermal Conductivity with Temperature [3]

2.3 Strength and Deformation Properties of Materials at Elevated Temperatures

This section deals with the strength and deformation properties used in the structural analysis of planar reinforced concrete members in fire conditions. These properties are entered into the computer programme, FPPRCM-S, which evaluates the structural response of planar reinforced concrete members to fire.

Temperature change in the structural members causes changes in its strength and dimensions. In order to be able to predict the structural response of the members at different times during exposure to fire, it is necessary to know the strength and deformation properties of the constituent materials, steel and concrete, at temperatures met with in fires. The strength and deformation properties of concrete and steel are all temperature-dependent, some are also stress-dependent, and some are time-dependent.

In this study, structural members were modelled as an assemblage of quadrilateral concrete elements and main reinforced bar elements (see Chapter 4). Therefore, any point in the concrete elements may be considered to be in a state of plane stress and the bar element is treated as a structural member capable of transmitting stresses only in the direction normal to the cross-section. The strength and deformation properties of steel in the one dimensional state at elevated temperatures are generally well known. However, the strength and deformation properties of concrete at high temperatures, especially under combined states of stress, have not been thoroughly investigated.

2.3.1 Constitutive Modelling of Plain Concrete

At present, there is still very little data and few theoretical models available on the constitutive modelling of concrete under biaxial states of stress at elevated temperatures. Therefore, in this study the models at room temperature were extended to elevated temperatures simply considering all the relevant parameters of the material as temperature dependent.

2.3.1.1 Failure Envelope

There is very little data available in the literature on the effect of heating on the failure of concrete under biaxial loading. However, several investigators have studied the biaxial strength of concrete at room temperature [19, 20]. These results show that the biaxial tensile strength of concrete is approximately equal to its uniaxial tensile strength. In the region of biaxial compression-tension, the results show that the tensile stress at failure decreased as the simultaneously acting compressive stress was increased. Finally, in the region of biaxial compression, the results show that considerably higher strength is obtained in biaxial compression than in uniaxial compression.

Examination of the crack pattern in flat specimens after failure indicates that the failure can be classed into two distinct modes: cracking and yielding. Tests have shown that in the biaxial tension region or biaxial tension-compression region failure is characterised by the formation of a single cleavage perpendicular to the maximum tensile stress. On the other hand, in biaxial compression, numerous micro cracks parallel to the free surfaces of the specimen (plane of loading) are formed. However, the specimen can still undergo some apparent plastic deformation before it collapses completely. The eventual failure is by tensile splitting in a plane parallel to the load, when the third dimension is unrestrained. This suggests that tensile deformation is vital in the failure mechanism of concrete.

As mentioned before, there is very little data on the biaxial strength of concrete at higher temperatures. For this study, however, the formulation of the failure envelope proposed by Barzegar-Jamshidi [21] (see Figure 2.3) which was based on a slight modification of the Kupfer and Gerstle [22] expressions was adopted with the parameters considered temperature dependent.

In Figure 2.3, the failure surfaces of the biaxial strength envelope is divided into four regions, which depend on the stress state as represented by the principal-stress ratio $\alpha = \sigma_{c1}/\sigma_{c2}$. Compressive stresses are assumed to be negative and tensile stresses

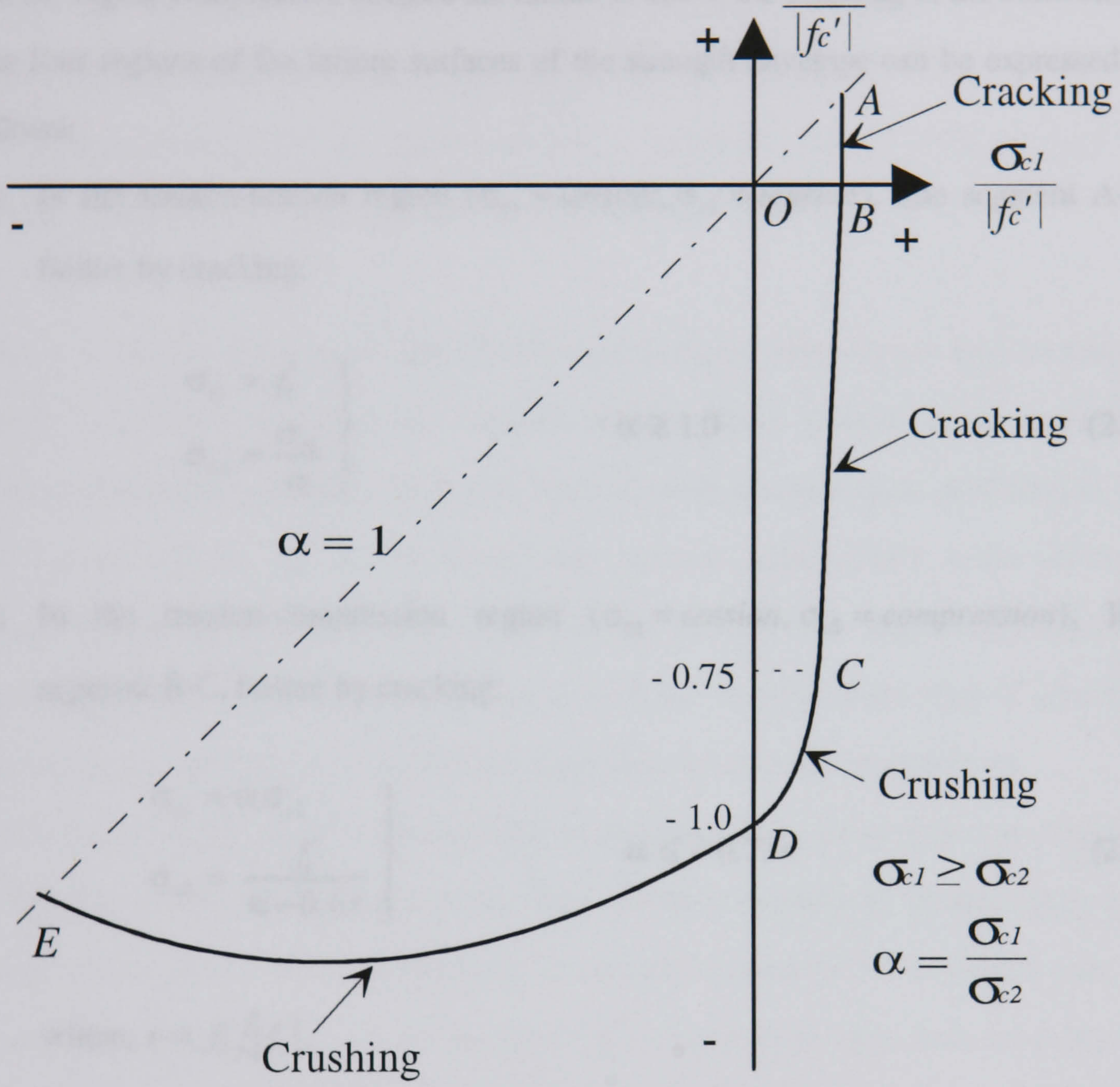

Figure 2.3 Concrete Biaxial Failure Envelope: Representative Relationship of the Variation of Biaxial Tensile and Compressive Stresses in Concrete at Failure [21]

positive, and the principal directions are chosen so that $\sigma_{c1} \geq \sigma_{c2}$ algebraically. It can be seen that for compression stresses smaller than $0.75\ f_c^{'}$ failure is assumed to occur by the cracking of the concrete perpendicular to the principal tensile stress direction, and for higher compressive stresses the failure is due to the crushing of the concrete. The four regions of the failure surfaces of the strength envelope can be expressed as follows:

(1) In the tension-tension region ($\sigma_{c1} = tension$, $\sigma_{c2} = tension$), line segment A-B, failure by cracking:

$$\left.\begin{aligned} \sigma_{c1} &= f_t^{'} \\ \sigma_{c2} &= \frac{\sigma_{c1}}{\alpha} \end{aligned}\right\} \qquad \alpha \geq 1.0 \qquad (2.7)$$

(2) In the tension-compression region ($\sigma_{c1} = tension$, $\sigma_{c2} = compression$), line segment B-C, failure by cracking:

$$\left.\begin{aligned} \sigma_{c1} &= \alpha\,\sigma_{c2} \\ \sigma_{c2} &= \frac{f_t^{'}}{\alpha - 0.6r} \end{aligned}\right\} \qquad \alpha \leq -0.73r \qquad (2.8)$$

where, $r = f_t^{'} \big/ \left| f_c^{'} \right|$.

(3) In the tension-compression region ($\sigma_{c1} = tension$, $\sigma_{c2} = compression$), line segment C-D, failure by crushing:

$$\left.\begin{aligned} \sigma_{c1} &= \alpha\,\sigma_{c2} \\ \sigma_{c2} &= \frac{f_c^{'}}{12.8r}\left[9r + \alpha + \sqrt{(9r+\alpha)^2 - 66.56r^2}\right] \end{aligned}\right\} \qquad -0.73r < \alpha \leq 0 \qquad (2.9)$$

(4) In the compression-compression region ($\sigma_{c1} = compression$, $\sigma_{c2} = compression$), line segment D-E, failure by crushing:

$$\left.\begin{aligned} \sigma_{c1} &= \alpha\,\sigma_{c2} \\ \sigma_{c2} &= \frac{1+3.65\alpha}{(1+\alpha)^2}\,f_c' \end{aligned}\right\} \qquad 0< \alpha \leq 1 \qquad (2.10)$$

Within this model the initiation of a cracking or crushing process at any location occurs when the concrete stresses reach one of the failure surfaces.

The main advantages of this model are that it is simple and the required data are readily obtainable from uniaxial tests on the concrete.

2.3.1.2 Concrete Stiffness: Integral Values and Stiffness After Failure by Crushing

Ideally a constitutive model for concrete should reflect definite strain hardening characteristics before failure, the failure itself, as well as some strain softening in the post-failure regime. The model should also perform satisfactorily under different states of multiaxial loading and yet be simple, flexible and numerically feasible. Finally, the material model must be easy to calibrate to a particular type of concrete. Therefore, a model which is constructed upon uniaxial test data is preferable.

A non-linear elastic model encompassing most of the above properties was proposed by Ottosen [23] at room temperature. This model is capable of representing, in a simple way, most of the characteristics of concrete behaviour for a general state of stress. These features include: (1) the effect of all three stress invariants provided the failure criteria are formulated based on those invariants; (2) consideration of dilation; (3) the production of completely smooth stress-strain curves; (4) the prediction of realistic failure stresses; (5) the simulation of post-crushing behaviour; and (6) the applicability to all stress states including those where tensile stresses occur. In addition, its calibration to a specific concrete requires only uniaxial test data. Any failure criterion can be employed in conjunction with the constitutive model and this is accomplished by modifying a single parameter in the model.

Barzegar-Jamshidi [21] used this model for the constitutive modelling of plain concrete at room temperature. In this study the model is extended to fire conditions simply by considering all the relevant parameters as temperature dependent.

In this isotropic model the stress-strain relationship is described by appropriate changes in the secant values of Young's modulus and Poisson's ratio. The adopted constitutive model is a specialised 2-D form of the actual 3-D model by Ottosen [23].

In this isotropic model the stress-strain relationship of the concrete is expressed as:

$$\begin{Bmatrix} \sigma_{c,x} \\ \sigma_{c,y} \\ \tau_{c,xy} \end{Bmatrix} = \frac{\overline{E}_c}{1-\overline{\nu}_c^2} \begin{bmatrix} 1 & \overline{\nu}_c & 0 \\ \overline{\nu}_c & 1 & 0 \\ 0 & 0 & \dfrac{1-\overline{\nu}_c}{2} \end{bmatrix} \begin{Bmatrix} \varepsilon_{c,x} \\ \varepsilon_{c,y} \\ \gamma_{c,xy} \end{Bmatrix} \tag{2.11}$$

and the constitutive matrix of the concrete is

$$[C]_c = \frac{\overline{E}_c}{1-\overline{\nu}_c^2} \begin{bmatrix} 1 & \overline{\nu}_c & 0 \\ \overline{\nu}_c & 1 & 0 \\ 0 & 0 & \dfrac{1-\overline{\nu}_c}{2} \end{bmatrix} \tag{2.12}$$

in which the secant value of Young's modulus, $\overline{E}_c$, and Poisson's ratio, $\overline{\nu}_c$, are modified and described in following section to account for material nonlinearites such as softening and dilatation.

(1) Change in the secant value of Young's modulus:

The expression used to describe Young's modulus, $\overline{E}_c$, is as follows [21]:

$$\overline{E}_c = \frac{E_c}{2} - \gamma\left(\frac{E_c}{2} - E_f\right) \pm \sqrt{\left[\frac{E_c}{2} - \gamma\left(\frac{E_c}{2} - E_f\right)\right]^2 + E_f^{\,2}\,\gamma\left[D(1-\gamma)-1\right]} \tag{2.13}$$

In which the positive and negative signs apply to the ascending and descending part of the stress-strain curves, respectively.

In equation (2.13) the non linearity index, γ, is a measure of the actual loading in relation to the failure envelope. Its value determines the amount of non linearity in the stress-strain curves. Assuming tension as positive and compression as negative, for a biaxial compression loading the non linearity index, γ, is defined as (see Figure 2.4):

$$\gamma = \frac{\sigma_{c2}}{\sigma_{c2,f}} \tag{2.14}$$

where, σ_{c2} is the actual maximum compressive principal stress, and $\sigma_{c2,f}$ is its corresponding failure value. Provided that the other principal stress, σ_{c1}, is unchanged ($\sigma_{c1} \geq \sigma_{c2}$). $\sigma_{c2,f}$ can be calculated using following formula:

$$\sigma_{c2,f} = -\frac{|f_c'|}{2}\left[\frac{2\sigma_{c1}}{|f_c'|} + 1.0 + \sqrt{1.0 - 10.6\frac{\sigma_{c1}}{|f_c'|}}\right] \tag{2.15}$$

Using equations (2.14) and (2.15) γ can be calculated, $\gamma < 1$, $\gamma = 1$, $\gamma > 1$ correspond to stress states located inside, on, and outside the failure envelope, respectively.

When tensile stresses occur, the actual state of stress (σ_{c1}, σ_{c2}), where at least σ_{c1} is a tensile stress, is transformed to a uniaxial compressive case by superposing a hydrostatic pressure, $-\sigma_{c1}$, on to the existing field thereby obtaining the new stress state (0, σ_{c2}') in which $\sigma_{c2}' = \sigma_{c2} - \sigma_{c1}$, then γ is defined as:

$$\gamma = \frac{\sigma_{c2}'}{\sigma_{c2,f}'} = \frac{\sigma_{c2}'}{f_c'} \tag{2.16}$$

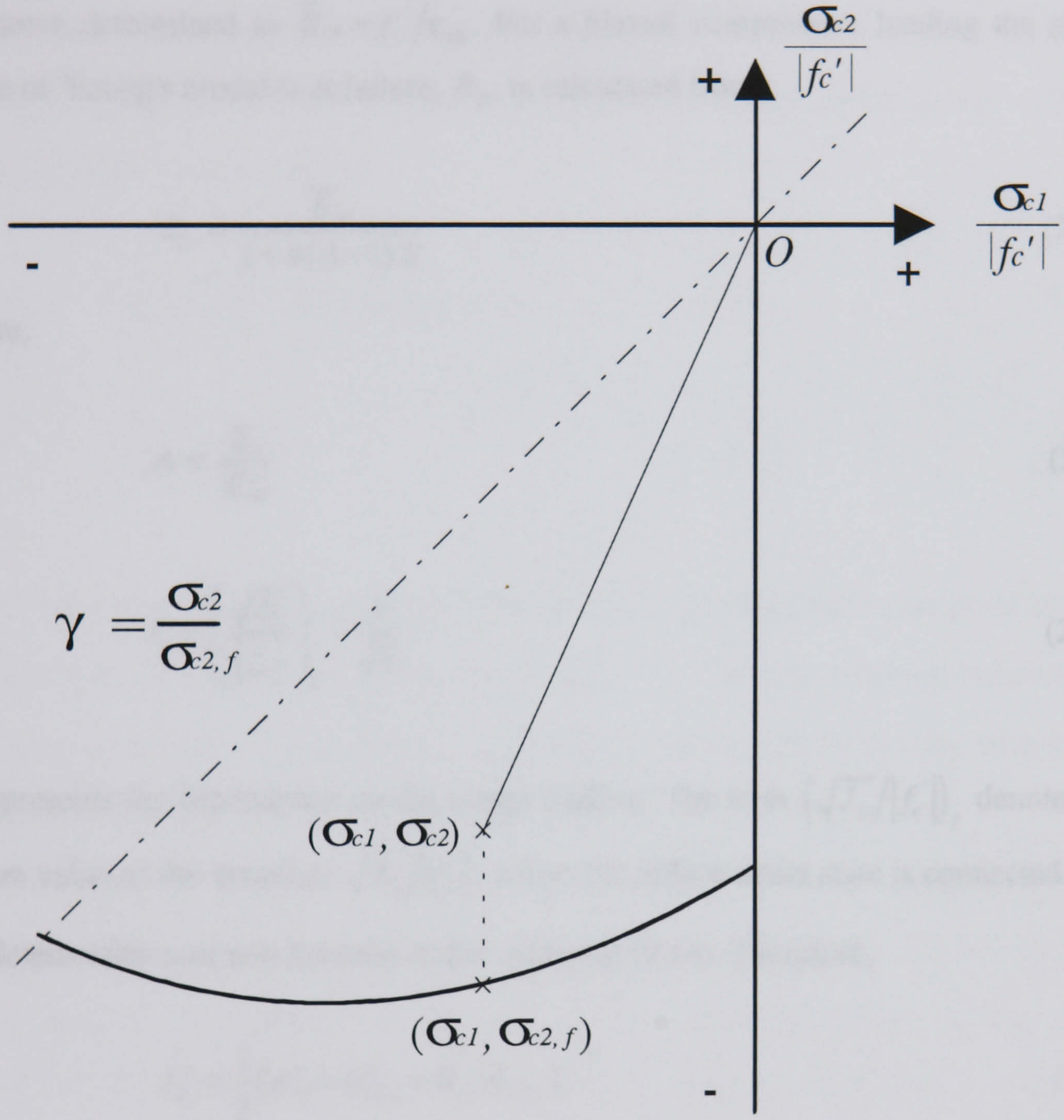

Figure 2.4 Determination of Non-linear Index, γ, [21]

In this case, $\gamma < 1$ always holds. This reduction in the non linearity index is consistent with the fact that the more the stress state involves tensile stresses. the more the concrete behaviour is linear. In equation (2.13) E_c is the elastic modulus, and $E_f = \overline{E}_{cp}$ is the secant modulus at peak stress of a uniaxially loaded compressive specimen determined as $\overline{E}_{cp} = f_c^{'}/\varepsilon_{c0}$. For a biaxial compressive loading the secant value of Young's modulus at failure, E_f, is calculated from:

$$E_f = \frac{\overline{E}_{cp}}{1+4(A-1)X} \tag{2.17}$$

where,

$$A = \frac{E_c}{\overline{E}_{cp}} \tag{2.18}$$

$$X = \left(\frac{\sqrt{J_2}}{|f_c^{'}|}\right)_f - \frac{1}{\sqrt{3}} \tag{2.19}$$

X represents the dependence on the actual loading. The term $\left(\sqrt{J_2}/|f_c^{'}|\right)_f$ denotes the failure value of the invariant $\sqrt{J_2}/|f_c^{'}|$, where the failure stress state is connected with the determination of non linearity index, equation (2.14). Therefore,

$$J_2 = \frac{1}{3}\left(\sigma_{c1}^2 + \sigma_{c2,f}^2 - \sigma_{c1}\,\sigma_{c2,f}\right) \tag{2.20}$$

$1/\sqrt{3}$ is the value of $\left(\sqrt{J_2}/|f_c^{'}|\right)_f$ for the case of a uniaxially loaded specimen in compression. When tensile stress occur, it is assumed that $E_f = E_{cp}$. Note that we presently only deal with compressive stress states and have $X \geq 0$. where $X = 0$ holds for uniaxial compressive loading. The value $E_f = \overline{E}_{cp}$ holds when $X = 0$. otherwise $E_f < \overline{E}_{cp}$ applies. The dependence of E_f on the actual type of concrete is represented in equation (2.17) by the parameters $\overline{E}_{cp}$ and A.

The parameter D in equation (2.13) determines the degree of strain softening when crushing of concrete occurs. It affects the stress-strain curves before failure only slightly. The parameter D determines the post-failure behaviour, the precise form of this part of the curve is unknown, and is in fact, not obtained by a standard uniaxial compressive test. Therefore, the actual value of D is simply chosen so that a convenient post-failure curve results. However, there are certain limitations to D, its range of value is determined as:

$$\left(1-\frac{A}{2}\right)^2 < D \le 1+A(A-2) \qquad A \le 2 \qquad (2.21a)$$

$$0 \le D \le 1 \qquad A \ge 2 \qquad (2.21b)$$

Under uniaxial or biaxial compression, crushing occurs when the stress point reaches segment DE of the failure envelope (see Figure 2.3). The post-crushing behaviour in this zone is controlled by equation (2.13) using negative sign before the square root along with a suitable choice of the parameter D.

The post-crushing behaviour in tension-compression zone has not been determined experimentally but can be modelled conveniently as follows: for a given state of biaxial tension-compression that lies on segment CD of the failure envelope (see Figure 2.3) the non linearity index at failure, $\gamma_f < 1$, is determined from $\gamma_f = \sigma_{c2}^{'} / f_c^{'}$, where $\sigma_{c2}^{'} = \sigma_{c2} - \sigma_{c1}$. As shown in Figure 2.5 the post-crushing curve AB is then assumed to be obtained by the translation parallel to the horizontal axis of the part MN of the original descending branch of the curve. Corresponding to some actual γ value, in the post-crushing region the secant value is obtained as:

$$\overline{E}_c = \frac{\gamma\, \overline{E}_{MN}\, \overline{E}_A\, \overline{E}_M}{\gamma\, \overline{E}_A\, \overline{E}_M + \gamma_f\, \overline{E}_{MN}\left(\overline{E}_M - \overline{E}_A\right)} \qquad (2.22)$$

in which, $\overline{E}_{MN}$ is determined from equation (2.13) with the negative sign before the square root, using γ. $\overline{E}_A$ and $\overline{E}_M$ are the secant value corresponding to γ_f which are determined from equation (2.13) using the positive and negative signs before the square root, respectively.

(2) Change in the secant value of Poisson's ratio:

Experimental evidence indicates that under uniaxial and biaxial compression concrete first compacts and then dilates due to internal micro cracking. To take this into account the expressions for the secant value of Poisson's ratio are assumed to have the following form:

$$\overline{\nu}_c = \nu_c \qquad \gamma \le \gamma_a \qquad (2.23a)$$

$$\overline{\nu}_c = \nu_f - (\nu_f - \nu_c)\sqrt{1-\left(\frac{\gamma-\gamma_a}{1-\gamma_a}\right)^2} \qquad \gamma > \gamma_a \qquad (2.23b)$$

where, ν_c is the initial secant Poisson's ratio and ν_f is the secant Poisson's ratio at the failure of crushing. Figure 2.6 is the plot of the non linearity index, γ vs. the secant Poisson's ratio as determined from equations (2.23a) and (2.23b). Equation (2.23) is valid up to crushing of the concrete. Although very little is known of the amount of increase in Poisson's ratio in the post crushing regime it is an experimental fact that dilatation continues in this region. In order to incorporate volumetric increases in the post-crushing region, the value of the secant bulk modulus at failure, $M_f = E_f / 3(1-2\nu_f)$ is slightly increased. For a given value of the secant Young's modulus, $\overline{E}_c$, in the post-crushing phase there exists a corresponding secant Poisson's ratio $\overline{\nu}_c^*$, so that the corresponding secant bulk modulus, M, is unchanged, that is

$$M = \frac{\overline{E}_c}{3(1-2\overline{\nu}_c^*)} = M_f = \text{constant} \qquad (2.24a)$$

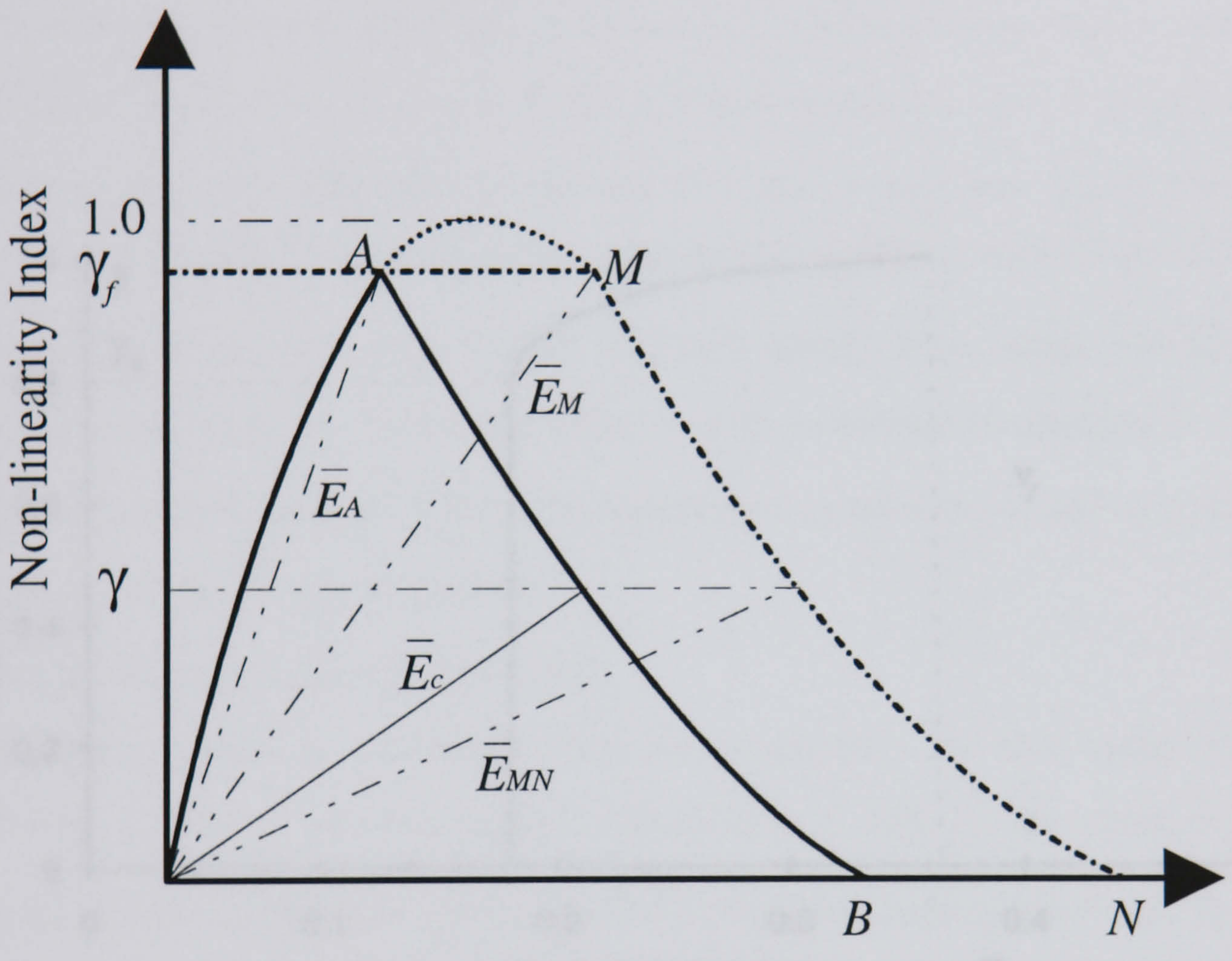

Figure 2.5 Post-failure Behaviour for Tension-compression States of Stress that Result in Crushing of Concrete [21]

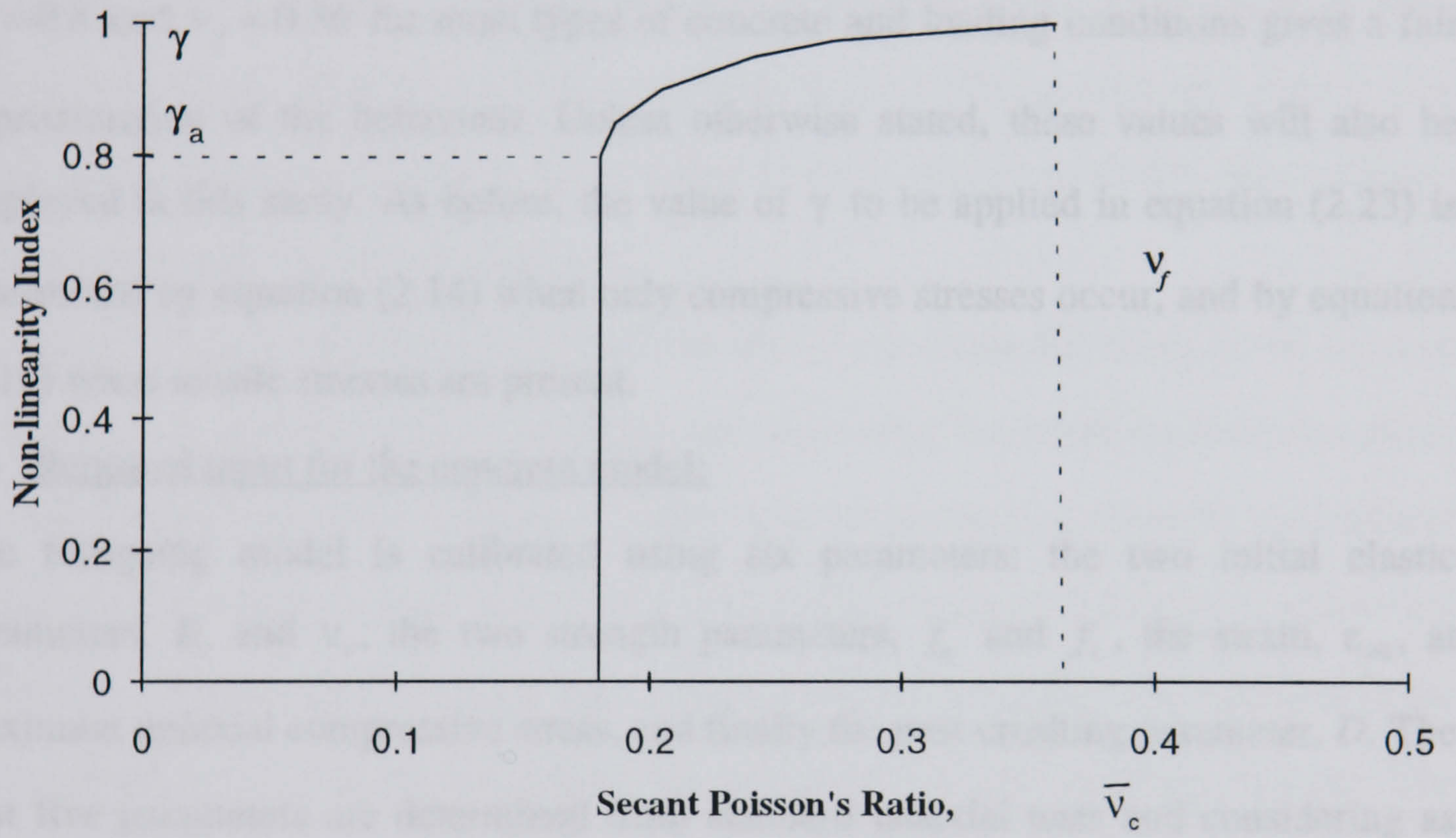

Figure 2.6 Variation of Secant Value of Poisson's Ratio, $\bar{\nu}_c$: The Relationship Presents Calculated Values of $\bar{\nu}_c$ Using Equation (2.23)

or

$$\bar{\nu}_c^* = 0.5 - \frac{\bar{E}_c}{6 M_f} \tag{2.24b}$$

In this study $\bar{\nu}_c = \bar{\nu}_c^*$ is employed in the post-crushing region.

For a biaxial tension-compression state of stress leading to crushing of concrete the same procedure is used to calculated ν_c in the post-crushing phase. In the model an upper bound $\bar{\nu}_c \leq 0.45$ is set to eliminate problems associated with Poisson's ratio approaching 0.5. It is suggested by Ottosen [23] that in equation (2.23) selecting $\gamma_a = 0.8$ and $\nu_f = 0.36$ for most types of concrete and loading conditions gives a fair approximation of the behaviour. Unless otherwise stated, these values will also be employed in this study. As before, the value of γ to be applied in equation (2.23) is determined by equation (2.14) when only compressive stresses occur, and by equation (2.16) when tensile stresses are present.

(3) Required input for the concrete model:

The foregoing model is calibrated using six parameters: the two initial elastic parameters, E_c and ν_c, the two strength parameters, f_c' and f_t', the strain, ε_{c0}, at maximum uniaxial compressive stress, and finally the post-crushing parameter, D. The first five parameters are determined from standard uniaxial tests and considering as temperature dependent for extending the model to fire conditions.

Detailed experimental verification of the above constitutive modelling of plain concrete at room temperature can be found in Reference 21. The performance of the model under uniaxial and biaxial stress state were illustrated and in general good agreement with the experimental results was found.

2.3.1.3 Concrete Stiffness after Cracking

The tensile weakness of concrete and the ensuing cracking that results therefrom, is a major factor contributing to the non-linear behaviour of reinforced concrete (R/C) structures [24]. During monotonic loading of a R/C structure continued up to its

failure, cracking occurs at an early stage of loading and introduces a distinct geometrical discontinuity within the structure. Therefore, the modelling of cracking is very important for finite element analysis of R/C structures. In order to model crack initiation and post-cracking behaviour three basic components must be incorporated in the analytical model. These include: a criterion for crack initiation, a method for crack representation and finally, a criterion for crack propagation [24].

At present, two methods of crack representation (discrete crack or smeared crack) have been introduced. Most models rely on a strength criterion for crack initiation. Therefore, in this study the strength criterion is employed and the crack is initiated once a stress point violates the failure envelope in the cracking zone (see Figure 2.3). In the finite element analysis of R/C structures crack can be modelled using either a discrete or smeared cracking approach.

The discrete crack modelling introduces an actual gap in the FE mesh at the location of a crack . It achieves this by doubling and separating the nodal co-ordinates along the crack path. This implies important changes in the numbering of nodes and element connectivities which in turn affects the global stiffness matrix. From the numerical point of view there are two major disadvantages for such an approach. The first is the crack propagation path has to follow the boundaries of the existing element. The second is to redefine the FE mesh as cracking propagates. These appear to require intricate programming techniques and to be still significantly restricted in use because complicated mesh refinements become necessary to accommodate the propagation of only a few discrete cracks. On the other hand, the discrete model is suitable for cases in which only a few cracks dominate the behaviour of the structure such as a shear beam. In plate and shell type structures, if punching shear failure can be avoided, in general, many cracks form before the failure is reached and no single crack dominates the behaviour.

The smeared crack approach makes use of drastic material property changes at the location of cracking as a means of simulating discontinuity. Such a change is achieved by reducing the stiffness properties in the direction orthogonal to the crack, without

involving any real gap in the mesh. Since material properties are evaluated only at sampling point in an element, such as the integration points or the nodes, such an approach represents average behaviour of some tributary area around that point. This has the effect of smearing the cracks over a certain area and imposes discontinuities in the stress field without making the displacement field discontinuous. Using the smeared approach cracks in different directions can be generated automatically without the need for redefining the initial finite element mesh. Due to its generality and simplicity, the smeared crack approach is employed in this study for crack representation.

Within this model the initiation of a cracking process at any Gauss Point happens when the concrete stress reach one of the failure surfaces (see Figure 2.3) either in biaxial tension, segment AB or in a combined tension-compression region, segment BC. After single cracking has taken place, the concrete is treated as an orthotropic material with principal axes normal and parallel to the crack direction (see Figure 2.7(a)). The concrete parallel to the crack direction is still capable of resisting either tensile or compressive forces. When it is subjected to tension, a pure linear elastic behaviour is assumed and when tensile stress exceeds the tensile strength a second crack is formed normal to the first crack (see Fig. 2.7(b)). On the other hand, when it is subjected to compression, experimental results show that the tensile cracks have caused damage to the concrete with the transverse tensile strain, having a degrading effect not only on the compressive strength but also on the compressive stiffness. Therefore, concrete in this situation is softer, with weaker values than those recorded from a standard cylinder test. The possibility of the crack closing and reopening was considered in this model. That is, when cracks closed the concrete was assumed to act as un-cracked concrete.

A model to determine the principal compressive stress (parallel to the crack direction) suggested by Vecchio [25] is used in this study, that is

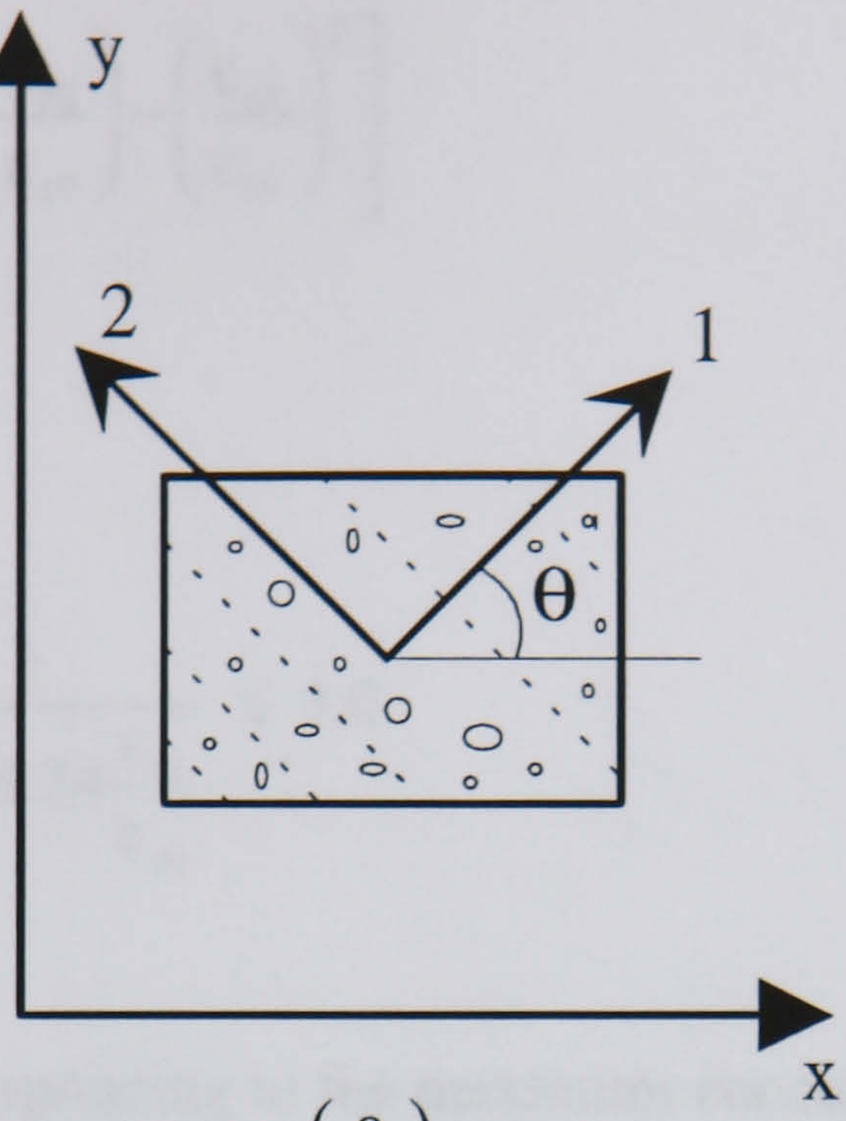

(a)

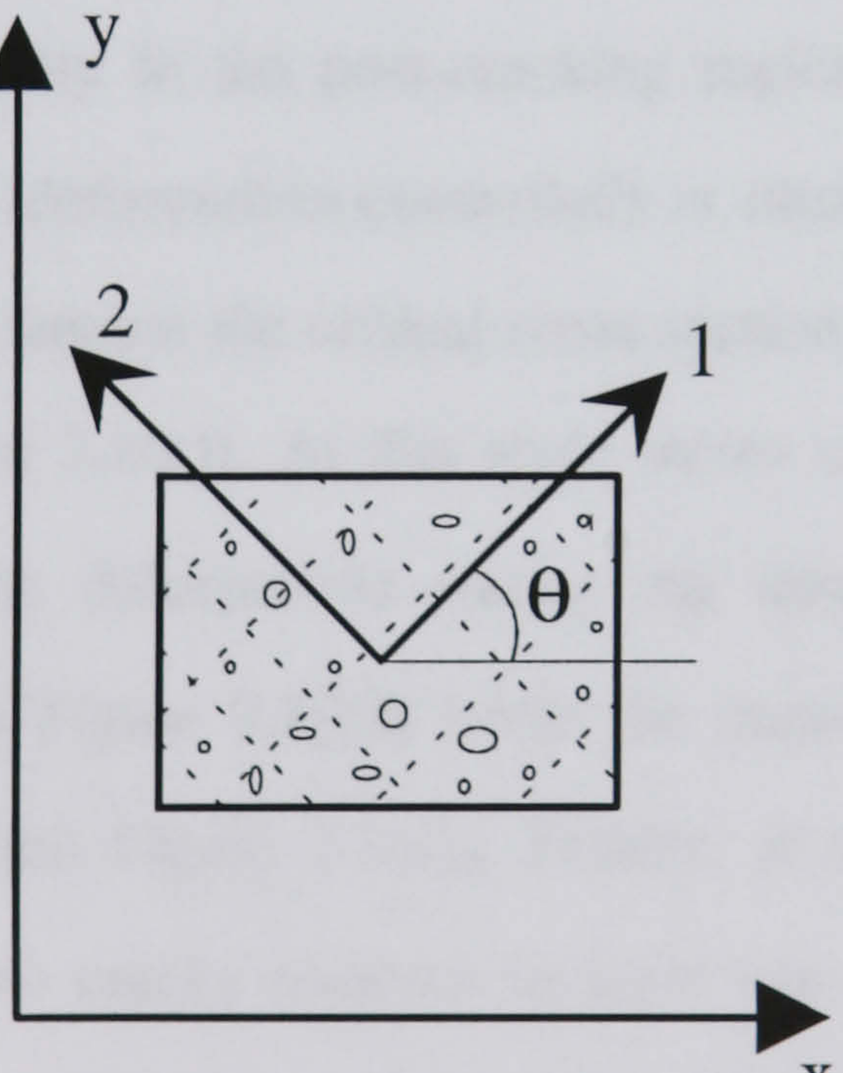

(b)

Figure 2.7 Orientation of Cracks in Concrete Elements

(a) Cracking in One Principal Direction

(b) Cracking in Both Principal Directions

$$\sigma_{c2} = \sigma_{c,max}\left[2\left(\frac{\varepsilon_{c2}}{\varepsilon_{c0}}\right)-\left(\frac{\varepsilon_{c2}}{\varepsilon_{c0}}\right)^2\right] \tag{2.25}$$

where

$$\frac{\sigma_{c,max}}{f_c'} = \frac{1}{0.8-0.34\frac{\varepsilon_{c1}}{\varepsilon_{c0}}} \leq 1.0 \tag{2.26}$$

where, ε_{c0} is the strain corresponding to the maximum concrete compressive strength, f_c'.

(1) Tension stiffening:

Fracture and crack propagation in concrete depend on the properties of the material in tension and its post-cracking behaviour. The experimental studies carried out by Willan, et al [26] indicate that the behaviour after cracking is not completely brittle and that there is some ductility in the post-cracking region. The behaviour of the uniaxially loaded specimen (deformation-controlled) is illustrated in more detail in Figure 2.8. Upon increasing tension the critical cross section of specimen reaches the strength limit, f_t' (see Figure 2.8(a)). At this stage micro cracks develop to form a fracture zone. Increasing the deformation causes the intact concrete outside the fracture zone to unload (see Figure 2.8(b)) while the material in the fracture zone undergoes strain softening (see Figure 2.8(c)). Finally, at the termination of strain softening behaviour the micro cracks coalesce to form one continuous macro crack and stresses in the specimen diminish to zero. This phenomenon is termed tension stiffening.

For modelling the tension stiffening behaviour of concrete in this study the secant normal stiffness is determined using a bilinear tension stiffening curve suggested by Rots et at [27] (see Figure 2.9 curve ABC). The curve ABC can be expressed mathematically as follows:

For line AB,

$$\sigma_{ct} = f_t^{'} - \frac{6 f_t^{'} (\varepsilon_{ct} - \varepsilon_{cr})}{2\varepsilon_{cu} - 9\varepsilon_{cr}} \qquad \varepsilon_{cr} < \varepsilon_{ct} \le \frac{2}{9}\varepsilon_{cu} \tag{2.27}$$

For line BC:

$$\sigma_{ct} = \frac{f_t^{'}}{3} - \frac{3 f_t^{'}}{7\varepsilon_{cu}}\left(\varepsilon_{ct} - \frac{2}{9}\varepsilon_{cu}\right) \qquad \frac{2}{9}\varepsilon_{cu} < \varepsilon_{ct} \le \varepsilon_{cu} \tag{2.28}$$

where, ε_{cr} is the strain in concrete at cracking, $\varepsilon_{cr} = f_t^{'}/E_c$, and ε_{cu} is the strain levels to terminate the artificially assigned softening branch, $\varepsilon_{cu} = \alpha_1 \varepsilon_{cr}$, $\alpha_1 = 10 \sim 25$ [21].

(2) Stiffness matrix for cracked concrete:

With the smeared crack representation, cracked concrete can be considered as a orthotropic material with its principal axes, normal and parallel to the crack direction (see Figure 2.7). Further, after cracking, Poisson's effect can be considered to be negligible due to the lack of interaction between the two orthogonal directions. Thus, the concrete material stiffness matrix evaluated with respect to the principal 1, 2 axes system is

$$\begin{Bmatrix} \sigma_{c1} \\ \sigma_{c2} \\ \tau_{c12} \end{Bmatrix} = \begin{bmatrix} \overline{E}_{c1} & 0 & 0 \\ 0 & \overline{E}_{c2} & 0 \\ 0 & 0 & \beta G_c \end{bmatrix} \begin{Bmatrix} \varepsilon_{c1} \\ \varepsilon_{c2} \\ \gamma_{c12} \end{Bmatrix} \tag{2.29a}$$

or

$$\{\sigma_c\}_{12} = [C^{'}]\{\varepsilon_c\}_{12} \tag{2.29b}$$

where, $\overline{E}_{c1}$ and $\overline{E}_{c2}$ are the secant moduli. They can be evaluated using following formulas:

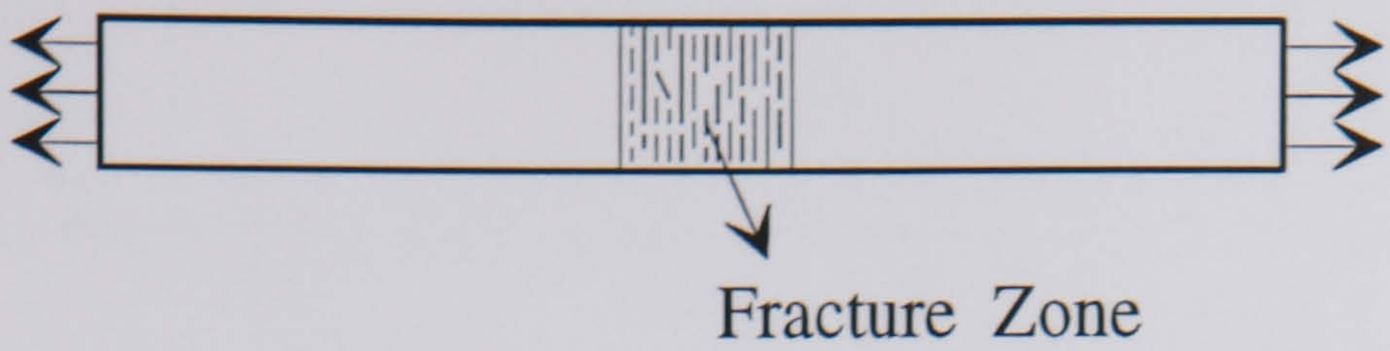

(a)

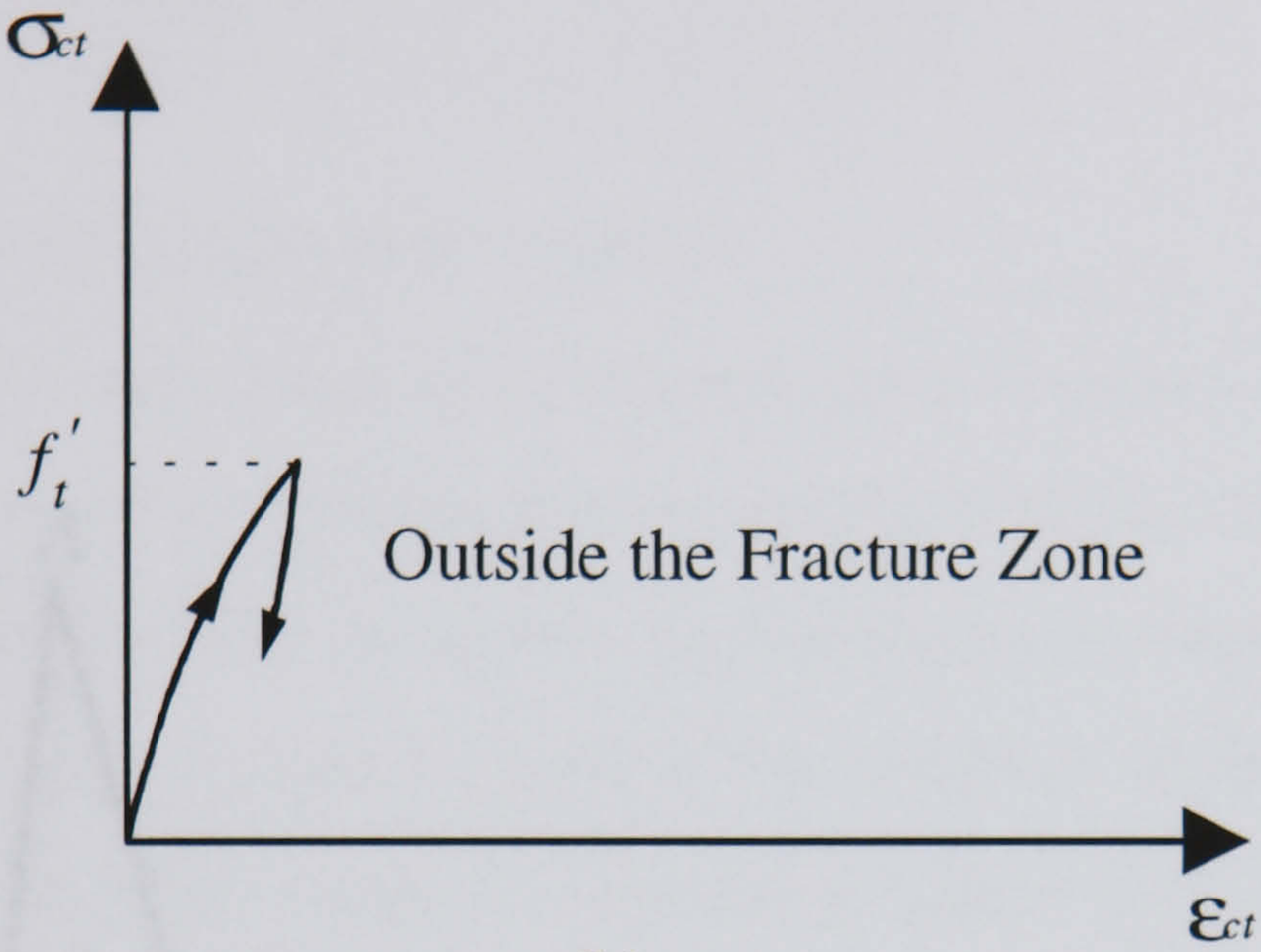

(b)

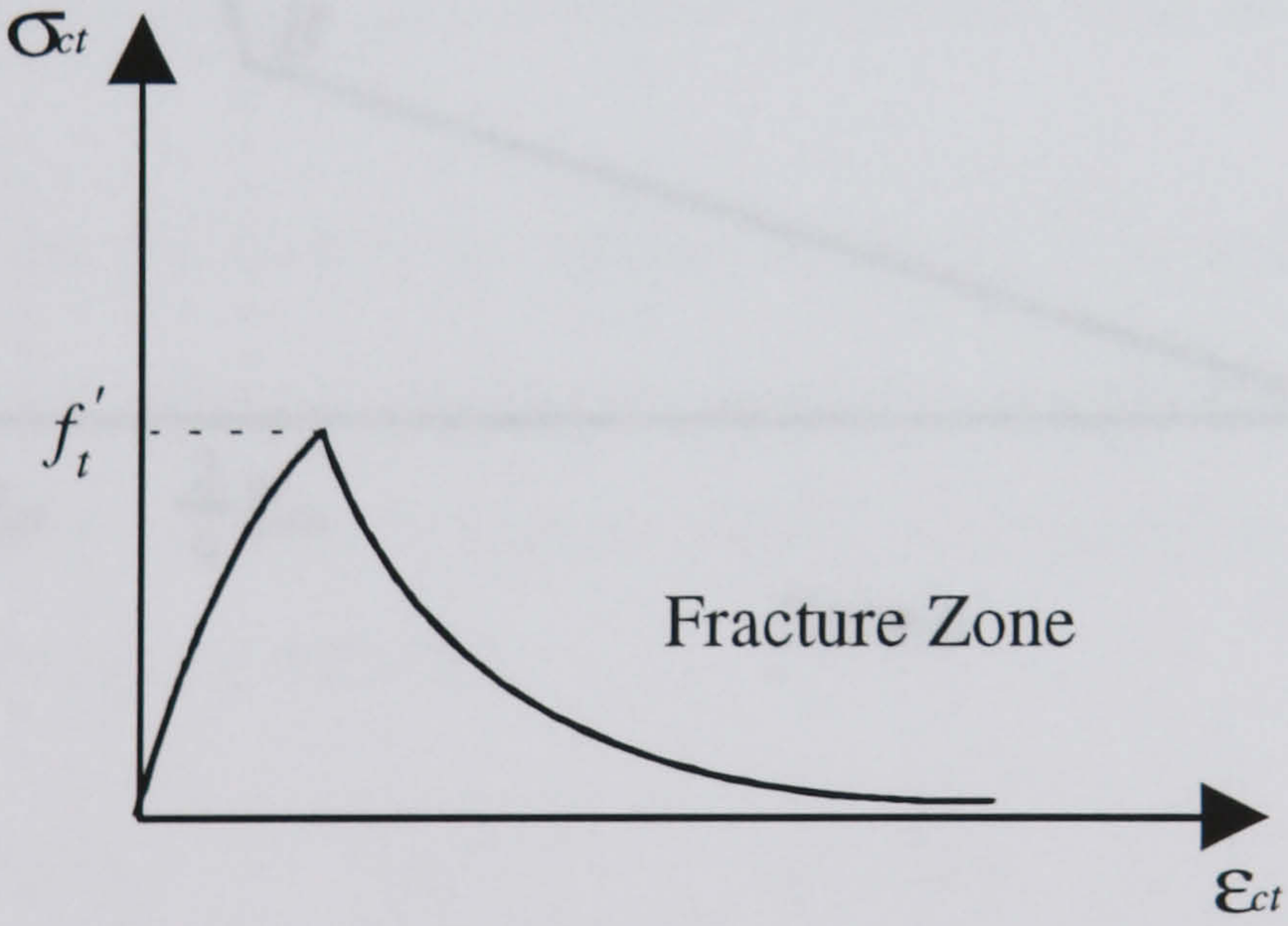

(c)

Figure 2.8 Stress-strain Curves for the Concrete Specimen under Uniaxial Tension [21]

(a) Representation of Test Specimen Subject to Uniaxial Tensile Loading

(b) Stress-Strain Relationship for Concrete outside the Fracture Zone

(c) Stress-Strain Relationship for Concrete within the Fracture Zone

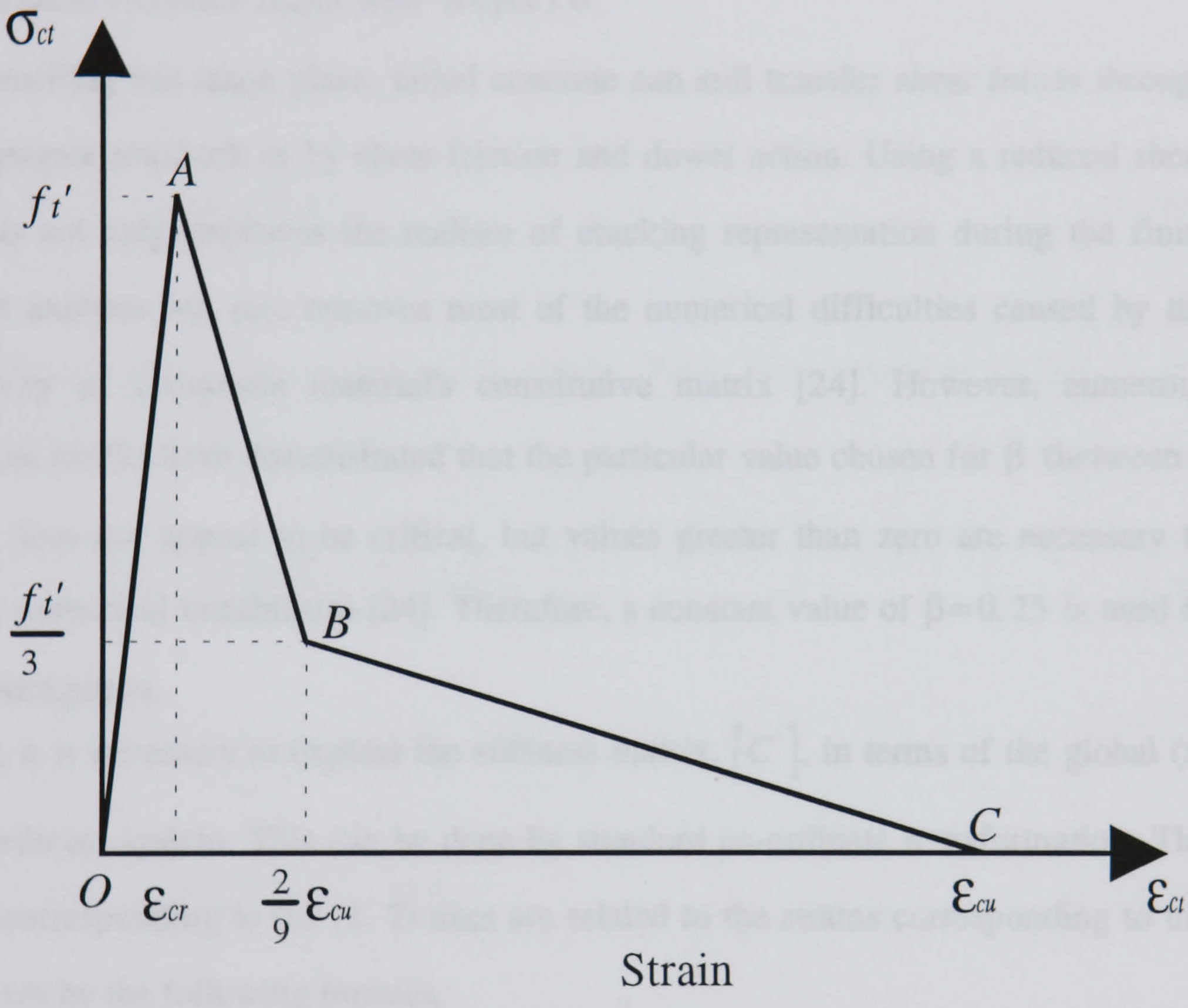

Figure 2.9 Tension Constitutive Relation of Concrete Used in Analysis Procedure

$$\overline{E}_{c1} = \frac{\sigma_{c1}}{\varepsilon_{c1}} \tag{2.30}$$

$$\overline{E}_{c2} = \frac{\sigma_{c2}}{\varepsilon_{c2}} \tag{2.31}$$

β is the shear retention factor with $0<\beta\leq 1.0$.

After cracking has taken place, failed concrete can still transfer shear forces through the aggregate interlock or by shear friction and dowel action. Using a reduced shear modulus not only improves the realism of cracking representation during the finite element analysis but also removes most of the numerical difficulties caused by the singularity of composite material's constitutive matrix [24]. However, numerous analytical results have demonstrated that the particular value chosen for β (between 0 and 1) does not appear to be critical, but values greater than zero are necessary to prevent numerical instabilities [24]. Therefore, a constant value of $\beta=0.25$ is used in this investigation.

Finally, it is necessary to express the stiffness matrix, $[C']$, in terms of the global (x, y) co-ordinate system. This can be done by standard co-ordinate transformation. The strains corresponding to the (1, 2) axes are related to the strains corresponding to the (x, y) axes by the following formula:

$$\begin{Bmatrix} \varepsilon_{c1} \\ \varepsilon_{c2} \\ \gamma_{c12} \end{Bmatrix} = \begin{bmatrix} \cos^2\theta & \sin^2\theta & \sin\theta\cos\theta \\ \sin^2\theta & \cos^2\theta & -\sin\theta\cos\theta \\ -2\sin\theta\cos\theta & 2\sin\theta\cos\theta & \cos^2\theta-\sin^2\theta \end{bmatrix} \begin{Bmatrix} \varepsilon_{c,x} \\ \varepsilon_{c,y} \\ \gamma_{c,xy} \end{Bmatrix} \tag{2.32a}$$

or

$$\{\varepsilon_c\}_{12} = [T(\theta)]\{\varepsilon_c\}_{xy} \tag{2.32b}$$

where, θ is the angle from the x-axis to the 1-axis (see Figure 2.7).

Similarly, the stresses in the two co-ordinate systems are related by:

$$\begin{Bmatrix} \sigma_{c,x} \\ \sigma_{c,y} \\ \tau_{c,xy} \end{Bmatrix} = \begin{bmatrix} \cos^2\theta & \sin^2\theta & -2\sin\theta\cos\theta \\ \sin^2\theta & \cos^2\theta & 2\sin\theta\cos\theta \\ \sin\theta\cos\theta & -\sin\theta\cos\theta & \cos^2\theta - \sin^2\theta \end{bmatrix} \begin{Bmatrix} \sigma_{c1} \\ \sigma_{c2} \\ \tau_{c12} \end{Bmatrix} \tag{2.33a}$$

or

$$\{\sigma_c\}_{xy} = [T(\theta)]^T \{\sigma_c\}_{12} \tag{2.33b}$$

where, T signifies the transpose of the matrix. Thus, from equations (2.29), (2.32), and (2.33) one can be obtained:

$$\{\sigma_c\}_{xy} = [T(\theta)]^T [C'][T(\theta)]\{\varepsilon_c\}_{xy} \tag{2.34}$$

and

$$[C]_c = [T(\theta)]^T [C'][T(\theta)] \tag{2.35}$$

2.3.1.4 Modulus of Elasticity of Concrete, E_c

The modulus of elasticity of concrete, E_c, has been studied by several investigators e.g. [28, 29]. Most of the investigation show that the modulus of elasticity of concrete decreases with increasing temperature.

(1) The main factor affecting E_c

(a) Moisture:

Lankard et al [30] show that the loss of moisture due to heating leads to a decrease in E_c. Dehydration at high temperatures leads to a further reduction in E_c.

(b) Mix characteristics

i. Water-cement ratio: The higher the water-cement ratio the greater the reduction in E_c at high temperatures [31].

ii. Curing and age: Curing and age have a slight effect on the initial value of E_c. This effect becomes negligible at high temperatures.

iii. Mix ratio and compactness: This effect becomes negligible on E_c at high temperatures.

iv. Aggregate type: Effect of aggregate type becomes apparent at the temperatures where mineralogical changes in aggregate occur. The temperature at which transformations in minerals take place depends on the amount of impurities present in the minerals. The influence of aggregate type obtained by Zoldners [32] shows that the concrete with more expansive aggregates are subjected to a great reduction in E_c at high temperatures.

v. Cement type: E_c is reduced more at high temperatures, when the cement has low C_3A and high C_3S and C_4AF content [30].

(c) Test conditions:

i. Maximum temperature reached: The temperature level reached has a significant effect on the amount of dehydration and on the transformations that take place. Wherein the higher the temperature, the greater the reduction in E_c.

ii. Exposure time at high temperature, and the rate of heating: The longer the specimen is left at high temperature, the greater is the loss in E_c. This is due to loss of moisture, dehydration, and possible subsequent deterioration.

iii. Furnace temperature condition at test: Test data indicates that, in general, there is a greater reduction in E_c if the specimen is cooled prior to loading [30]. The extent of reduction in E_c depends on the method of cooling. For example, a great drop in E_c occurs if the specimen is quenched.

iv. State of stress while heating: The drop in E_c is less if the specimen is stressed while heating [33].

(2) General form of the mathematical model:

Available data from various investigations on the modulus of elasticity of concrete at elevated temperatures are quite spread. In this study a model proposed by Nizamuddin [10] is modified to represent as a function of temperature (see Figure 2.10(a)). It can be expressed mathematically as follows:

$$E_c = [1.0 - 1.175\times10^{-3}(T-20)]E_{c,0} \qquad 20 \le T < 315\ ^0C \qquad (2.36a)$$

$$E_c = [0.6534 - 5.1597\times10^{-4}(T-315)]E_{c,0} \qquad 315 \le T < 650\ ^0C \qquad (2.36b)$$

$$E_c = 0.4806\,E_{c,0} \qquad 650\ ^0C \le T \qquad (2.36c)$$

where $E_{c,0}$ is the value of E_c at 20 ^0C.

2.3.1.5 Compressive Strength of Concrete, f_c'

The compressive strength of concrete has been the most widely investigated at high temperatures. The general tendency is for the compressive strength to decrease when concrete is heated. However, some of the research [32] indicates that an increase in f_c'

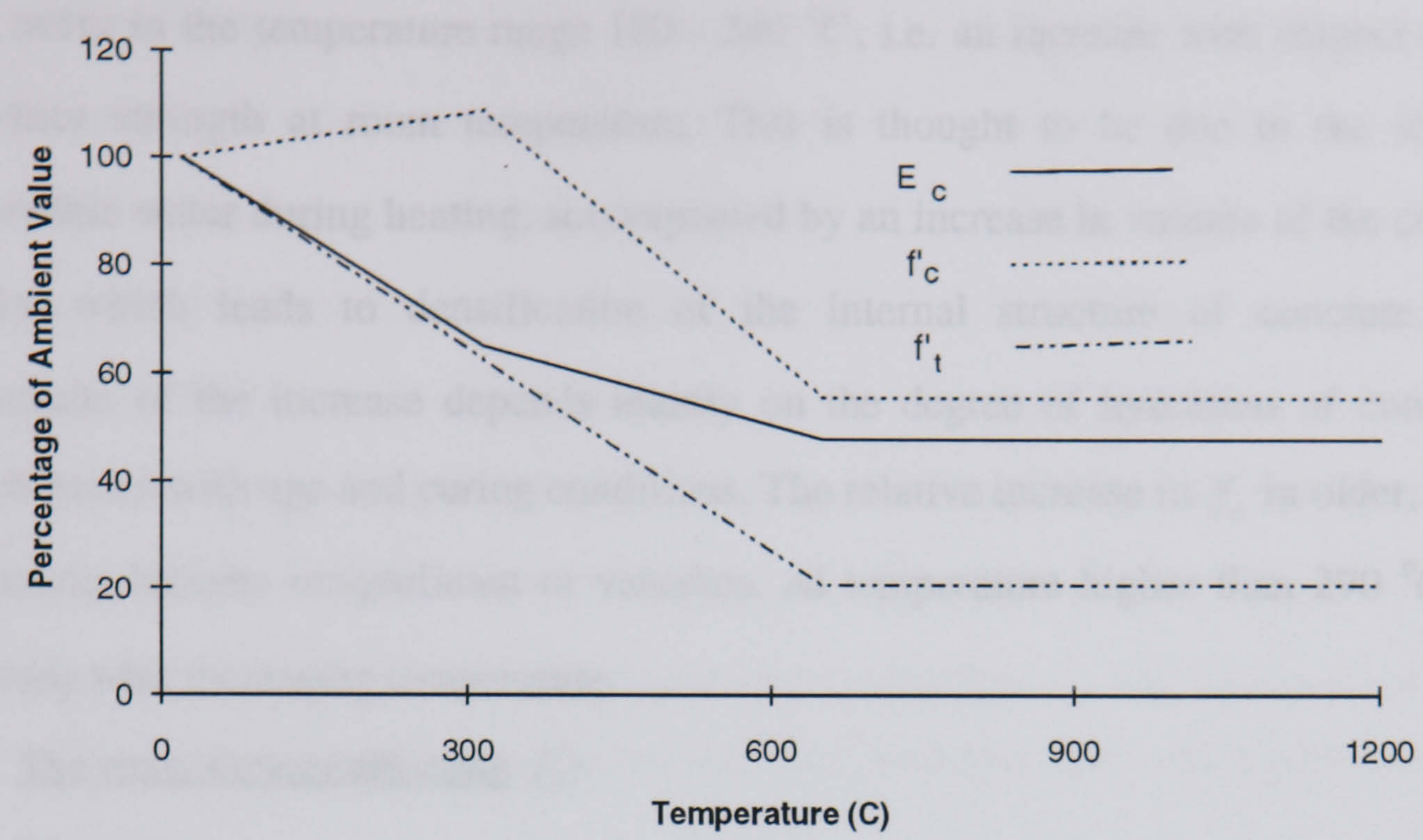

(a)

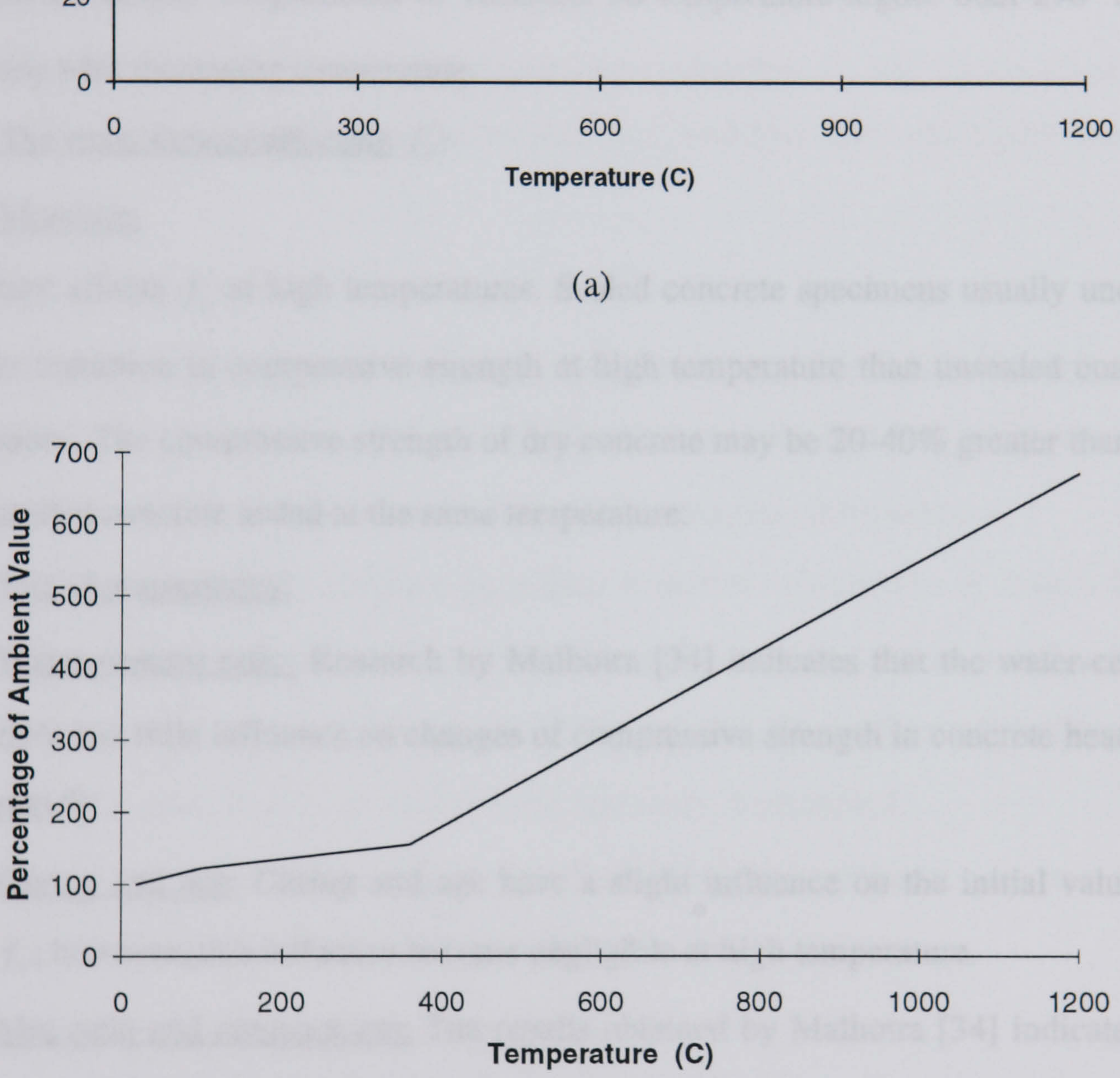

(b)

Figure 2.10 The Relationship of the Percentage Change of Ambient Values of the Material Properties of Concrete with Temperature [10]:

(a) Compressive Strength, $f_c^{'}$; Tensile Strength, $f_t^{'}$; Modulus of Elasticity, E_c

(b) Strain at Compressive Strength.

may occur in the temperature range 180 - 290 ^0C, i.e. an increase with respect to the reference strength at room temperature. This is thought to be due to the loss of evaporable water during heating, accompanied by an increase in volume of the cement grains, which leads to densification of the internal structure of concrete. The magnitude of the increase depends mainly on the degree of hydration of concrete, which varies with age and curing conditions. The relative increase in $f_c^{'}$ in older, dried specimens become insignificant or vanishes. At temperature higher than 290 ^0C, $f_c^{'}$ decrease with increasing temperature.

(1) The main factors affecting $f_c^{'}$:

(a) Moisture:

Moisture affects $f_c^{'}$ at high temperatures. Sealed concrete specimens usually undergo greater reduction in compressive strength at high temperature than unsealed concrete specimens. The compressive strength of dry concrete may be 20-40% greater than that of saturated concrete tested at the same temperature.

(b) Mix characteristics:

i. Water-cement ratio: Research by Malhotra [34] indicates that the water-cement ratio has little influence on changes of compressive strength in concrete heated to 600 ^0C.

ii. Curing and age: Curing and age have a slight influence on the initial values of $f_c^{'}$: however, this influence become negligible at high temperature.

iii. Mix ratio and compactness: The results obtained by Malhotra [34] indicate that lean mixes (low cement/aggregate ratio) exhibit less reduction in $f_c^{'}$ at high temperature than rich mixes (high cement/aggregate ratio).

iv. Aggregate type: Zoldners [32] indicated that aggregates exert considerable influencing on the compressive strength of concrete at high temperature. Concrete containing limestone aggregate is thought to be more suitable than concrete containing igneous gravel or sandstone aggregate at high temperature. Concrete made with expanded slag was found to have the worst effect on $f_c^{'}$ at high temperature. Crispino [15] proposed that in order to eliminate the reductions

in the compressive strength of concrete at high temperature. the thermal incompatibility between the aggregate and cement paste should be as small as possible. At temperatures below the ones at which mineralogical changes in the aggregates occur, the effect of aggregate type is not very significant (except its obvious effect on the initial values of $f_c^{'}$ at room temperature). But when the aggregate nature changes, there are further reductions in the values of $f_c^{'}$ at high temperatures.

v. Cement type: There is a pronounced deterioration in the concrete at high temperatures, when the cement has low C_3A and high C_3S and C_4AF contents [30].

(c) Test conditions:

i. Exposure time at high temperature, and the rate of heating: The longer the specimen is left at high temperature, the greater is the loss in $f_c^{'}$. This is due to loss of moisture, dehydration, and possible subsequent deterioration.

ii. Furnace temperature condition at testing: A greater reduction in $f_c^{'}$ results if it is determined after heat treatment and subsequent cooling to room temperature [30]. The extent of reduction in $f_c^{'}$ depends on the method of cooling. For example, great drop in $f_c^{'}$ occurs if the specimen is quenched.

iii. State of stress while heating: The drop in $f_c^{'}$ due to heating is less if the specimen is loaded while heating it [33].

(2) General form of the mathematical model:

Available data from various investigation on the compressive strength, $f_c^{'}$, at elevated temperatures are quite broad. A model proposed by Nizamuddin [10] is modified to represent as a function of temperature (see Figure 2.10(a)). It can be expressed mathematically as follows:

$$f_c^{'} = [1.0 + 3.1573\times10^{-4}(T-20)]\, f_{c,0}^{'} \qquad 20\le T< 315\ ^{0}C \qquad (2.37a)$$

$$f_c^{'} = [1.0931 - 1.5930\times10^{-3}(T-315)]\, f_{c,0}^{'} \qquad 315\le T<650\ ^{0}C \qquad (2.37b)$$

$$f_c^{'} = 0.5594\, f_{c,0}^{'} \qquad 650\ ^0C \le T \qquad (2.37c)$$

where $f_{c,0}^{'}$ is the value of $f_c^{'}$ at 20 ^0C.

2.3.1.6 Strain of Concrete at Compressive Strength, ε_{c0}

In general, ε_{c0} at room temperature varies within a very limited range, 0.002 to 0.0025, for concrete of different compositions and strengths [35]. The data available in the literature on the variation with temperature of ε_{c0}, the strain at maximum stress $f_c^{'}$, is the data taken from Furumura's stress-strain curves [36]. Furumura's data shows that ε_{c0} increase significantly with temperature.

Based on Furumura's data a model proposed by Nizamuddin [10] is modified to represent ε_{c0} as a function of temperature (see Figure 2.10(b)). It is expressed mathematically as follows:

$$\varepsilon_{c0} = [1.0 + 2.7818\times10^{-3}(T-20)]\, \varepsilon_{c0,0} \qquad 20 \le T < 100\ ^0C \qquad (2.38a)$$

$$\varepsilon_{c0} = [1.2225 + 1.2453\times10^{-3}(T-100)]\, \varepsilon_{c0,0} \qquad 100 \le T < 360\ ^0C \qquad (2.38b)$$

$$\varepsilon_{c0} = [1.5463 + 6.1411\times10^{-3}(T-360)]\, \varepsilon_{c0,0} \qquad 360\ ^0C \le T \qquad (2.38c)$$

where $\varepsilon_{c0,0}$ is the value of ε_{c0} at 20 ^0C. A typical value for $\varepsilon_{c0,0}$ is 2.46×10^{-3}.

2.3.1.7 Tensile Strength of Concrete, $f_t^{'}$

While the compressive strength test is virtually standardised, there are fundamentally different types of tensile strength tests such as the flexure test, the splitting test, and the ring test. Each type of test yields a different value for the tensile strength of concrete.

The effect of heating on the tensile strength has been studied by relatively few investigators. The results of these investigation [30, 37] show that. in general. the tensile strength of concrete decreases with increased temperature, with the fastest deterioration in the interval 300 to 600 ^0C. At 600 ^0C the tensile strength has decreased to 20 to 30% of the original strength.

(1) The main factors affecting f_t':

(a) Moisture:

In the temperature interval of 20 to 260 ^0C, if the moisture content is high, the heating results in increased drying and hardening of the concrete and, compared with the initial value, the strength tends to increase. At temperature higher than 260 to 320 ^0C, dehydration leads to a drop in f_t'. On the other hand, if the concrete has been dried prior to heating the increase in strength has already taken place and thus heating results in a relative decrease in f_t'. Sealed concrete specimens usually undergo greater reduction in f_t' at high temperature than unsealed concrete specimens.

(b) Mix characteristics:

i. Water-cement ratio: Water-cement ratio has little influence on changes of f_t' at high temperatures. Weigler and Fischer [38] point out that the reduction in f_t' in the interval 20 to 260 ^0C depends markedly on age and curing conditions. If the concrete is fresh and humid, the heating results in drying and hardening of the concrete and, compared with the initial value, the strength increase.

ii. Mix ratio and compactness: Thelandersson [39] point out that the relative decrease of tensile strength at high temperatures is somewhat less in concrete of higher quality. where the percentage of cement is larger than that in concrete of low quality. The difference, however, is of little practical importance.

iii. Aggregate type: Zoldners [32] indicates that at temperatures below the ones at which mineralogical changes in the aggregates occur, the effect of aggregate type is not very important (except its obvious effect on the initial value of f_t' at room temperature). But when the aggregate nature changes at high temperatures the effect of aggregate type on the reductions in f_t' become important. Concrete

containing limestone aggregate is more suitable than concrete containing igneous gravel or sandstone aggregate.

(c) Test conditions:

i. Exposure time at high temperature and the rate of heating: Thelandersson [39] indicates that the rate of heating has very little or no effect upon the tensile strength of concrete.

ii. Furnace temperature conditions on testing: Some investigator have dealt with the residual tensile strength determined after heat treatment and subsequent cooling to room temperature. The residual tensile strength is, as a rule, somewhat lower than the strength at high temperature [39]. Lankard et al [30] reported that below 80 ^0C both methods of testing give the same results; between 80 and 120 ^0C the residual tensile strength (cooled specimens) is greater than the strength of the hot specimens; and above 120 ^0C hot specimens are stronger than the cooled ones. The difference between the tensile strength in the hot state and the tensile strength immediately after cooling may be due to the further mechanical influence taking place when cooling.

iii. State of stress while heating: The drop in f_t' due to heating is less if the specimen is loaded while heating it.

(2) General form of the mathematical model:

Based on the reviewed literature, available data on f_t' at elevated temperatures are quite spread. A model proposed by Nizamuddin [10] is modified to represent f_t' as a function of temperature (see Figure 2.10(a)). It can be expressed as follows:

$$f_t' = [1.0 - 1.2579\times10^{-3}(T-20)]\, f_{t,0}' \qquad 20 \le T < 650\ ^0C \qquad (2.39a)$$

$$f_t' = 0.2075\, f_{t,0}' \qquad 650\ ^0C \le T \qquad (2.39b)$$

where $f_{t,0}'$ is the value of f_t' at 20 ^0C. A typical value for $f_{t,0}'$ is 2.0 MPa for normal weight concrete.

2.3.1.8 Elastic Poisson's Ratio of Concrete, ν_c

Like other materials, concrete deforms laterally under the action of a longitudinal (axial) stress. The Poisson's ratio of concrete at high temperatures has not been thoroughly investigated. At room temperature concrete has a Poisson's ratio of 0.15 to 0.20 regardless of the type of aggregate used [35]. Under biaxial stress, Poisson's ratio has been measured to be 0.20 in compression-compression, 0.18 in tension-tension, and between 0.18 and 0.20 for compression-tension [40].

The results from various investigations of Poisson's ratio determined at higher temperatures are very erratic. Some investigators indicate that the Poisson's ratio of concrete, in general, decreases as the temperature increases [28, 31], while other investigators indicate that Poisson's ratio increases as the testing temperature increases [15]. The deference in test results can be partially attributed to the differences in testing methods.

Therefore, in this research, the elastic Poisson's ratio, ν_c is assumed as constant. A typical value adopted for ν_c is 0.18 [10].

During the cooling phase the concrete does not recover its initial strength because of initial degradation and chemical decomposition of the cement paste. Therefore, in this research the values of E_c, $f_c^{'}$, ε_{c0}, $f_t^{'}$ during the cooling phase of the SDHI fire (short duration high intensity fire) [5] are assumed to be the same as their values at maximum temperatures.

2.3.2 Constitutive Modelling of Steel

The present study is confined to non-prestressed steel, which is generally called 'reinforcing'. In order to estimate the behaviour of reinforced concrete structures exposed to fire, it is necessary to know the strength and deformation properties of the reinforcing steel under fire conditions. In this research, the reinforcement steel is considered as carrying only uniaxial stress and the steel is assumed to have the same properties in tension and compression.

2.3.2.1 Modulus of Elasticity, E_s, and Yield Strength, f_y, of Steel

In general, the modulus of elasticity, E_s, and yield strength , f_y, of steel decrease gradually with increasing temperature.

According to the AISE manual [41] the yield strength of carbon steel at 540 ^0C (1000 ^0F) is approximately 70% of its room temperature value while the modulus of elasticity decreases linearly to about 86% of its room temperature value. There is some spread between the results obtained by various authors, probably owing to variability of the quality and dimensions of test specimens and the accuracy of the testing methods.

In this research a model proposed by Ellingwood and Lin [5] is used to represent E_s as a function of temperature (see Figure 2.11). The mathematical expressions for the modulus of elasticity of steel at high temperature is given as follows:

$$E_s = \left[1.0 - 3.2609\times10^{-4}(T-20)\right] E_{s,0} \qquad 20 \le T < 480\ ^0C \qquad (2.40a)$$

$$E_s = \left[0.85 - 1.9101\times10^{-3}(T-480)\right] E_{s,0} \qquad 480\ \le T \le 925\ ^0C \qquad (2.40b)$$

$$E_s = 0 \qquad 925\ ^0C \le T \qquad (2.40c)$$

where, $E_{s,0}$ is the value of E_s at room temperature.

The model for calculation of yield strength at high temperature is expressed mathematically as follows:

$$f_y = \left[1.0 - 6.1728\times10^{-4}(T-20)\right] f_{y,0} \qquad 20 \le T < 425\ ^0C \qquad (2.41a)$$

$$f_y = \left[0.75 - 1.4925\times10^{-3}(T-425)\right] f_{y,0} \qquad 425 \le T < 760\ ^0C \qquad (2.41b)$$

$$f_y = \left[0.25 - 6.4103\times10^{-4}(T-760)\right] f_{y,0} \qquad 760 \le T < 1150\ ^0C \qquad (2.41c)$$

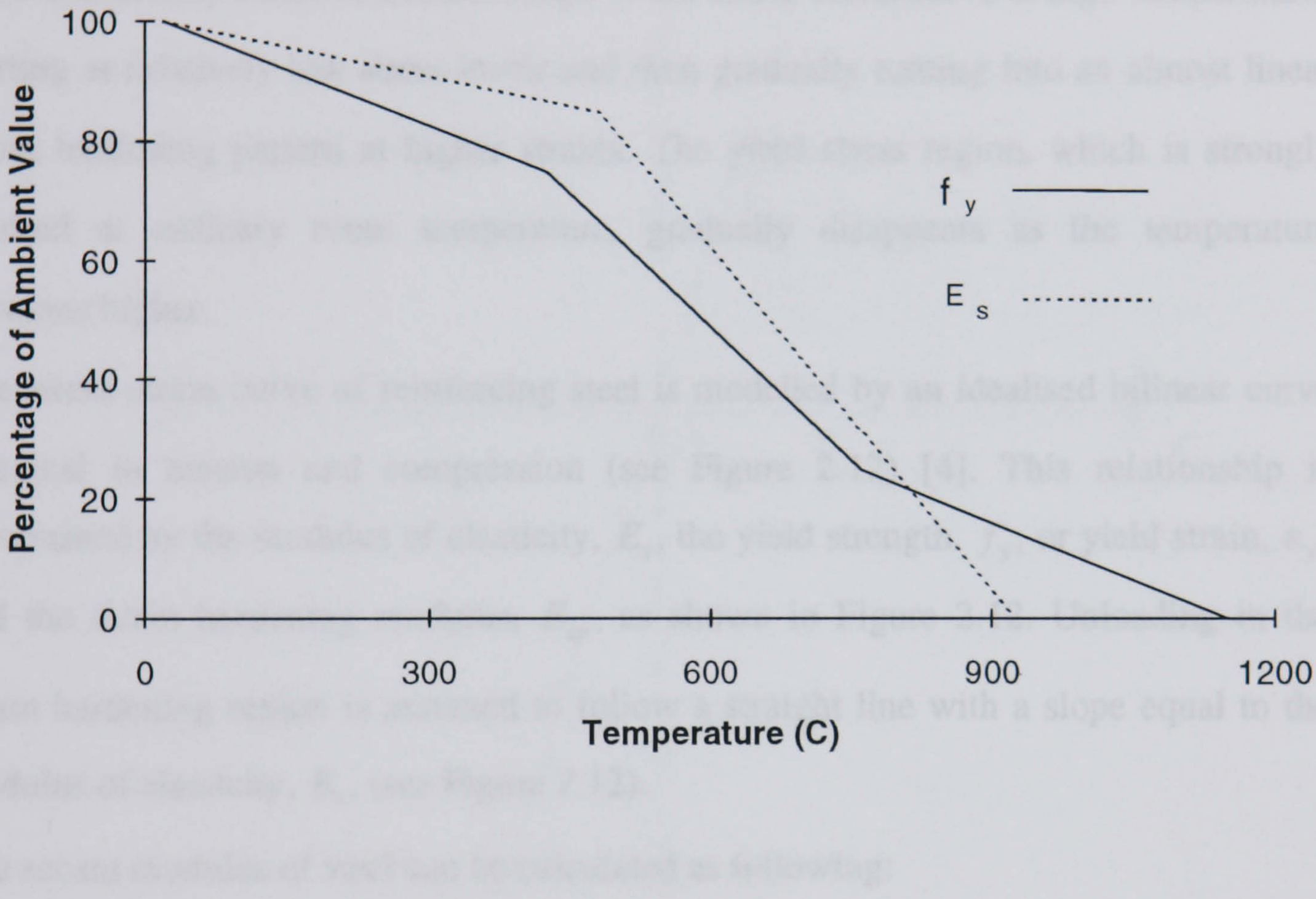

Figure 2.11 The Relationship of the Percentage Change of Ambient Values of the Modulus of Elasticity, E_s, and Yield Strength, f_y, of Steel with Temperature [5]

$$f_y = 0 \qquad 1150\ ^0C \leq T \qquad (2.41d)$$

where, $f_{y,0}$ is the yield strength at room temperature.

2.3.2.2 Stress Strain Relationship of Steel

Stress-strain diagrams have been reported by Harmathy and Stanzak [42]. The results show a markedly consistent round shape of the stress-strain curve at high temperatures starting at relatively low stress levels and then gradually turning into an almost linear strain hardening pattern at higher strains. The yield stress region, which is strongly marked at ordinary room temperature, gradually disappears as the temperature becomes higher.

The stress-strain curve of reinforcing steel is modelled by an idealised bilinear curve identical in tension and compression (see Figure 2.12) [4]. This relationship is determined by the modulus of elasticity, E_s, the yield strength, f_y, or yield strain, ε_y, and the strain hardening modulus, E_{sp}, as shown in Figure 2.12. Unloading in the strain hardening region is assumed to follow a straight line with a slope equal to the modulus of elasticity, E_s, (see Figure 2.12).

The secant modulus of steel can be calculated as following:

Before yielding,

$$\overline{E}_s = E_s \qquad (2.42)$$

After yielding,

$$\overline{E}_s = \frac{\sigma_s}{\varepsilon_s} \qquad (2.43)$$

where, if σ_s is tensile then

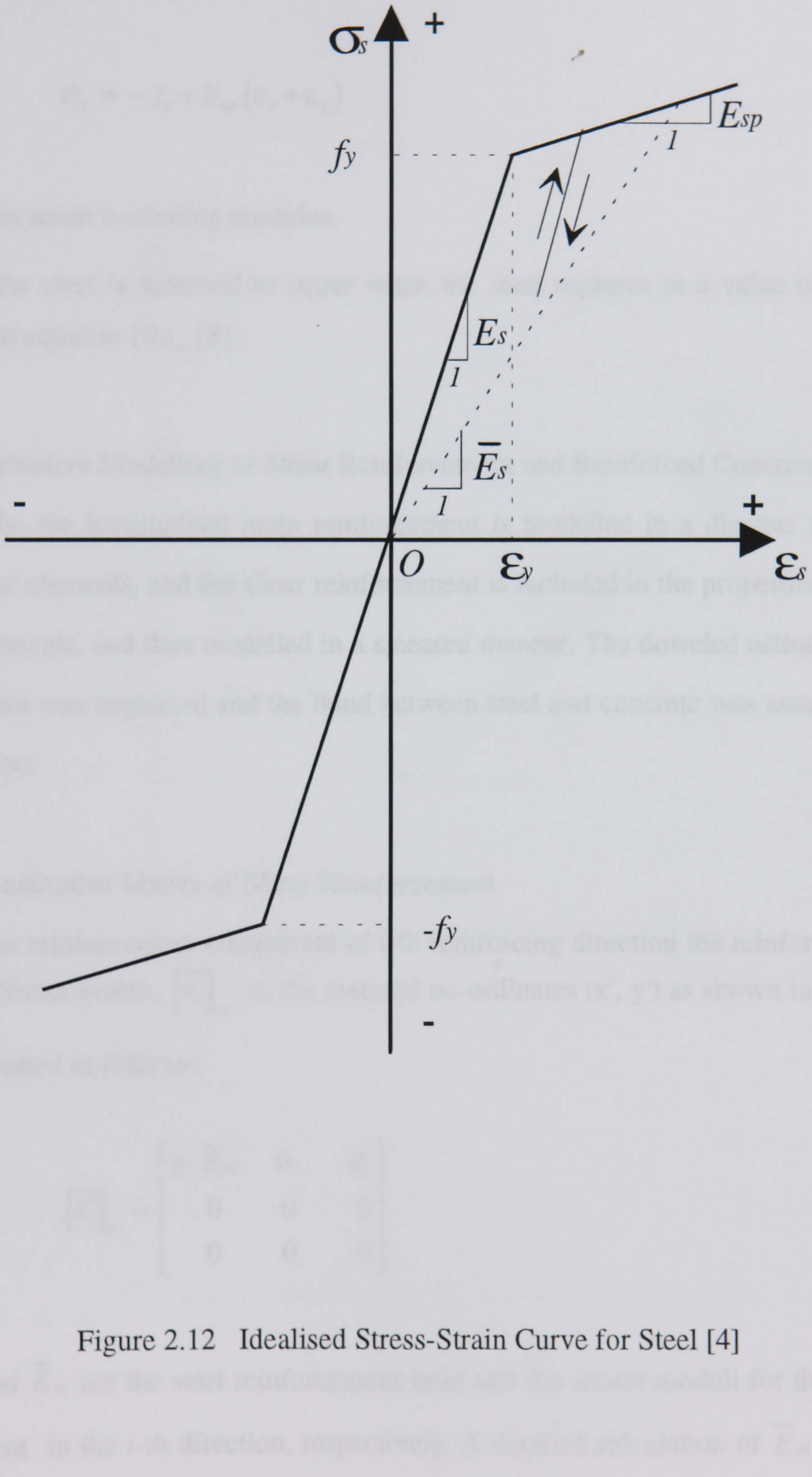

Figure 2.12 Idealised Stress-Strain Curve for Steel [4]

$$\sigma_s = f_y + E_{sp}\left(\varepsilon_s - \varepsilon_y\right) \tag{2.44}$$

or if σ_s is compression then

$$\sigma_s = -f_y + E_{sp}\left(\varepsilon_s + \varepsilon_y\right) \tag{2.45}$$

where, E_{sp} is strain hardening modulus.

Failure of the steel is assumed to occur when the steel ruptures at a value of stress related strain equal to $10\varepsilon_y$ [8].

2.3.3 Constitutive Modelling of Shear Reinforcement and Reinforced Concrete

In this study, the longitudinal main reinforcement is modelled in a discrete manner using the bar elements, and the shear reinforcement is included in the properties of the concrete elements, and thus modelled in a smeared manner. The doweled action of the reinforcement was neglected and the bond between steel and concrete was assumed to remain perfect.

2.3.3.1 Constitutive Matrix of Shear Reinforcement

For the shear reinforcement component of i-th reinforcing direction the reinforcement material stiffness matrix, $\left[\overline{C}\right]_{si}$, in the material co-ordinates (x', y') as shown in Figure 2.13 is evaluated as follows:

$$\left[\overline{C}\right]_{si} = \begin{bmatrix} \rho_i \overline{E}_{si} & 0 & 0 \\ 0 & 0 & 0 \\ 0 & 0 & 0 \end{bmatrix} \tag{2.46}$$

where ρ_i and $\overline{E}_{si}$ are the steel reinforcement ratio and the secant moduli for the shear reinforcement in the i-th direction, respectively. A detailed calculation of $\overline{E}_{si}$ can be found in Section 2.3.2.

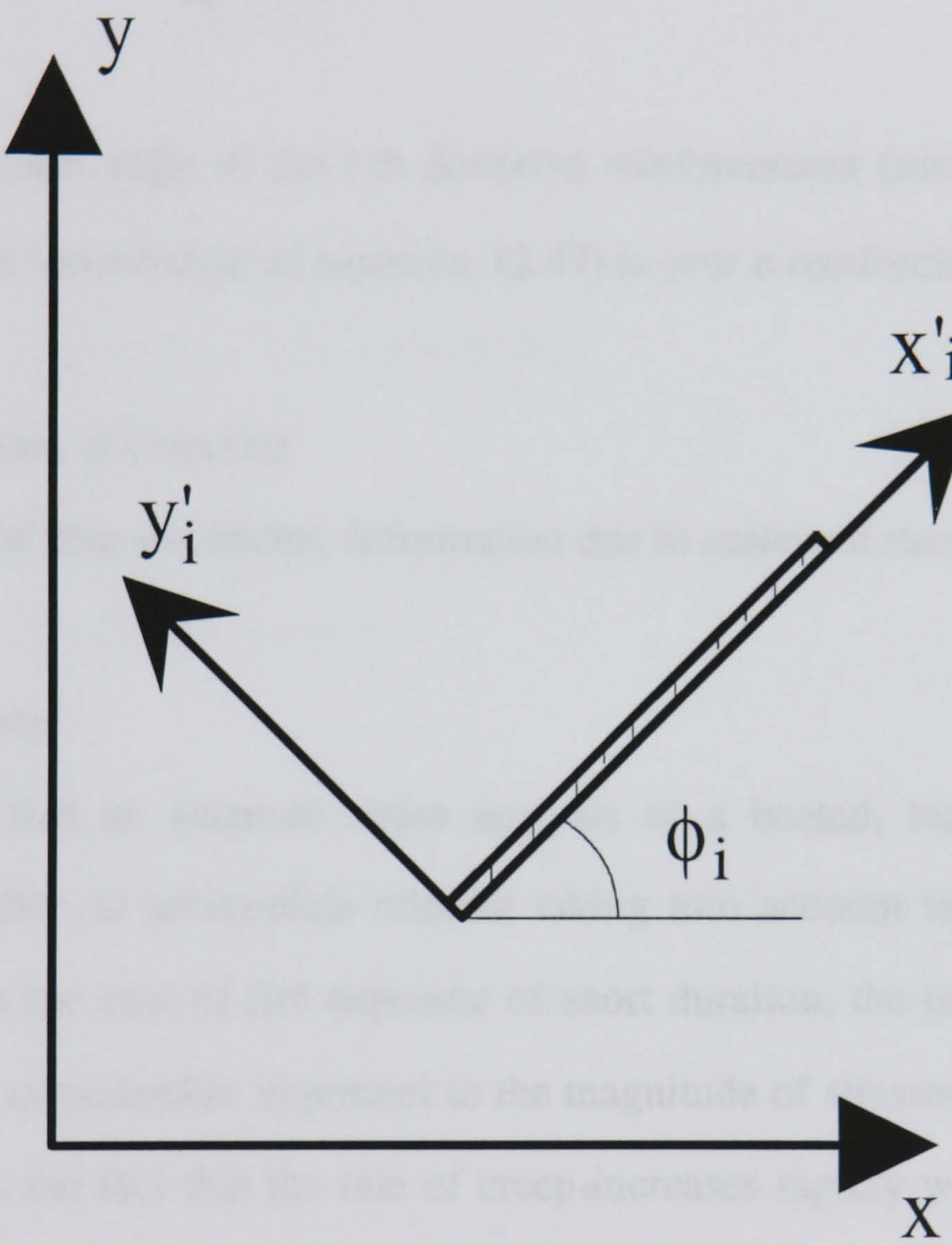

Figure 2.13 *i*-th Shear Reinforcement Components

2.3.3.2 Constitutive Matrix of Reinforced Concrete

The total material stiffness matrix for reinforced concrete, $[C]_{rc}$, is the sum of transformed component matrices of concrete and shear steel reinforcement. It can be written as:

$$[C]_{rc} = [C]_c + \sum_{i=1}^{n} \left[T(\phi_i)\right]^T \left[\overline{C}\right]_{si} \left[T(\phi_i)\right] \tag{2.47}$$

where ϕ_i is the direction angle of the i-th direction reinforcement (see Figure 2.13). The summation in the second term of equation. (2.47) is over n reinforcing directions.

2.3.4 Free Creep Strain of Concrete

Creep is defined as the time-dependent deformation due to sustained stress

2.3.4.1 Uniaxial Creep

It has been known that an accurate stress analysis of a heated, loaded concrete structure is not possible to accomplish without taking into account time-dependent deformation. Even in the case of fire exposure of short duration, the time dependent strains seem to be of considerable important to the magnitude of stresses and restraint forces. This is due to the fact that the rate of creep increases rapidly with increasing temperature. The creep strains at room temperature have been extensively investigated, and both experimental results and various mathematical models are available.

On the other hand, information on creep at high temperatures for application in fire simulation models is limited. From the review of the research literature, the most pertinent data on creep for fire applications is that of Cruz [43]. Cruz conducted creep tests on a concrete cylinder made with sand and gravel aggregate to grade 28 MPa. The specimens were heated until the test temperature was reached, and then this temperature was held constant throughout the test.

The model used in this research was that suggested by M. Mukaddam [44]. This model is based on a temperature compensated time model that reflects the thermal acceleration of creep. Moreover, this model uses the superposition principle combined with an effective stress concept that accounts for non-linear effects at higher stress levels. The model can be expressed mathematically as the following:

$$C(t,T) = \sum_{i=1}^{m} J_i \left[1 - e^{-\lambda_i \phi(T) t}\right] \tag{2.48}$$

where,

$C(t,T)$ = creep compliance in millionths/MPa;

J_i = linear constant;

λ_i = exponential constants;

$\phi(T)$ = temperature shift function;

t = time.

Using the experimental data of Cruz [43] the following coefficients were evaluated for the first four terms of equation (2.48), m=4, by assuming certain values for the λ_i's and then using a least squares curve fitting technique to obtain four values for the J_i's (see Table 2.1) when is measured in hours.

Table 2.1 The List of J_i's Values

i	1	2	3	4
λ_i	0.1	0.01	0.001	0.0001
J_i	20.70	24.58	10.23	397.06

Moreover, based on Cruz's data, the following temperature shift function was derived:

$$\phi(T) = e^{\psi(T)} \tag{2.49}$$

where,

$$\psi(T) = 0 \qquad T \leq 25\ ^{0}C \tag{2.50a}$$

$$\psi(T) = 1.841\times10^{-2}(17.7778+T)-0.767 \qquad 25<T\leq 150\ ^{0}C \tag{2.50b}$$

$$\psi(T) = 1.248\times10^{-2}(17.7778+T)+0.220 \qquad 150<T\leq 480\ ^{0}C \tag{2.50c}$$

$$\psi(T) = 7.128\times10^{-3}(17.7778+T)+2.900 \qquad 480\ ^{0}C<T \tag{2.50d}$$

To account for the non-linear creep at high stress levels, an effective stress model is used, which is based the work of Roll [45] and Freundenthal and Roll [46]. This model accounts for the increased specific creep at high stress levels and takes the following form:

$$\sigma_{eff} = \begin{cases} \sigma & \dfrac{\sigma}{f_c^{'}} \leq 0.35 \\ 2.330\,\sigma - 0.465\,f_c^{'} & 0.35 < \dfrac{\sigma}{f_c^{'}} \leq 1.0 \end{cases} \tag{2.51}$$

A general expression for the overall creep strain of a concrete element at time t_n can be obtained by assuming the stresses to be constant through each time step (see Figure 2.14), the temperature to be constant through each time step (average temperature, $\overline{T}_n$) and using the well-known superposition principal as follows:

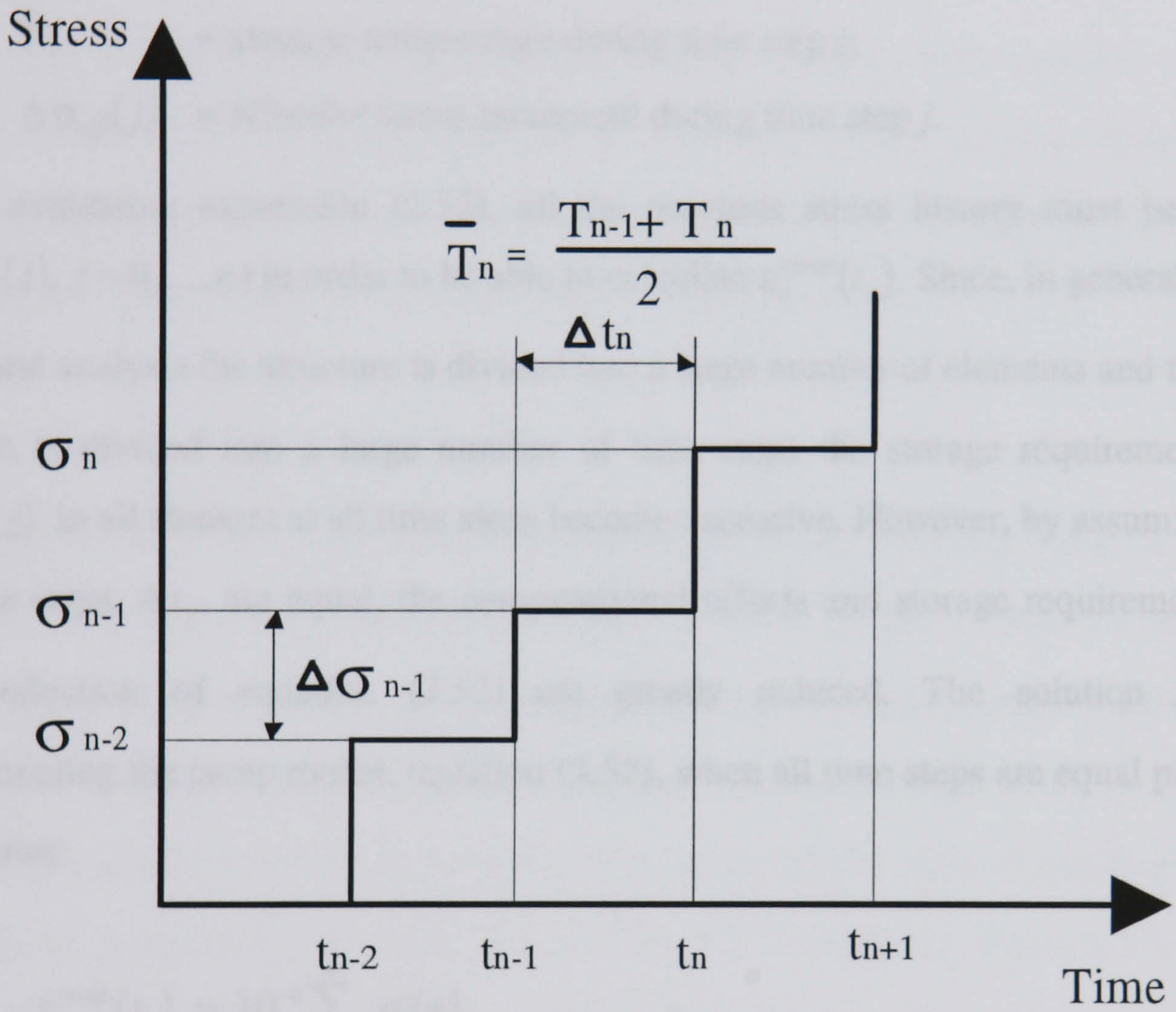

Figure 2.14 Stress History Considered in Determination of Concrete Creep Strain.

$$\varepsilon_c^{creep}(t_n) = \sum_{j=0}^{n-1} C(\Delta t_j, \overline{T}_j)\Delta\sigma_{eff}(j) \tag{2.52}$$

where,

$\varepsilon_c^{creep}(t_n)$ = total creep strain at time t_n;

$t_n = \sum_{j=0}^{n} \Delta t_j$;

Δt_j = time interval for time step j;

$\overline{T}_j$ = average temperature during time step j;

$\Delta\sigma_{eff}(j)$ = effective stress increment during time step j.

When evaluating expression (2.52), all the previous stress history must be stored ($\Delta\sigma_{eff}(j)$, $j=0,\ldots,n$) in order to be able to calculate $\varepsilon_c^{creep}(t_n)$. Since, in general, in the structural analysis the structure is divided into a large number of elements and the time domain is divided into a large number of time steps the storage requirements for $\Delta\sigma_{eff}(j)$ in all element at all time steps become excessive. However, by assuming that all time steps, Δt_j, are equal, the computational efforts and storage requirements for the evaluation of equation (2.52) are greatly reduced. The solution scheme implementing the creep model, equation (2.52), when all time steps are equal proceeds as follows:

$$\varepsilon_c^{creep}(t_n) = 10^{-6}\sum_{i=0}^{m} a_i(n) \tag{2.53}$$

where,

$$a_0(n) = a_0(n-1) + \Delta\sigma_{eff}(n-1)\left[\sum_{i=1}^{m} J_i\right] \tag{2.54}$$

$$a_i(n) = \left[a_i(n-1) - J_i\,\Delta\sigma_{eff}(n-1)\right]e^{-\lambda_i\phi(\overline{T}_n)\Delta t} \tag{2.55}$$

and

$$a_0(0) = 0 \tag{2.56}$$

$$a_i(0) = 0 \tag{2.57}$$

Finally, since only limited research data is presently available on tensile creep. it is assumed in this research that the creep of concrete in tensile or compression is the same for equal stresses (in absolute values). The results of a study on tensile creep in concrete at room temperature conducted by Akatsuka et al [47] indicated that the difference between the magnitude of tensile creep being slightly higher than compressive creep. Therefore, the error introduced by the assumption that tensile creep and compressive creep are equal will be negligible.

2.3.4.2 Creep Poisson's Ratio, ν_{cr}

A generalisation of the uniaxial creep relation to the biaxial case requires a knowledge of Poisson's ratio for creep strains, which may be called the creep Poisson's ratio. The experimental work undertaken to investigate the creep of concrete under biaxial stress conditions at room temperature and moderately high temperatures is limited. Moreover, there is very little experimental data on the biaxial creep of concrete at high temperature associated with fires (up to 1100 ^0C). Fortunately, Poisson effects are generally small and the reported data provides a basis for making acceptable approximations in the value of the creep Poisson's ratio. Kordina [48] observed that the creep Poisson's ratio of concrete fluctuates with time between 0.1 and 0.3. Zienkiewicz and Watson [49] stated that with viscoelastic strain in concrete, the creep Poisson's ratio remains constant. The effect of heating on the creep Poisson's ratio of concrete has been investigated by Geymager [50]. Geymager reviewed 34 reports on the effect of elevated temperatures (up to 150 ^0C) on the creep of concrete. Based on the results of this literature review, Geymayer concluded that the creep Poisson's ratio is not affected by elevated temperatures. In this study, the creep Poisson's ratio is

taken as constant, that is, it is assumed not to vary with time, temperature, or ratio of lateral stress to axial stress. A typical value of ν_{cr} is 0.15 [10].

2.3.4.3 Biaxial Creep

From the fact that there is lateral creep induced by an axial stress, it follows that under biaxial stresses in any direction there is creep due to the stress applied in that direction and also creep due to the Poisson's ratio effect of creep strain in the other normal direction. The general procedure for dealing with the biaxial creep is to find a pair of specific compliance in shear and isotropic compression. Taylor, et al [51] represented the behaviour of viscoelastic materials by a shear relaxation modulus while considering that bulk modulus remains constant with time.

The above general procedure can be simplified at the outset by considering that the creep Poisson's ratio is independent of time, In this case, creep behaviour under biaxial stress can be predicted, approximately, from uniaxial creep test results by applying the method of superposition to creep strains. That is, creep strain resulting from the lateral stress due to Poisson's effect is superimposed on creep strain resulting from the axial stress [52, 53]. Hence, this method is used in this research.

The shear creep function, $C_{xy}(t,T)$, is related to the uniaxial creep function by Arutyunyan [54], that is

$$C_{xy}(t,T) = 2\left(1+\nu_{cr}\right)C(t,T) \tag{2.58}$$

Based on the assumption that concrete is an homogeneous, isotropic body and that the application of the method of superposition to creep strain valid, the two-dimensional relationship between stresses and creep strains may therefore be expressed as:

$$\varepsilon_{c,x}^{creep}(t_n) = \sum_{j=0}^{n-1} C\left(\Delta t_j, \overline{T}_j\right)\Delta\sigma_{eff,x}(j) - \sum_{j=0}^{n-1} \nu_{cr}\, C\left(\Delta t_j, \overline{T}_j\right)\Delta\sigma_{eff,y}(j) \tag{2.59a}$$

$$\varepsilon_{c,y}^{creep}(t_n) = \sum_{j=0}^{n-1} C\left(\Delta t_j, \overline{T}_j\right)\Delta\sigma_{eff,y}(j) - \sum_{j=0}^{n-1} \nu_{cr}\, C\left(\Delta t_j, \overline{T}_j\right)\Delta\sigma_{eff,x}(j) \qquad (2.59b)$$

$$\gamma_{c,xy}^{creep}(t_n) = 2\sum_{j=0}^{n-1}\left(1+\nu_{cr}\right)C\left(\Delta t_j, \overline{T}_j\right)\Delta\tau_{eff,xy}(j) \qquad (2.59c)$$

When the creep Poisson's ratio is taken as constant with temperature, then ν_{cr} could be taken out of the summation sign. Equation (2.59) can be expressed in matrix form as:

$$\begin{Bmatrix} \varepsilon_{c,x}^{creep}(t_n) \\ \varepsilon_{c,y}^{creep}(t_n) \\ \gamma_{c,xy}^{creep}(t_n) \end{Bmatrix} = \begin{bmatrix} \sum & -\nu_{cr}\sum & 0 \\ -\nu_{cr}\sum & \sum & 0 \\ 0 & 0 & 2\left(1+\nu_{cr}\right)\sum \end{bmatrix} \begin{Bmatrix} \Delta\sigma_{eff,x}(j) \\ \Delta\sigma_{eff,y}(j) \\ \Delta\tau_{eff,xy}(j) \end{Bmatrix} \qquad (2.60)$$

where $\sum$ represents the operator $\sum_{j=0}^{n-1} C\left(\Delta t_j, \overline{T}_j\right)$ and ν_{cr} is considered to be constant.

2.3.5 Free Shrinkage Strain of Concrete

Shrinkage is defined as the time-dependent volume change which occurs independently of externally applied stresses and of temperature volumetric expansion (or contraction). In general, shrinkage and creep interact in a complex manner with changes in environmental conditions to produce stresses and deformations in concrete. However, from a mathematical standpoint, it is convenient to consider the creep and shrinkage as independent phenomena. That is, creep strains and shrinkage strains are assumed to be additive.

Some experimental and theoretical investigations have been conducted to study the time dependent shrinkage strain in concrete members at room temperature [55]. However, very little systematic study of shrinkage at elevated temperatures has yet been made. The reason for this is probably that it is difficult to make relevant tests

when elevated temperatures are involved. The limited data available indicates that shrinkage in concrete due to moisture loss is highly temperature dependent [56].

2.3.5.1 Uniaxial Free Shrinkage

Shrinkage in concrete due to moisture loss is highly temperature dependent. This dependence is reflected both in the total amount of shrinkage that may occur and the rate at which it occurs.

Free shrinkage is defined as the contraction an element of material would undergo if it were unrestrained by neighbouring elements. The basic free shrinkage model is given below [7] (in the following discussion, free shrinkage will simply be referred to as shrinkage).

$$\frac{d\varepsilon_c^{sh}(t,T)}{dt} = a(T)\left[\varepsilon_{c,\infty}^{sh}(T) - \varepsilon_c^{sh}(t)\right] \tag{2.61}$$

where,

$\frac{d\varepsilon_c^{sh}(t,T)}{dt}$ = shrinkage rate at time t and temperature T ($1/hr$);

$\varepsilon_c^{sh}(t)$ = cumulative shrinkage strain at time t, (note: in this case, contraction is positive);

$\varepsilon_{c,\infty}^{sh}(T)$ = total potential shrinkage, function of temperature, T;

$a(T)$ = rate constant, function of temperature T, ($1/hr$);

t = time, hrs;

It is assumed that shrinkage continues until the temperature of 100 ^0C is reached. Upon reaching 100 ^0C, all remaining shrinkage is considered to occur within the current time step. In addition, the total amount of shrinkage occurring within any time step cannot cause the cumulative shrinkage to exceed the total potential shrinkage for the temperature at that time step. Lastly, shrinkage is considered to be an irreversible process.

The rate parameter, $a(T)$, may be assumed to be a quadratic function of temperature, while the ultimate potential shrinkage, $\varepsilon_{c,\infty}^{sh}(T)$, is assumed to be a linear function of temperature. Such expressions for $a(T)$ and $\varepsilon_{c,\infty}^{sh}(T)$ are given below [10]:

$$a(T) = 0.001 + \left[\frac{T-20}{80}\right]^2 \tag{2.62}$$

$$\varepsilon_{c,\infty}^{sh}(T) = 0.0005\left(1+\frac{T-20}{80}\right) \tag{2.63}$$

Both equation (2.62) and (2.63) are valid in the range 20 ^0C to 100 ^0C. The maximum ultimate shrinkage strain at the upper range, 100 ^0C, is 0.001.

The incremental free shrinkage strain during time step i is calculated with the following equation:

$$\Delta\varepsilon_c^{sh}\left(t_i,\overline{T}_i\right) = a\left(\overline{T}_i\right)\left[\varepsilon_{c,\infty}^{sh}\left(\overline{T}_i\right)-\varepsilon_c^{sh}\left(t_{i-1}\right)\right]\Delta t_i \tag{2.64}$$

where,

$\Delta\varepsilon_c^{sh}\left(t_i,\overline{T}_i\right)$ = incremental free shrinkage strain;

$\overline{T}_i$ = average temperature during time step i;

Δt_i = time step i.

The total free shrinkage strain, $\varepsilon_c^{sh}\left(t_n\right)$, is then calculated as follows:

$$\varepsilon_c^{sh}\left(t_n\right) = \sum_{i=1}^{n} \Delta\varepsilon_c^{sh}\left(t_i,\overline{T}_i\right) \tag{2.65}$$

2.3.5.2 Biaxial Free Shrinkage

In this study, it is assumed that free shrinkage strains at a point in the material are the same in all directions. Free shrinkage shear strains are therefore assumed to be zero.

Thus, for the two dimensional problems, the free shrinkage strain vector is taken as follows:

$$\begin{Bmatrix} \varepsilon_{c,x}^{sh}(t_n) \\ \varepsilon_{c,y}^{sh}(t_n) \\ \gamma_{c,xy}^{sh}(t_n) \end{Bmatrix} = \begin{Bmatrix} \varepsilon_c^{sh}(t_n) \\ \varepsilon_c^{sh}(t_n) \\ 0 \end{Bmatrix} \tag{2.66}$$

For temperatures above 100 ^0C, the incremental shrinkage strain, $\Delta\varepsilon_c^{sh}(t_i, \overline{T}_i)$, is assumed to be zero. At these temperatures, the values of the coefficients of expansion are assumed to include the effect of any remaining shrinkage.

2.3.6 Free Thermal Strain of Concrete

Like most engineering materials, concrete has a positive coefficient of thermal expansion. The thermal expansion of concrete depends primarily on the thermal expansion of the individual constituents, e.g. cement paste and aggregate, since the overall expansion of concrete is a resultant of the two values.

A comprehensive review of the thermal expansion behaviour of concrete at high temperature has been made by Zoldners [14]. In general, the coefficient of expansion of concrete is a function of the quantity of aggregate by itself. The data of the thermal expansion of concrete at high temperatures, obtained from various investigations [31, 38] is subject to great variability. However, from these results a mathematical expression of the typical model for the coefficient of thermal expansion of concrete, α_c ($^0C^{-1}$), as a function of temperature can be given as the following [10]:

$$\alpha_c(T) = 1.08\times10^{-5} \qquad 0 \le T < 540\ ^0C \tag{2.67a}$$

$$\alpha_c(T) = 1.62\times10^{-5} \qquad 540\ ^0C \le T \tag{2.67b}$$

The determination of changes in thermal strain for concrete is achieved through the product of temperature dependent coefficient of expansion and change in temperature. The free thermal strain increment in concrete in time step i is thus calculated as shown below:

$$\Delta \varepsilon_c^T(i) = \alpha_c(T_i)(T_i - T_{i-1}) \tag{2.68}$$

The total free thermal strain at time step n is then calculated as follows:

$$\varepsilon_c^T(n) = \sum_{i=1}^{n} \Delta \varepsilon_c^T(i) \tag{2.69}$$

For the biaxial case, it is assumed that free thermal expensing produces zero shear strains. Hence, the free thermal strain vector is formed as follows:

$$\begin{Bmatrix} \varepsilon_{c,x}^T(n) \\ \varepsilon_{c,y}^T(n) \\ \gamma_{c,xy}^T(n) \end{Bmatrix} = \begin{Bmatrix} \varepsilon_c^T(n) \\ \varepsilon_c^T(n) \\ 0 \end{Bmatrix} \tag{2.70}$$

2.3.7 Free Transient Strain of Concrete

Transient strains are those strains that cannot otherwise by accounted for due to the decomposition of the cement paste. They occur under compressive stresses as temperature increases, are essentially permanent, unrecoverable and only occur under initial heating.

Transient strains are temperature dependent and independent of time. When the transient strain is not included in the structural analysis, the computed thermal stresses becomes very large and leads to a prediction of failure much earlier than would be observed [5].

A model proposed by Anderberg and Thelandersson [57] is adopted to calculate uniaxial free transient strain of concrete in this research and described as follows:

$$\Delta \varepsilon_c^{tr} = \frac{\sigma_c}{f_{c,0}^{'}} g(T) \tag{2.71}$$

where,

$g(T)$ = a function of temperature,

$f_{c,0}^{'}$ = compressive strength of concrete at ambient condition.

σ_c = applied compressive stress in the concrete from the previous time increment.

Inspection shows that $g(T)$ is approximately proportional to $\Delta\varepsilon_c^T$, that is,

$$\Delta \varepsilon_c^{tr} = -k_2 \frac{\sigma_c}{f_{c,0}^{'}} \Delta\varepsilon_c^T \qquad 20 \leq T < 500\ ^0C \tag{2.72}$$

where, k_2 is a dimensionless constant varying with cement type. Anderberg and Thelanderson [57] found by mean of linear regression that a value of k_2 equal to 2.35 best describes the quartzite concrete used in their tests. This value is used in this research.

For temperatures above 500 ^0C there is an accelerated effect on transient strains. Anderberg [58] proposed the following expression for the incremental change in ε_c^{tr}:

$$\Delta \varepsilon_c^{tr} = -0.1 \times 10^{-3}\, \Delta T \frac{\sigma_c}{f_{c,0}^{'}} \qquad 500\ ^0C \leq T \tag{2.73}$$

where, ΔT is temperature increment during time step i.

The total free transient strain at time step n is then calculated as following:

$$\varepsilon_c^{tr}(n) = \sum_{i=1}^{n} \Delta \varepsilon_c^{tr}(i) \tag{2.74}$$

For the biaxial case, the transient shear strains are ignored for the purpose of simplicity. Therefore the free transient strain vector is expressed as:

$$\begin{Bmatrix} \varepsilon_{c,x}^{tr}(n) \\ \varepsilon_{c,y}^{tr}(n) \\ \gamma_{c,xy}^{tr}(n) \end{Bmatrix} = \begin{Bmatrix} \varepsilon_{c}^{tr}(n) \\ \varepsilon_{c}^{tr}(n) \\ 0 \end{Bmatrix} \tag{2.75}$$

Since transient strains are considered as therefore irrecoverable and only occur under initial heating, in this study the transient strain is assumed to remain unchanged and equal to the value attained at the maximum temperature of the concrete which is reached during the cooling period of the concrete. This assumption is used, for example, when the concrete is exposed to SDHI Fire [5].

2.3.8. Free Creep Strain of Steel

Previous investigations concerning creep tests on steel specimens have used the conventional method, e.g. constant temperature and constant stress. Strain-time relation curves were obtained which can be divided into three creep stages [7]: they are illustrated in Figure 2.15. The primary creep state (OA) is the stage where the creep rate decreases with time. The creep rate decreases up to point at which the creep rate becomes relatively constant (point A). The secondary creep stage is the stage where the creep rate remains constant with time (AB). As creep deformation proceeds the creep rate eventually begins to increase (point B), and after some time rupture occurs (point C). The stage of increasing creep rate (BC) is known as the tertiary creep stage.

The model for creep in reinforcing steel used in this study considers only the primary and secondary phases of creep behaviour, neglecting tertiary creep. It is assumed that creep rates are identical in both tension and compression.

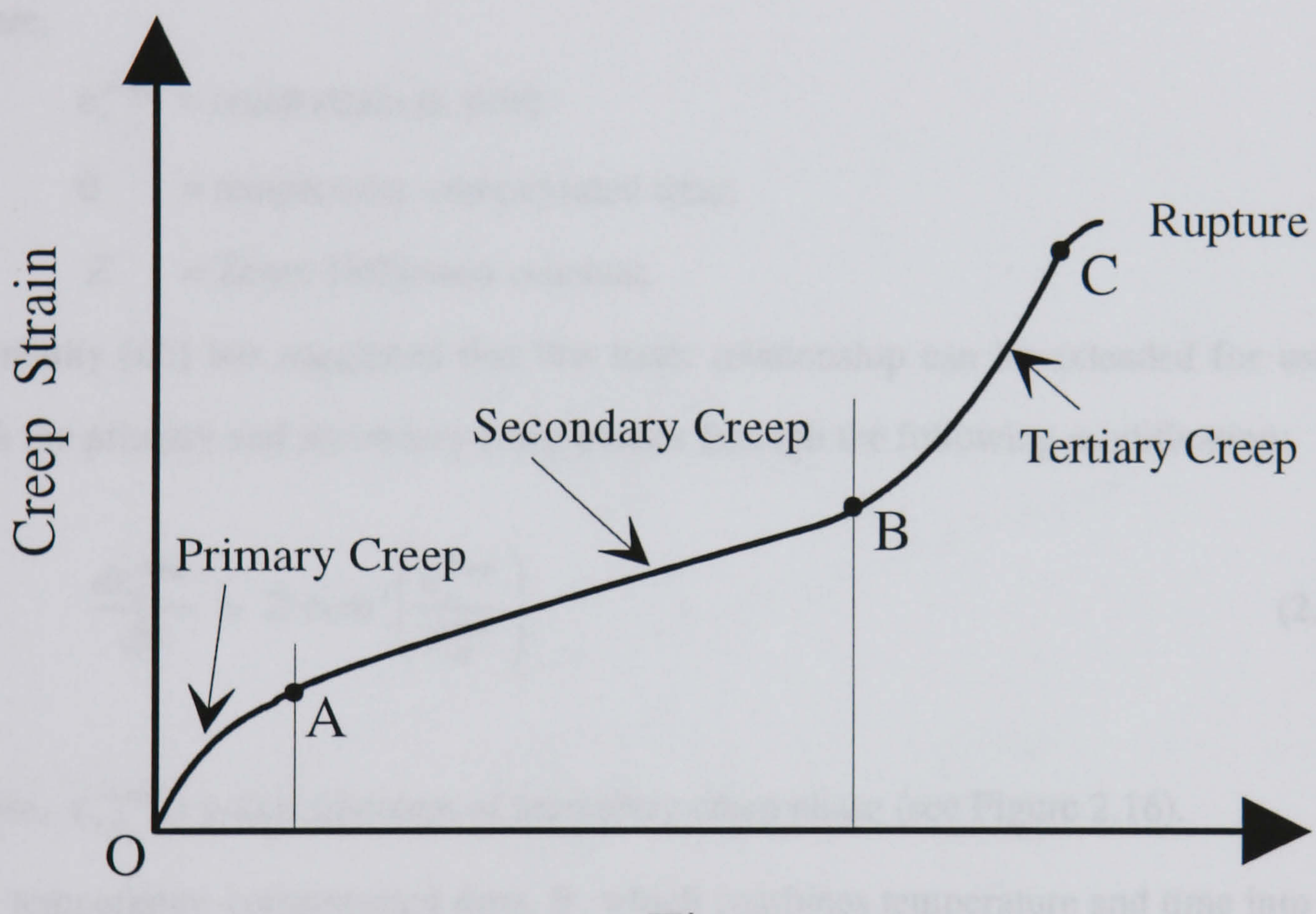

Figure 2.15 Typical Creep Curve [7]

A creep model for constant temperature and stress can be extended to variable temperature by use of Dorn's θ-Method [59] and to variable stress by a strain hardening rule. It is known that the creep rate for secondary creep is a constant in the domain of temperature-compensated time, thus

$$\frac{d\varepsilon_s^{creep}}{d\theta} = Z \tag{2.76}$$

where,

ε_s^{creep} = creep strain in steel;

θ = temperature-compensated time;

Z = Zener-Hollomon constant.

Harmathy [60] has suggested that this basic relationship can be extended for use in both the primary and secondary creep phases through the following modification:

$$\frac{d\varepsilon_s^{creep}}{d\theta} = Z \coth^2\left(\frac{\varepsilon_s^{creep}}{\varepsilon_{s,0}^{creep}}\right) \tag{2.77}$$

where, $\varepsilon_{s,0}^{creep}$ is y-axis intercept of secondary creep phase (see Figure 2.16).

The temperature-compensated time, θ, which combines temperature and time into one single parameter, can be calculated by the following equation:

$$\theta = \int_0^t \left[e^{-\frac{\Delta H}{R(T+273)}} \right] dt \tag{2.78}$$

or

$$\frac{d\theta}{dt} = e^{-\frac{\Delta H}{R(T+273)}} \tag{2.79}$$

where,

ΔH = activation energy of creep, ($J/kg.mole$)

R = the gas constant, ($J/kg.mole.K$)

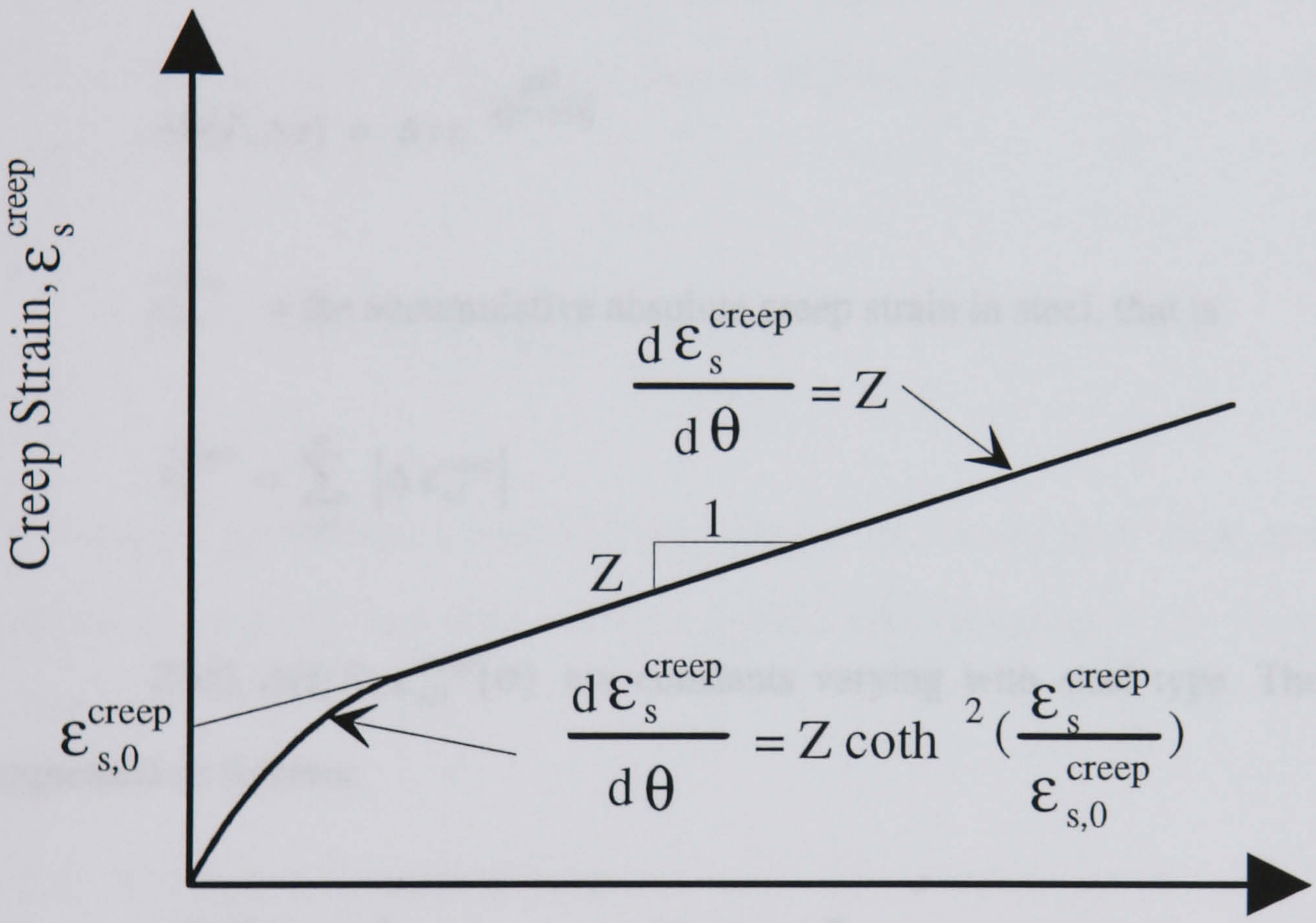

Figure 2.16 Harmathy's Formulation of Creep Model [7]

Harmathy [61] has suggested a computational algorithm that combines his creep model with Dom's θ-Method and a strain-hardening rule. It is this method with minor modifications [7] that is used in this investigation. The incremental creep strain is given by the following equation:

$$\Delta \varepsilon_s^{creep} = Z(\sigma)\Delta\theta(T,\Delta t)\coth^2\left(\frac{\bar{\varepsilon}_s^{creep}}{\varepsilon_{s,0}^{creep}(\sigma)}\right) \tag{2.80}$$

where,

$$\Delta\theta(T,\Delta t) = \Delta t\, e^{-\frac{\Delta H}{R(T+273)}} \tag{2.81}$$

$\bar{\varepsilon}_s^{creep}$ = the accumulative absolute creep strain in steel, that is

$$\bar{\varepsilon}_s^{creep} = \sum_{i=1}^{n} \left|\Delta \varepsilon_{s,i}^{creep}\right| \tag{2.82}$$

$Z(\sigma)$, $\Delta H/R$, $\varepsilon_{s,0}^{creep}(\sigma)$ are constants varying with steel type. They may be expressed as follows:

$$Z(\sigma) = A\,\sigma^B \qquad \text{for } \sigma \le \sigma^* \tag{2.83a}$$

$$Z(\sigma) = C\,e^{D\sigma} \qquad \text{for } \sigma > \sigma^* \tag{2.83b}$$

$$\varepsilon_{s,0}^{creep} = E\,\sigma^F \tag{2.84}$$

Where, σ is the steel stress in MPa, A, B, C, D, E, F and σ^* are empirical constants. The terms A to F and σ^* as well as the $\Delta H/R$ term are defined in Table 2.2 for several reinforcing steels. The values for ASTM A36, CSA G40.12, ASTM A421

steels are from Harmathy and Stanzack [42], and for $Ks40\phi10$, $Ks40\phi8$ and $Ks60\phi8$ are from Weeks [8].

The results obtained using this creep model can be very sensitive to the experimental coefficients used. If a steel of a yield strength higher than that intended for the set of coefficient is used, excessive creep will be predicted. Likewise, if a steel of lower yield strength is used, the creep affect may be underestimated. Because of this sensitivity to experimental coefficients, the steel creep model should be used with caution.

In the first time step where $\bar{\varepsilon}_s^{creep} = 0$, the hyperbolic cotangent term goes to infinity. The creep strain for the first time step is calculated by the following approximate equation:

$$\Delta \varepsilon_s^{creep} = \varepsilon_s^{creep} = \left[3 Z \theta \left(\varepsilon_{s,0}^{creep} \right)^2 \right]^{\frac{1}{3}} + Z\theta \tag{2.85}$$

This initial approximation was first suggested by Harmathy [60]. From this work the expression is considered as providing a reliable approximation of the creep strain for values of ε_s^{creep} up to 0.5 $\bar{\varepsilon}_s^{creep}$.

2.3.9 Free Thermal Strain of Steel

Skinner [62] collected data from some 80 different sources covering a much wider range of steel composition than would be encountered in any type of structural steel. Test data indicates that the coefficient of thermal expansion for steel, α_s, increases with an increase in temperature up to 650 ^0C (1200 ^0F). Test results indicate that α_s is not significantly dependent on the carbon content [18].

Table 2.2 Empirical Constants, A, B, C, D, E, F, σ^*, Used in Equations (2.83) to (2.84) For Several Reinforcing Steels [8, 42]

Steel Type	ASTM A36	CSA G40.12	ASTM A421	Ks40 Φ10	Ks40 Φ8	Ks60 Φ8
A	3.7485 $\times 10^{8}$	2.8341 $\times 10^{9}$	1.9524 $\times 10^{8}$	6.9600 $\times 10^{10}$	4.5800 $\times 10^{7}$	5.1100 $\times 10^{7}$
B	4.7	3.25	3.0	4.7	4.72	2.93
C	1.23×10^{16}	3.69 $\times 10^{14}$	8.21 $\times 10^{13}$	5.28 $\times 10^{18}$	7.50 $\times 10^{14}$	1.59 $\times 10^{16}$
D	0.04351	0.0319	0.0145	0.0443	0.5120	0.0313
E	1.0304 $\times 10^{-6}$	1.8129 $\times 10^{-5}$	9.2618 $\times 10^{-5}$	2.8500 $\times 10^{-8}$	3.3900 $\times 10^{-7}$	2.0600 $\times 10^{-6}$
F	1.75	1.0	0.67	1.037	0.531	0.439
σ^*	104	104	172	84	90	90
$\Delta H/R$	38900	36110	30560	45000	40000	40000

ΔH = activation energy of creep
R = the gas constant

A model developed by Nizamuddin [10] is adopted for calculation of the coefficient of thermal expansion of steel, α_s ($^0C^{-1}$), at high temperature in this study. This model can be expressed mathematically as follows:

$$\alpha_s = \left[1.10+9.7029\times10^{-4}(T-20)\right]\times10^{-5} \qquad 20\le T<650\ ^0C \qquad (2.86a)$$

$$\alpha_s = 1.728\times10^{-5} \qquad 650\ ^0C < T \qquad (2.86b)$$

The determination of changes in thermal strain for steel is achieved through the multiplication of the temperature dependent coefficient of expansion by the change in temperature. The free thermal strain increment in steel in time step i is thus calculated as shown below:

$$\Delta\varepsilon_s^T(i) = \alpha_s\left(T_i - T_{i-1}\right) \qquad (2.87)$$

The total free thermal strain at time step n is then calculated as follows:

$$\varepsilon_s^T(n) = \sum_{i=1}^{n} \Delta\varepsilon_s^T(i) \qquad (2.88)$$

2.4 Summary

In this chapter, available experimental data on thermal, strength, and deformation properties of concrete and steel at elevated temperatures were reviewed and mathematical models describing these properties were proposed based on this review. The results of this review showed that:

(1) the conductivity of concrete and steel decrease with an increase in temperature;

(2) the specific heat of concrete and steel increases with an increase in temperature;

(3) the strength and stiffness of concrete and steel decrease. in general. with an increase in temperature, except that the compressive strength of concrete in some cases showed an initial increase up to about 300 ^{0}C;

(4) creep of concrete and steel increase significantly with an increase in temperature;

(5) shrinkage of concrete increases with an increase in temperature;

(6) the coefficients of expansion of concrete and steel increase with an increase in temperature, and

(7) Practically little information is available on the mechanical properties of biaxially loaded concrete at elevated temperatures.

(8) The material model developed in this chapter will be used to calculate the properties of materials for the thermal and structural analysis of reinforced concrete structure in fire conditions.

3. THERMAL ANALYSIS

3.1 Introduction

In this Chapter, a two-dimensional finite element simulation to evaluate the temperature distribution histories of cross-section of structural member for fire conditions will be described (see Figure 3.1). The model will comprise a two-dimensional representation of the cross-section of structural member based on the assumption that no heat flows along the longitudinal axis of a structural member. This assumption is because the longitudinal dimension of a structural member is much larger than the dimensions of cross-section of the member. Therefore, the temperature gradient along the longitudinal axis of the member is much smaller than that for the lateral directions of the member. The heat transferred along the longitudinal axis of the member is so small compared to that for the lateral directions of the member that the heat flow along the longitudinal axis can be neglected. However, if the longitudinal and lateral dimensions of the member are of the same order three-dimensional thermal analysis must be applied.

In this model, the presence of moisture will be taken into account and the thermal properties of concrete will be considered as both temperature and moisture dependent (see Chapter 2). The heat flow problem solved by this model is non-linear because of the variable thermal properties of materials and fire boundary conditions. These non-linearities are handled by local linearization about a current temperature distribution. Simulation of the fire environment is through the use of standard fire curves [1, 2, 63], expressed as a time dependent curve, while convective and radiative mechanisms are used to model the fire boundary conditions.

The finite element method will be used as the solution technique. This general approach has been presented in the works of Wilson and Nicked [64] and Zienkiewicz [65], and extended to the fire situation by Bizri [3] and Becker [4].

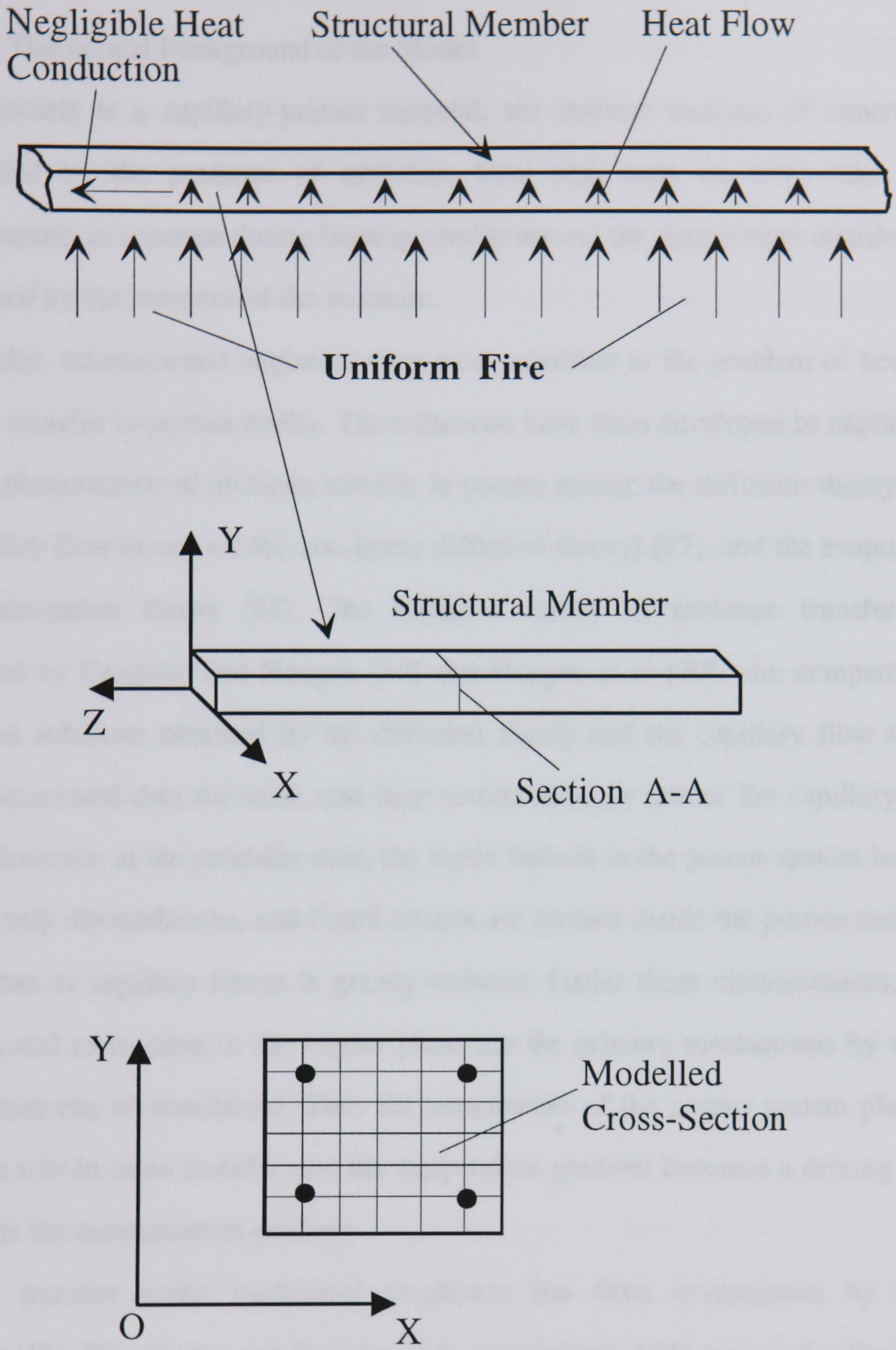

Section A-A

Figure 3.1 Geometric Idealisation for Two-dimensional Heat Transfer Model.

3.2 The Theoretical Background of the Model

Since concrete is a capillary-porous material, the thermal analysis of concrete is complicated by the presence of moisture. Heat and mass transfer take place simultaneously in concrete during heating conditions and the temperature distributions are affected by the presence of the moisture.

For decades, scientists and engineers have paid attention to the problem of heat and moisture transfer in porous media. Three theories have been developed to explain the physical phenomenon of moisture transfer in porous media: the diffusion theory [66], the capillary flow theory (or the non-linear diffusion theory) [67], and the evaporation and condensation theory [68]. The diffusion theory of moisture transfer was questioned by Ceaglske and Hougen [69] and Hougen et al [70] who compared the theoretical solutions obtained by the diffusion theory and the capillary flow theory with experimental data for sand, and their results strongly favour the capillary flow theory. However, at the pendular state, the liquid threads in the porous system become progressively discontinuous, and liquid islands are formed inside the porous medium. Motion due to capillary forces is greatly reduced. Under these circumstances, both diffusion and convection in the vapour phase are the primary mechanisms by which the moisture can be transferred. Thus the temperature of the porous system plays an important role in mass transfer, and the temperature gradient becomes a driving force along with the concentration gradient.

Moisture transfer under isothermal conditions has been investigated by many researchers[71-73]. Phillip and DeVries [74] and DeVries [75] proposed a theory of moisture movement in porous materials under combined temperature and moisture gradients which included a set of governing equations describing moisture and heat transfer. Similarly governing equations for heat and mass transfer in porous systems were published by Luikov [76]. For solving such a set of governing equations, the heat and mass transport properties of moist porous media are of fundamental importance. However, there is very little data available and few convenient means for the

measurement of these properties. Wang and Yu [77] proposed a method for the evaluation of heat and mass transport properties of moist porous media at different temperatures in the range $0 < T < 100\ ^{0}C$, based on the measured mass diffusivity and thermo-mass diffusivity data at a specified reference temperature. They indicated that all the transport properties are sensitive to both temperature and moisture content. However, the research was limited and did not consider the total pressure gradient in the porous media.

In all of the previous theoretical treatments of heat and moisture transfer in porous media, the governing differential equations were inferred in a phenomenological manner. Based on the principles of transport phenomena and non-equilibrium thermodynamics, Harmathy [17] derived a set of governing differential equations of heat and mass transfer in porous media during the pendular state and gave the solution with particular reference to clay bricks. Huang et al [78] extended the Harmathy's [17] work to the inclusion of the funicular state. Whitaker [79] developed a theory of drying in porous media based on the transport equations with an averaging technique. Wei et al [80] indicated that the models developed by Huang et al [78] and Harmathy [17] for predicted temperature, moisture content, and pressure profiles in the pendular state were not sufficient to explain the dynamic phenomena occurring in heated materials. They modified Whitaker's [79] derivations and applied the model to a sandstone subjected to mild heating conditions.

Most of the literature cited above does not take into account the pressure build up inside the porous medium due to evaporation and subsequent movement of the fluids. This phenomena is very important when porous media is heated under fire conditions. If the temperature in the porous body is not in excess of the boiling point of the liquid the mass diffusion will be important because most of the evaporation takes place below the boiling point.

Previous works concerning heat and mass transfer in porous media considered the issue of phase change [81-82], but the researches were limited to the steady-state and the heat pipe effect. Motakef and El-masri [83] analytically investigated simultaneous

heat and mass transfer with phase change in a porous slab. The medium was divided into three regions of dry-wet-dry by two internal boundaries. The research was extended by Shapiro and Motakef [84] and unsteady one-dimensional heat and mass transfer with phase change in a porous slab was investigated analytically. The criteria for the validity of the analytical solutions were compared with experimental data. Saito and Seki [85] analysed a one-dimensional moist porous material subjected to sudden heating; neglecting mass diffusion, postulating a dry-wet interface, and neglecting the volume occupied by the liquid. These researches contain a common disadvantage: that is the problem of locating the dry-wet interface in the porous medium. This is very inconvenient for the analysis of multi-dimensional systems.

Rubin and Schweitzer [86] considered the flow of liquid from a reservoir at high pressure entering a porous medium that was heated from the other side causing evaporation of the liquid within the medium. But they ignored mass diffusion completely. Sahota [11] proposed a theoretical model which takes into account mass diffusion, convection, evaporation, and condensation. No dry-wet interface was postulated. The advantages of this are: (1) the problem of locating the dry-wet interface is eliminated, which is particularly useful in multi-dimensional systems; (2) no boundary conditions at the interface are required. Movement of the liquid was neglected.

Based on the literature review above the theoretical model developed by Sahota [11] will be adopted as the theoretical foundation of thermal analysis of reinforced concrete in fire conditions in this study.

3.2.1 One-dimensional Energy Equation

In one dimensional form the energy equation can be expressed as [11]

$$\frac{\partial T}{\partial t} = \alpha \frac{\partial^2 T}{\partial x^2} + \left\{ \frac{1}{\rho C_p} \frac{\partial k}{\partial x} - C_r \left[u_m + \frac{D(C_{p,v} - C_{p,a})}{C_{p,m}} \frac{\partial w_a}{\partial x} \right] \right\} \frac{\partial T}{\partial x} - \frac{1}{\rho C_p} \left[h_{fg} \Gamma_m - \frac{\partial}{\partial t} (\rho_m R_m T) \right] \tag{3.1}$$

Sahota [11] carried out an order of magnitude analysis for the various terms in the governing equation. Sahota's analysis provides guidelines to determine the range of parameters required to describe the general result and the following simplifications may be made in the energy equation (3.1): the orders of magnitude of terms $C_r u_m$ and $C_r \frac{D(C_{p,v} - C_{p,a})}{C_{p,m}} \frac{\partial w_a}{\partial x}$, which respectively represent energy transfer by convection and mass diffusion, are <<1.

For the term $\frac{\partial}{\partial t}(\rho_m R_m T)$, which is the result of the difference between the enthalpy and internal energy of air-vapour mixture, the order of magnitude is also << 1.

Compared to the conduction terms for which the orders of magnitude are unity, the three terms noted above may be neglected. Thus the simplified energy equation can be written as:

$$\frac{\partial T}{\partial t} = \alpha \frac{\partial^2 T}{\partial x^2} + \frac{1}{\rho C_p} \frac{\partial k}{\partial x} \frac{\partial T}{\partial x} - \frac{1}{\rho C_p} h_{fg} \Gamma_m \tag{3.2}$$

Which is the ordinary conduction equation with a heat sink term due to evaporation of water.

Equation (3.2) holds, if

a) $\overline{\rho_m} << 1$, which is always the case,

b) $C_r \overline{u}_m << 1$, which will be the case if $\overline{u}_m$ is not too large (>> 100) due to strong heating and if the porous medium is not very light weight with a very low specific heat so as to make C_r larger this is the case in the majority of practical cases.

c) $C_r L_e << 1$, which is again mostly true if the modified Lewis number is < 100 and if C_r is not too large ($>> 10^{-3}$).

If one is interested only in the temperature field, equation (3.2) can be solved for T with initial and boundary conditions if Γ_m. the rate at which moisture vapour is produced, is known. The following assumptions are made to evaluate Γ_m:

(1) Under physically realistic conditions, the energy transfer due to mass diffusion is negligible compared to that by conduction. Neglecting the contribution of the mass diffusion term to heat transfer implies that the contribution due to evaporation of water is unimportant as long as liquid water does not start to boil.

(2) It should be noted that the boiling point temperature of water depends upon the pressure inside the concrete. Fortunately, it is observed that the saturation temperature for water is a weak function of the saturation pressure. For example, water boils at 100 ^0C at one atmosphere pressure and at ten atmospheres the boiling point temperature is about 180 ^0C. From experimental evidence [87], the boiling point of water in concrete is seen to be in the range from 100 to 140 ^0C. In this study it is assumed that water boils at 120^0C; that is for the purpose of calculating the temperature field inside the concrete the average pressure is taken as two atmospheres.

(3) Movement of the liquid water is neglected. This means the value of Darcy's coefficient for movement of liquid water is so small compared to that for the gases in concrete that the liquid water movement is considered not to be of significance. This is substantiated by Harmalthy [17] and Min and Emmoms [88] who claim that the liquid water, particularly at low moisture content, is present in the pendular state. That is, the liquid water in different pores is not interconnected.

As a result of assumption (1), Γ_m in equation (3.2) is put equal to zero at each point in the wet region in the interior of the concrete elements where temperature is less than 120^0C. Γ_m is also zero in the dry region. As the temperature at a wet node approaches 120^0C, it cannot increase further according to assumption (2) until all the liquid water

at that node is evaporated. So, the temperature at all the wet nodes is kept at 120^0C while liquid water evaporates. Γ_m is non-zero only when the liquid water is boiling. when the temperature is known to be 120^0C. Therefore. equation (3.2) can be used to calculate the value of Γ_m:

$$\Gamma_m = \frac{1}{h_{fg}}\left[k\frac{\partial^2 T}{\partial x^2} + \frac{\partial k}{\partial x}\frac{\partial T}{\partial x}\right] \tag{3.3}$$

As $\frac{\partial T}{\partial t} = 0.$

Physically, equation (3.3) represents a simple energy balance at a point. Usually, this energy balance is used to calculate temperature. but since the temperature is known. the same energy balance gives Γ_m. Once Γ_m is known, a new liquid density is calculated at that node using the continuity equation for the liquid. That is,

$$\frac{\partial \rho_l}{\partial t} = -\Gamma_m \tag{3.4}$$

Once the liquid density becomes zero, the temperature increases again with $\Gamma_m = 0$.

3.2.2 Two-dimensional Energy Equation

From equation (3.2), the two-dimensional energy equation can be expressed as follows:

$$\rho C_p \frac{\partial T}{\partial t} = \frac{\partial}{\partial x}\left(k\frac{\partial T}{\partial x}\right) + \frac{\partial}{\partial y}\left(k\frac{\partial T}{\partial y}\right) + H \tag{3.5}$$

where, H is internal heat generation.

for concrete:

$$H = -h_{fg}\Gamma_m \tag{3.6}$$

for steel:

$$H = 0 \tag{3.7}$$

Equation (3.3) can be used for calculation of Γ_m in the two-dimensional analysis, that is

$$\Gamma_m = \frac{1}{h_{fg}}\left[\frac{\partial}{\partial x}\left(k\frac{\partial T}{\partial x}\right) + \frac{\partial}{\partial y}\left(k\frac{\partial T}{\partial y}\right)\right] \tag{3.8}$$

where $\partial T/\partial t = 0$.

3.2.3 Initial and Boundary Conditions

There are five principal boundary conditions which are used for solving equation (3.5). Over any portion of the bounding surface of the body one of the following conditions are usually used:

(1) Known surface temperature:

$$T(P,t) = f(P,t) \tag{3.9}$$

where, the point P is on the surface and $f(P,T)$ is a prescribed function.

(2) Known heat input:

$$k\frac{\partial T}{\partial n}(P,t) = q(P,t) \tag{3.10}$$

where, n is the outward normal to the surface at point P, and $q(P,t)$ is the heat flow at point P.

(3) Perfectly insulated surface: By definition such a surface is one across which there is no heat flux, that is,

$$\frac{\partial T}{\partial n}(P,t) = 0 \tag{3.11}$$

(4) Convection and radiation boundary condition:

a) Convection heat transfer between reinforced concrete element and ambient

$$k\frac{\partial T}{\partial n}(P,t) = h\left(T_{\infty} - T_{s}\right) \tag{3.12}$$

b) Non-linear heat transfer from fire to the reinforced concrete element:

$$k\frac{\partial \theta}{\partial n}(P,t) = A\left(\theta_{f} - \theta_{s}\right)^{N} + v\sigma\left[a\ \varepsilon_{f}\ \theta_{f}{}^{4} - \varepsilon_{s}\ \theta_{s}{}^{4}\right] \tag{3.13}$$

(5) Two solid bodies in contact: For this study it is assumed that the interface between steel and concrete is in perfect thermal contacted. That means the following equation is satisfied at all such interfaces.

$$\left.\begin{aligned} T_{c}(P,t) &= T_{st}(P,t) \\ k_{c}\frac{\partial T_{c}}{\partial n}(P,t) &= k_{st}\frac{\partial T_{st}}{\partial n}(P,t) \end{aligned}\right\} \tag{3.14}$$

The initial condition will, naturally, be the temperature distribution at the initial time, prior to fire exposure.

3.3 Finite Element Solution Procedure

A number of approximate numerical methods are sufficiently well developed to solve a large variety of heat transfer problems. The finite difference method has been the

most widely used. Another numerical method is the finite element method which has become widely accepted as a valuable technique for solving complex problems.

The finite element method is completely general with respect to geometry, material properties, complex shapes composed of many different materials are easily represented. Non-linearity of material and boundary conditions can be treated by the finite element method easily. Therefore, the finite element method will be used as the solution technique in this research.

3.3.1 The Basic Equation

The heat transfer equation for a solid idealised by a system of finite elements can be physically interpreted as a statement of heat flow equilibrium at each node of the system at any time. That is

Rate at which heat is stored in the controlled volume of a node contributed by its adjacent elements	+	Rate at which heat flows by conduction into a node from its adjacent elements	=	Rate at which external heat enters a node	(3.15)

If all nodes are considered, the above heat flow equilibrium equation can be written in matrix form as follows:

$$\underline{C}\left(\rho, C_p\right)\dot{\underline{T}} + \underline{K}(k)\underline{T} = \underline{Q}\left(T, w, F(t)\right) \tag{3.16}$$

In the above equation, $\underline{C}$, $\underline{K}$, and $\underline{Q}$ are known matrices at each instant of time. Therefore, the equation can be solved by a numerical integration scheme.

3.3.2 Conductivity Matrix, $\underline{K}$

The terms of the conductivity matrix are associated with the rate of heat flow from the elements adjacent to each node. The conductivity matrix for the system being analysed is assembled from element conductivity matrices, $\underline{k}_m$. That is

$$\underline{K} = \sum_{m=1}^{M} \underline{k}_m \tag{3.17}$$

where, m is the element number and M is the total number of elements.

In order to have geometric flexibility, the isoparametric three-node triangular and four-node quadrilateral elements are used as basic elements for the idealisation of the two-dimensional body in this research. This assumes a linear temperature distribution within the element.

3.3.2.1 Conductivity Matrix of Isoparametric Three-node Triangular Element

The element is called "isoparametric" since the geometry of the element and the assumed temperature distribution within the element are described in terms of the same "parameters" (or shape functions) and are of the same order (linear in this case). For the three-node triangle (see Figure 3.2), the temperature at any point within the element is expressed in the natural co-ordinate system (L_1, L_2, L_3) in terms of the temperatures at nodes 1 to 3 by the following equation:

$$T = L_1 T_1 + L_2 T_2 + L_3 T_3 = [N]\{T_i\} \tag{3.18}$$

Similarly, the global co-ordinates are defined with the same shape function:

$$x = L_1 x_1 + L_2 x_2 + L_3 x_3 = [N]\{x_i\} \tag{3.19a}$$

and $$y = L_1 y_1 + L_2 y_2 + L_3 y_3 = [N]\{y_i\} \tag{3.19b}$$

where, $[N]=[L_1 \;\; L_2 \;\; L_3]$.

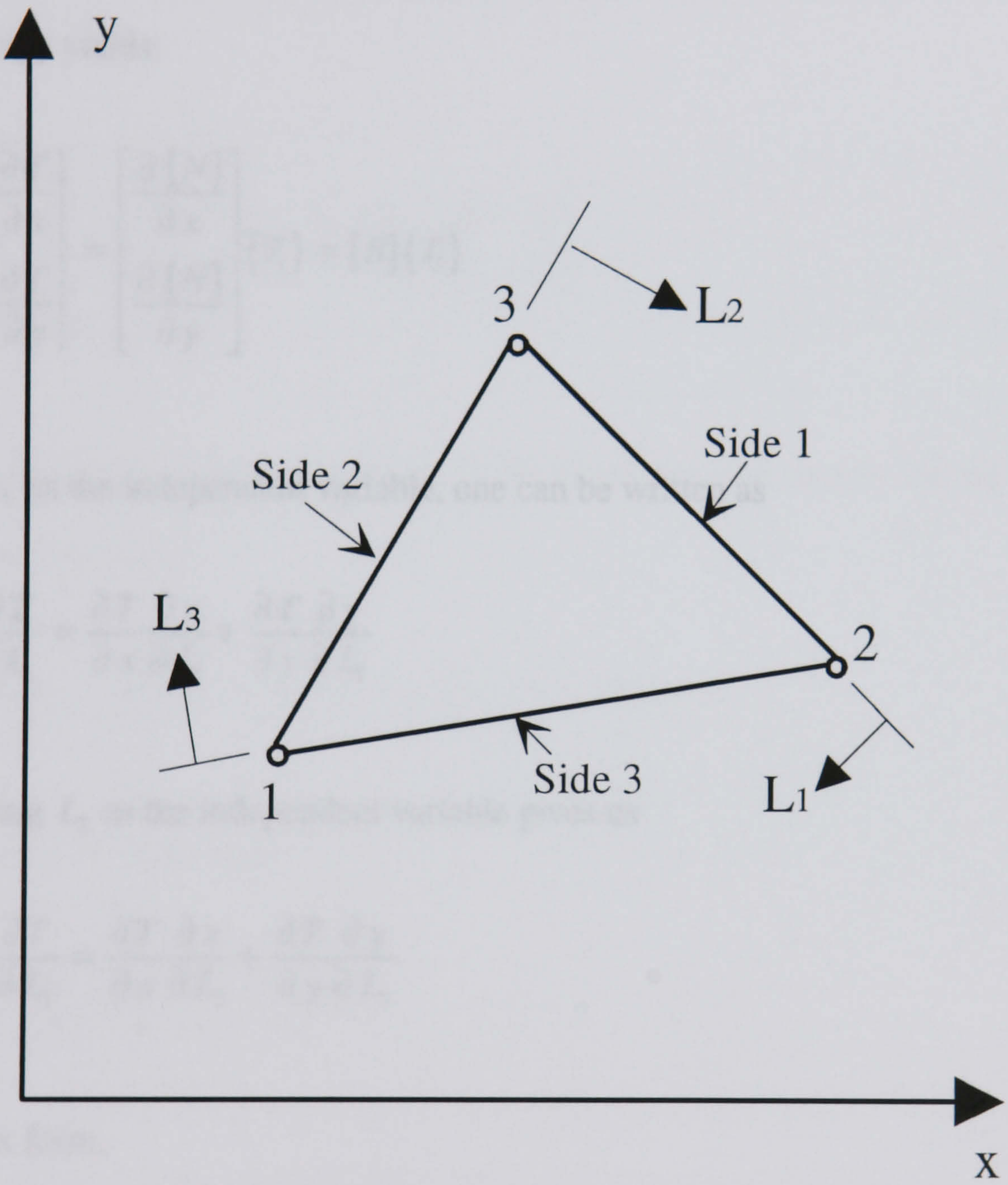

Figure 3.2 Triangle Natural Co-ordinates and Side Designation

The natural co-ordinates are related through the expression

$$L_1 + L_2 + L_3 = 1 \tag{3.20}$$

When calculating the element conductivity matrix, an expression for temperature gradient within the element will be needed. Differentiation of equation (3.18) with respect to x, y yields:

$$\begin{Bmatrix} \frac{\partial T}{\partial x} \\ \frac{\partial T}{\partial y} \end{Bmatrix} = \begin{bmatrix} \frac{\partial [N]}{\partial x} \\ \frac{\partial [N]}{\partial y} \end{bmatrix} \{T_i\} = [B]\{T_i\} \tag{3.21}$$

Treating L_1 as the independent variable, one can be written as

$$\frac{\partial T}{\partial L_1} = \frac{\partial T}{\partial x}\frac{\partial x}{\partial L_1} + \frac{\partial T}{\partial y}\frac{\partial y}{\partial L_1}$$

Also, treating L_2 as the independent variable gives us

$$\frac{\partial T}{\partial L_2} = \frac{\partial T}{\partial x}\frac{\partial x}{\partial L_2} + \frac{\partial T}{\partial y}\frac{\partial y}{\partial L_2}$$

or in matrix form,

$$\begin{bmatrix} \frac{\partial x}{\partial L_1} & \frac{\partial y}{\partial L_1} \\ \frac{\partial x}{\partial L_2} & \frac{\partial y}{\partial L_2} \end{bmatrix} \begin{Bmatrix} \frac{\partial T}{\partial x} \\ \frac{\partial T}{\partial y} \end{Bmatrix} = \begin{Bmatrix} \frac{\partial T}{\partial L_1} \\ \frac{\partial T}{\partial L_2} \end{Bmatrix} \tag{3.22}$$

Now, substituting the derivative of equations (3.18) and (3.19) into equation (3.22) yields

$$\begin{bmatrix} x_1 - x_3 & y_1 - y_3 \\ x_2 - x_3 & y_2 - y_3 \end{bmatrix} \begin{Bmatrix} \dfrac{\partial T}{\partial x} \\ \dfrac{\partial T}{\partial y} \end{Bmatrix} = \begin{Bmatrix} T_1 - T_3 \\ T_2 - T_3 \end{Bmatrix} \tag{3.23}$$

Solving for the global co-ordinate derivatives from equation (3.23), one can be obtained as:

$$\begin{Bmatrix} \dfrac{\partial T}{\partial x} \\ \dfrac{\partial T}{\partial y} \end{Bmatrix} = \frac{1}{|J|} \begin{bmatrix} y_2 - y_3 & y_3 - y_1 \\ x_3 - x_2 & x_1 - x_3 \end{bmatrix} \begin{Bmatrix} T_1 - T_3 \\ T_2 - T_3 \end{Bmatrix}$$

where $|J|$ is the Jacobian determinant of the transformation matrix for the two co-ordinate systems, that is

$$|J| = (x_1 - x_3)(y_2 - y_3) - (x_2 - x_3)(y_1 - y_3) = 2(area)$$

Now substitute the following:

$$\begin{Bmatrix} T_1 - T_3 \\ T_2 - T_3 \end{Bmatrix} = \begin{bmatrix} 1 & 0 & -1 \\ 0 & 1 & -1 \end{bmatrix} \{T_i\}$$

The resultant form of the expression is

$$\begin{Bmatrix} \dfrac{\partial T}{\partial x} \\ \dfrac{\partial T}{\partial y} \end{Bmatrix} = \frac{1}{|J|} \begin{bmatrix} y_2 - y_3 & y_3 - y_1 & y_1 - y_2 \\ x_3 - x_2 & x_1 - x_3 & x_2 - x_1 \end{bmatrix} \{T_i\} \tag{3.24}$$

$$= \frac{1}{|J|} \begin{bmatrix} b_1 & b_2 & b_3 \\ c_1 & c_2 & c_3 \end{bmatrix} \{T_i\}$$

Comparing equations (3.21) and (3.24),

$$[B]=\frac{1}{|J|}\begin{bmatrix} b_1 & b_2 & b_3 \\ c_1 & c_2 & c_3 \end{bmatrix} \tag{3.25}$$

According to the energy minimisation principle, it can be shown that the element conductivity matrix is given by [89]

$$\underline{k}_m = \iint_A [B]^T k [B] b \, dx \, dy \tag{3.26}$$

where, k is material isotropic thermal conductivity, b is the thickness of the element. Substituting equation (3.25) into (3.26) and integrating it, the element conductivity matrix can be given as:

$$\underline{k}_m = \frac{k\,b}{2|J|}\begin{bmatrix} b_1^2+c_1^2 & b_1b_2+c_1c_2 & b_1b_3+c_1c_3 \\ & b_2^2+c_2^2 & b_2b_3+c_2c_3 \\ symm. & & b_3^2+c_3^2 \end{bmatrix} \tag{3.27}$$

3.3.2.2 Conductivity Matrix of Isoparametric Four-node Quadrilateral Element

For the four-node quadrilateral element (see Figure 3.3), the temperature at any point within the element is expressed in the natural co-ordinate system ($\bar{x}$, $\bar{y}$) in terms of the temperatures at nodes 1 to 4 by the following equation

$$T = N_1 T_1 + N_2 T_2 + N_3 T_3 + N_4 T_4 = [N]\{T_i\} \tag{3.28}$$

For global co-ordinates

$$x = N_1 x_1 + N_2 x_2 + N_3 x_3 + N_4 x_4 = [N]\{x_i\} \tag{3.29a}$$

and $$y = N_1 y_1 + N_2 y_2 + N_3 y_3 + N_4 y_4 = [N]\{y_i\} \tag{3.29b}$$

where, $[N]=[N_1 \ N_2 \ N_3 \ N_4]$ and,

$$N_1 = \frac{(1-\bar{x})(1-\bar{y})}{4}, \qquad N_2 = \frac{(1+\bar{x})(1-\bar{y})}{4},$$

$$N_3 = \frac{(1+\bar{x})(1+\bar{y})}{4}, \qquad N_4 = \frac{(1-\bar{x})(1+\bar{y})}{4}.$$

The expression of temperature gradient within the element is same as equation (3.21). treating $\bar{x}$ as the independent variable,

$$\frac{\partial T}{\partial \bar{x}} = \frac{\partial T}{\partial x}\frac{\partial x}{\partial \bar{x}} + \frac{\partial T}{\partial y}\frac{\partial y}{\partial \bar{x}}$$

and with $\bar{y}$ as the independent variable,

$$\frac{\partial T}{\partial \bar{y}} = \frac{\partial T}{\partial x}\frac{\partial x}{\partial \bar{y}} + \frac{\partial T}{\partial y}\frac{\partial y}{\partial \bar{y}}$$

or in matrix form,

$$\begin{bmatrix} \frac{\partial x}{\partial \bar{x}} & \frac{\partial y}{\partial \bar{x}} \\ \frac{\partial x}{\partial \bar{y}} & \frac{\partial y}{\partial \bar{y}} \end{bmatrix} \begin{Bmatrix} \frac{\partial T}{\partial x} \\ \frac{\partial T}{\partial y} \end{Bmatrix} = \begin{Bmatrix} \frac{\partial T}{\partial \bar{x}} \\ \frac{\partial T}{\partial \bar{y}} \end{Bmatrix} \tag{3.30}$$

Solving for the spatial derivative terms, one can be obtained:

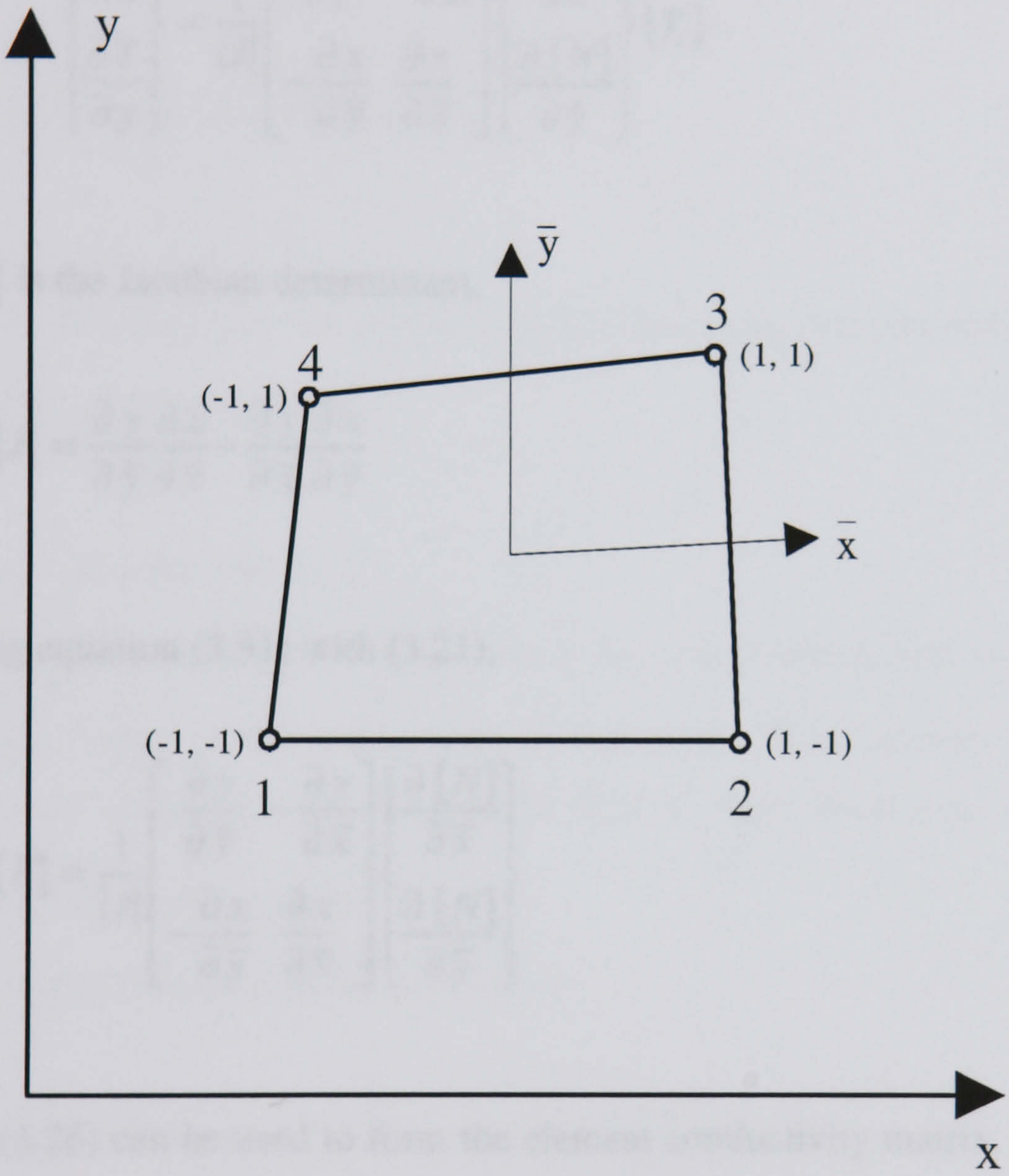

Figure 3.3 Standard Local Node Numbering and Co-ordinate Axes of Quadrilateral

$$\begin{Bmatrix} \frac{\partial T}{\partial x} \\ \frac{\partial T}{\partial y} \end{Bmatrix} = \frac{1}{|J|} \begin{bmatrix} \frac{\partial y}{\partial \bar{y}} & -\frac{\partial y}{\partial \bar{x}} \\ -\frac{\partial x}{\partial \bar{y}} & \frac{\partial x}{\partial \bar{x}} \end{bmatrix} \begin{Bmatrix} \frac{\partial T}{\partial \bar{x}} \\ \frac{\partial T}{\partial \bar{y}} \end{Bmatrix} \tag{3.31a}$$

or

$$\begin{Bmatrix} \frac{\partial T}{\partial x} \\ \frac{\partial T}{\partial y} \end{Bmatrix} = \frac{1}{|J|} \begin{bmatrix} \frac{\partial y}{\partial \bar{y}} & -\frac{\partial y}{\partial \bar{x}} \\ -\frac{\partial x}{\partial \bar{y}} & \frac{\partial x}{\partial \bar{x}} \end{bmatrix} \begin{Bmatrix} \frac{\partial [N]}{\partial \bar{x}} \\ \frac{\partial [N]}{\partial \bar{y}} \end{Bmatrix} \{T_i\} \tag{3.31b}$$

where, $|J|$ is the Jacobian determinant,

$$|J| = \frac{\partial y}{\partial \bar{y}} \frac{\partial x}{\partial \bar{x}} - \frac{\partial y}{\partial \bar{x}} \frac{\partial x}{\partial \bar{y}}$$

Comparing equation (3.31) with (3.21),

$$[B] = \frac{1}{|J|} \begin{bmatrix} \frac{\partial y}{\partial \bar{y}} & -\frac{\partial y}{\partial \bar{x}} \\ -\frac{\partial x}{\partial \bar{y}} & \frac{\partial x}{\partial \bar{x}} \end{bmatrix} \begin{Bmatrix} \frac{\partial [N]}{\partial \bar{x}} \\ \frac{\partial [N]}{\partial \bar{y}} \end{Bmatrix} \tag{3.32}$$

Equation (3.26) can be used to form the element conductivity matrix. Because matrix $[B]$ is not constant the determination of the conductivity matrix, $\underline{k}_m$, requires integration of the matrix product over the volume, $b\ dA$, of the element. There are two "difficulties":

(1) The $[B]$ matrix has entries that involve ratios of functions of the natural co-ordinates $\bar{x}$ and $\bar{y}$.

(2) The differential area dA can be easily expressed as $dxdy$, but this integration variable is not the same as the $[B]$ matrix variable, so a change of variable must be undertaken. Therefore, first the integration will be done numerically, and second, the co-ordinates of the differential area will be changed from the physical x, and y to the

natural $\bar{x}$ and $\bar{y}$ by application of the Jacobian determinant of the transformation equations for the two co-ordinate systems. Note that [89].

$$dV = b\,dx\,dy = b|J|\,d\bar{x}\,d\bar{y} \tag{3.33}$$

So, equation (3.26) become as follows:

$$\underline{k}_m = k\,b\int_{A^*}[B]^T[B]\,|J|\,d\bar{x}\,d\bar{y} \tag{3.34}$$

To carry out the integration of equation (3.34), two-point formula of Gauss quadrature is employed here to calculate $\underline{k}_m$.

3.3.3 Heat Capacity Matrix, $\underline{C}$

The heat capacity associated with a node is the rate at which heat is absorbed for a unit rate of change of the temperature at that node. This capacity matrix contains terms that are dependent on the specific heat C_p and density ρ of the elements immediately adjacent to each node.

The heat capacity for an element is given by:

$$\underline{C}_m = V_m\,\rho\,C_p \tag{3.35}$$

where, V_m is volume of element that is equal to unit thickness multiplied by the area of element.

The contribution of an element, m, to a particular node, i, is given by (see Figure 3.4):

$$\underline{C}_{m,i} = \rho\;C_p\,\frac{A_m}{n_1} \tag{3.36}$$

where, A_m is area of element adjacent to node, i; n_1 is number of vertexes of the element; so that, the heat capacity matrix of a node, i, is

$$\underline{C}_i = \sum_{m=1}^{M'} \underline{C}_{m,i} \tag{3.37}$$

where, M' is the number of elements adjacent to node i. The heat capacity matrix of the system is

$$\underline{C} = \sum_{i=1}^{n_2} \underline{C}_i \tag{3.38}$$

where, n_2 is the number of nodes of system.

3.3.4 External Heat Flow Vector, $\underline{Q}$

For the solution of a heat flow problem one of two conditions must be known for each node: the temperature of the node, or the external heat flow associated with the node. The external heat flow is expressed in the following summation:

$$\underline{Q} = \underline{Q}_E + \underline{Q}_F + \underline{Q}_K \tag{3.39}$$

For this study:

(1) $\underline{Q}_E$ is to be considered as the internal heat generation vector. So, for an element, m, $\underline{Q}_{E,m}$ can be expressed by

$$\underline{Q}_{E,m} = V_m H_m \tag{3.40}$$

where, V_m is volume of the m-th element; and H_m is internal heat generation rate for m-th element.

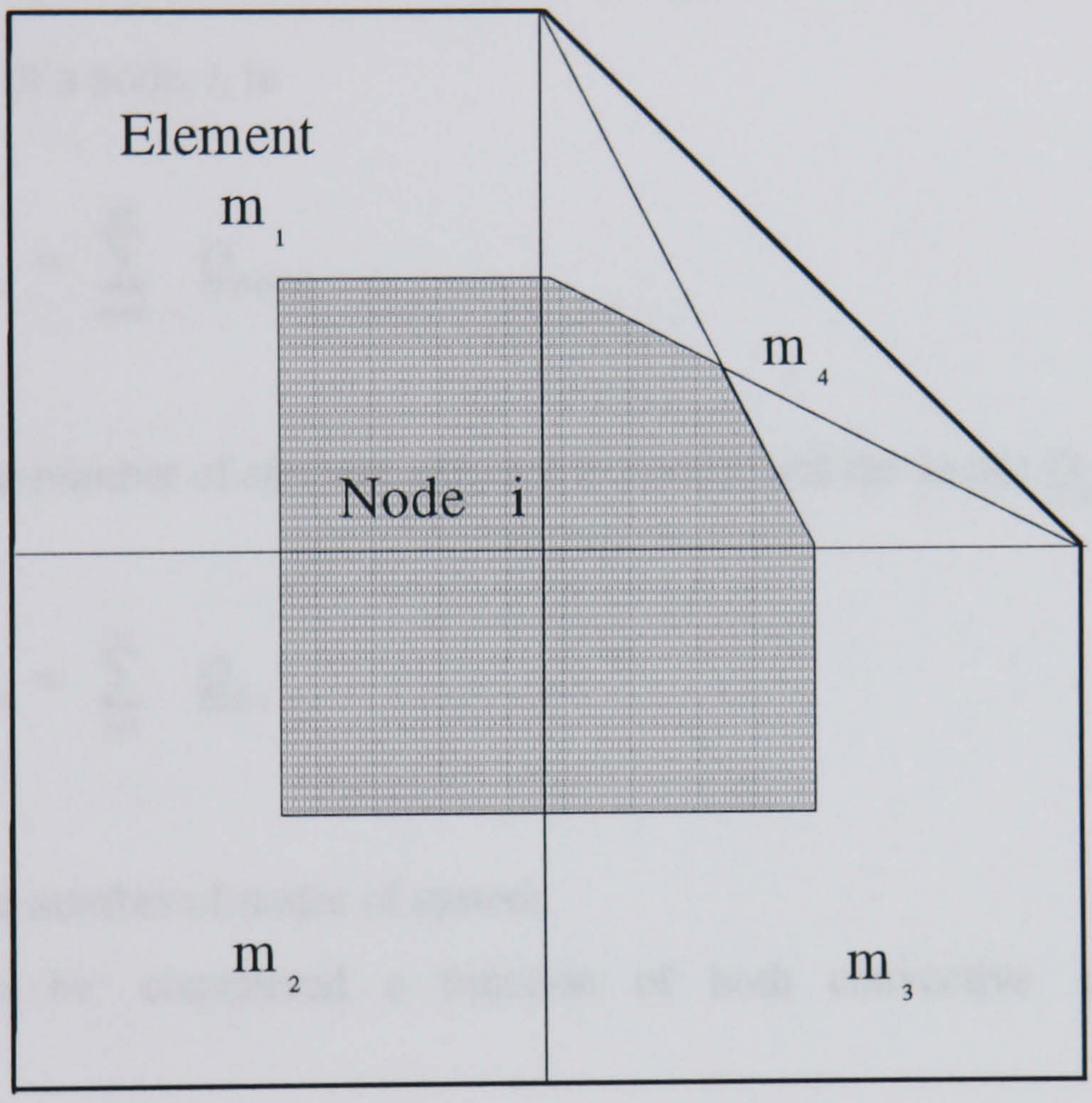

Figure 3.4 Heat Capacity and Internal Heat Generation Idealisation

Using the same analysis as for the heat capacity matrix (see Figure 3.4), the contribution of an element, m, to a particular node, i, is given by:

$$\underline{Q}_{E(m,i)} = H_m \frac{A_m}{n_1} \tag{3.41}$$

where, A_m and n_1 have the same meaning as in equation (3.36). So that, the internal heat generation of a node, i, is

$$\underline{Q}_{E,i} = \sum_{m=1}^{M'} \underline{Q}_{E(m,i)} \tag{3.42}$$

where, M' is the number of element adjacent to node i; and the vector $\underline{Q}_E$ is then

$$\underline{Q}_E = \sum_{i=1}^{n_2} \underline{Q}_{E,i} \tag{3.43}$$

where, n_2 is the number of nodes of system.

(2) $\underline{Q}_F$ is to be considered a function of both convective and radiative mechanisms.

Fires affecting structures are here considered to be those in a post-flashover regime, which allows the assumption of a uniform room temperature. This time-temperature relationship for a fire is represented by the fire curve F(t). The boundary of the system exposed to a fire or ambient is assumed to be made up of surfaces of a unit thickness connecting adjacent nodes (e.g., i and j). Thus, the external heat flow over a surface can be represented by:

$$\underline{Q}_{F,m} = 0.5 \times l \; q, \quad m=i, j \tag{3.44}$$

where, l is separation of nodes i and j, q is rate of external heat flow per unit area.

For fire boundary, q can be expressed as (see equation (3.13))

$$q = A\left(\theta_f - \theta_s\right)^N + v\sigma\left[a\varepsilon_f \theta_f^{\,4} - \varepsilon_s \theta_s^{\,4}\right] \tag{3.45}$$

Where, θ_s = average absolute surface temperature, $\left(\theta_i + \theta_j\right)/2$

θ_f = absolute temperature of pseudo-fire, $F(t)$.

For ambient boundary, q can be calculated by (see equation (3.12))

$$q = h\left(T_\infty - T_s\right) \tag{3.46}$$

where, T_s is average surface temperature, $\left(T_i + T_j\right)/2$.

For the internal nodes of the system,

$$\underline{Q}_{F,m} = 0, \quad m = i, j \tag{3.47}$$

and the vector $\underline{Q}_F$ is then

$$\underline{Q}_F = \sum_{i=1}^{n_2} \underline{Q}_{F,i} \tag{3.48}$$

where, n_2 is the number of nodes of system.

(3) $\underline{Q}_K$ is a prescribed heat flow vector and it is directly entered as data.

3.3.5 Numerical Scheme

The heat flow equation and associated boundary conditions are solved using a finite element method. The technique reduces the differential equation to a system of algebraic equations. Equation (3.16) can now be simplified in representation to:

$$\underline{C}\ \dot{\underline{T}}_i + \underline{K}\ \underline{T}_i = \underline{Q} \tag{3.49}$$

where, i is to represent the i-th time step. Using a linear approximation for the temperature rate of change vector $\underline{\dot{T}}_i$, that is

$$\underline{\dot{T}}_i = \frac{\left(\underline{T}_i - \underline{T}_{i-1}\right)}{\Delta t} \tag{3.50}$$

where, Δt is the time step interval. Substituting equation (3.50) into equation (3.49) yields

$$\frac{1}{\Delta t}\,\underline{C}\left(\underline{T}_i - \underline{T}_{i-1}\right) + \underline{K}\,\underline{T}_i = \underline{Q} \tag{3.51}$$

By defining two new matrices, the modified conductivity matrix $\underline{K}^*$ and the modified external heat flow vector $\underline{Q}^*$, that is,

$$\underline{K}^* = \underline{K} + \frac{1}{\Delta t}\underline{C} \tag{3.52}$$

$$\underline{Q}^* = \underline{Q} + \frac{1}{\Delta t}\underline{C}\,\underline{T}_{i-1} \tag{3.53}$$

Substituting equations (3.52), (3.53) into equation (3.51) the following is obtained:

$$\underline{K}^*\,\underline{T}_i = \underline{Q}^* \tag{3.54}$$

where, both K^* and Q^* are functions of the current temperature $\underline{T}_i$. In particular, $\underline{K}$, $\underline{C}$, and $\underline{Q}$ are functions of $\underline{T}_i$. There are two basic approaches that can be used in resolving this problem.

(1) Use the temperature distribution from the previous time step, $\underline{T}_{i-1}$ to calculate the necessary values (that is, $\underline{K}$, $\underline{C}$, and $\underline{Q}$) and thus solve equation(3.54) directly.

(2) Use an iterative solution technique that allows the necessary variables to be continually revised on the basis of the converging solution. This method was employed by Becker et al [4].

Evidently, method (1) is simpler than method (2), and can save a lot of computing time. However, since $\underline{Q}_F$ is more sensitive to the surface temperature of the structural member (see equation (3.45)). An approximation is used to linearize the equation (3.54) to solve the problem, that is, for a function $\phi = f(z)$,

$$\phi \equiv \phi_0 + \left.\frac{\partial \phi}{\partial z}\right|_0 \Delta z \tag{3.55}$$

So, equation (3.45) can be linearised as:

$$\begin{aligned} q = A\Big[& N\left(\theta_{f,i-1} - \theta_{s,i-1}\right)^{(N-1)}\left(\theta_{f,i} - \theta_{s,i}\right) - (N-1)\left(\theta_{f,i-1} - \theta_{s,i-1}\right)^{N}\Big] \\ & + v\,\sigma\Big[a\varepsilon_f\,\theta_{f,i}^{4} - \varepsilon_s\left(4\theta_{s,i-1}^{3}\,\theta_{s,i} - 3\theta_{s,i-1}^{4}\right)\Big] \end{aligned} \tag{3.56}$$

Now, equation (3.54) can be solved easily with the previous time step (i-1) information known. In this research, method (1) with the approximation described above has been employed to solve equation (3.54).

3.3.6 Fire Boundary Conditions

A building fire has three main phases: ignition and growth, full development and decay. It is during the fully developed phase that most of the structural damage occurs. The severity of a real fire in a compartment depends upon three main factors: (1) fuel for the fire or fire load; (2) Ventilation (i.e. air supply) to promote its growth, and (3) the characteristics of the compartment. Therefore, rational modelling of real fire is more complicated and need further investigation.

At present, building code requirements for fire resistant design in most countries are based on the standard fire endurance test. In those tests the temperature in furnaces are following the standard fire curve (temperature-time relation).

3.3.6.1 Standard Fire Curves

The International Organisation of Standardisation has defined in ISO 834 [1], the standardised temperature-time relation in the standard fire test that is used by the national building codes of most countries, and has been adopted by British Standard BS 476 [2]. The standard fire exposure is defined as (see Figure 3.5)

$$T_f - T_0 = 345\log_{10}(8t+1) \tag{3.57}$$

where, t = the time (minutes)

T_f = the furnace temperature at time t (^0C)

T_0 = the initial furnace temperature (^0C)

Another standard fire curve commonly used in the North American countries is ASTM-E119 Fire [63] which is defined by American Society for Testing and Materials. This temperature course can be approximately described by the following expression [90]

$$T_f = 20+750\left[1-\exp\left(-3.79553\sqrt{t}\right)+170.41\sqrt{t}\right] \tag{3.58}$$

where, t = the time (hours)

T_f = the furnace temperature at time t (^0C)

Most laboratory tests used to determine fire resistance of building elements are conducted in furnaces following these temperature relationships. However, it is noted that the standard fire curve is not a realistic model of an actual fire. For most real fires, the temperature of internal concrete and steel does not reach the levels indicated in the standard fire test [91]. The standard fire curve will be employed in this research for

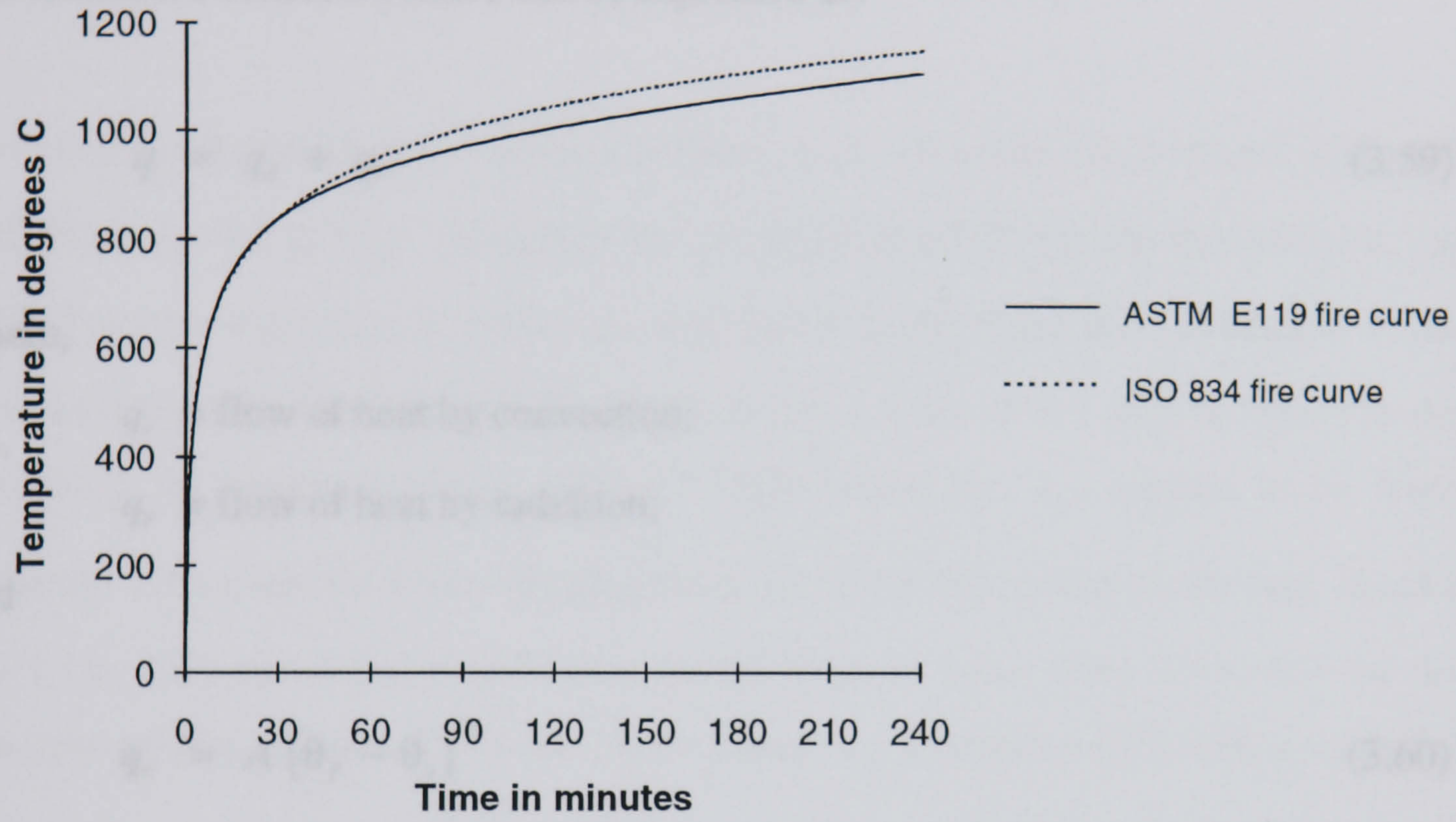

Figure 3.5 ISO 834 and ASTM-E119 Fire Curves [1, 63]

the computer simulation. However, it is a relatively easily process to modify the model to use other kinds of fire curves.

3.3.6.2 The Parameters of Fire Boundary Condition

A non-linear boundary condition will be used in this research. The surface heat transfer will be calculated by equation (3.45), that is, the heat transfer between fire and reinforced concrete surface can be expressed as:

$$q = q_c + q_r \tag{3.59}$$

where,

q_c = flow of heat by convection;

q_r = flow of heat by radiation;

and

$$q_c = A\left(\theta_f - \theta_s\right)^N \tag{3.60}$$

Many researchers [58, 91, 92] suggested a simple estimation of the heat transfer coefficient, A, in the range of 10 to 30 ($W m^{-2} K^{-1}$), while suggesting the convection power, N, equal to 1.0 is adequate in most standard fire resistance calculations. Odeen and Nordstrom [92] indicated the coefficient should be in the interval of 23 to 29 ($W m^{-2} K^{-1}$), while CEB [93] and Malhotra [91] took a value of 25 ($W m^{-2} K^{-1}$). Theoretical calculations verified by tests Anderberg [58] employed a value equal to 12 ($W m^{-2} K^{-1}$).

Wickström [6] has evaluated the parameters A and N based on a complex theoretical approach in relation to a specific test programme and found that for a cool side A=2.2 ($W m^{-2} K^{-1.25}$), N=1.25 and for an exposed side A=1.0 ($W m^{-2} K^{-1.33}$), N=1.33. According to Harmathy [94] A=1.78 ($W m^{-2} K^{-1.25}$) for vertical surface, A=2.50 ($W m^{-2} K^{-1.25}$) for horizontal surface, and N =1.25.

At elevated temperatures in fire conditions the heat flow rate from convection is of secondary importance when compared to the heat flow from radiation and, therefore, the values of A and N proposed by Harmathy [94] will be used for the proving test (see Chapter 5).

The radiation term, q_r, can be expressed as:

$$q_r = \nu\sigma\left(a\varepsilon_f\theta_f^4 - \varepsilon_s\theta_s^4\right) \tag{3.61}$$

The phenomena associated with heat transfer in the turbulent environment of fire is difficult to model exactly. Assuming the acceptability of the pseudo-fire concept, the critical parameters appear to be the emissivity of both the flame and the surface of the structural element. According to Becker et al [4], a value of 0.9 may be used for the emissivity of concrete, ε_s, the value of flame emissivity, ε_f, appears to be more uncertain with potential values ranging from 0.3 to 0.9 depending on the fuel. Bresler and Iding [95] stated that emissivities should range in value from 0.5 to 0.9 for the concrete surface, ε_s, and 0.5 or 0.7 for the flame, ε_f. Pettersson [96] took a value for the emissivity of a steel surface of 0.8 and stated the emissivity of flames should be in the interval of 0.6 to 0.9, with 0.85 used in his calculation.

It should be noted that the flame emissivity will depend on the particulate content of the flame, which may very greatly between the controlled fire of a test furnace and the uncontrolled environment of an actual fire.

Bresler and Iding [95] suggested a radiation view factor, ν, may be taken in the interval of 0.0 to 1.0, and employed a value of 1.0 for horizontal surfaces and 0.5 for vertical surfaces in calculations. The surface absorption, a, is usually set to around 0.9.

Because of the complexity of fire boundary conditions, Based on the literature review above, a range of 0.6 to 0.9 for the values of fire emissivity, ε_f, will be used in proving test to evaluate their sensitive to the thermal analysis (see Chapter 5).

3.3.7 Description of Computer Programme, FPRCBC-T

FPRCBC-T is a computer programme for the Fire Performance of Reinforced Concrete Building Components - Thermal, which is a two dimensional non-linear thermal model for predicting the temperature histories of the cross-sections of reinforced concrete structural members subjected to a fire environment. The cross-section is modelled through the use of quadrilateral or triangular finite elements. FPRCBC-T is written in FORTRAN77. The flow chart of the programme is presented in Figure 3.6.

The temperature distributions generated by FPRCBC-T will be used for predicting the mechanical response of a reinforced concrete structure, providing an overall capability of predicting the fire endurance of structures subjected to fires (see Chapter 5).

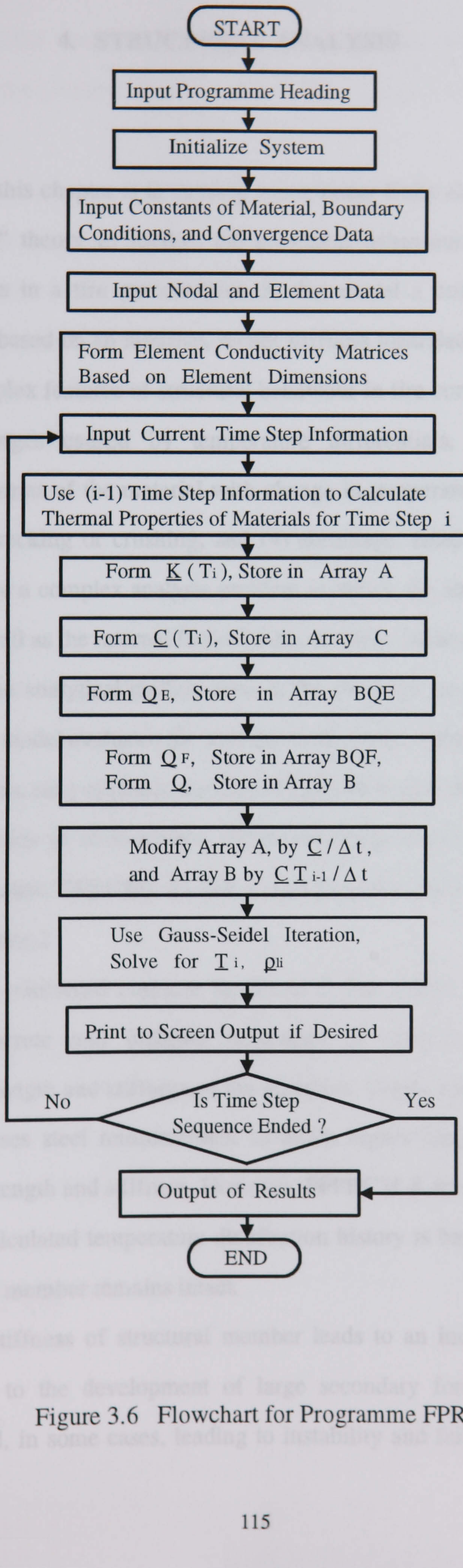

Figure 3.6 Flowchart for Programme FPRCBC-T

4. STRUCTURAL ANALYSIS

4.1 Introduction

The objective of this chapter is to develop a non-linear finite element model based on the "plane stress" theory to predict the structural behaviour of planar reinforced concrete members in a fire environment. In this model a non-linear finite element method which is based on an iterative, secant stiffness formulation, is used in order to consider the complex features of structural behaviour in fire conditions. These are: (1) dimensional changes caused by temperature differentials. (2) changes in the mechanical properties of the material with change in temperature, (3) degradation of the element by cracking or crushing, and (4) shrinkage, creep and transient strains. These effects pose a complex analysis problem in which the strength and stiffness of the structure as well as the internal forces in the structure continually change.

In this chapter, the analytical method used in the computer programme, FPPRCM-S, is described. The model evaluates the non-linear structural response history (i.e. stress, strain, deterioration, etc.) of planar reinforced concrete members subjected to fire. The temperature histories of cross-section of the structural member is predicted by the computer programme, FPRCBC-T. The material models used in FPPRCM-S were described in Chapter 2.

The exposure of reinforced concrete members to fire results in local cracking and crushing of concrete and inelastic behaviour of steel reinforcement, causing degradation in strength and stiffness of the members. Under some conditions, spalling of concrete exposes steel reinforcement to much higher temperatures with further degradation of strength and stiffness. However, FPPRCM-S does not attempt to model spalling as the calculated temperature distribution history is based on the assumption that the structural member remains intact.

Degradation of stiffness of structural member leads to an increase in deformation, possibly leading to the development of large secondary forces due to geometric nonlinearities and, in some cases, leading to instability and failure. These effects are

not considered in this study since it is not concerned with various modes of failure. but, rather with a time-history of structural response prior to failure.

4.2 Mathematical Background of Plane Stress Problem

In this research the analysis of two-dimensional plane stress is introduced to model the structural behaviours of planar reinforced concrete members. Mathematical formulations for this kind of problem are briefly discussed as follows:

4.2.1 Plane Stress Behaviour

The following relations can be found in many texts on theory of elasticity, for example by Timshenko and Goodier [97]. These relations are derived on the basis of small displacement theory.

4.2.1.1 Stress-strain Relations.

Refer to Figure 4.1, for this case the normal and shear stress components act in two co-ordinate directions only. In general, the longitudinal strain is non zero in all co-ordinate directions and, $\sigma_z = 0$, $\tau_{zx} = \tau_{zy} = 0$.

The relation between stress and strain is

$$\begin{Bmatrix} \sigma_x \\ \sigma_y \\ \tau_{xy} \end{Bmatrix} = \frac{E}{1-\nu^2} \begin{bmatrix} 1 & \nu & 0 \\ \nu & 1 & 0 \\ 0 & 0 & \frac{1-\nu}{2} \end{bmatrix} \begin{Bmatrix} \varepsilon_x \\ \varepsilon_y \\ \gamma_{xy} \end{Bmatrix} \qquad (4.1a)$$

or

$$\{\sigma\} = [C]\{\varepsilon\} \qquad (4.1b)$$

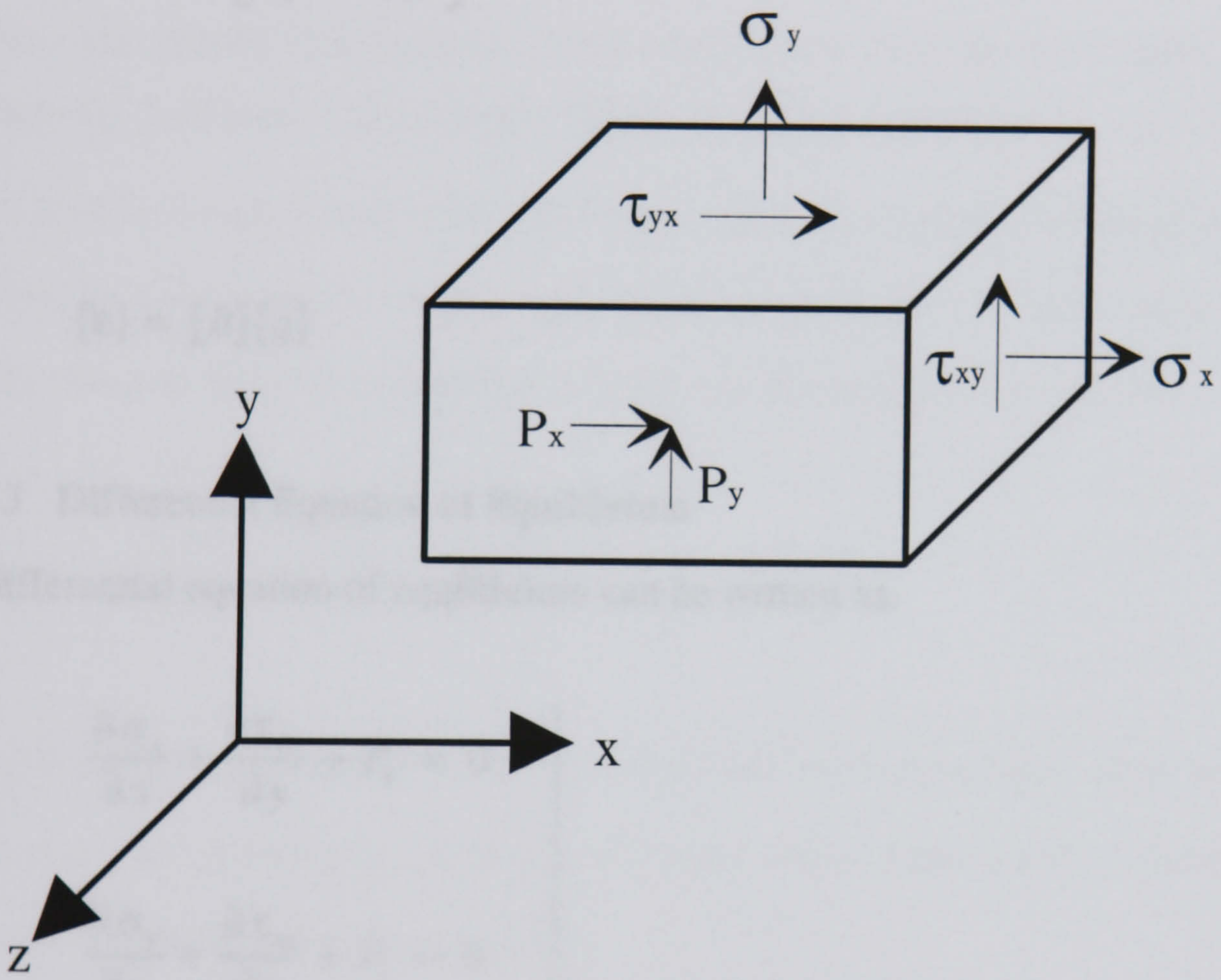

Figure 4.1 Normal and Shear Stresses on the x and y Faces of a Differential Solid [97]

4.2.1.2 Strain-displacement Relations

The relation between strain and displacement can be expressed as follows:

$$\begin{Bmatrix} \varepsilon_x \\ \varepsilon_y \\ \gamma_{xy} \end{Bmatrix} = \begin{bmatrix} \frac{\partial}{\partial x} & 0 \\ 0 & \frac{\partial}{\partial y} \\ \frac{\partial}{\partial y} & \frac{\partial}{\partial x} \end{bmatrix} \begin{Bmatrix} u \\ v \end{Bmatrix} \tag{4.2a}$$

or

$$\{\varepsilon\} = [B]\{q\} \tag{4.2b}$$

4.2.1.3 Differential Equation of Equilibrium

The differential equation of equilibrium can be written as:

$$\left.\begin{aligned} \frac{\partial \sigma_x}{\partial x} + \frac{\partial \tau_{xy}}{\partial y} + P_x &= 0 \\ \frac{\partial \sigma_y}{\partial y} + \frac{\partial \tau_{xy}}{\partial x} + P_y &= 0 \end{aligned}\right\} \tag{4.3}$$

where, P_x, P_y are body forces in x and y directions, respectively.

4.2.1.4 Boundary Conditions

Equation (4.3) must be satisfied at all points throughout the volume of the body. The stress components vary over the volume of the plate. At the boundary points they must be such as to be in equilibrium with the external forces on the boundary of the plate, so that external forces must be regarded as a continuation of the internal stress

distribution. Hence, at the plate boundaries either boundary forces or boundary displacements must be specified.

4.2.1.5 Compatibility Equations

The equation (4.3) derived by application of the equations of static and containing three stress components σ_x, σ_y, τ_{xy}, are not sufficient for the determination of these components. The problem is a statically indeterminate one. and in order to obtain the solution, the elastic deformation of the body must also be considered. For two-dimensional problems we consider three strain components, ε_x, ε_y, γ_{xy}. From equation (4.2) it can be seen that these three strain components are expressed by two functions *u* and *v*, hence, they cannot be taken arbitrarily. There exists a certain relation between the strain components which can be expressed as follows:

$$\frac{\partial^2 \varepsilon_x}{\partial y^2} + \frac{\partial^2 \varepsilon_y}{\partial x^2} = \frac{\partial^2 \gamma_{xy}}{\partial x \partial y} \tag{4.4}$$

This differential relationship, called the condition of compatibility, must be satisfied by the strain components to secure the existence of functions *u* and *v* connected with the strain components by equation (4.2).

The equations of equilibrium (4.3) together with the boundary conditions and compatibility equation (4.4) produce a system of equations that is usually sufficient for the complete determination of the stress distribution in a two-dimensional problem.

4.3 Non-linear Finite Element Analysis Procedure

At present, the exact method for the solution of equations (4.3) to (4.4) for reinforced concrete members in fire conditions is not available. Therefore, approximate numerical methods must be used. With the help of a computer, approximate numerical methods such as the finite difference, and finite element methods have become

practical. The most recent and one of the most potentially powerful techniques for the analysis of structural problems is the technique of finite element. Therefore a non-linear finite element method coupled with a time step integration is employed to deal with the complex features of the behaviour of planar reinforced concrete members in the fire environment.

4.3.1 Discretization by Finite Element Method

In this research, structural members are modelled as an assemblage of concrete elements and main reinforced bar elements (see Figure 4.2). The Concrete element is sub-divided into several layers and every layer is assumed to have a uniform temperature (see Figure 4.2). The longitudinal main steel reinforcements are modelled in a discrete manner using the bar element and this bar element is a structural member capable of transmitting stresses only in the direction normal to the cross-section. It is assumed that this normal stress is constant over the cross-sectional area of bar and that during deformation the area itself remains constant. The shear reinforcement is induced in the properties of the concrete elements and thus modelled in a smeared manner (see Chapter 2).

In this chapter all parameters are relative to global co-ordinates except where stated otherwise. The basic analytical problem is to find the deformation history of the nodes, $\{U(t)\}$, when external loading at the nodes, $\{R(t)\}$, and temperature histories within the members, are specified. In this procedure all parameters are time dependent. The basic equilibrium equation at time t, that define the structural system is as follows:

$$\{R(t)\} - \{Q(\{U(t)\})\} = 0 \tag{4.5}$$

where, the vector $\{R(t)\}$ is the externally applied nodal loads, and $\{Q(\{U(t)\})\}$ is the vector of internal nodal point forces that are equivalent to the element stresses. Equation (4.5) means that the internal forces acting at the nodes, $\{Q\}$, must be equal

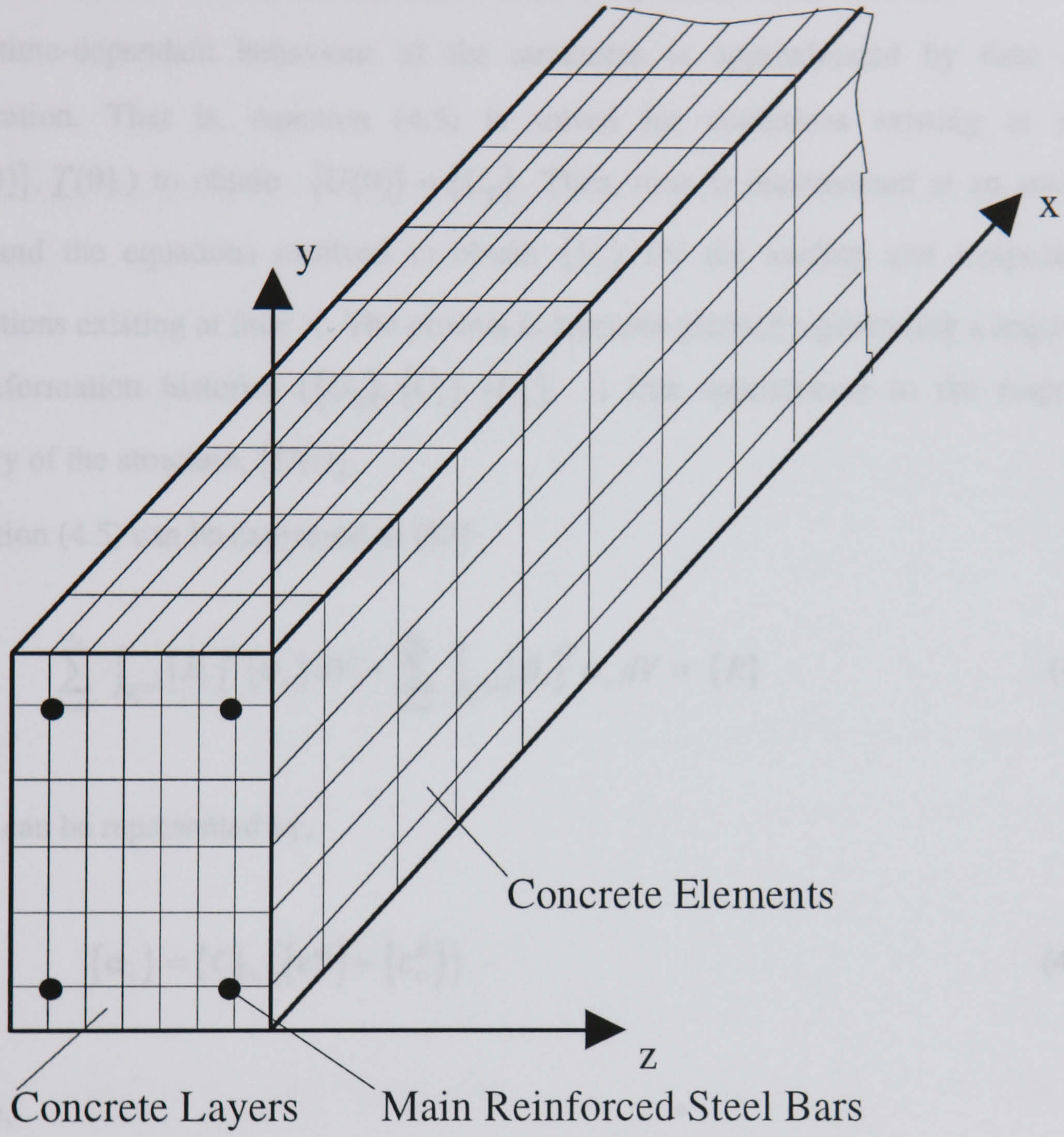

Figure 4.2 Division of Reinforced Concrete Member into Concrete and Main Reinforced Steel Bar Elements

to the external forces at nodes, $\{R\}$, at all time t. The internal forces at each node represent the deformational resistance contributed by each element attached to that node and depend on the geometry and material composition of the elements.

The time-dependant behaviour of the structures is approximated by time step integration. That is, equation (4.5) is solved for conditions existing at $t=0$ ($\{R(0)\}, \underline{T}(0)$) to obtain $\{U(0)\} = \{U_0\}$. Then, time is incremented at an amount Δt, and the equations resolved to obtain $\{U_1\}$ for the loading and temperature conditions existing at time t_1. The process is repeated gradually generating a sequence of deformation histories ($\{U_0\}, \{U_1\}, \{U_2\}, \ldots$) that approximate to the response history of the structure, $\{U(t)\}$.

Equation (4.5) can be expressed as [89]:

$$\sum_{m=1}^{n_c} \int_{V_c^{(m)}} [B_c]^T \{\sigma_c\} dV + \sum_{m=1}^{n_s} \int_{V_s^{(m)}} [B_s]^T \sigma_s \, dV = \{R\} \tag{4.6}$$

$\{\sigma_c\}$ can be represented by,

$$\{\sigma_c\} = [C]_{rc} \left(\{\varepsilon_c^m\} - \{\varepsilon_c^F\} \right) \tag{4.7}$$

where,

$$\{\varepsilon_c^m\} = [B_c]\{u_c\} \tag{4.8}$$

$$\{\varepsilon_c^F\} = \{\varepsilon_c^{creep}\} + \{\varepsilon_c^{sh}\} + \{\varepsilon_c^{tr}\} + \{\varepsilon_c^T\} \tag{4.9}$$

and σ_s can be written as,

$$\sigma_s = \overline{E}_s \left(\varepsilon_s^m - \varepsilon_s^F \right) \tag{4.10}$$

where,

$$\varepsilon_s^m = [B_s]\{u_s\} \tag{4.11}$$

$$\varepsilon_s^F = \varepsilon_s^{creep} + \varepsilon_s^T \tag{4.12}$$

Substituting equations (4.7), (4.8), (4.10), and (4.11) into equation (4.6) one can be obtained:

$$[K]\{U\} = \{R\} + \{F\} \tag{4.13}$$

where,

$$[K] = \sum_{m=1}^{n_c} [k_c]_m + \sum_{m=1}^{n_s} [k_s]_m \tag{4.14}$$

where,

$$[k_c]_m = \int_{V_c^{(m)}} [B_c]^T [C]_{rc} [B_c]\, dV \tag{4.15}$$

$$[k_s]_m = \int_{V_s^{(m)}} [B_s]^T \overline{E}_s [B_s] dV \tag{4.16}$$

and

$$\{F\} = \sum_{m=1}^{n_c} \{F_c\}_m + \sum_{m=1}^{n_s} \{F_s\}_m \tag{4.17}$$

where,

$$\{F_c\}_m = \int_{V_c^{(m)}} [B_c]^T \{\sigma_c^F\} dV \tag{4.18}$$

$$\{F_s\}_m = \int_{V_s^{(m)}} [B_s]^T \sigma_s^F \, dV \tag{4.19}$$

For a reinforced concrete structural member in the fire conditions, equation (4.13) is highly non-linear because of the non-linear stress-strain laws for concrete and steel, and the tendency of concrete to crack or crush. Also, the nominal nodal forces produced by the free strains, $\{F\}$, are influenced by temperature history and time dependent factors such as creep and shrinkage. Therefore, in this study the non-linear time dependent equation (4.13) is solved by an iterative procedure which is based on secant stiffness approach. In each cycle a linear analysis is performed. Details of this procedure are given in Section 4.3.5. Calculation of the stiffness matrix, $[K]$, and the nominal node forces vector, $\{F\}$, are discussed next.

4.3.2 Structural Stiffness Matrix, $[K]$

The stiffness matrix for the reinforced concrete structure being analysed is assembled from stiffness matrix of concrete elements and reinforcing steel bar elements (see equation (4.14)).

4.3.2.1 Stiffness Matrix of Concrete Element, $[k_c]_m$

In this study, the concrete elements are modelled through the use of isoparametric four-node quadrilateral elements because of its simplicity and economy. With reference to Chapter 3 Section 3.3.2.2, the quadrilateral with the local node numbering convention is shown in Figure 3.3 in real x-y space and also in terms of the natural co-ordinates.

Strain displacement transformation matrix of concrete element $[B_c]$:

The interpolation formulas for displacements in x-direction, u, and y-direction, v, can be expressed as follows:

$$u = N_1 u_1 + N_2 u_2 + N_3 u_3 + N_4 u_4 \tag{4.20a}$$

$$v = N_1 v_1 + N_2 v_2 + N_3 v_3 + N_4 v_4 \tag{4.20b}$$

Global co-ordinates, x, y, can be expressed by equation (3.29) and the shape functions N_1, N_2, N_3, N_4 can be found in Section 3.3.2.2.

The determination of strain requires partial differentiation of the displacement functions with respect to the global co-ordinates. The displacement functions are written in terms of the natural co-ordinates (see equation (4.20)). Replacing T by u in equation (3.31a) one can be obtained,

$$\begin{Bmatrix} \frac{\partial u}{\partial x} \\ \frac{\partial u}{\partial y} \end{Bmatrix} = \frac{1}{|J|} \begin{bmatrix} \frac{\partial y}{\partial \bar{y}} & -\frac{\partial y}{\partial \bar{x}} \\ -\frac{\partial x}{\partial \bar{y}} & \frac{\partial x}{\partial \bar{x}} \end{bmatrix} \begin{Bmatrix} \frac{\partial u}{\partial \bar{x}} \\ \frac{\partial u}{\partial \bar{y}} \end{Bmatrix} \tag{4.21}$$

Instead of T by v in equation (3.31a) again one can be obtained,

$$\begin{Bmatrix} \frac{\partial v}{\partial x} \\ \frac{\partial v}{\partial y} \end{Bmatrix} = \frac{1}{|J|} \begin{bmatrix} \frac{\partial y}{\partial \bar{y}} & -\frac{\partial y}{\partial \bar{x}} \\ -\frac{\partial x}{\partial \bar{y}} & \frac{\partial x}{\partial \bar{x}} \end{bmatrix} \begin{Bmatrix} \frac{\partial v}{\partial \bar{x}} \\ \frac{\partial v}{\partial \bar{y}} \end{Bmatrix} \tag{4.22}$$

where,

$$|J| = \frac{\partial y}{\partial \bar{y}} \frac{\partial x}{\partial \bar{x}} - \frac{\partial y}{\partial \bar{x}} \frac{\partial x}{\partial \bar{y}} \tag{4.23}$$

Performing the differentiation of equations (3.29) yields

$$\begin{aligned} \frac{\partial x}{\partial \bar{x}} &= \sum_{i=1}^{4} \frac{\partial N_i}{\partial \bar{x}} x_i, & \frac{\partial y}{\partial \bar{x}} &= \sum_{i=1}^{4} \frac{\partial N_i}{\partial \bar{x}} y_i \\ \frac{\partial x}{\partial \bar{y}} &= \sum_{i=1}^{4} \frac{\partial N_i}{\partial \bar{y}} x_i, & \frac{\partial y}{\partial \bar{y}} &= \sum_{i=1}^{4} \frac{\partial N_i}{\partial \bar{y}} y_i \end{aligned} \tag{4.24}$$

Substituting equation (4.24) into (4.23) an expression for the Jacobian determinant, $|J|$, is

$$|J| = \begin{bmatrix} y_1 & y_2 & y_3 & y_4 \end{bmatrix} [g] \begin{Bmatrix} x_1 \\ x_2 \\ x_3 \\ x_4 \end{Bmatrix} \tag{4.25}$$

where,

$$g_{ij} = \frac{\partial N_i}{\partial \bar{y}} \frac{\partial N_j}{\partial \bar{x}} - \frac{\partial N_i}{\partial \bar{x}} \frac{\partial N_j}{\partial \bar{y}} \tag{4.26}$$

From equation (4.21),

$$\frac{\partial u}{\partial x} = \frac{1}{|J|} \left[\frac{\partial y}{\partial \bar{y}} \frac{\partial u}{\partial \bar{x}} - \frac{\partial y}{\partial \bar{x}} \frac{\partial u}{\partial \bar{y}} \right]$$

whereas from equation (4.20),

$$\begin{aligned} \frac{\partial u}{\partial \bar{x}} &= \sum_{i=1}^{4} \frac{\partial N_i}{\partial \bar{x}} u_i, & \frac{\partial v}{\partial \bar{x}} &= \sum_{i=1}^{4} \frac{\partial N_i}{\partial \bar{x}} v_i \\ \frac{\partial u}{\partial \bar{y}} &= \sum_{i=1}^{4} \frac{\partial N_i}{\partial \bar{y}} u_i, & \frac{\partial v}{\partial \bar{y}} &= \sum_{i=1}^{4} \frac{\partial N_i}{\partial \bar{y}} v_i \end{aligned} \tag{4.27}$$

and using equation (4.24), one can be obtained as,

$$\varepsilon_{xx}^{m} = \frac{\partial u}{\partial x} = \frac{1}{|J|} \begin{bmatrix} y_1 & y_2 & y_3 & y_4 \end{bmatrix} [g] \begin{Bmatrix} u_1 \\ u_2 \\ u_3 \\ u_4 \end{Bmatrix} \tag{4.28}$$

Return to equation (4.21),

$$\frac{\partial u}{\partial y} = \frac{-1}{|J|}\left[\frac{\partial x}{\partial \bar{y}}\frac{\partial u}{\partial \bar{x}} - \frac{\partial x}{\partial \bar{x}}\frac{\partial u}{\partial \bar{y}}\right]$$

in matrix form,

$$\frac{\partial u}{\partial y} = \frac{-1}{|J|}\begin{bmatrix} x_1 & x_2 & x_3 & x_4 \end{bmatrix}[g]\begin{Bmatrix} u_1 \\ u_2 \\ u_3 \\ u_4 \end{Bmatrix} \tag{4.29}$$

From equation (4.22),

$$\frac{\partial v}{\partial x} = \frac{1}{|J|}\left[\frac{\partial y}{\partial \bar{y}}\frac{\partial v}{\partial \bar{x}} - \frac{\partial y}{\partial \bar{x}}\frac{\partial v}{\partial \bar{y}}\right]$$

that is,

$$\frac{\partial v}{\partial x} = \frac{1}{|J|}\begin{bmatrix} y_1 & y_2 & y_3 & y_4 \end{bmatrix}[g]\begin{Bmatrix} v_1 \\ v_2 \\ v_3 \\ v_4 \end{Bmatrix} \tag{4.30}$$

and

$$\frac{\partial v}{\partial y} = \frac{-1}{|J|}\left[\frac{\partial x}{\partial \bar{y}}\frac{\partial v}{\partial \bar{x}} - \frac{\partial x}{\partial \bar{x}}\frac{\partial v}{\partial \bar{y}}\right]$$

that is,

$$\varepsilon_{c,y}^{m} = \frac{\partial v}{\partial y} = \frac{-1}{|J|}\begin{bmatrix} x_1 & x_2 & x_3 & x_4 \end{bmatrix}[g]\begin{Bmatrix} v_1 \\ v_2 \\ v_3 \\ v_4 \end{Bmatrix} \tag{4.31}$$

The shear strain is defined as

$$\gamma_{c,xy}^{m} = \frac{\partial u}{\partial y} + \frac{\partial v}{\partial x}$$

This is the sum of equations (4.29) and (4.30). So, the mechanical strain matrix of concrete element can be expressed as,

$$\left\{\varepsilon_c^m\right\} = \begin{Bmatrix} \varepsilon_{c,x}^{m} \\ \varepsilon_{c,y}^{m} \\ \gamma_{c,xy}^{m} \end{Bmatrix} = \left[B_c\right]\begin{Bmatrix} u_1 \\ v_1 \\ u_2 \\ \vdots \\ u_4 \\ v_4 \end{Bmatrix} = \left[B_c\right]\left\{u_c\right\} \tag{4.32}$$

From equation (4.28) the entries of matrix $\left[B_c\right]$, $B_{c,(1,j)}$, can be identified as follows:

$$B_{c,(1,(2j-1))} = \frac{1}{|J|}\sum_{i=1}^{4} y_i\, g_{ij} \qquad j=1,2,3,4 \tag{4.33a}$$

$$B_{c,(1,j)} = 0 \qquad j=2,4,6,8 \tag{4.33b}$$

From equation (4.31),

$$B_{c,(2,2j)} = -\frac{1}{|J|}\sum_{i=1}^{4} x_i\, g_{ij} \qquad j=1,2,3,4 \tag{4.33c}$$

$$B_{c,(2,j)} = 0 \qquad j = 1,3,5,7 \qquad (4.33d)$$

From equations (4.29) and (4.30),

$$B_{c,(3,j)} = B_{c,(2,(j+1))} \qquad j = 1,3,5,7 \qquad (4.33e)$$

$$B_{c,(3,j)} = B_{c,(1,(j-1))} \qquad j = 2,4,6,8 \qquad (4.33f)$$

The entries in the matrix $[B_c]$ are recognised to be functions of the natural co-ordinates $\bar{x}$ and $\bar{y}$.

The element stiffness matrix, $[k_c]_m$:

According to the energy minimisation principle, the element stiffness matrix can be found as follows:

$$[k_c]_m = \int_{V_c^{(m)}} [B_c]^T [C]_{rc} [B_c] \, dV \qquad (4.34a)$$

or

$$\begin{aligned} [k_c]_m &= \iiint_{V_c^{(m)}} [B_c]^T [C]_{rc} [B_c] \, dx \, dy \, dz \\ &= \iint_A [B]^T \left(\int [C]_{rc} \, dz \right) [B_c] \, dx \, dy \end{aligned} \qquad (4.34b)$$

using $[\overline{C}] = \int [C]_{rc} \, dz$,

$$[k_c]_m = \iint_A [B_c]^T [\overline{C}] [B_c] \, dx \, dy \qquad (4.34c)$$

Changing the integration variable, one can be obtained as the following:

$$[k_c]_m = \int_{A'} [B_c]^T [\overline{C}] [B_c] |J| \, d\bar{x} \, d\bar{y} \qquad (4.35)$$

In this study two-point formula of Gauss quardrature is used to calculate $[k_c]_m$. Therefore, in this chapter all stresses, strains, and the constitutive matrix of materials discussed are correspondent to Gauss integration points.

Since the concrete elements are divided into layers along z axis direction (see Figure 4.2), material properties are assumed to be constant within each layer at each time step. Therefore, the matrix $[\overline{C}]$ at a Gauss point is a function of z only, and the inner integration $\int [C]_{rc}\, dz$ in equation (4.34b) can be carried out separately. This integration along the z-axis are replaced by summation over the layers as:

$$[\overline{C}] = \int [C]_{rc}\, dz = \sum_{i=1}^{n} (z_{i+1} - z_i)[C]_{rc,i} \tag{4.36}$$

where, $[C]_{rc,i}$ is the material constitutive matrix of i-th layer, and n is number of the layers.

4.3.2.2 Stiffness Matrix of Steel Bar Element, $[k_s]_m$

In this research, steel bar elements are used to model the main longitudinal reinforcement. The steel bar element is modelled as two-point isoparametric truss element in conjunction with the concrete elements.

In the following model we consider a truss element that has an arbitrary orientation in x-y plane and is described by two nodes, as shown in Figure 4.3. The global co-ordinate of nodal points of the element are $(x_1, y_1), (x_2, y_2)$ and r is natural co-ordinate.

Strain displacement transformation matrix of reinforcing steel bar element, $[B_s]$:

The interpolation formula for displacement in the global co-ordinates are:

$$u = N_1 u_1 + N_2 u_2 \tag{4.37a}$$

$$v = N_1 v_1 + N_2 v_2 \tag{4.37b}$$

For the global co-ordinates:

$$x = N_1 x_1 + N_2 x_2 \tag{4.38a}$$

$$y = N_1 y_1 + N_2 y_2 \tag{4.38b}$$

For the arc length, s, at the material point (x, y) given by

$$s = N_1 s_1 + N_2 s_2 \tag{4.39}$$

where, the shape function for one independent variable, r, are define as

$$N_1 = \frac{1}{2}(1-r), \quad N_2 = \frac{1}{2}(1+r)$$

Since, for the truss element the only stress is the normal stress on its cross-sectional area,, therefore only the corresponding longitudinal strain is considered. Hence, one can be obtained [89] as follows:

$$\varepsilon_s^m = \frac{dx}{ds}\frac{du}{ds} + \frac{dy}{ds}\frac{dv}{ds} \tag{4.40}$$

Since,

$$\frac{dx}{ds} = \frac{dx}{dr}\frac{dr}{ds} \qquad \frac{dy}{ds} = \frac{dy}{dr}\frac{dr}{ds}$$

$$\frac{du}{ds} = \frac{du}{dr}\frac{dr}{ds} \qquad \frac{dv}{ds} = \frac{dv}{dr}\frac{dr}{ds}$$

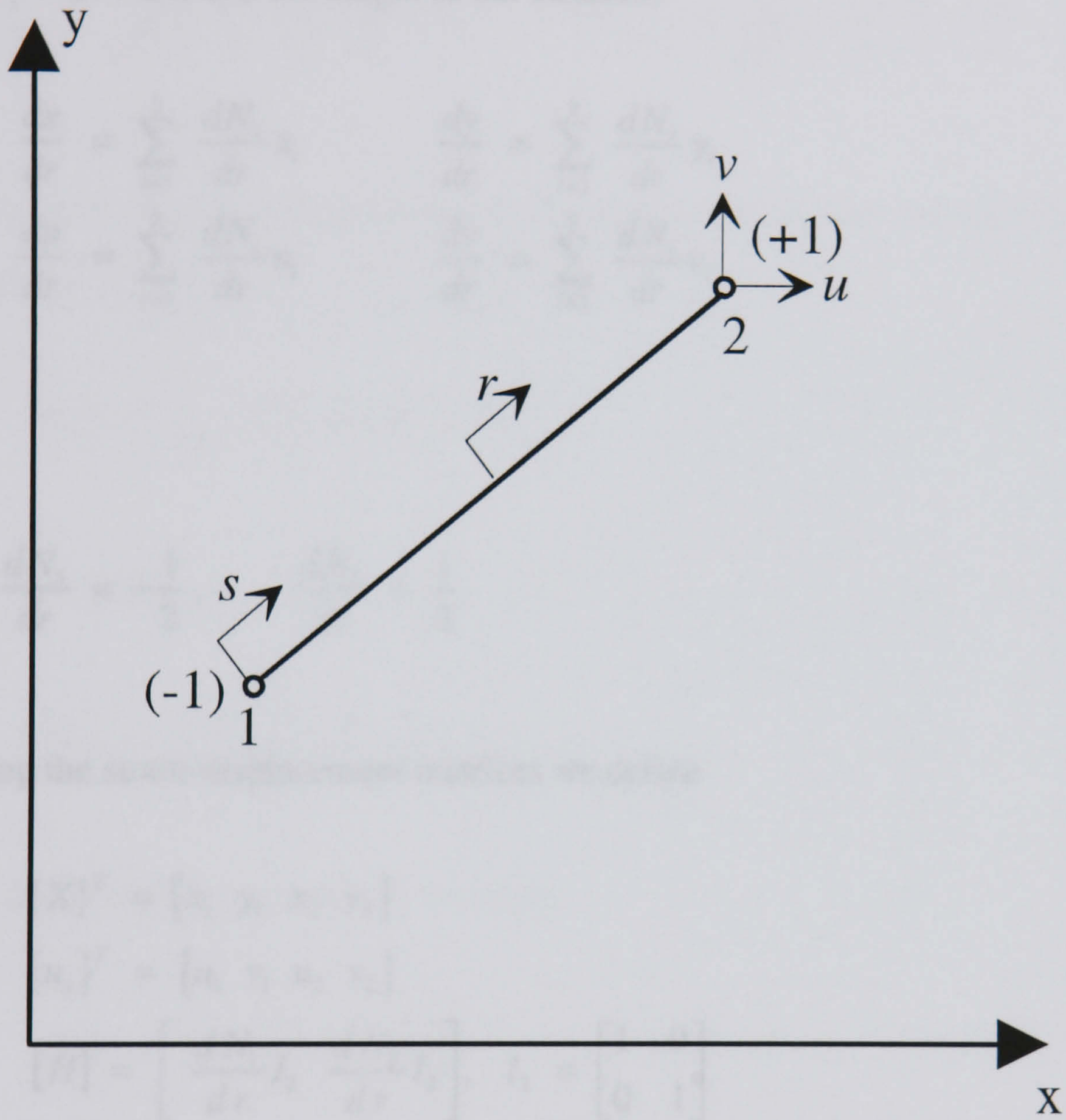

Figure 4.3 Two-node Bar Element

substituting these expression into equation (4.40), that is,

$$\varepsilon_s^m = \frac{1}{|J|^2}\left(\frac{dx}{dr}\frac{du}{dr}+\frac{dy}{dr}\frac{dv}{dr}\right) \tag{4.41}$$

where, $|J|= L/2$, and L is the length of bar element,

$$\frac{dx}{dr} = \sum_{i=1}^{2}\frac{dN_i}{dr}x_i \qquad \frac{dy}{dr} = \sum_{i=1}^{2}\frac{dN_i}{dr}y_i$$

$$\frac{du}{dr} = \sum_{i=1}^{2}\frac{dN_i}{dr}u_i \qquad \frac{dv}{dr} = \sum_{i=1}^{2}\frac{dN_i}{dr}v_i$$

and

$$\frac{dN_1}{dr} = -\frac{1}{2}, \qquad \frac{dN_2}{dr} = \frac{1}{2}$$

To develop the strain-displacement matrices we define

$$\{X\}^T = [x_1 \;\; y_1 \;\; x_2 \;\; y_2]$$

$$\{u_s\}^T = [u_1 \;\; v_1 \;\; u_2 \;\; v_2]$$

$$[H] = \left[\frac{dN_1}{dr}I_2 \;\; \frac{dN_2}{dr}I_2\right], \quad I_2 = \begin{bmatrix}1 & 0\\ 0 & 1\end{bmatrix}$$

Hence, equation (4.41) can be expressed as

$$\varepsilon_s^m = \frac{1}{|J|^2}\{X\}^T[H]^T[H]\{u_s\} \tag{4.42}$$

So that

$$[B_s] = \frac{1}{|J|^2}\{X\}^T[H]^T[H] \tag{4.43}$$

where, the entries in the $[B_s]$ are,

$$B_{s,(1,1)} = \frac{1}{|J|^2}\left(\frac{dN_1}{dr}\sum_{i=1}^{2}\frac{dN_i}{dr}x_i\right), \qquad B_{s,(1,2)} = \frac{1}{|J|^2}\left(\frac{dN_1}{dr}\sum_{i=1}^{2}\frac{dN_i}{dr}y_i\right)$$

$$B_{s,(1,3)} = \frac{1}{|J|^2}\left(\frac{dN_2}{dr}\sum_{i=1}^{2}\frac{dN_i}{dr}x_i\right), \qquad B_{s,(1,4)} = \frac{1}{|J|^2}\left(\frac{dN_2}{dr}\sum_{i=1}^{2}\frac{dN_i}{dr}y_i\right)$$

The stiffness of element corresponding to the global co-ordinates can be expressed as the following:

$$[k_s]_m = \int_{V_s^m} [B_s]^T \overline{E}_s [B_s]\, dV \tag{4.44}$$

Since, $dV = A_s\, ds$, so

$$[k_s]_m = \int_s [B_s]^T \overline{E}_s [B_s]\, A_s\, ds$$

Because items in $[B_s]$ are constant, therefore

$$[k_s]_m = L\, A_s\, \overline{E}_s [B_s]^T [B_s] \tag{4.45}$$

4.3.3 Nominal Nodal Force Vector, $\{F\}$

The nominal nodal force vector for the structure being analysed, $\{F\}$, is assembled from the nominal nodal force vector of concrete elements and steel bar elements (see equation (4.17)).

4.3.3.1 Nominal Nodal Force Vector of Concrete Element, $\{F_c\}_m$

According to equation (4.18),

$$\{F_c\}_m = \int_{V_c^{(m)}} [B_c]^T \{\sigma_c^F\}\, dV$$
$$= \iiint_{V_c^{(m)}} [B_c]^T \{\sigma_c^F\}\, dx\, dy\, dz \qquad (4.46a)$$
$$= \iint_A [B_c]^T \left(\int \{\sigma_c^F\} dz\right) dx\, dy$$

Using $\{\overline{\sigma}\} = \int \{\sigma_c^F\} dz$,

$$\{F_c\}_m = \iint_A [B_c]^T \{\overline{\sigma}\}\, dx\, dy \qquad (4.46b)$$

Changing the integration variable, that is

$$\{F_c\}_m = \iint_{A^*} [B_c]^T \{\overline{\sigma}\} |J|\, d\overline{x}\, d\overline{y} \qquad (4.47)$$

As discussed in Section 4.3.2.1 the two-point formula of Gauss quardrature is used to calculate $\{F_c\}_m$ therefore $\{\overline{\sigma}\}$ at a Gauss point is a function of z only and the inner integration $\int \{\sigma_c^F\} dz$ in equation (4.46a) can be expressed by summation over the layers as,

$$\{\overline{\sigma}\} = \int \{\sigma_c^F\} dz = \sum_{i=1}^{n} (z_{i+1} - z_i) \{\sigma_c^F\}_i \qquad (4.48)$$

where $\{\sigma_c^F\}_i$ is nominal stress vector in the i-th concrete layer and n is the number of the layers.

4.3.3.2 Nominal Nodal Force Vector of Steel Bar Elements, $\{F_s\}_m$

From equation (4.19),

$$\{F_s\}_m = \int_{V_s^{(m)}} [B_s]^T \sigma_s^F\, dV$$
$$= \int_{V_s^{(m)}} [B_s]^T \sigma_s^F A_s\, ds \qquad (4.49)$$

In equation the terms of $[B_s]$ are constant therefore,

$$\{F_s\}_m = L\, A_s\, \sigma_s^F [B_s]^T \tag{4.50}$$

4.3.4. External Loading Vector, $\{R\}$

External loading vector, $\{R\}$, in equation (4.13) is represented as nodal force vector of the system being analysed. $\{R\}$ is assembled from element nodal loading force vector $\{R\}_m$, that is

$$\{R\} = \sum_{m=1}^{n} \{R\}_m \tag{4.51}$$

where, n is the number of elements.

4.3.4.1 Element Nodal Loading Force Vector, $\{R\}_m$

There are three types of element loading to be considered:

(1) Concentrated forces applied to nodes, $\{r\}_{NF}$, that is,

$$\{r\}_{NF} = \begin{Bmatrix} r_{1,x} \\ r_{1,y} \\ \vdots \\ r_{4,x} \\ r_{4,y} \end{Bmatrix} \tag{4.52}$$

(2) Equivalent nodal forces for distributed surface traction, $\{r\}_{TF}$

Distributed edge loading intensities are specified as force per unit length or force per unit area. The force per unit area at a particular point is called the stress traction vector, $\{S\}$. Distributed stress traction on one side of the element is shown in Figure 4.4. The general expression for the equivalent nodal loads for this distributed surface traction is [98].

$$\{r\}_{TF} = b\int_{\ell} [N]^T \begin{Bmatrix} S_x \\ S_y \end{Bmatrix} d\ell \tag{4.53}$$

where,

$[N]$ = shape function matrix, for the four-node quadrilateral,

$$[N] = \begin{bmatrix} N_1 & 0 & N_2 & 0 & N_3 & 0 & N_4 & 0 \\ 0 & N_1 & 0 & N_2 & 0 & N_3 & 0 & N_4 \end{bmatrix} \tag{4.54}$$

b = the thickness of the element

ℓ = the length of the element edge

$\begin{Bmatrix} S_x \\ S_y \end{Bmatrix}$ = the force vector per unit area at a particular point.

(3) Equivalent nodal forces for distributed body forces, $\{r\}_{BF}$

Forces that are exerted on each element of mass throughout the continuum (element) are called body forces, gravitational loading is a common example of a body force. The units of the loading are force per unit volume. As the same principal as equation (4.53) equivalent nodal forces for distributed body forces, $\{r\}_{BF}$, can be expressed as following:

$$\{r\}_{BF} = b\int_{A} [N]^T \begin{Bmatrix} B_x \\ B_y \end{Bmatrix} dx\, dy \tag{4.55}$$

where, B_x, B_y are the body forces in the x and y directions.

The element nodal loading force vector, $\{R\}_m$, is

$$\{R\}_m = \{r\}_{NF} + \{r\}_{TF} + \{r\}_{BF} \tag{4.56}$$

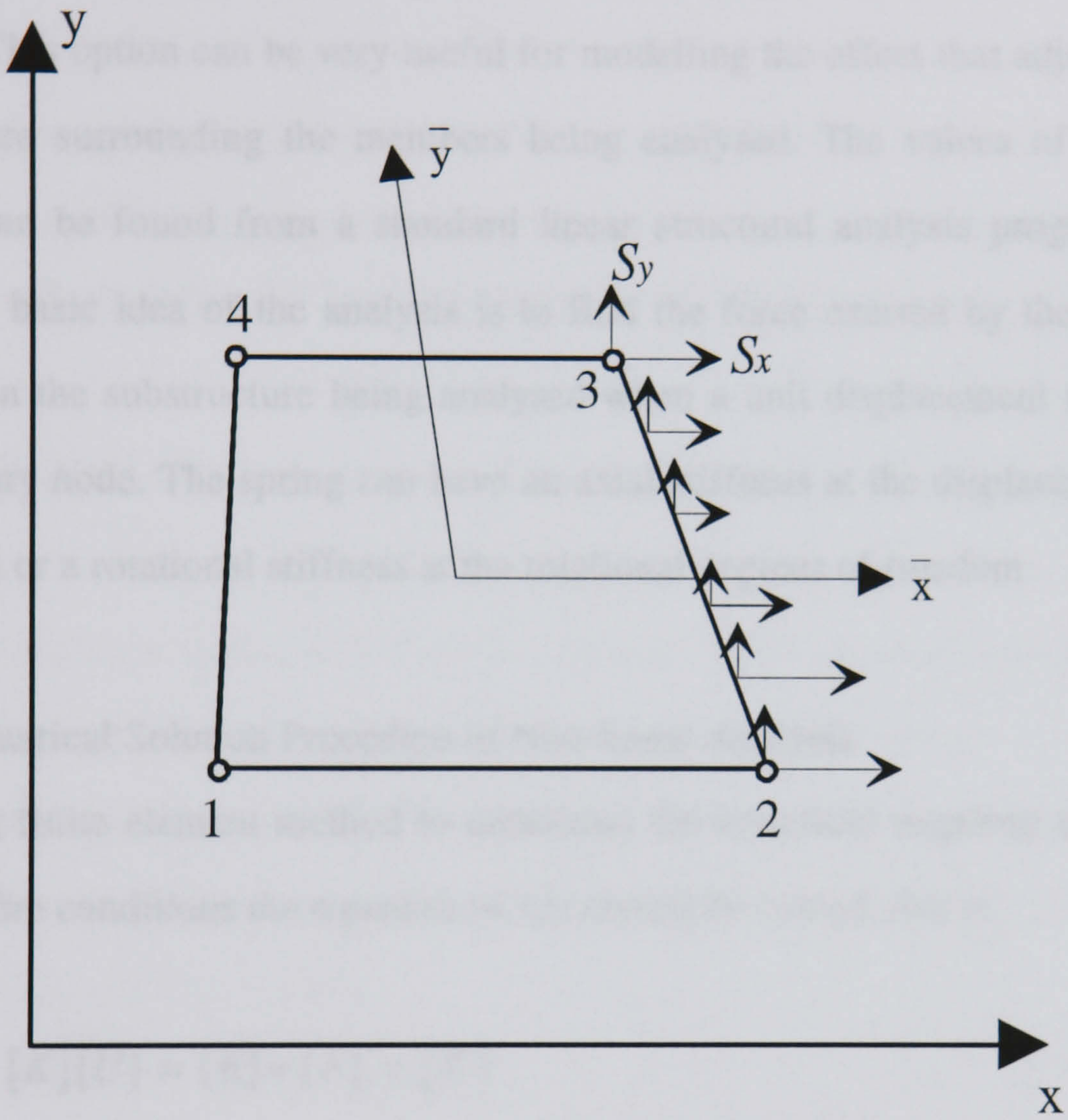

Figure 4.4 Distributed Stress Traction on One Side of the Element

4.3.5 Boundary Conditions

In the solution of the non-linear equilibrium equations for the structure being analysed, one of two conditions must be known for each node: the externally applied load at the node, or displacement of the node.

It is also possible to model flexible supports by using flexible spring stiffness at these supports. This option can be very useful for modelling the effect that adjacent parts of the structure surrounding the members being analysed. The values of these spring stiffness can be found from a standard linear structural analysis programme (e. g. [99]). The basic idea of the analysis is to find the force exerted by the surrounding structure on the substructure being analysed when a unit displacement is imposed at the boundary node. The spring can have an axial stiffness at the displacement degrees of freedom or a rotational stiffness at the rotational degrees of freedom.

4.3.6 Numerical Solution Procedure of Non-linear Analysis

Employing finite element method to determine the structural response under applied loads and fire conditions the equation (4.13) should be solved, that is.

$$[K]\{U\} = \{R\}+\{F\} = \{R'\} \tag{4.57}$$

The procedure contains two parts, the first part is to analyse the structural behaviour subject to applied loading before fire conditions and the second part is to analyse the structural behaviour during the fire.

Considering the non-linear material behaviour, $[K]$ to be a function of the load vector, $\{R'\}$, an iterative method should employed to reach the solution of the system of equations in (4.57). In this study since a secant non-linear elastic model is used for concrete, the system of equations in (4.57) is set up so that the nodal force vector $\{R'\}$ is equal to the total load corresponding to the structure. This implies that a secant method of solution rather than the usual tangent technique is employed. At any load step (previous fire) or time step (during fire), iterations are carried out and at each

iteration $[K]$ is updated until the constitutive equations for concrete and reinforcement are in accordance with the total loads, $\{R^{'}\}$.

In the following sections all stresses, strains, and the constitutive matrix of materials discussed are correspondent to Gauss integration points of each layer of concrete elements and each steel bar element.

4.3.6.1 Numerical Solution Procedure Preceding the Fire

During the actual loading applied to the structure before fire, the nominal nodal load vector $\{F\}=0$, therefore $\{R^{'}\}=\{R\}$ equation (4.57) become,

$$[K]\{U\} = \{R\} \tag{4.58}$$

The secant stiffness approach for solving equation (4.58) is illustrated in Figure 4.5.

The basic steps of this solution procedure is described as following:

(1) Determining the external nodal loading vector $\{R\}_i$, for load step i,

$$\{R\}_i = \{R\}_{i-1} + \{\Delta R\}_i \tag{4.59}$$

where, $\{\Delta R\}_i$ is the load increment vector at load step i.

(2) Assuming secant stiffness matrix of materials, for the first iteration of the first load step, the isotropic elastic module of concrete and steel is used as the secant stiffness value. After this, at each iteration j of load step i the material stiffness matrix calculated at iteration $(j-1)$, $[C]^{'}$, is used as the new estimate secant stiffness value, $[C]$.

(3) Using the secant stiffness matrix of material formed in step (2) layer stiffness of concrete elements are calculated and integrated to form element stiffness matrixes, $[k_c]_m$, and stiffness matrixes of steel bar elements, $[k_s]_m$, are formed. These are then assembled into the structural stiffness matrix, $[K]$.

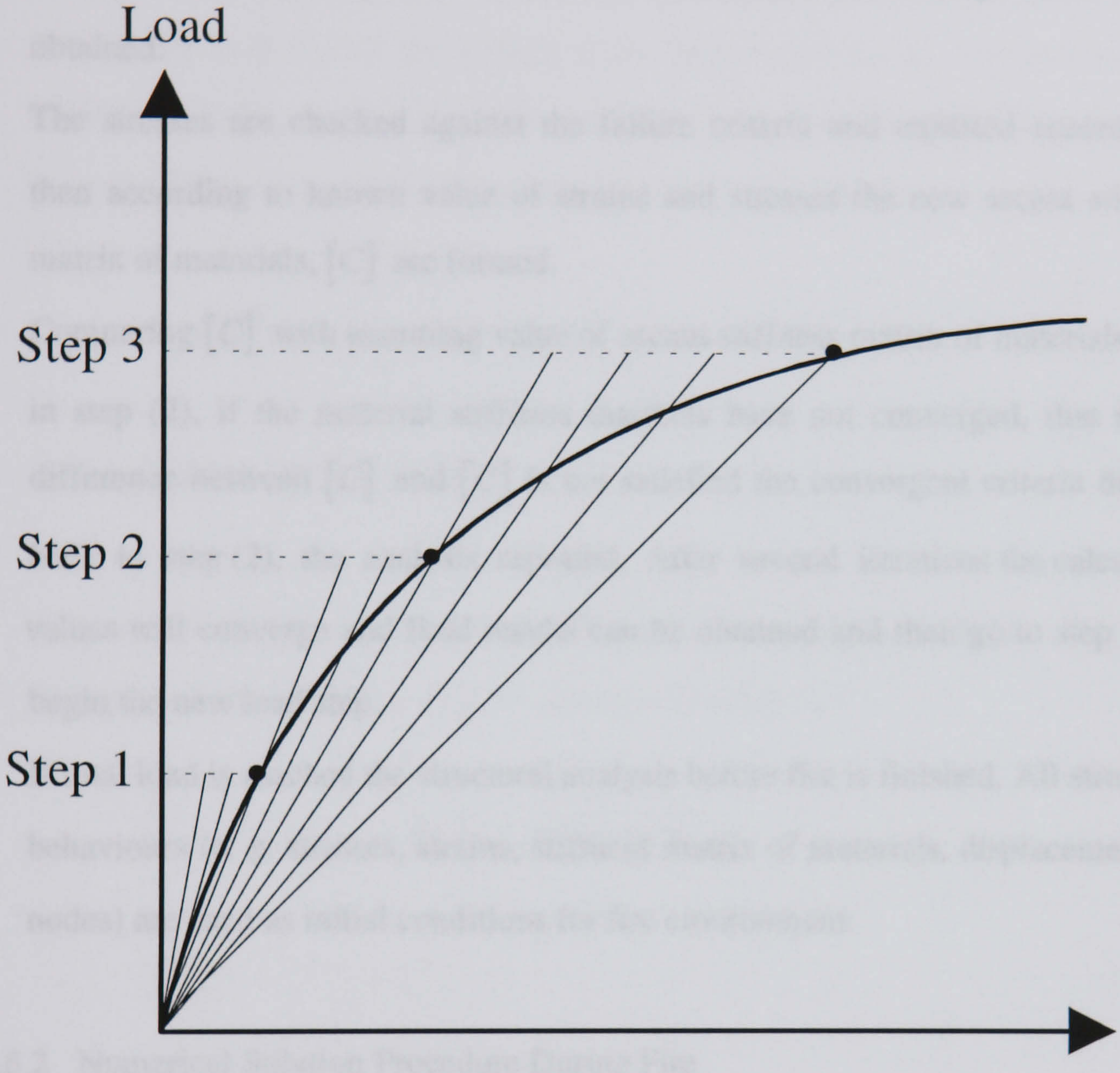

Figure 4.5 Iterative Procedure for the Solution of Non-linear Equilibrium Equations (4.58)

(4) Equilibrium equations are solved to obtain the nodal displacement vector, $\{U\}$. For each element step (5) is executed to obtain the current state of stresses and strains.

(5) Strain vectors are computed and from the constitutive relationships stress state is obtained.

(6) The stresses are checked against the failure criteria and adjusted accordingly, then according to known value of strains and stresses the new secant stiffness matrix of materials, $[C]'$ are formed.

(7) Comparing $[C]'$ with assuming value of secant stiffness matrix of materials, $[C]$, in step (2), if the material stiffness matrixes have not converged, that is, the difference between $[C]'$ and $[C]$ is not satisfied the convergent criteria then go back to step (2), the analysis repeated. After several iterations the calculated values will converge and final results can be obtained and then go to step (1) to begin the new load step.

(8) If total load is reached the structural analysis before fire is finished. All structural behaviours (e. g. stresses, strains, stiffness matrix of materials, displacements of nodes) are used as initial conditions for fire environment.

4.3.6.2 Numerical Solution Procedure During Fire

During the fire environment the nominal load vector $\{F\}\neq 0$, therefore $\{R'\}=\{R\}+\{F\}$. So, equation (4.57) has to be solved. A finite element secant stiffness formulation coupled with a step-by-step integration scheme in the time domain is used to solve equation (4.57). The entire time period, for which the response history of the structure is to be traced, is divided into a number of time steps, $\Delta t_1, \Delta t_2, \Delta t_3, \cdots, \Delta t_n$. As mentioned in Chapter 2, in this study the same time increment Δt is used, that is, $\Delta t_1 = \Delta t_2 = \Delta t_3 = \cdots = \Delta t_n = \Delta t$ (see Figure 4.6). it is assumed that changes in the external nodal loads and temperature, if any, occur only at the beginning or at the end of a time step. During a time step the external loads and

temperature in the layers of concrete elements and steel bar elements are assumed to remain constant.

The basic steps of this computational procedure are discussed as follows. All superscript j and subscript i represent iteration j and time step i.

(1) A time step begins with the reading of the time increment, Δt, and external load increment, $\{\Delta R\}_i$, which are added to the previous time and load values to obtain the current time, t_i, and the current load vector, $\{R\}_i$, that is,

$$t_i = t_{i-1} + \Delta t \tag{4.60}$$

$$\{R\}_i = \{R\}_{i-1} + \{\Delta R\}_i \tag{4.61}$$

Moreover, current temperature distribution in the member is entered.

(2) Free strain vector for time step i is calculated as follows:

$$\left\{\varepsilon_c^F\right\}_i = \left\{\varepsilon_c^{creep}\right\}_i + \left\{\varepsilon_c^{sh}\right\}_i + \left\{\varepsilon_c^{tr}\right\}_i + \left\{\varepsilon_c^T\right\}_i \tag{4.62a}$$

$$\left(\varepsilon_s^F\right)_i = \left(\varepsilon_s^{creep}\right)_i + \left(\varepsilon_s^T\right)_i \tag{4.62b}$$

(3) Assuming secant stiffness matrix of materials at each iteration j of time step i the material stiffness matrix calculated at iteration $(j-1)$, $[C]'$, is used as the new estimate secant stiffness value, $[C]$.

(4) Using the secant stiffness matrix of material formed in step (3), layer stiffness of concrete elements are calculated and integrated to form element stiffness matrixes, $\left(\left[k_c\right]_m\right)_i^j$, and stiffness matrixes of steel bar elements, $\left(\left[k_s\right]_m\right)_i^j$ are formed. These are then assembled into the structural stiffness matrix, $[K]_i^j$. Using the free strain vector calculated in step (2), $\left\{\varepsilon_c^F\right\}_i, \left(\varepsilon_s^F\right)_i$, the nominal nodal force vector of concrete elements and steel bar elements, $\left(\left\{F_c\right\}_m\right)_i^j, \left(\left\{F_s\right\}_m\right)_i^j$, are

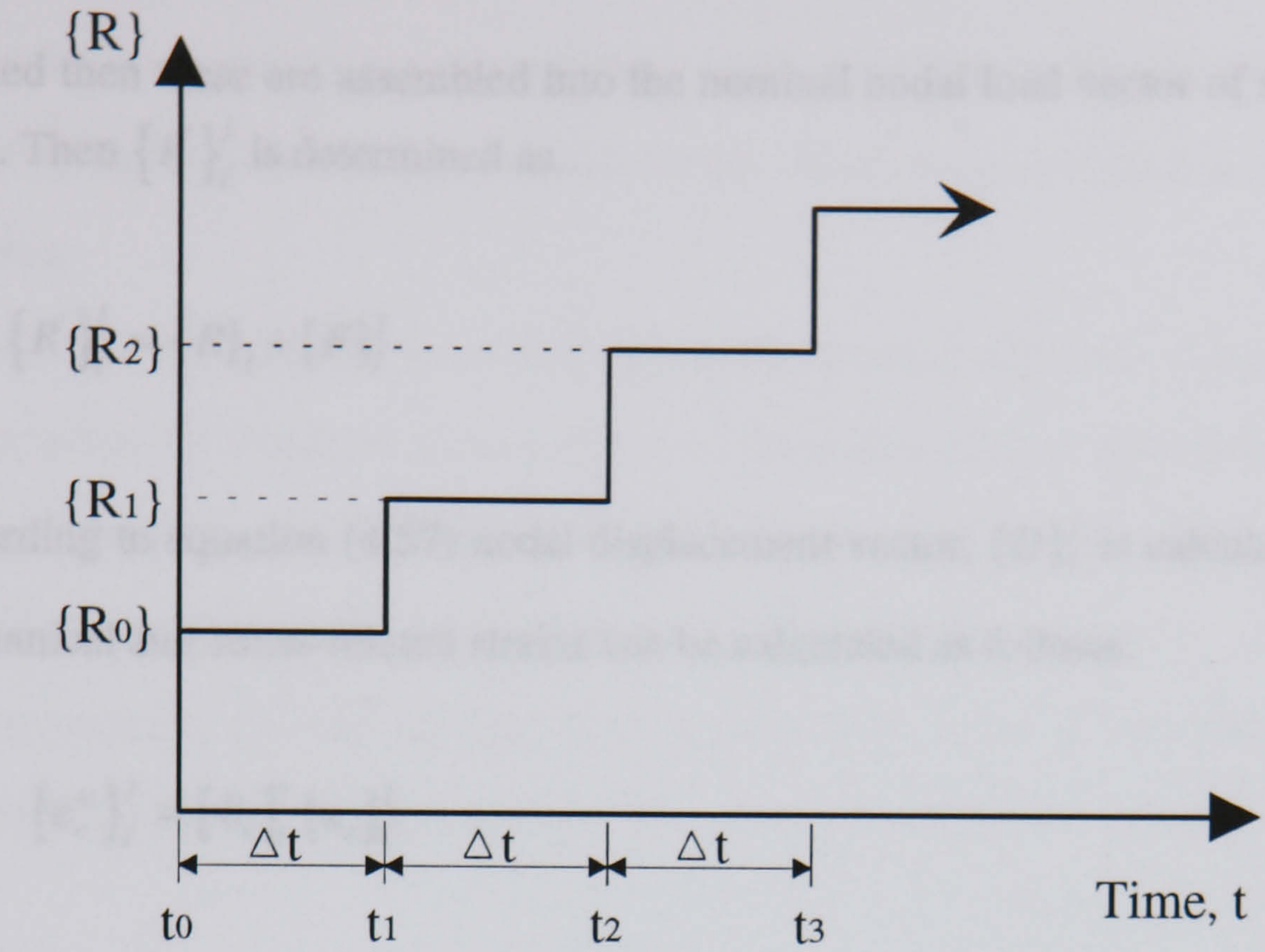

(a) External Load History

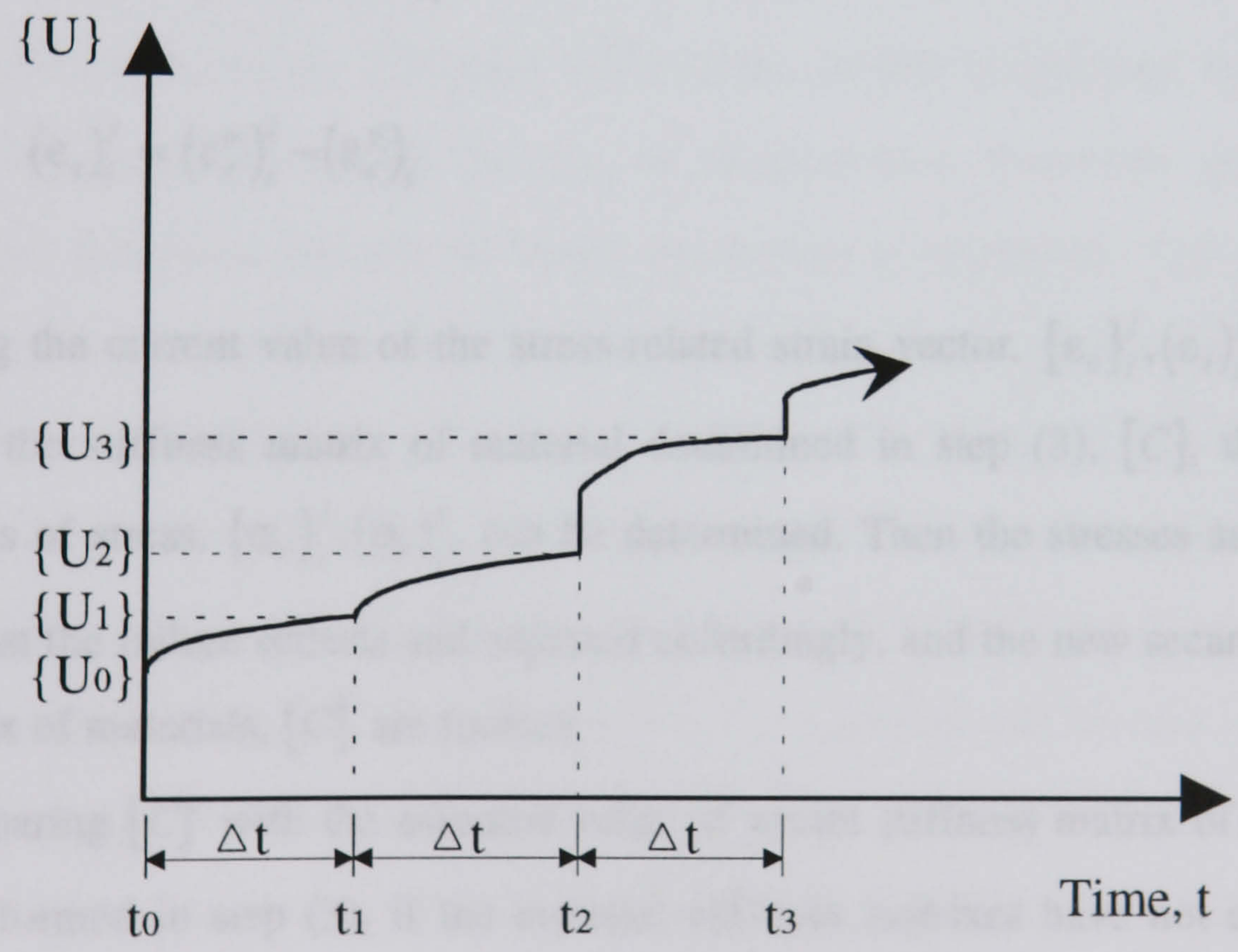

(b) Displacement History

Figure 4.6 Load and Displacement History for Non-linear Analysis Procedure

formed then these are assembled into the nominal nodal load vector of structure, $\{F\}_i^j$. Then $\left\{R^{'}\right\}_i^j$ is determined as,

$$\left\{R^{'}\right\}_i^j = \{R\}_i + \{F\}_i^j \tag{4.63}$$

(5) According to equation (4.57) nodal displacement vector, $\{U\}_i^j$ is calculated. The mechanical and stress-related strains can be calculated as follows:

$$\left\{\varepsilon_c^m\right\}_i^j = \left[B_c\right]_i^j \left\{u_c\right\}_i^j \tag{4.64a}$$

$$\left(\varepsilon_s^m\right)_i^j = \left[B_s\right]_i^j \left\{u_s\right\}_i^j \tag{4.64b}$$

$$\left\{\varepsilon_c\right\}_i^j = \left\{\varepsilon_c^m\right\}_i^j - \left\{\varepsilon_c^F\right\}_i \tag{4.65a}$$

$$\left(\varepsilon_s\right)_i^j = \left(\varepsilon_s^m\right)_i^j - \left(\varepsilon_s^F\right)_i \tag{4.65b}$$

(6) Using the current value of the stress-related strain vector, $\left\{\varepsilon_c\right\}_i^j, \left(\varepsilon_s\right)_i^j$, together with the stiffness matrix of material determined in step (3), $[C]$, the current values of stress, $\left\{\sigma_c\right\}_i^j, \left(\sigma_s\right)_i^j$, can be determined. Then the stresses are checked against the failure criteria and adjusted accordingly, and the new secant stiffness matrix of materials, $[C]^{'}$ are formed.

(7) Comparing $[C]^{'}$ with the assumed value of secant stiffness matrix of materials, $[C]$, formed in step (3), if the material stiffness matrixes have not converged, that is, the difference between $[C]^{'}$ and $[C]$ dose not satisfy the convergent criteria, go back to step (3) and repeat the iteration procedure $j+1$. After several iterations the calculated values will converge and final results can be obtained and then return to step (1) to begin the new time step $i+1$.

(8) The calculation procedure is continued until the required time is reached or failure of the structure being analysed occurs, which means solution procedure is unstable.

(9) It is noted that because of the complexity of the concrete material, a large number of iterations are required to satisfy the convergent criterion during some time steps. Therefore, in this study a small time step, one minute, and a limited iteration number, 15, is employed. This means that the automatic increamentation of load or time step is used only if the convergence is not achieved during the iteration process.

4.3.7 Description of Computer Programme, FPPRCM-S

Based on the previous analysis a special finite element programme, FPPRCM-S, has been developed. FPPRCM-S is a computer programme for the Fire Performance of Planar Reinforced Concrete Members - Structural. In this programme the concrete elements are modelled through the use of isoparametric four-node quadrilateral element, and two-point formula of Gauss quadrature is employed. The main steel reinforcing bar are modelled as a two-point bar element in conjunction with the concrete elements. FPPRCM-S is written in FORTRAN77. The main flow chart of the programme is presented in Figure 4.7. The temperature histories of cross-section of the member are predicted by the computer programme FPRCBC-T (see Chapter 3).

Programme FPPRCM-S has been developed as an analytical tool for use in studying the fire response of planar reinforced concrete members. The programme is capable of providing a broad spectrum of response data including time history of displacements, internal stresses and strains in concrete and reinforcing bar, as well as the current states of concrete (cracking and crushing) and steel reinforcement (yielding).

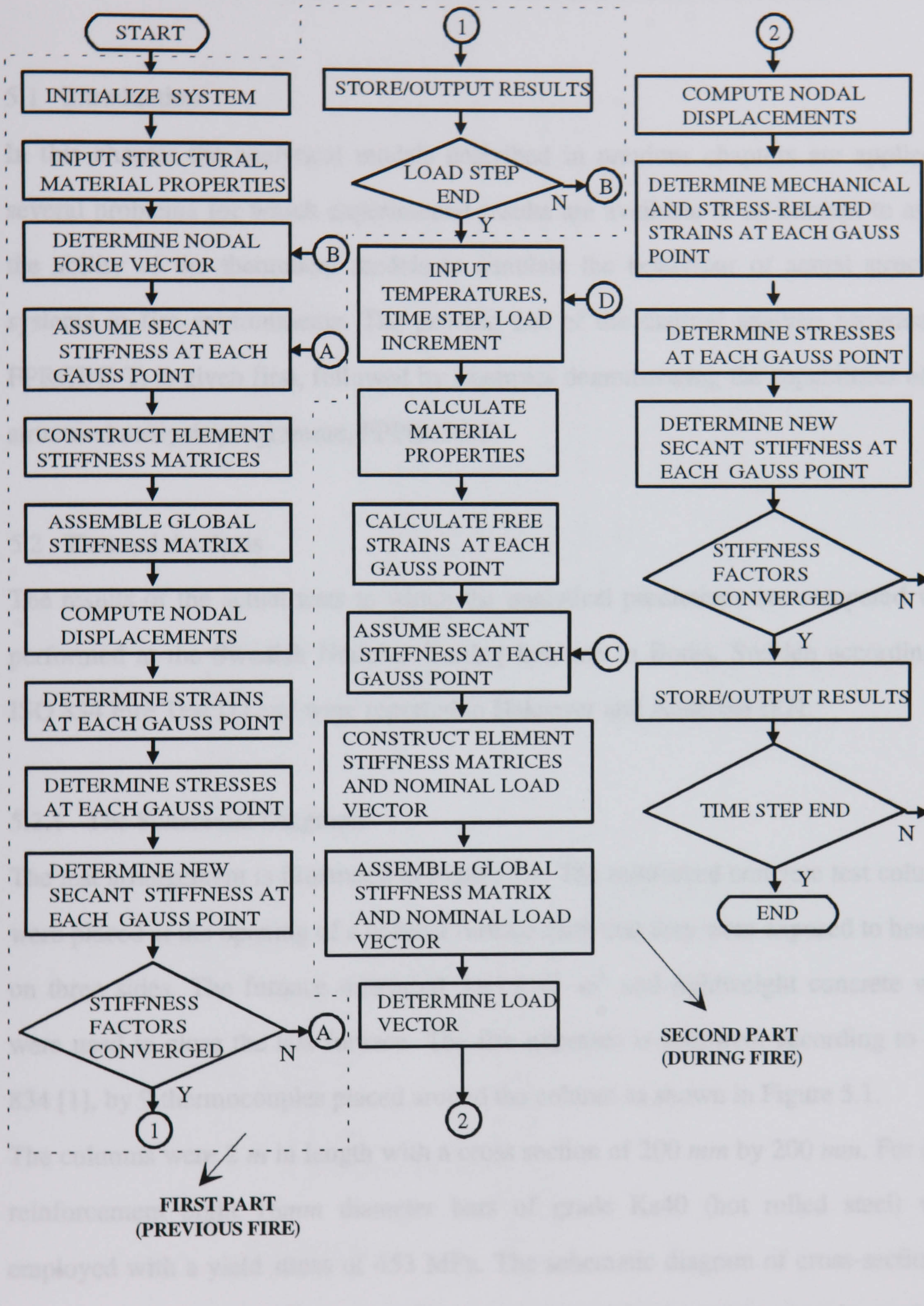

Figure 4.7 The Main Flowchart of FPPRCM-S

5. VERIFICATION OF ANALYTICAL METHODS

5.1 Introduction

In this chapter the analytical models described in previous chapters are applied to several problems for which experimental results are available in an attempt to assess the ability of the theoretical models to simulate the behaviour of actual structural systems in fire environments. The proving test of the thermal analysis programme, FPRCBC-T, is given first, followed by examples demonstrating the capabilities of the structural analysis programme, FPPRCM-T.

5.2 Thermal Analysis

The results of the actual tests to which the analytical predictions are compared were performed at the Swedish National Testing Institute in Boras, Sweden according to ISO 834 Fire Test [1] and were reported in Haksever and Anderber [87].

5.2.1 The Schematic Diagrams

The test arrangement is illustrated in Figure 5.1. The reinforced concrete test columns were placed at the opening of a vertical furnace such that they were exposed to heating on three sides. The furnace measured $3\times1.8\times3$ m^3 and lightweight concrete walls were used to close the test furnace. The fire exposure is followed, according to ISO 834 [1], by 9 thermocouples placed around the column as shown in Figure 5.1.

The columns were 2 *m* in length with a cross section of 200 *mm* by 200 *mm*. For steel reinforcement eight 16*mm* diameter bars of grade Ks40 (hot rolled steel) were employed with a yield stress of 453 MPa. The schematic diagram of cross-section of the column is shown in Figure 5.2. The concrete used for the column specimens had a cube strength of about 46 MPa with a testing age of 110 days. The moisture content of the concrete was measured on cubes of size $0.15\times0.15\times0.15$ m^3 and was about 6% (by weight). This value is taken into account in temperature calculations.

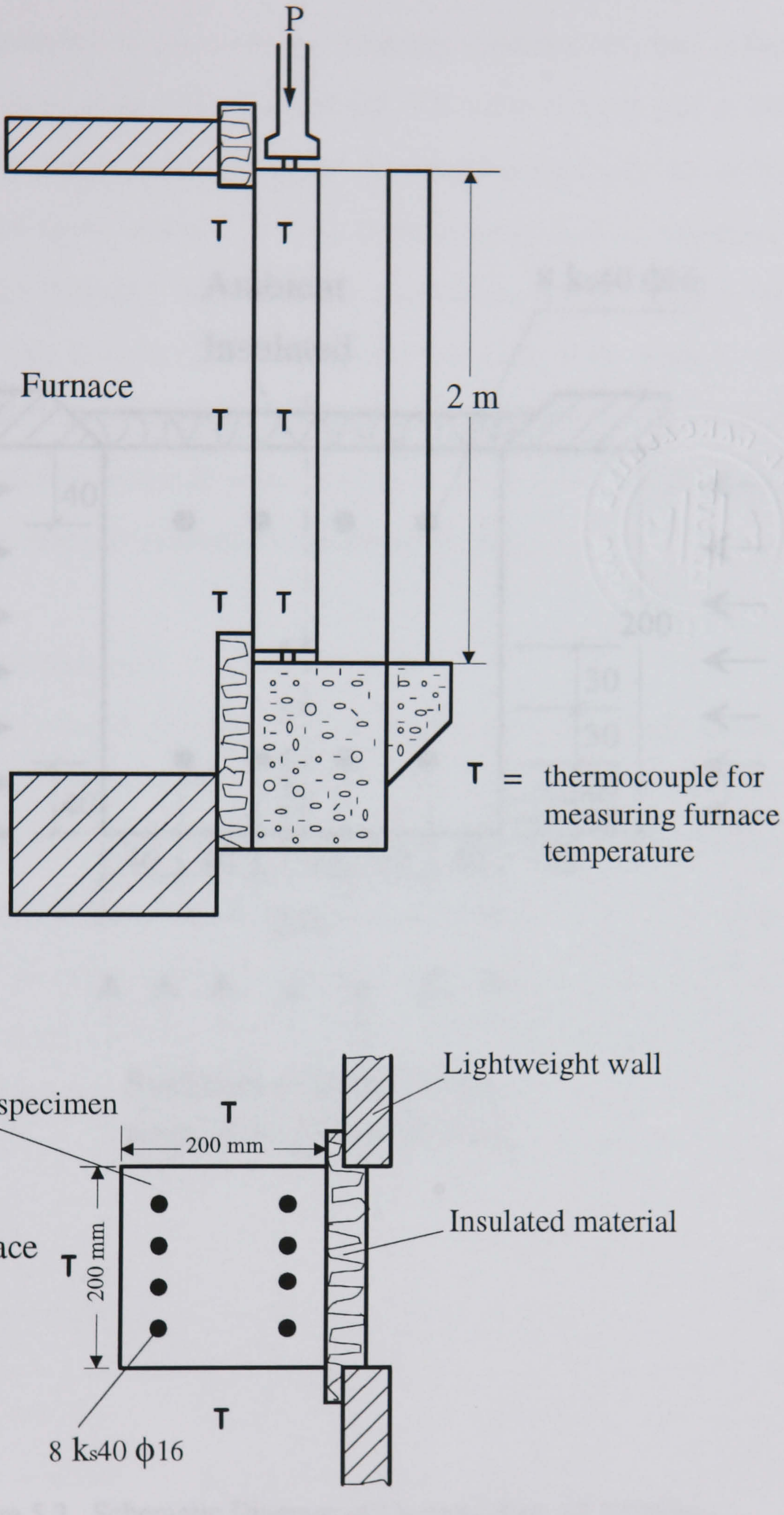

Figure 5.1 Illustration of Testing Arrangement [87]

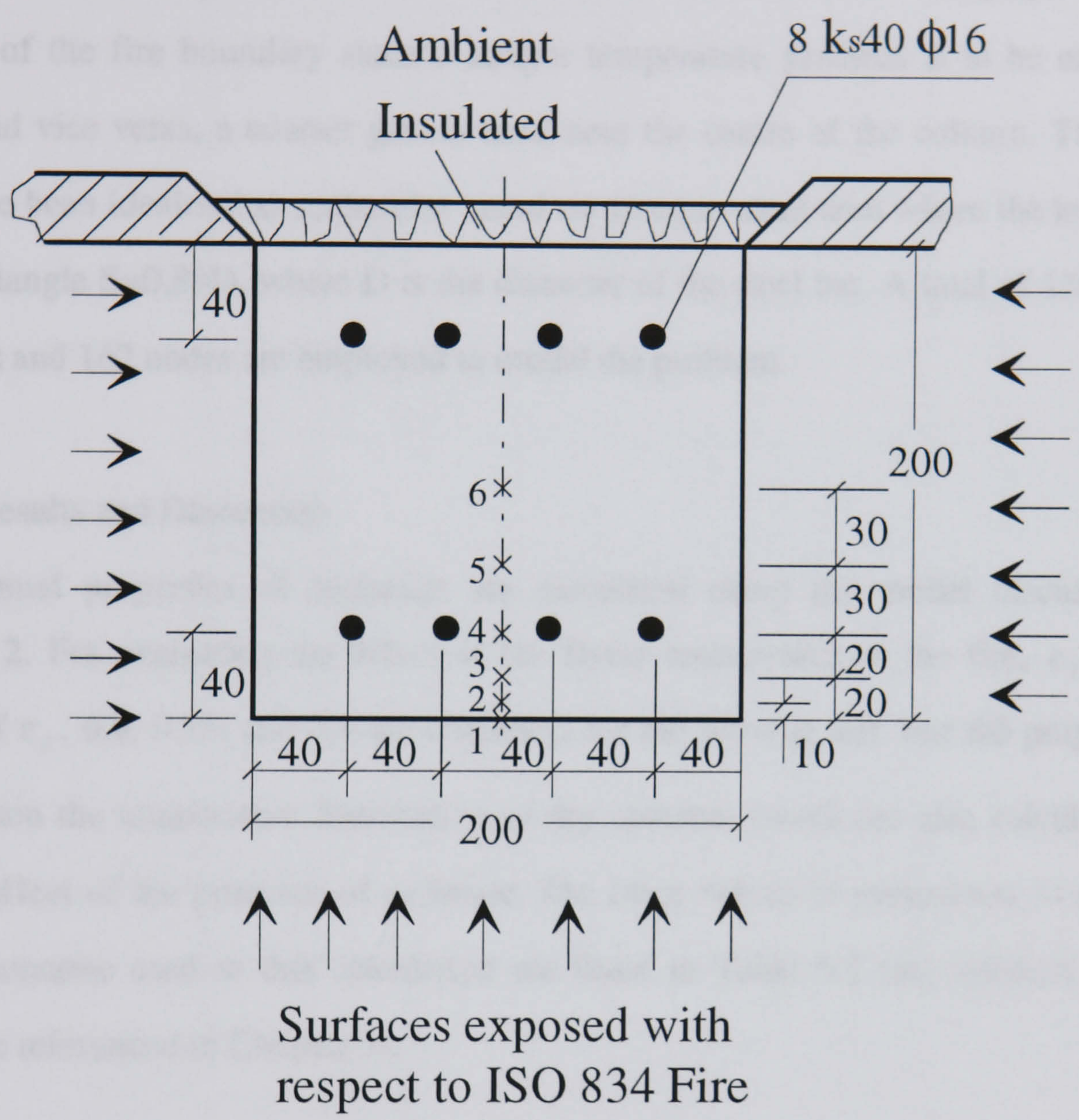

Figure 5.2 Schematic Diagram of Cross-section of Column for Thermal Proving Tests (Dimensions in mm) [87]

Because of the symmetry of geometric and boundary condition only half of the cross-section of the column is needed for modelling. The finite element grid is shown in Figure 5.3, where planes of symmetry and the insulated cool side are modelled as perfectly insulated (q=0) surfaces. A finer finite element mesh is employed in the vicinity of the fire boundary since a steeper temperature gradient is to be expected there, and vice versa, a coarser grid is used near the centre of the column. The steel bars have been idealised as rectangles based on an equivalent area where the length of each rectangle S=0.89D, where D is the diameter of the steel bar. A total of 136 finite elements and 162 nodes are employed to model the problem.

5.2.2 Results and Discussion

The thermal properties of materials are calculated using the model discussed in Chapter 2. For evaluating the effect of the flame emissivities of the fire, ε_f, three values of ε_f, 0.6, 0.75, and 0.9 are employed for the proving test. For the purpose of comparison the temperature distribution of dry concrete (w=0) are also calculated to see the effect of the presence of moisture. The other values of parameters of normal weight concrete used in this calculation are listed in Table 5.1 (the symbols in the Table are referenced in Chapter 3).

Table 5.1 Values of the Parameters Used in Figures 5.4-5.6

$\varepsilon = 0.21$	$\rho_l^* = 985.0$	$C_{p,l} = 4187.0$	$k_m = 0.026$	$k_{d,0} = 1.75$
$\varepsilon_s = 0.9$	$\rho_d = 2400.0$	$h_{fg} = 2.1991 \times 10^6$	$k_{s'} = 3.31$	$\nu_2 = 0.5$
$\nu_1 = 1.0$	$C_{p,d,0} = 850.0$	$\sigma = 5.67 \times 10^{-8}$	$N = 1.25$	$A = 2.5$
$a = 0.9$	$k_l = 0.651$			

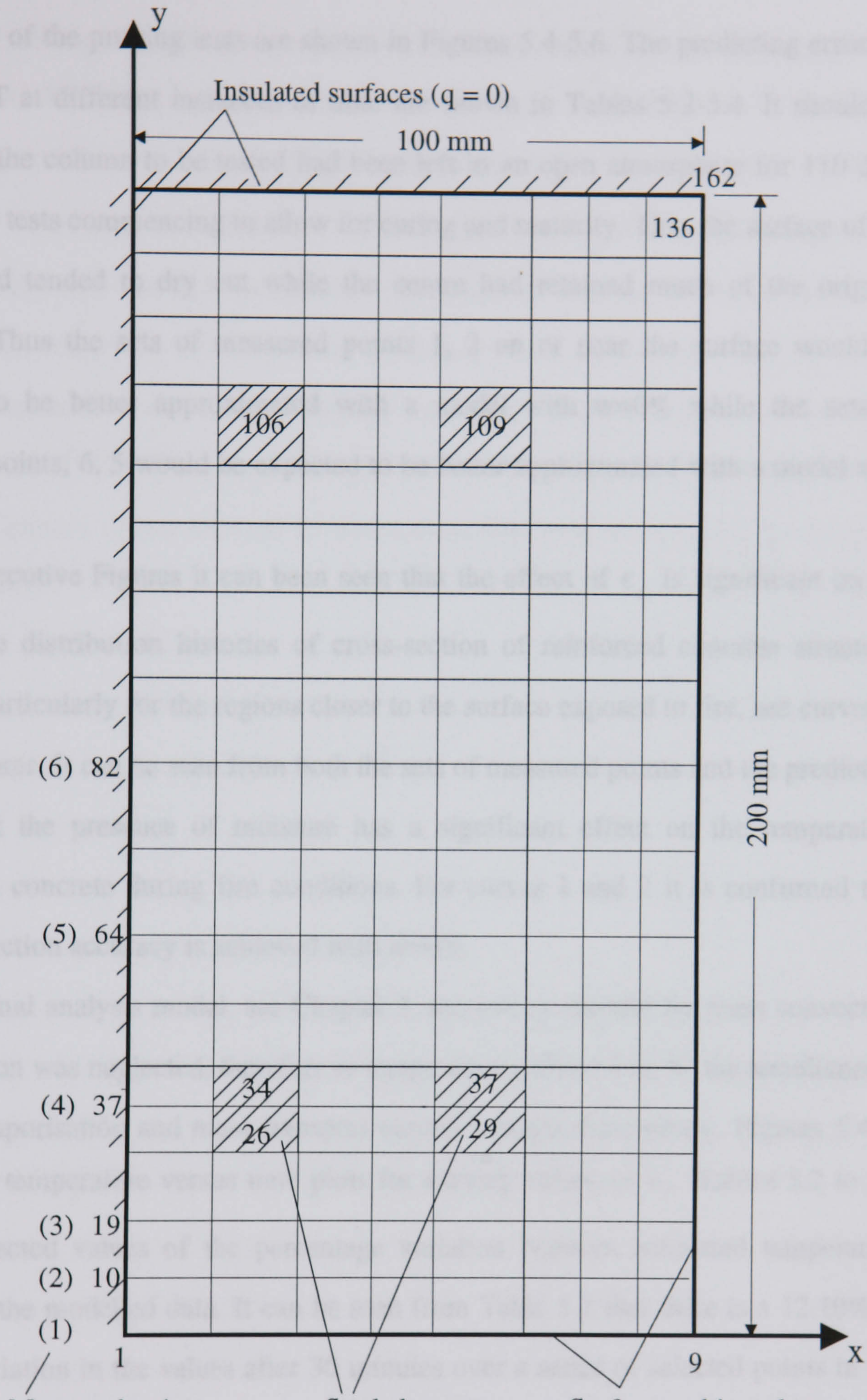

Figure 5.3 Finite Element Mesh for Modelled Half Cross-section of Column

The results of the proving tests are shown in Figures 5.4-5.6. The predicting errors of FPRCBC-T at different instances of time are shown in Tables 5.2-5.4. It should be noted that the column to be tested had been left in an open atmosphere for 110 days prior to the tests commencing to allow for curing and maturity. Thus the surface of the column had tended to dry out while the centre had retained much of the original moisture. Thus the sets of measured points 1, 2 on or near the surface would be expected to be better approximated with a model with w=0% while the sets of measured points, 6, 5 would be expected to be better approximated with a model with w=6%.

From consecutive Figures it can been seen that the effect of ε_f is significant on the temperature distribution histories of cross-section of reinforced concrete structural member, particularly for the regions closer to the surface exposed to fire, see curves 1, 2, 3 in Figures. It can be seen from both the sets of measured points and the prediction curves that the presence of moisture has a significant effect on the temperature histories in concrete during fire conditions. For curves 1 and 2 it is confirmed that better prediction accuracy is achieved with w=0%.

In the thermal analysis model, see Chapter 3, the energy transfer by mass convection and diffusion was neglected, therefore at temperatures below 140 ^0C the simultaneous moisture vaporisation and mass transport caused a slight discrepancy. Figures 5.4 to 5.6 present temperature versus time plots for varying values of ε_f. Tables 5.2 to 5.4 present selected values of the percentage variation between measured temperature values and the modelled data. It can be seen from Table 5.2 that there is a 12.10% to 35.45% variation in the values after 30 minutes over a series of selected points in the cross-section of the column (refer to Figure 5.4 (a)). The greatest deviation occurs at point 6, which is at the centre of the cross-section. However, after 120 minutes the variation is reduced to the range of 0.42% to 13.97%. Again the greatest variation is at point 6. This data represents a worst case situation in using of the ε_f value at 0.6. In contrast in Table 5.3 which presents values for ε_f=0.75 the variation of data ranges from 1.5% to 32.54% at 30 minutes and from 2.59 to 8.28% after 120 minutes (refer

to Figure 5.5 (a)). This represents a close match between the simulation and experimental data for a ε_f value which more closely reasonable actual conditions. Table 5.4 provides data for ε_f=0.9 providing a variation in the range of 2.63% to 30.06% at 30 minutes and 0.66% to 14.86% after 120 minutes (refer to Figure 5.6 (a)). In Tables 5.3 and 5.4 the greatest variations do not occur exclusively in the internal elements of the model. It may be summarised at this stage that the model shows a reasonable match to the measured data if the initial material conditions and ε_f can be specified accurately. To improve upon the accuracy of the prediction, the thermal properties of the material at elevated temperatures are required from further investigations.

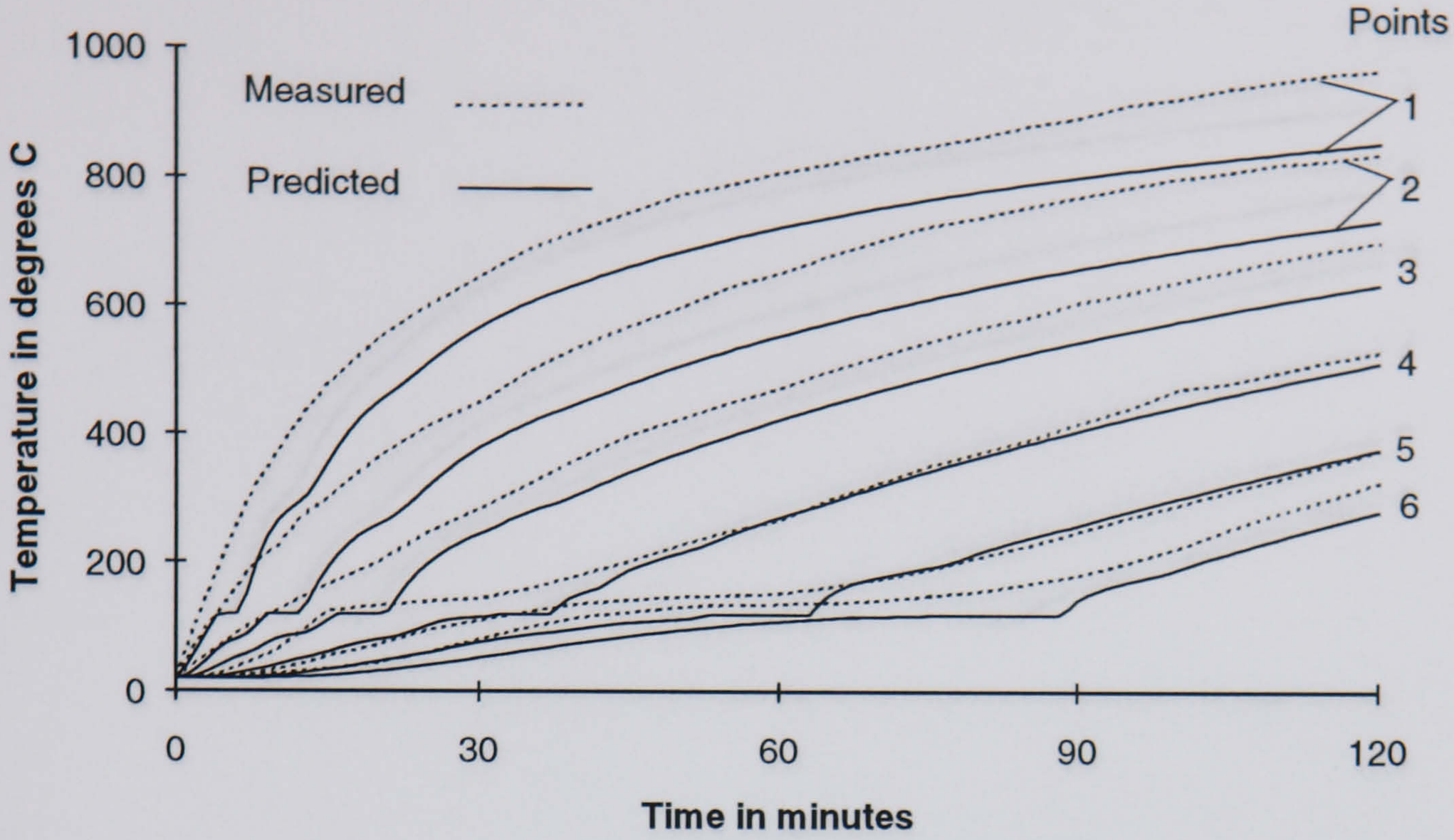

(a)

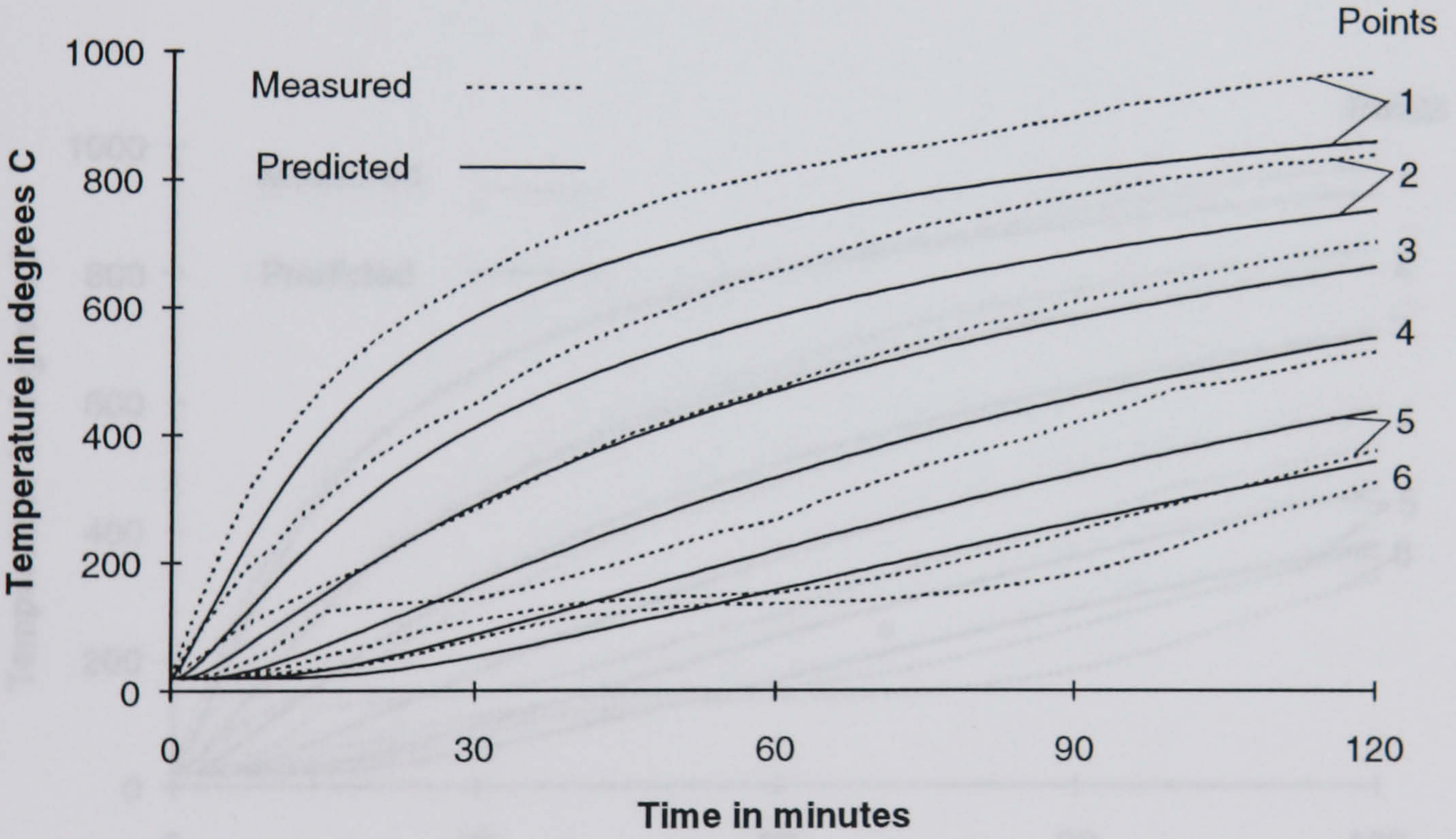

(b)

Figure 5.4 Comparison of Predicted and Measured [87] Temperature at Mid-section of the Column Exposed to ISO 834 Fire ($\varepsilon_f = 0.6$)

(a) $w = 6\%$

(b) $w = 0$

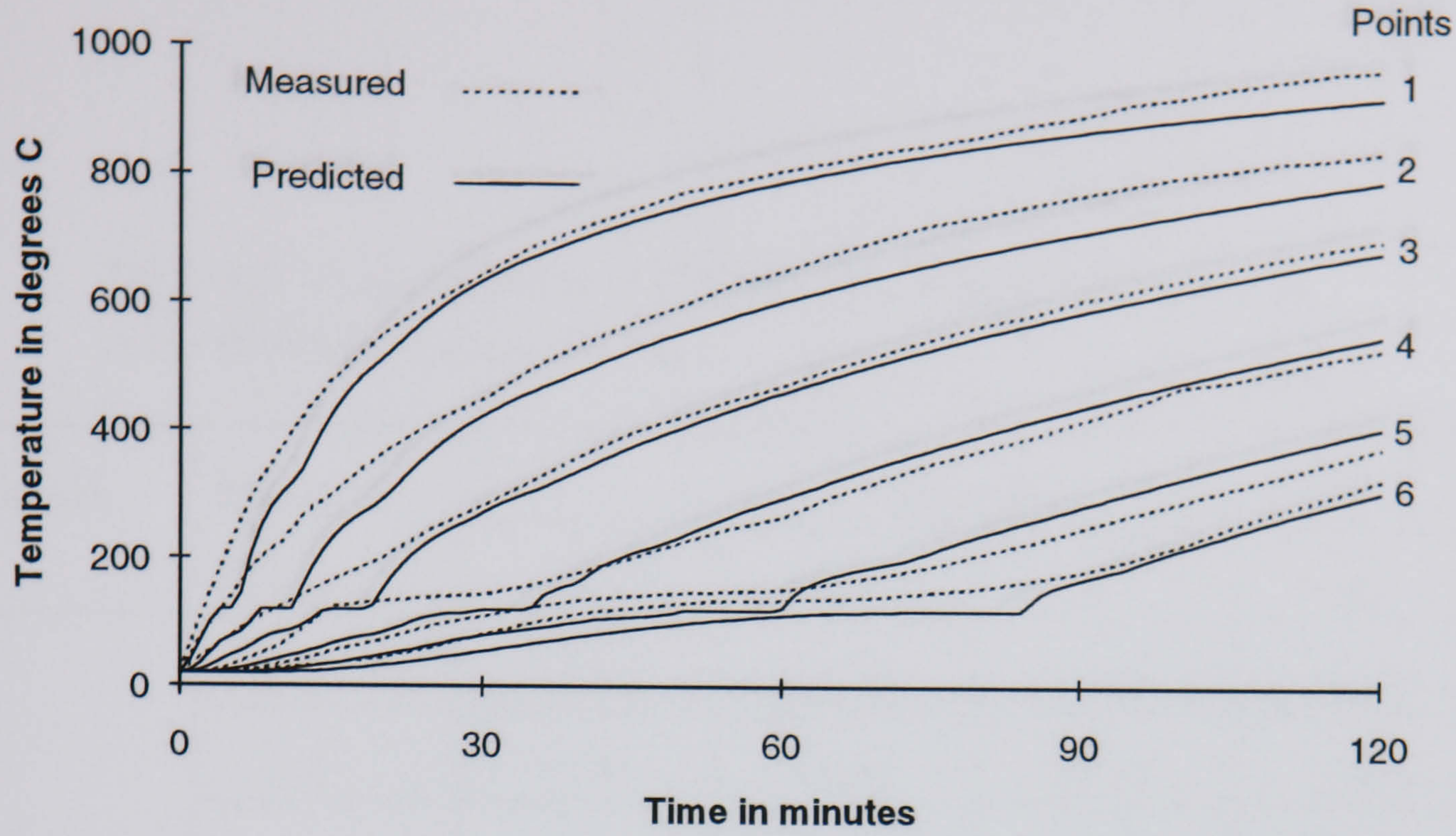

(a)

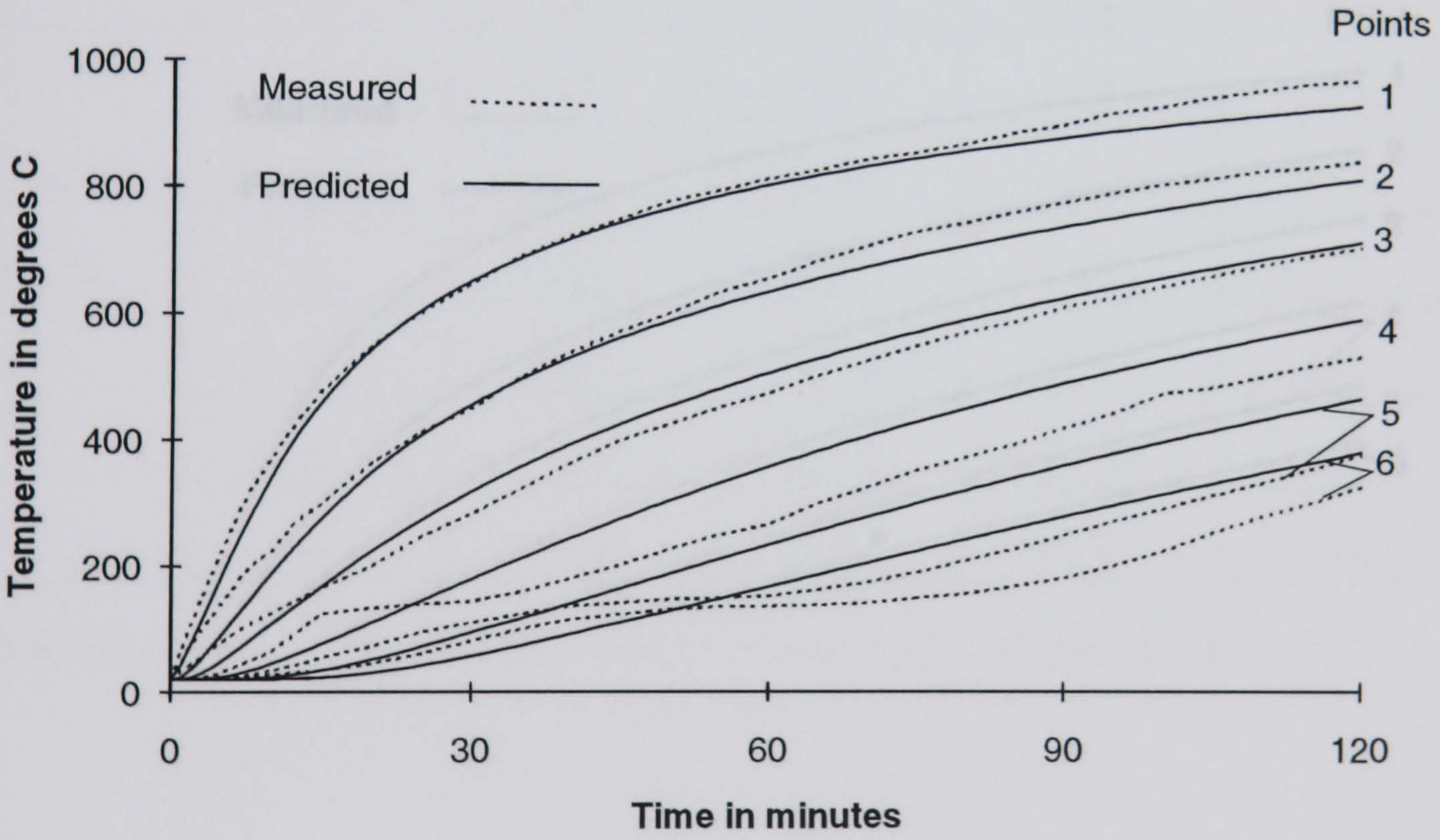

(b)

Figure 5.5 Comparison of Predicted and Measured [87] Temperature at Mid-section of the Column Exposed to ISO 834 Fire ($\varepsilon_f = 0.75$)

(a) $w = 6\%$

(b) $w = 0$

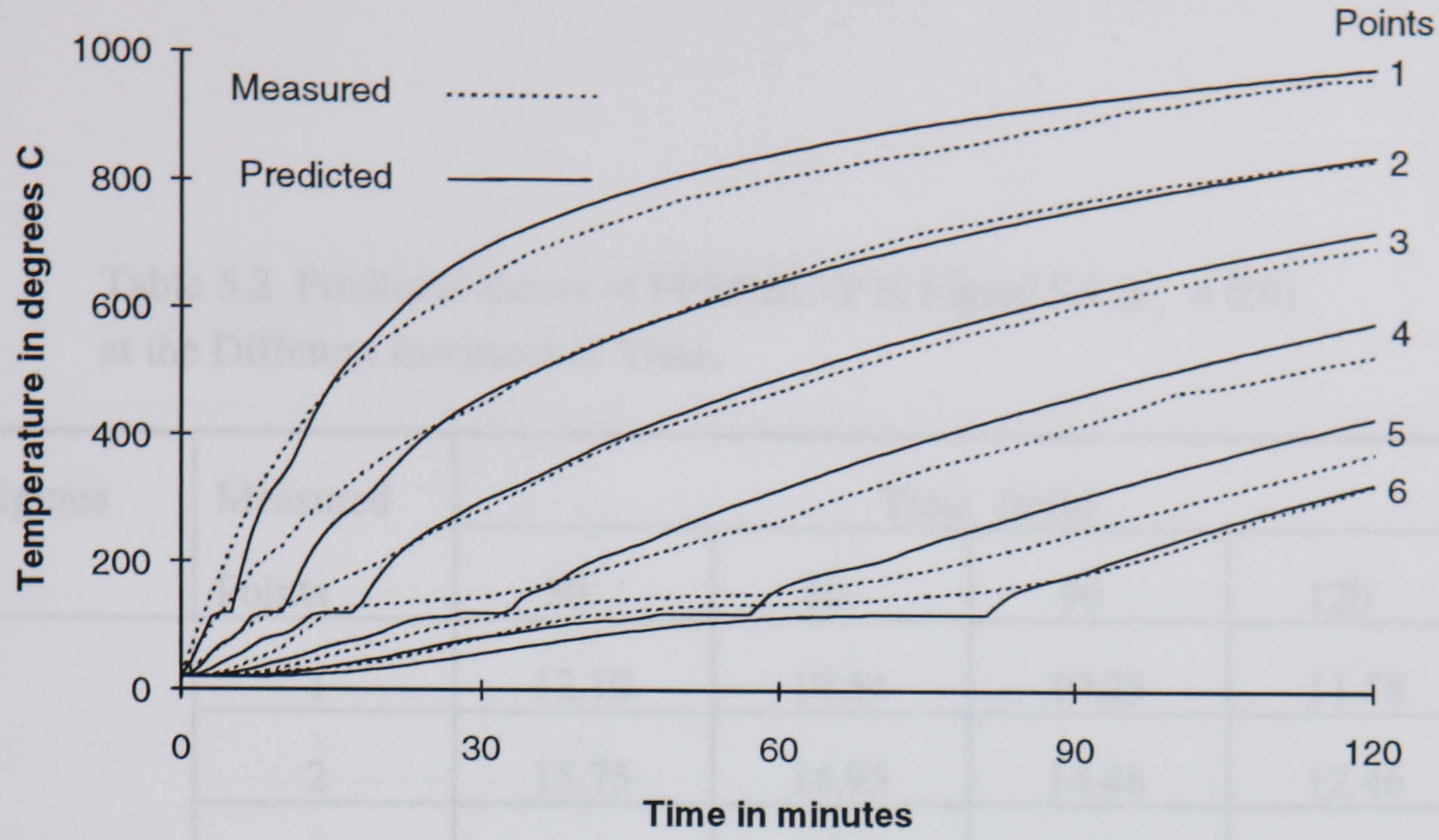

(a)

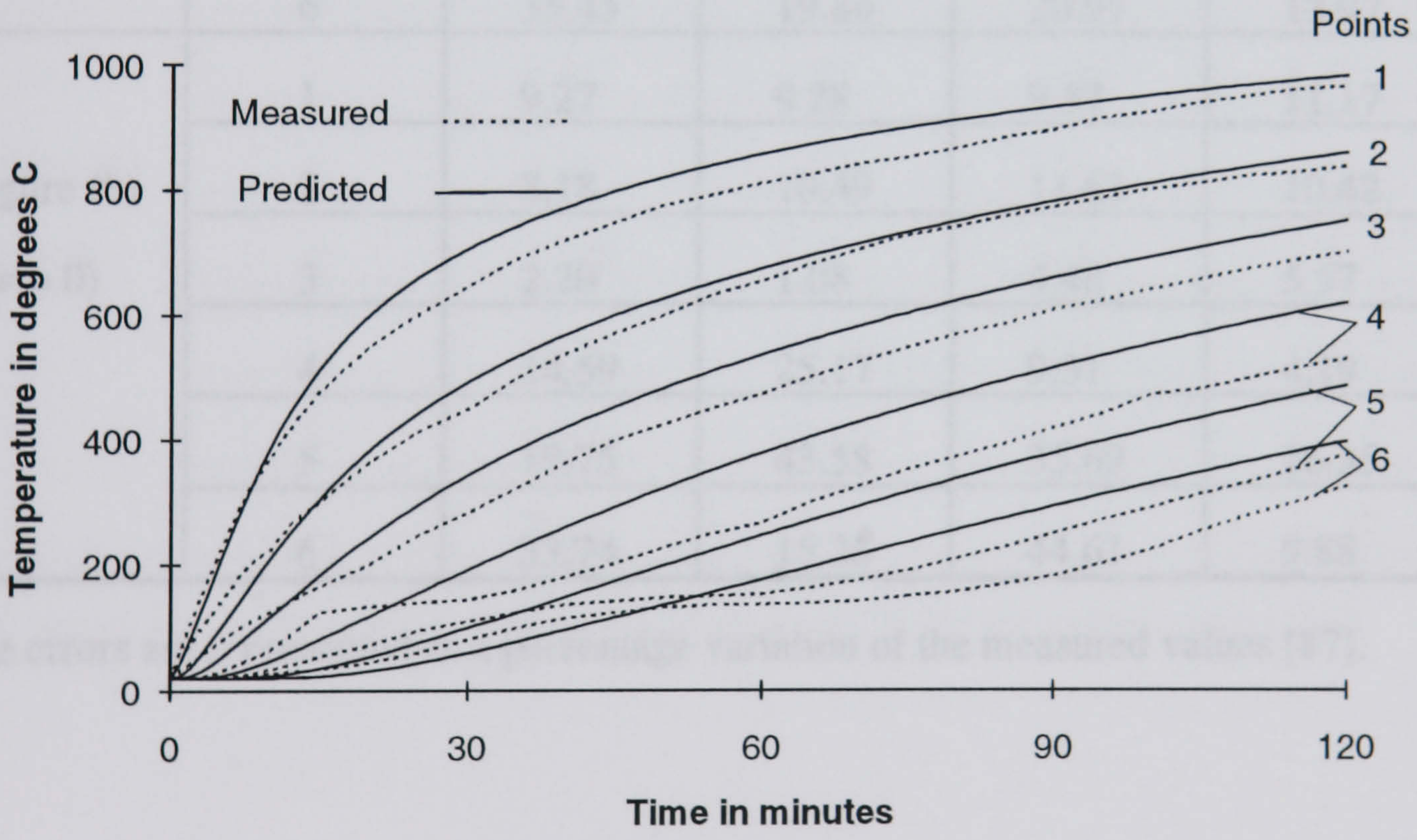

(b)

Figure 5.6 Comparison of Predicted and Measured [87] Temperature at Mid-section of the Column Exposed to ISO 834 Fire ($\varepsilon_f = 0.9$)

(a) $w = 6\%$

(b) $w = 0$

Table 5.2 Predicted Errors of FPRCBC-T in Figure 5.4 ($\varepsilon_f = 0.6$) at the Different Instances of Time.

Figures	Measured Points	Time (min)			
		30	60	90	120
Figure (a) ($w = 6\%$)	1	12.10	10.54	10.25	11.58
	2	15.75	14.95	14.48	12.46
	3	13.77	10.30	10.15	9.46
	4	20.23	1.87	2.77	3.44
	5	30.61	21.57	4.16	0.42
	6	35.45	19.84	20.97	13.97
Figure (b) ($w = 0$)	1	9.27	9.28	9.57	11.17
	2	8.18	10.49	11.63	10.42
	3	2.20	1.08	4.48	5.57
	4	14.59	25.17	9.31	4.19
	5	19.75	43.58	35.69	16.35
	6	33.74	15.26	44.61	9.88

The errors are represented as a percentage variation of the measured values [87].

Table 5.3 Predicted Errors of FPRCBC-T in Figure 5.5 ($\varepsilon_f = 0.75$) at the Different Instances of Time.

Figures	Measured Points	Time (min)			
		30	60	90	120
Figure (a) ($w = 6\%$)	1	1.50	2.27	2.75	4.61
	2	5.70	7.36	7.68	5.47
	3	3.91	2.29	3.12	2.59
	4	16.92	11.16	4.97	3.65
	5	27.48	18.76	13.94	8.28
	6	32.54	17.95	6.51	5.99
Figure (b) ($w = 0$)	1	0.75	1.24	2.20	4.27
	2	1.39	3.09	4.91	3.48
	3	12.40	6.72	2.40	1.23
	4	24.49	34.44	16.91	11.10
	5	14.02	53.32	44.47	23.64
	6	29.68	22.71	53.70	16.58

The errors are represented as a percentage variation of the measured values [87].

Table 5.4 Predicted Errors of FPRCBC-T in Figure 5.6 ($\varepsilon_f = 0.9$) at the Different Instances of Time.

Figures	Measured Points	Time (min)			
		30	60	90	120
Figure (a) ($w = 6\%$)	1	7.47	4.82	3.65	1.43
	2	2.63	0.96	1.56	0.66
	3	4.66	4.41	2.96	3.38
	4	16.92	19.21	11.46	9.72
	5	25.31	4.88	22.02	14.86
	6	30.06	15.98	1.27	0.51
Figure (b) ($w = 0$)	1	9.42	5.71	4.12	1.72
	2	9.62	3.19	1.21	2.57
	3	21.20	13.29	8.47	7.16
	4	33.06	42.29	23.10	17.07
	5	9.02	61.63	51.87	29.86
	6	26.04	29.12	61.43	22.25

The errors are represented as a percentage variation of the measured values [87].

5.3 Structural Analysis

In order to examine the accuracy of the proposed non-linear finite element procedure, it is necessary to carry out a series of proving tests. This is achieved through a quantitative verification of the analytical method against literature test results.

A series of fire tests of reinforced beams were carried out at the Fire Research Laboratory of Portland Cement Association according to ASTM E119 Fire and SDHI Fire and reported by Lin at al [100].

Three different beams exposed to different fire conditions are analysed using the programme, FPPRCM-S, and the results are compared to the test data. Also the predicted responses were obtained [100] using a modified computer programme originally developed by Becker and Bresler [7] and examined for comparative purposes with FPPRCM-S.

5.3.1 The Details of Analysed Beam Specimens

From [100] it was ascertained that the three reinforced concrete beams used were cast at the Construction Technology Laboratories of the Portland Cement Association. All beams were designed according to ACI Standard 318 [100] with a 6.1 *m* (20-ft) span and 1.83 *m* (6-ft) cantilever. Beams were fabricated using normal weight concrete (Type I Portland Cement, calcareous sand, and gravel aggregate, the maximum size of coarse aggregate was 25 *mm*) and Grade 60 reinforcing bars. All beams were reinforced with $8^{\#}$ bars at top, $7^{\#}$ bars at bottom, and $3^{\#}$ bars for stirrups.

Table 5.5 and Figure 5.7 provide details of the beam specimens. Beam No. 3 was tested using the ASTM E119 fire exposure, and beams No.5 and 6 were exposured to a short duration high intensity (SDHI) exposure. The average furnace temperature measured during the ASTM and SDHI fire tests are shown in Figure 5.8.

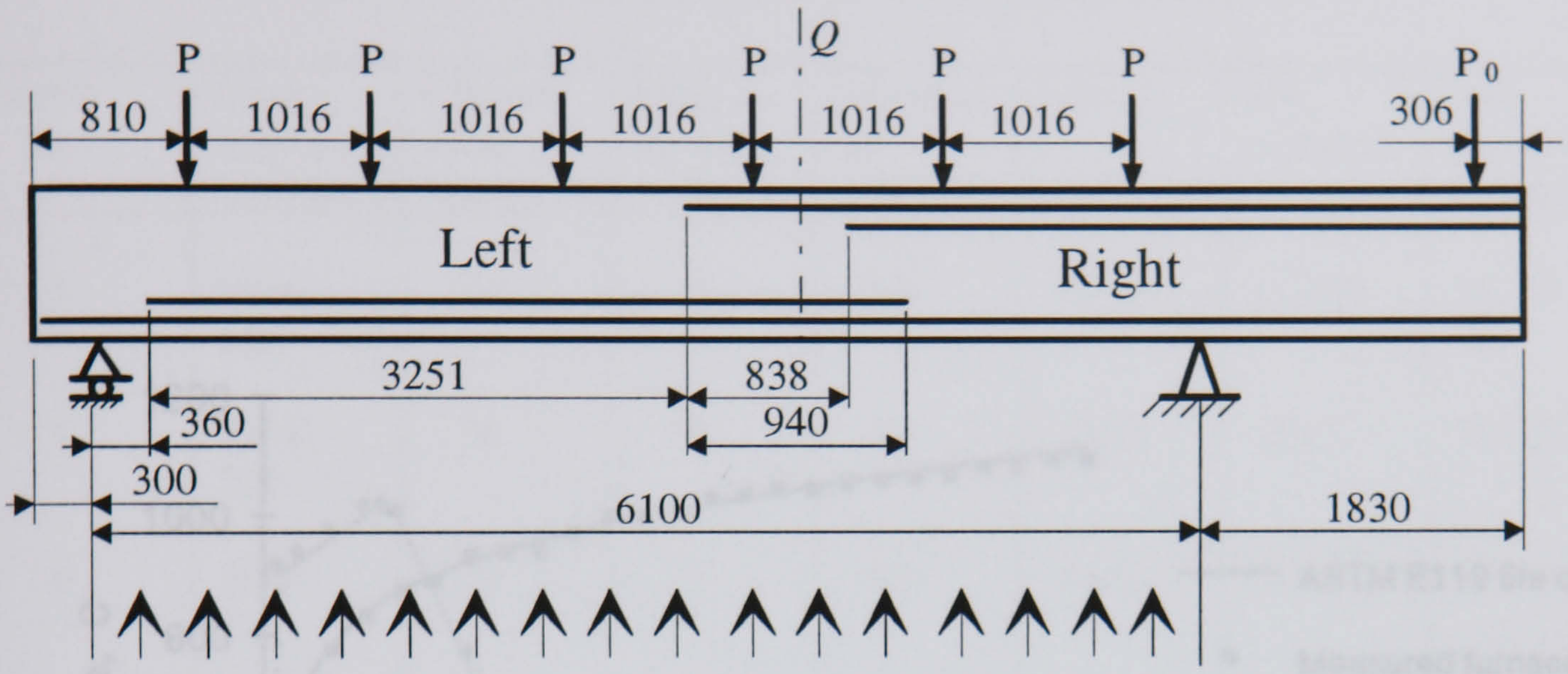

Surface exposure to fire conditions

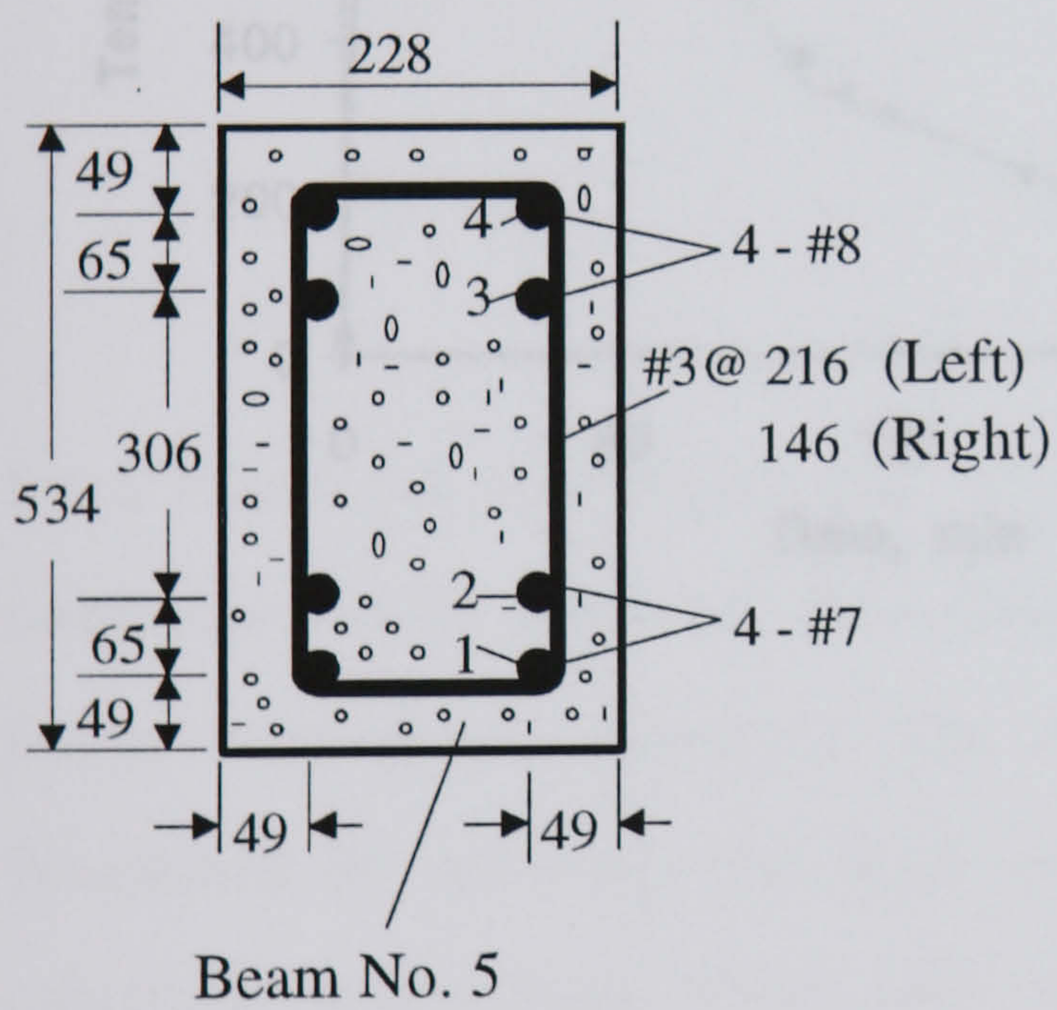

Beam No. 5

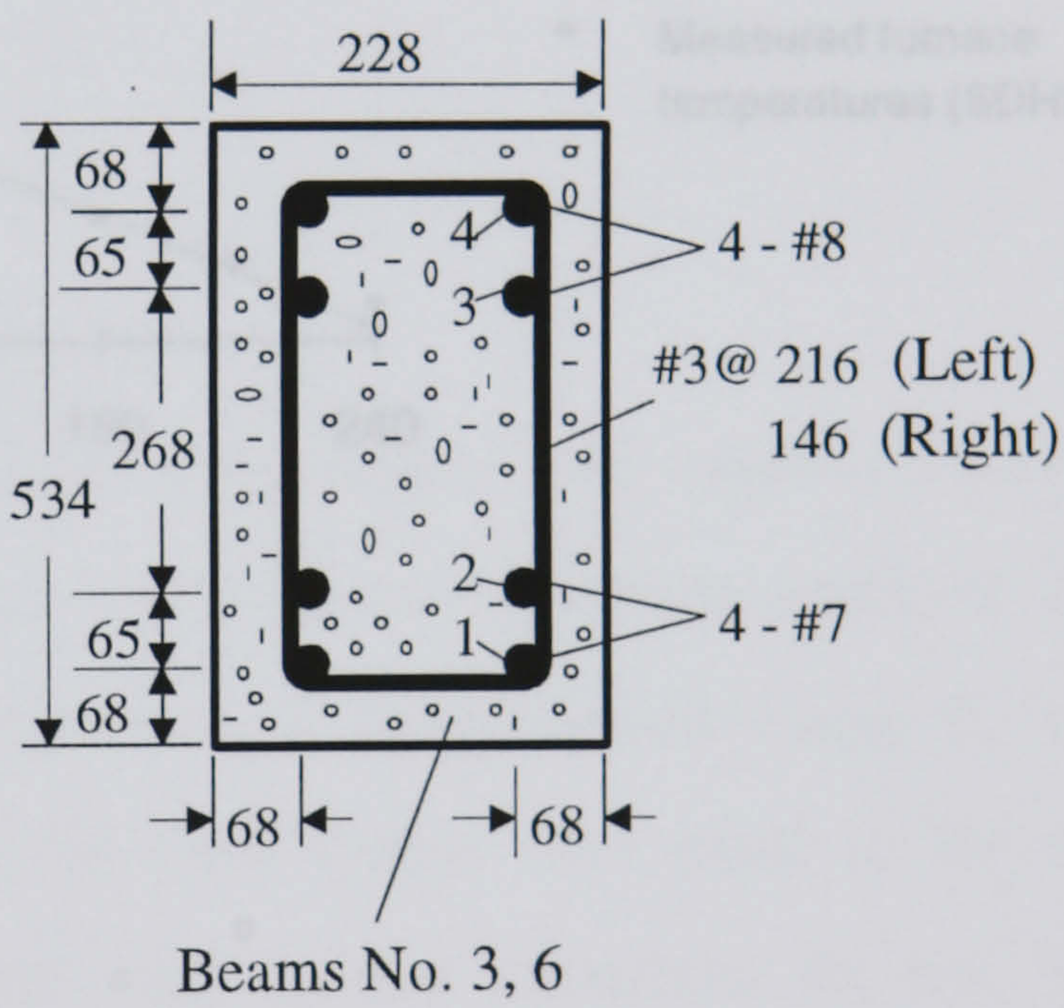

Beams No. 3, 6

All dimensions in mm

Figure 5.7 Analysed Beam Specimen Details [100]

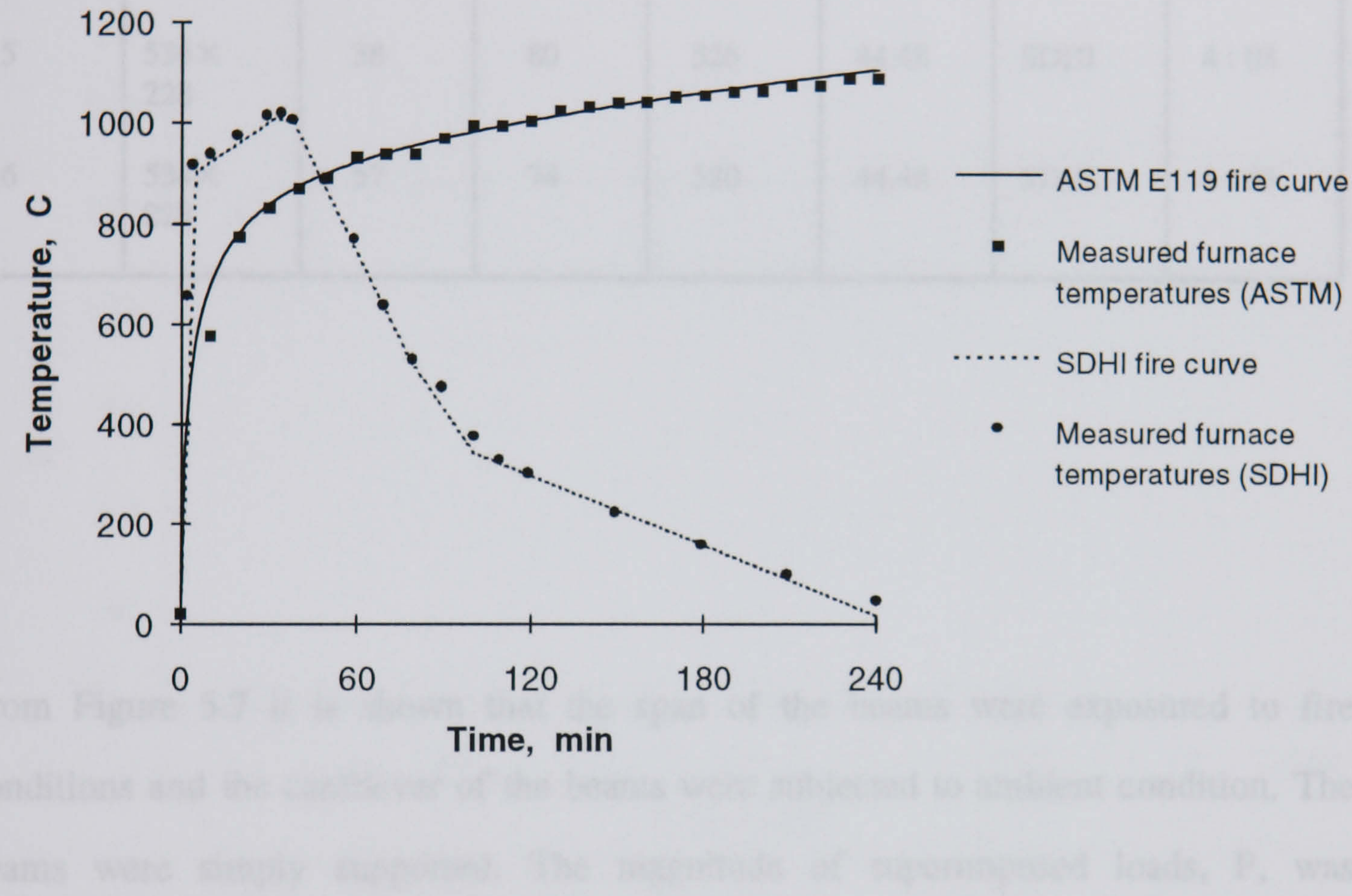

Figure 5.8 Furnace Atmosphere Temperature for ASTM and SDHI Fire Exposures [100]

Table 5.5 Details of Beam Test Conditions [100]

Beam No	Cross section (*mm*)	Concrete cover (*mm*)	Relative humidity (%)	Specimen age (days)	Load P (KN)	Fire exposure	Test duration (hr : min)
3	534× 228	57	76	375	44.48	ASTM	4 : 03
5	534× 228	38	80	526	44.48	SDHI	4 : 03
6	534× 228	57	74	520	44.48	SDHI	4 : 03

From Figure 5.7 it is shown that the span of the beams were exposured to fire conditions and the cantilever of the beams were subjected to ambient condition. The beams were simply supported. The magnitude of superimposed loads, P, was determined by assuming that loads on the floor system were equal to the full unfactored design loads. These loads were held constant throughout the test. The cantilever load, P_0, applied at the start of the test was determined so that the induced negative moment was equal to 59% of the negative nominal moment strength at the continuous support. P_0 was changing during the fire test. Figure 5.9 shows how the measured cantilever loads, P_0, changed during the testing of the beams.

Some test values of material properties at room temperature are given in Table 5.6 (the symbolises in the Table are referenced to Chapter 4):

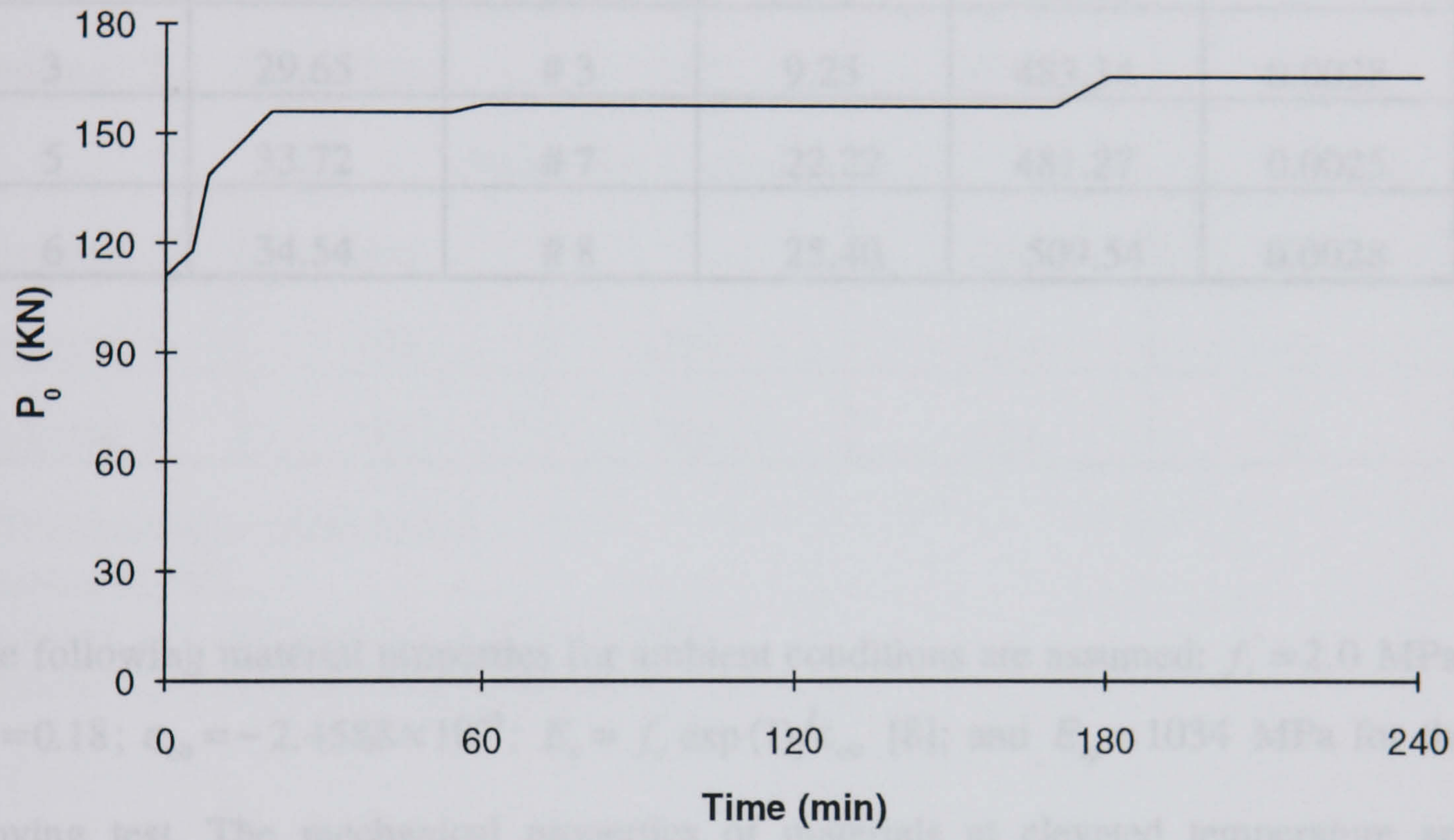

Figure 5.9 Measured Cantilever Loads [100]: Plot of Load Against Time

Table 5.6 Measured Material Properties at Ambient condition

Concrete		Steel			
Beams No.	$f_c^{'}$ (MPa)	Bar Designation	Diameter (mm)	f_y (MPa)	ε_y
3	29.65	# 3	9.25	483.34	0.0028
5	33.72	# 7	22.22	481.27	0.0025
6	34.54	# 8	25.40	509.54	0.0028

The following material properties for ambient conditions are assumed: $f_t^{'} = 2.0$ MPa; $\nu_c = 0.18$; $\varepsilon_{c0} = -2.4588 \times 10^{-3}$; $E_c = f_c^{'} \exp(1)/\varepsilon_{c0}$ [8]; and $E_{sp} = 1034$ MPa for the proving test. The mechanical properties of materials at elevated temperature are calculated using the model discussed in Chapter 2.

5.3.2 Results and Discussions

In this proving test the temperature distribution of the cross-sections of the beams are generated by FPRCBC-T. Beam No.3 was tested using the ASTM E119 fire exposure, and beams No 5 and 6 were exposured to a short duration high intensity (SDHI) fire. The comparison of predicted and measured temperatures in the main reinforcement of beams No.3 and 5 at testing time of 3 hr and 1 hr respectively are given in Table 5.7. There "Predicted 1" is the temperature history used for the structural analysis by Lin et al [100], and "Predicted 2" is calculated using FPRCBC-T, to give a temperature input for this proving test.

Table 5.7 Comparison of Predicted and Measured Temperatures in Main Reinforcement

Thermocouple layer (Fig. 5.7)	Top Reinforcement		Bottom Reinforcement	
	4 (^0C)	3 (^0C)	2 (^0C)	1 (^0C)
Beam No. 3 (t = 3 hr)				
Measured	349	367	463	523
Predicted 1	366	406	478	566
Predicted 2	320	347	396	500
Beam No. 5 (t = 1 hr)				
Measured	206	*	248	316
Predicted 1	196	210	251	397
Predicted 2	187	195	211	326

* Thermocouple malfunction
Measured [100]
Predicted 1 = calculated by Lin et al [100]
Predicted 2 = calculated by FPRCBC-T

The results of comparison between measured and predicted maximum deflection of beams are shown in Figures 5.10-5.12. The predicting errors of analytical models in Figures 5.10-5.12 at the different instances of time are shown in Tables 5.8. In these figures, "Predicted 1" were calculated by Lin et al [100] and "Predicted 2" were produced by the analytical model proposed in this thesis. In Figure 5.10 the data "Predicted 3" is produced without considering effect of steel creep.

From Table 5.8 calculated values of the percentage variation in deflection between the tests conducted at the Portland Cement Association and the models proposed by Lin et al [100] and FPPRCM-S are presented. It can be seen that at selected time intervals Lin et al obtained variations of 17.18% to 43.1% over the 210 minutes test for beam 3.

In comparison FPPRCM-S exhibited a variation of 6.58% to 32.74%. thereby indicating a closer match to the measured values. For beam 5 and 6 the variation from Lin et al were 25.59% to 36.36% and 4.9% to 35.31% respectively. In comparison FPPRCM-S showed a variation of 0.25% to 24.63% for beam 5 (with an initial error of 42.24% at time=0) and 1.08% to 20.99% for beam 6 (with a initial error of 29.98% at time=0). In summary, it is clear that the model FPPRCM-S is able to provide a closer agreement to the measured values, despite an initial error occurring at the start of the test. In a fire simulation model it may be of more importance that the model provides a closer accuracy at elevated temperatures and this is clearly evident after 210 minutes of testing in the case of beams 5 and 6. A further point to note relates to the inherent variability in concrete where in mix design, material quality and composition will often lead to variation in ambient strength and thus elasticity, which are within the range of 1.64 standard deviations.

From the curve "Predicted 2" in Figure. 5.10, it can be seen that before approximately 180 min the model provided quite good agreement with measured values. After that time the model appears to over predict the maximum deflection of the beam and structure rapidly undergoes failure but the trend produced appears to have the same shape as the measured data.

The overprediction is caused by the creep model of the reinforced steel bar. As discussed in Section 2.3.8, the creep model used in this study is very sensitive to the experimental coefficient which is used. Since there is no exact coefficient available related to the main reinforced steel bar in this proving test, a set coefficient derived from CSA G40.12 (yield strength 350 MPa) [42] was used. The yield strength of CSA G40.12 is lower than the steel bars #7, #8 (481 MPa, 509 MPa) used here. Therefore, the predicted free creep strains were higher than the actual values, particularly when the temperatures of reinforced bar are higher (over 500 ^{0}C). For Beams 5 and 6 the steel creep strains were small because these beams were exposed to the SDHI Fire, wherein the bar temperatures were lower (below 400 ^{0}C).

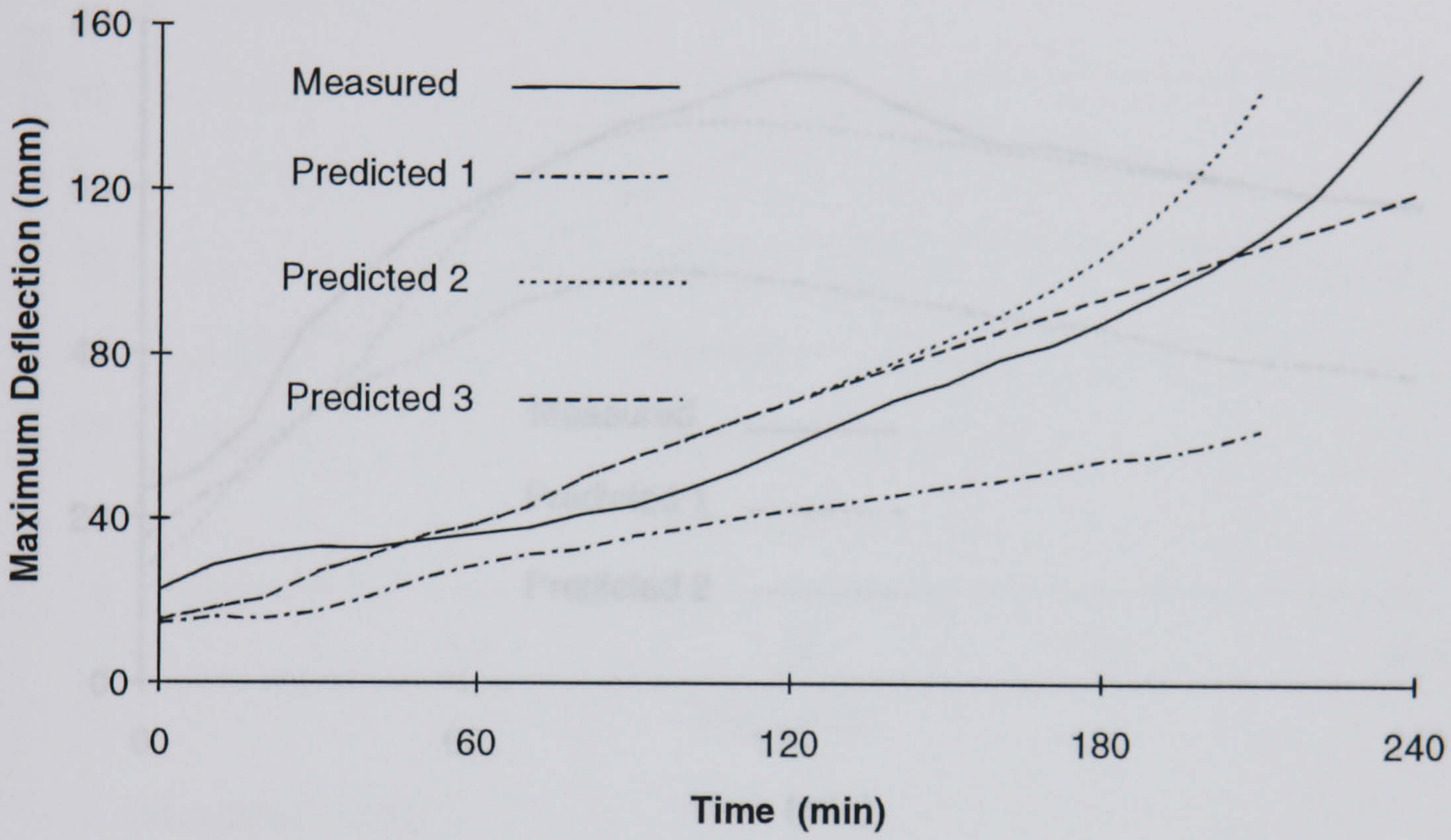

Measured [100]
Predicted 1 = calculated by Lin et al [100]
Predicted 2 = calculated by FPPRCM-S
Predicted 3 = calculated by FPPRCM-S (excluded effect of steel creep)

Figure 5.10 Comparison of Predicted and Measured Maximum Deflection of Beam No. 3 (ASTM Fire)

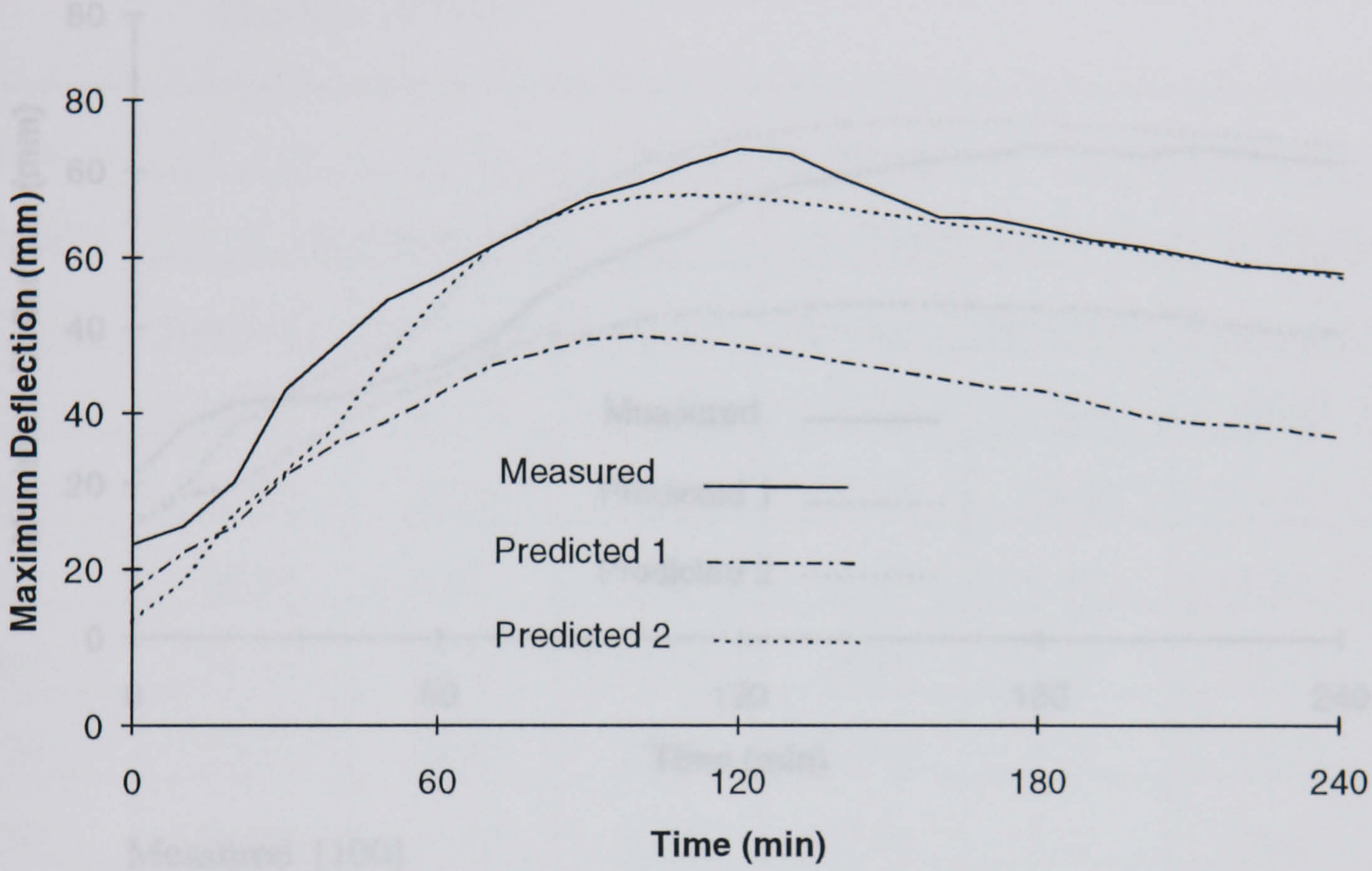

Measured [100]
Predicted 1 = calculated by Lin et al [100]
Predicted 2 = calculated by FPPRCM-S

Figure 5.11 Comparison of Predicted and Measured Maximum Deflection of Beam No. 5 (SDHI Fire)

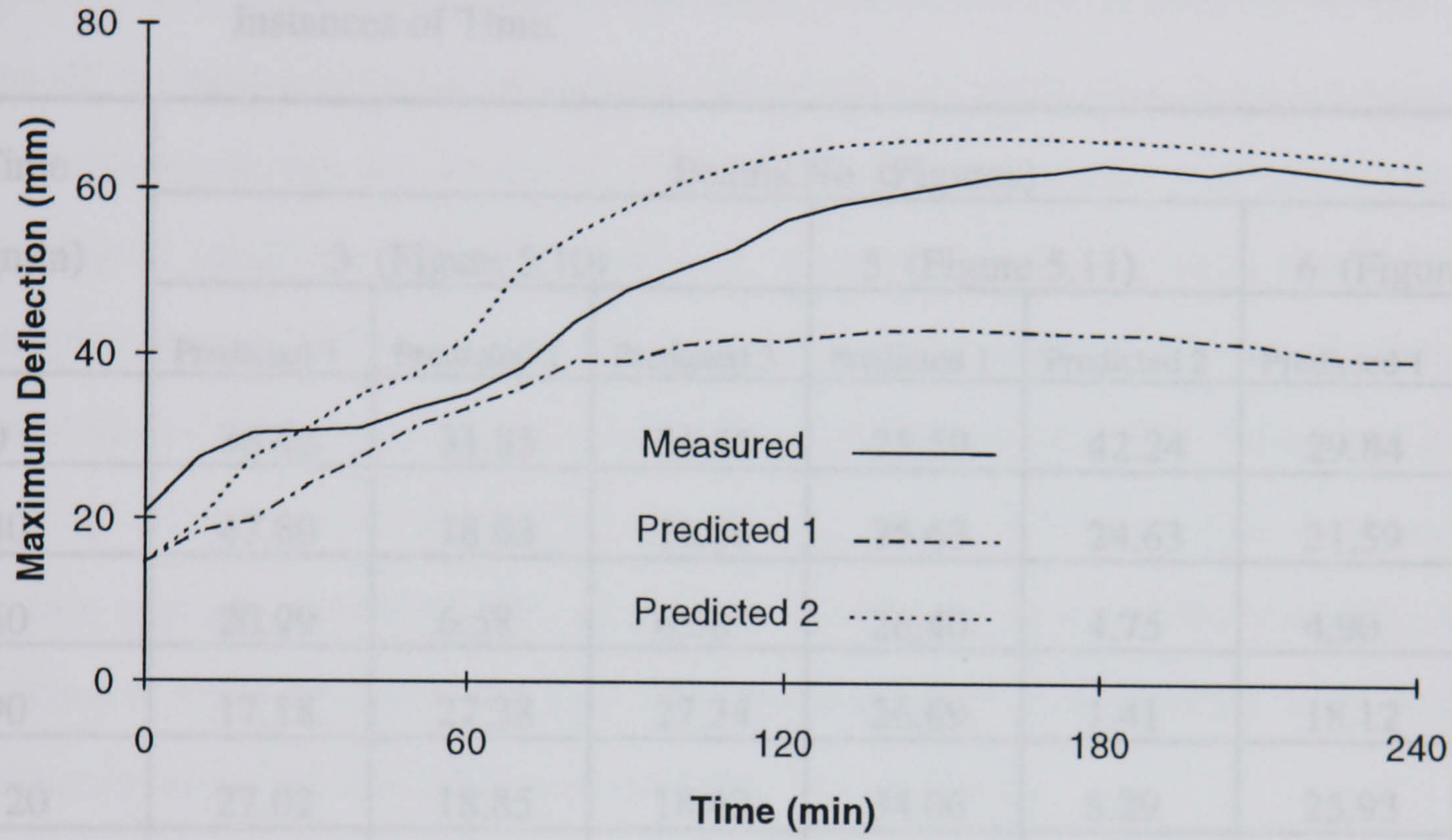

Measured [100]
Predicted 1 = calculated by Lin et al [100]
Predicted 2 = calculated by FPPRCM-S

Figure 5.12 Comparison of Predicted and Measured Maximum Deflection of Beam No. 6 (SDHI Fire)

Table 5.8 The Predicted Percentage Errors in Deflection between Measured Values and Analytical Models in Figures 5.10 - 5.12 at the Different Instances of Time.

Time (min)	Beams No. (Figures)						
	3 (Figure 5.10)			5 (Figure 5.11)		6 (Figure 5.12)	
	Predicted 1	Predicted 2	Predicted 3	Predicted 1	Predicted 2	Predicted 1	Predicted 2
0	36.42	31.85	31.85	25.59	42.24	29.84	29.98
30	47.80	18.63	18.66	25.63	24.63	21.59	1.08
60	20.99	6.58	6.58	26.40	4.75	4.90	19.95
90	17.18	27.38	27.34	26.69	1.41	18.12	20.99
120	27.02	18.85	18.42	34.06	8.29	25.93	14.02
150	34.17	14.48	11.54	32.50	3.29	28.47	9.53
180	37.95	18.12	6.57	32.54	1.56	32.43	4.80
210	43.11	32.74	2.28	35.59	0.25	34.28	3.10
240	---	---	19.30	36.36	0.95	35.31	3.42

The errors are represented as a percentage variation of the measured values [100].
Predicted 1 = calculated by Lin et al [100];
Predicted 2 = calculated by FPPRCM-S;
Predicted 3 = calculated by FPPRCM-S (excluded effect of steel creep).

From the curve "Predicted 3" in Figure 5.10, it can be seen that for the ASTM E119 exposure fire after 3 hr testing time the creep of main reinforced bar is a major factor which influences the structural behaviour of reinforced concrete members. Therefore for temperatures over 500 ^{0}C the creep strain of steel reinforced bar must be taken into account.

Figures 5.11-5.12 shown the comparison results of Beams 5 and 6. It can be seen that, over-all, the proposed model provides a fairly good agreement with measured values. From all three beams, the results indicated that the proposed model produced a better accuracy of prediction than the method of analysis used by Lin et al [100]. The example output of FPPRCM-S are shown in Appendix A. According to the calculation results most Gauss Points of the concrete layer fail by cracking. This infers that the cracking of concrete is the fundament problem to the behaviour of a reinforced concrete structure member in fire conditions. Therefore a more realistic modelling of cracking in concrete is the key matter for the non-linear finite element analysis of reinforced concrete member when subjected to fire conditions.

6. CONCLUSIONS AND RECOMMENDATIONS

6.1 Conclusions

6.1.1 Thermal Analysis

Based on the one-dimensional theoretical heat and mass transfer model proposed by Sahota [11], a two-dimensional non-linear finite element procedure was developed in this study to predict the temperature distribution history of the cross-section of a reinforced concrete structural member in fire conditions. In this procedure, the energy transfer by convection and mass diffusion, and the difference between the enthalpy and internal energy of air-vapour mixture in concrete were neglected. For evaluating the effect of water evaporation in concrete, three simplifying assumptions were made (Section 3.2.1). The thermal properties of concrete were considered as temperature and moisture dependent and the thermal properties of steel were temperature dependent.

In the thermal analysis, performed using FPRCBC-T, the fire conditions were described by time-temperature curves of the fire at some distance away from the member. For this purpose, convection and radiation boundary conditions were used. The results of thermal analysis were in the form of predicted temperatures at nodal points and within elements at specified times.

The validation of the proposed model was achieved through a quantitative verification against known experimental results [87]. Based on comparisons between the numerical predictions and the test results the following conclusions are made:

(1) The model proposed in this thesis is capable of predicting the temperature distribution histories of cross-sections of reinforced concrete structural members subjected to fire with fairly good accuracy. To improve the accuracy of the model, there is need for further investigation of the thermal properties of materials at elevated temperatures.

(2) When the temperature in the concrete is below 140 ^{0}C, neglecting the energy transfer by mass convection and diffusion this lead to a slight discrepancy between the values measured and model's predictions.

(3) The effect of the evaporation of the moisture is significant on the temperature distribution histories in concrete during fire conditions, especially for high initial moisture content (6% by weight) which should be taken into account in the thermal analysis of reinforced concrete.

(4) The temperature distribution histories in reinforced concrete are sensitive to the value of the flame emissivity of fire, ε_f, used. It appears reasonable to use values of 0.75 to 0.85 for the ε_f.

(5) The temperature distribution histories generated by FPRCBC-T can be used as temperature input for predicting the mechanical response of reinforced concrete structural member which are subjected to fires.

6.1.2 Structural Analysis

In this thesis a non-linear finite element procedure based on the "plane stress" theory for predicting the structural behaviour of planar reinforced concrete members subjected to fire was described. In this model an iterative, secant stiffness formulation was used to consider the complex features of structural behaviour in fire conditions. There were: (1) dimensional changes caused by temperature differences; (2) change in the mechanical properties of the material with change in temperature, (3) degradation of element by cracking or crushing; and (4) shrinkage and creep and transient strains. Spalling and geometric non-linearities and the various modes of failure were excluded.

In this proposed non-linear procedure, reinforced concrete members were modelled as an assemblage of concrete elements and main reinforced bar elements. The concrete element was sub-divided into several layers and every layer was assumed to have a uniform temperature at any time step. The main steel reinforcements were modelled in a discrete manner using the bar element and this bar element is a structural member capable of transmitting stresses only in the direction normal to the cross-section. The

shear reinforcement was induced in the properties of the concrete elements and thus modelled in a smeared manner. The concrete elements were modelled through the use of isoparametric four-node quadrilateral element and the two-point formula of Gauss quadrature was employed. The main steel reinforcing bars were modelled as two-point bar elements in conjunction with the concrete elements.

In this study crushing and cracking of concrete were also considered by suitably adjusting the stiffness at each Gauss point of concrete layers. A smeared crack model was adopted to model the crack of the concrete, within this model the initiation of a cracking process at any Gauss point happens when the concrete stress reach one of the cracking failure surface of the concrete failure envelope. After single cracking has taken place, the concrete is treated as an orthotropic material with principal axes normal and parallel to the crack direction. The concrete paralleled to the crack direction is still capable of resisting either tensile or compressive forces, when it is subjected to tension, a pure linear elastic behaviour is assumed and when the tensile stress exceeds the tensile strength a second crack is formed normal to the first crack.

At present, there is still very little data and few theoretical models available on the constitutive modelling of concrete under biaxial states of stress at elevated temperature. Therefore, in this study models at room temperature were extended to elevated temperatures simply by considering all the relevant parameters of the material as temperature dependent. For modelling concrete stiffness of integral and after crushing a non-linear elastic model, which is a specialised 2-D form of the actual 3-D model proposed by Ottosen [23] was employed. This model was extended to fire conditions simply by considering all the relevant parameters as temperature dependent.

The formulation of the concrete failure envelope proposed by Barzegar-Jamshidi [21] which was based on a slight modification of the Kupfer and Gerstle [22] expressions was adopted with the parameters considered temperature dependent. For considering the tension stiffening behaviour of concrete in this study the secant normal stiffness is determined using a bilinear tension stiffening curve suggested by Rots et al [27].

In order to examine the accuracy of the proposed non-linear finite element procedure, a series of proving tests have been carried out. Based on the results of the proving tests, conclusions include the following:

(1) The proposed method of analysis is a valid and powerful tool for the analysis of planer reinforced concrete members under fire conditions.

(2) A secant stiffness approach can be as successful as the more common tangent stiffness approach but can provide a good numerical stability. This is very important for the analysis of reinforced concrete in fire conditions. The structure can be analysed until failure occurs.

(3) The proposed material models are capable of capturing the dominant behaviour of the reinforced concrete members. However, there is still a need for the further investigation of the material properties at elevated temperatures particularly in respected of the failure envelope of concrete, the creep strain of steel reinforcement, material strength and stiffness to provide more realistic material models in conjunction with the non-linear finite element analysis model developed in this work for improving the accuracy of the model's predictions.

(4) The results show that when the temperature of the main steel reinforcing bar is over 500 ^{0}C the creep of the main bar is a major factor to dominate the structural behaviour of the reinforced concrete members.

(5) According to the calculated results the cracking of concrete is the fundament problem of reinforced concrete structural members in fire conditions. Therefore a more realistic model concerning the process of cracking in concrete is the key matter for the non-linear finite element analysis of reinforced concrete member subjected to fires.

(6) The model can also be used for the calculation of the fire resistance of planer reinforced concrete members made with mix designs other than those investigated in this study if the relevant material properties are known, for example light-weight concrete.

Computer programmes such as FPRCBC-T, and FPPRCM-S are intended to function as research tools to help explore and better understand the implications of fire environment for the design of structures. It is believed that numerical simulation supplemented by physical experiments, chosen judiciously, is not only a more economical approach to the fire problem, but will allow the important parameters to be isolated quickly and examined more thoroughly. Perhaps analytical studies with a realistic range of parameter values for material properties can be used to determine whether some of the parameters are of only minor importance.

6.2 Recommendation for Further Studies

It is clear from the conclusions to this study that a number of questions have been raised with reference to the behaviour of concretes at elevated temperatures and in-particular with respect to the failure of the material by cracking. In summary it is recommended that the following areas should be considered for further work:

(1) Extensive studies to determine the effect of high temperature on material properties, especially of biaxially loaded concrete, and the creep strain of steel reinforcement should be carried out.

(2) Explosive spalling and its influence on the behaviour of reinforced concrete structural members in fire should be investigated.

(3) More experimental work is needed to assess the validity of the various mathematical models proposed in this dissertation. In these experiments, temperature and moisture distribution, stresses, strains, forces, displacements, cracking, crushing, and spalling should be recorded.

(4) The result of the proposed analytical method should be compared with results from actual fire events. Such comparisons can help in resolving questions related to the design of structure for fire safety.

(5) Systematically parametric studies using the proposed analytical method should be carried out. These parametric studies can help the structural engineer in identifying important design parameters.

(6) The proposed analytical method should be extended to included geometric non-linearities.

REFERENCES

1. "Fire Resistance Tests on Elements of Building Construction", ISO834 International Organisation for Standardisation, 1975.
2. "BS476: Fire Tests on Building Materials and Structures: Part 20: Methods of Determination of the Fire Resistance of Elements of Construction (general principles)", British Standards Institution, London, 1987.
3. H. Bizri, "Structural Capacity of Reinforced Concrete Columns Subjected to Fire Induced Thermal Gradients", Structural Engineering Laboratory, Report No. 73-1, University of California, Berkeley, 1973.
4. J. M. Becker et al, "FIRES-T: A Computer Program for the Fire Response of Structures - Thermal", Report No. UCB FRG 74 - 1, University of California, Berkeley, 1974.
5. B. Ellingwood and T. D. Lin, "Flexure and Shear Behaviour of Concrete Beams During Fires", Journal of Structural Engineering, Vol. 117, No. 2, February, 1991, pp. 440-458.
6. U. Wickström, "A Computer Program for Temperature Analysis of Structures Exposed to Fire", Report No. 79-2, Lund Institute of Technology, Lund, Sweden, 1979.
7. J. Becker, and B. Bresler, "FIRES - RC, A Computer Program for the Fire Response of Structures Reinforced Concrete Frames", Report No. UCB FRG 74-3, Fire Research Group, University of California, Berkeley, 1974.
8. N. J. Weeks, "Lateral Instability of Slender Reinforced Concrete Columns in a Fire Environment", Ph.D. Thesis, Aston University, 1985.
9. T. T. Lie and R. J. Irwin, " Method to Calculate the Fire Resistance of ReinforcedConcrete Columns with Rectangular Cross Section", ACI Structural Journal, Vol. 90, No. 1, 1993, pp. 52-60.

10. Z. T. Nizamuddin, "Thermal and Structural Analysis of Reinforced Concrete Slabs in Fire Environments", Ph.D. Thesis. University of California, Berkeley. 1976.

11. M. S. Sahota, "Heat and Mass Transfer in Porous Concrete Structures Subject to Fire", Ph.D. Thesis, University of California, Berkeley, 1976.

12. T. Z. Harmathy, "Effect of Moisture on the Fire Endurance of Building Element", ASTM, STP-385, Moisture in Materials in Relation to Fire Test, 1965

13. T. Z. Harmathy, "Thermal Properties of Concrete at Elevated Temperatures". ASTM Journal of Materials, Vol. 5, No. 1, 1970. pp. 47-74.

14. N. G. Zoldners, "Thermal Properties of Concrete under Sustained Elevated Temperature", ACI, SP-25, Temperature and Concrete. 1968.

15. E. Crispino, "Studies on Technology of Concrete under Thermal Conditions ", ACI Seminar, Concrete for Nuclear Reactors, Berlin. 5-9 October 1970.

16. W. D. Kingery. "Introduction to Ceramics", John Willey & Sons. Inc, New York. 1960.

17. T. Z. Harmathy. "Simultaneous Moisture and Heat Transfer in Porous System with Particular Reference to Drying", Ind. Engng. Chem. Fundamentals, Vol. 8, No. 1, 1969, pp. 92 - 103.

18. "Physical Constants of Some Commercial Steels at Elevated Temperatures", The British Iron and Steel Association, Butterworths Scientific Publications, London, 1953.

19. H. B. Kupfer, et al. "Behaviour of Concrete under Biaxial Stresses", ACI Journal. Vol. 66, August 1969.

20. T. C. Y. Liu. et al, "Biaxial Stress-strain Relations for Concrete". Journal of the Structural Division of the ASCE. Vol. 98, No. ST5. Proceedings Paper No. 8905, May 1972. pp. 1025-1034.

21. F. Barzegar-Jamshidi. "Nonlinear Finite Element Analysis of Reinforced Concrete Under Short Term Monatomic Loading". Ph.D. Thesis. University of Illinois at Urbana-Champaign. 1987.

22. H. B. Kupfer and K. H. Gerstle, "Behaviour of Concrete Under Biaxial Stresses". Journal of the Structural Division, ASCE, Vol. 99, No. EM4, Proc. paper 9917. August 1973, pp. 853-866.

23. N. S. Ottosen, "Constitutive Model for Short-Time Loading of Concrete", Journal of the Engineering Mechanics Division, ASCE, Vol. 105, No. EM1, 1979, pp. 127-141.

24. "Finite Element Analysis of Reinforced Concrete", American Society of Civil Engineers, New York, 1982.

25. F. J. Vecchio, "Nonlinear Finite Element Analysis of Reinforced Concrete Membranes", ACI Structural Journal, Vol. 86, No. 1, 1989, pp. 26-35.

26. K. J. Willam, et al, "Constitutive and Computational Aspects of Strain-softening and Localization in Solids", WAM 84 Symposium on Constitutive Equations: Micro, Macro and Computational Aspects, New Orleans, LA, December 1984.

27. J. G. Rots, et al, "The Need for Fracture Mechanics Options in Finite Element Models for Concrete Structures", Proc. International Conference on Computer Aided Analysis and Design of Concrete Structures, F. Damjanic et al, Eds., Pineridge Press, Swansea, 1984, Part 1, pp. 19-32.

28. J. C. Marechal, "Variations in the Modulus of Elasticity and Poisson's Ratio with Temperature", ACI Special Publication, SP-34, Concrete for Nuclear Reactors, 1972, pp. 495-504.

29. T. Harada, et al, "Strength, Elasticity, and Thermal Properties of Concrete Subjected to Elevated Temperatures", ACI Special Publication, SP-34, Vol. 1 , Concrete for Nuclear Reactors, 1972.

30. D. Lankard, et al, "Effect of Moisture Concrete on the Structural Properties of Portland Cement Concrete Exposed to Temperatures up to 500 ^{0}F", ACI-SP-25, Temperature and Concrete, 1968.

31. R. Phileo, "Some Physical Properties of Concrete at High Temperature", ACI Journal, Vol. 54, 1958, pp. 857-864.

32. N. G. Zoldners, "Effect of High Temperature on Concrete Incorporating Different Aggregates", ASTM Proceedings, Vol. 60, 1960, pp. 1087-1108.

33. Y. Anderberg and S. Thelandersson, "Stress and Deformation Characteristics of Concrete at High Temperatures", Bulletin 34, Lund Institute of Technology, Lund, Sweden, 1973.

34. H. L. Malhotra, "The Effect of Temperature on the Compressive Strength of Concrete", Magazine of Concrete Research, Vol. 8, 1956, pp. 85-94.

35. B. Bresler, Editor, Reinforced Concrete Engineering, Vol. 1, John Wiley and Sons, 1974.

36. F. Furumura, "The Stress-strain Curve of Concrete at High Temperatures", Tokyo Institute of Technology, Report of Meeting of Architectural Institute of Japan, 1966.

37. G. Jonsson and C. Lassen, "Experimental Investigation of the Temperature Dependence of the Tensile Strength for Concrete in Temperature Range Associated with Fires", Graduate Work at Division of Structural Mechanics and Concrete Construction, Lund Institute of Technology, Lund, Sweden, 1969.

38. H. Weigler and R. Fischer, "Influence of High Temperatures on Strength and Deformations of Concrete", ACI SP-34, Vol. 1, Concrete for Nuclear Reactors, 1972.

39. S. Thelandersson, "Effect of High Temperatures on Tensile Strength of Concrete", Bulletin 26, Lund Institute of Technology, Lund, Sweden, 1972.

40. H. Kupfer et al, "Behaviour of Concrete Under Biaxial Stresses", ACI Journal, Vol. 66, August 1969.

41. "Manual of Steel Construction", American Institute of Steel Construction, Inc., New York, 1960, pp. 6-9 to 6-11.

42. T. Z. Harmathy and W. W. Stanzak, "Elevated-temperature Tensile and Creep Properties of Some Structural and Prestressing Steels", ASTM Special Technical Publication No. 464, 1970, pp. 186-208.

43. C. Cruz, "Apparatus for Measuring Creep of Concrete at High Temperatures". Journal of Portland Cement Association, Vol. 10, No. 3. September 1968.

44. M. Mukaddam, "Creep Analysis of Concrete at Elevated Temperatures". ACI Journal, Vol. 71, February 1974, pp. 72-79.

45. F. Roll, "Long-time Creep Recovery of Highly Stressed Concrete Cylinders", ACI SP-3, Paper No. 4, 1964, pp. 95-114.

46. A. M. Freundenthal and F. Roll, "Creep and Creep Recovery of Concrete Under High Compressive Stress", Proceeding of the American Concrete Institute, Vol. 54, 1957-58, pp. 1111-1142.

47. Y. Akutsuka, et al, "Method of Evaluating Tensile Creep and Stress Relation of Concrete Loads", Transactions of the Japan Society of Civil Engineers, No. 47. September 1963.

48. K. Kordina, "Experiments on the Influence of the Mineralogical Character of Aggregates on the Creep of Concrete", Rilem Bulletin, Vol. 6, March 1960, pp. 7-22.

49. O. C. Zienkiewicz and M. Watson, "Some Creep Effects in Stress Analysis with Particular Reference to Concrete Pressure Vessels", Department of Civil Engineering, University of Wales, Swansea, Great Britain. November. 1966.

50. H. G. Geymayer, "Effect of Temperature on Creep of Concrete: a Literature Review", ACI SP-34, Concrete for Nuclear Reactors, 1972, pp. 565-590.

51. R. Taylor, et al. "Thermo-mechanical Analysis of Viscoelatic Solids". SESM Report, 68-7. University of California, Berkeley, 1968

52. J. M. Illston and I. J. Jordan, "Creep Prediction for Concrete under Multi-axial Stress", ACI Journal. Proceedings, Vol. 69, No. 3. March 1972. pp. 158-164.

53. J. W. Chuang, et al, "Prediction of Multiaxial Creep from Uniaxial Creep Tests", ACI. SP-34. Concrete for Nuclear Reactors, 1972. pp. 701-734.

54. N. K. Arutyunyan, "Some Problems in the Theory of Creep". Pergamon Press. London. 1966.

55. B. Bresler, et al, "Non-uniform Drying Shrinkage in Reinforced Concrete". I. A. B. S. E. Symposium Proceedings, Madrid, 1970, pp. 171-179.

56. G. L. England and A. D. Ross, "Shrinkage, Moisture, and Pore Pressure in Hardened Concrete", ACI, SP-34, Concrete for Nuclear Reactors, 1972. pp. 883-908.

57. Y. Anderberg and S. Thelandersson, "Stress and Deformation Characteristics of Concrete at High Temperatures, 2 Experimental Investigation and Material Behaviour Model", Lund Institute of Technology, Bulletin 54, Lund, Sweden. 1976.

58. Y. Anderberg, "Fire Exposed Hyperstatic Concrete Structures-An Experimental and Theoretical Study", Lund Institute of Technology, Bulletin 55. Lund, Sweden 1976.

59. J. E. Dorn, "Some Fundamental Experiments on High Temperature Creep". Journal Mech. and Phys. Solids, Vol. 3, 1954.

60. T. Z. Harmathy, "A Comprehensive Creep Model", Transaction of the ASME, September 1967, pp. 496-502.

61. T. Z. Harmathy, "Creep Deflection of Beams", ASCE National Engineering Meeting Preprint No. 2216, April 1974, pp.25.

62. D. H. Skinner, "Measurement of High Temperature Properties of Steel", Melbourne Research Laboratories, Clayton, Australia, May 1972.

63. "ASTM Designation: E119, Standard Methods of Fire Tests of Building Construction and Materials", American Society for Testing and Materials. Philadelphia, 1983.

64. E. L. Wilson and R. E. Nickell, "Application of Finite Element Method to Heat Conduction Analysis". Nuclear Engineering and Design, Vol. 4, 1966. pp. 276 - 286.

65. O. C. Zienkiewicz. "The Finite Element Method in Structural and Continuum Mechanics". McGraw - Hill. London. 1967.

66. T. K. Sherwood, "Application of the Theoretical Diffusion Equations to the Drying of Solids", Trans. Am. Inst. Chem. Engrs., Vol. 27. 1931, pp. 190-202.

67. E. Buckingham, "Studies in the Movement of Soil Moisture", U. S. Dept. Agr. Bur. Soils Bull., Vol. 38, Washington D. C., 1907, pp. 29-61.

68. C. G. Gurr, et al, "Movement of Water in Soil due to a Temperature Gradient". Soil Science, Vol. 74, 1952, pp. 335-345.

69. N. H. Ceaglske and O. A. Hougen, "Drying Granular Solids". Ind. Engng. Chem.. Vol. 29, 1937, pp. 805-813.

70. O. A. Hougen, et al, "Limitations of Diffusion Equations in Drying", Trans. Am. Inst. Chem. Engrs. Vol. 36, 1940, pp. 183-210.

71. D. A. Rose, "Water Movement in Porous Material: Part 1 - Isothermal Vapour Transfer", Brit. J. Appl. Phys., Vol. 14, 1963, pp. 256-262.

72. A. K. Platten, "A Study of Evaporation and Drying in Porous Building Materials", Ph.D. Thesis, Dept. of Building, UMIST, 1985.

73. B. X. Wang and Z. H. Fang, "Water Absorption and Measurement of the Mass Diffusivity in Porous Media", Int. J. Heat Mass Transfer, Vol. 31, 1988, pp. 251-275.

74. J. R. Phillip and D. A. DeVries, "Moisture Movement in Porous Materials under Temperature Gradients", Trans. Am. Geophys. Union, Vol. 38, No. 2, 1957, pp. 222 - 232.

75. D. A. DeVries, "Simultaneous Transfer of Heat and Moisture in Porous Media", Trans. Am. Geophys. Union, Vol. 39, 1958, pp. 909-916.

76. A. V. Luikov, "Heat and Mass Transfer in Capillary-porous Bodies", Pergamon Press, Oxford, 1966.

77. B. X. Wang and W. P. Yu, "A Method for Evaluation of Heat and Mass Transport Properties of Moist Porous Media", Int. J. Heat Mass Transfer, Vol. 33, 1988, pp. 1005 - 1009.

78. C. L. D. Huang, et al, "Heat and Moisture Transfer in Concrete Slabs", Int. J. Heat Mass Transfer, Vol. 22, 1979, pp. 257-266.

79. S. Whitaker, "Simultaneous Heat, Mass and Momentum Transfer in Porous Media: a Theory of Drying", Advances in Heat Transfer, Vol. 13, 1977.

80. C. K. Wei, et al, "Heat and Mass Transfer in Water-laden Sandstone: Convective Heating", AIChE Journal, Vol. 31, 1985, pp. 1338-1348.

81. K. S. Udell, "Heat Transfer in Porous Media Considering Phase Change and Capillary - the Heat Pipe Effect", Int. J. Heat Mass Transfer, Vol. 28, 1985, pp. 485-495.

82. H. H. Bau and K. E. Torrance, "Boiling in Low-Permeability Porous Materials", Int. J. Heat Mass Transfer, Vol. 25, 1982, pp. 45 - 55.

83. S. Motakef and M. A. El-masri, "Simultaneous Heat and Mass Transfer with Phase Change in a Porous Slab", Int. J. Heat Mass Transfer, Vol. 29, 1986, pp. 1503 - 1512.

84. A. P. Shapiro and S. Motakef, "Unsteady Heat and Mass Transfer with Phase Change in Porous Slabs: Analytical Solution and Experimental Results", Int. J. Heat Mass Transfer, Vol. 33, 1990, pp. 163 - 173.

85. H. Saito and N. Seki, "Mass Transfer and Pressure Rise in Moist Porous Material Subjected to Sudden Heating", J. Heat Transfer, Vol. 99c, 1977, pp. 105-112.

86. A. Rubin and S. Schweitzer, "Heat Transfer in Porous Media with Phase Change", Int. J. Heat Mass Transfer, Vol. 15, 1972, pp. 43-60.

87. A. Haksever and Y. Anderberg, "Comparison Between Measured and Computed Structural Response of Some Reinforced Concrete Columns in Fire", Fire Safety Journal, Vol. 4, 1981/82, pp. 293-297.

88. K. Min and H. W. Emmons, "The Drying of Porous Media", Proc. 1972 Heat Transfer and Fluid Mech. Inst., Stanford University Press, 1972, pp. 1-18.

89. Klans-Jürgen Bathe, "Finite Element Procedures in Engineering Analysis", Prentice-Hall, Inc., Englewood Cliffs, New Jersey, 1982.

90. T. T. Lie and B. Celikkol, "Method to Calculate the Fire Resistance of Circular Reinforced Concrete Columns", ACI Materials Journal, Vol. 88, No. 1, January-February 1991, pp. 84-91.

91. H. L. Malhotra, "Design of Fire Resisting Structures", Surrey University Press. 1982.

92. K. Odeen and A. Nordstrom, "Thermal Properties of Concrete at High Temperature", Cement och Betong, Stockholm. 1972.

93. CEB, "Design of Concrete Structures for Fire Resistance". Preliminary Draft of an Appendix to the CEB/FIP Model Code, Bulletin d' information No. 145. Paris, 1982.

94. T. Z. Harmathy, "Temperature Distribution in Homogeneous Slabs During Fire Tests", Engineering Institute of Canada, Vol. 6, No. B-6, 1963.

95. B. Bresler and R. Iding, "Fire Response of Prestressed Concrete Members", Fire Safety of Concrete Structures, American Concrete Institute. Publication SP-80. 1983, pp. 69-113.

96. O. Pettersson, et al, "Fire Engineering Design of Steel Structures". Division of Structural Mechanics and Concrete Construction, Lund Institute of Technology. Sweden, 1976.

97. S. P. Timshenko and J. N. Goodier, "Theory of Elasticity", McGraw-Hill Book Company, 1970.

98. Jr. Hartley Grandin, "Fundamentals of the Finite Element Method". Macmillan Publishing Company, New York, 1986.

99. K. J. Bathe, et al, "SAP IV, A Structural Analysis Program for Static and Dynamic Response of Linear Systems", Report No. EERC 73-11, College of Engineering, University of California, Berkeley. 1974.

100. T. D. Lin, et al, "Flexural and Shear Behaviour of Reinforced Concrete Beams During Fire Tests". Report No. NBS-GCR-87-536, Center for Fire Research, National Bureau of Standards, Gaithersburg, MD 20899, 1987.

APPENDIX A. THE EXAMPLE OUTPUT OF FPPRCM-S

For demonstration of output of FPPRCM-S the stresses, strains, and degradation at each Gauss-point of some concrete layers and some main reinforcing steel bars of Beam No. 3 are listed in Tables A. 1 - A. 8. The location of concrete layers, elements. main reinforcing steel bars are shown in Figure A.1.

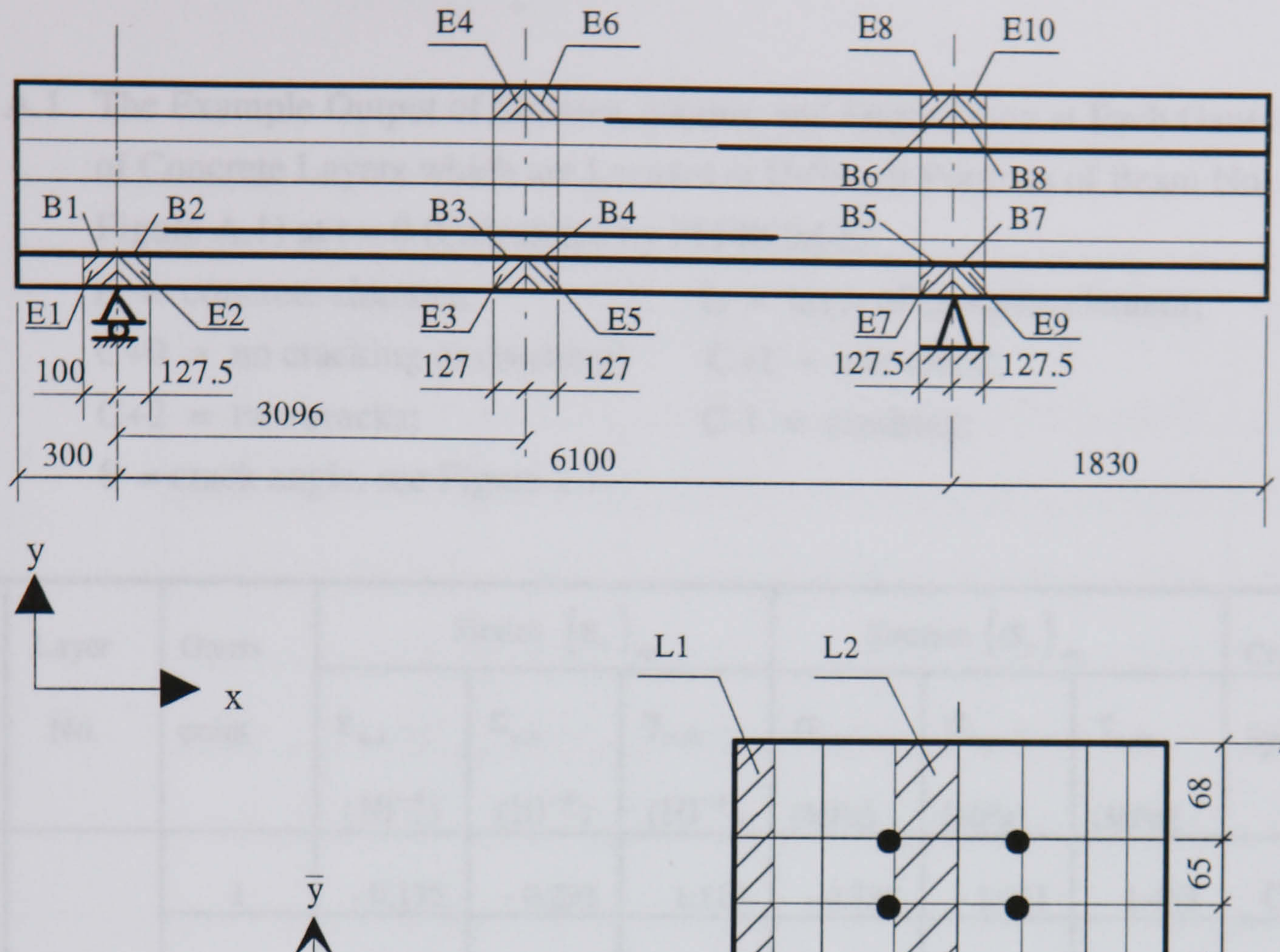

The location of Gauss-point in the concrete elements

Cross-section of beam

E = concrete element
B = reinforcing steel bar element
L = concrete layer

All dimensions in mm

Figure A.1 The Location of Reinforced Concrete Layers, Elements; Gauss-point; Main Reinforcing Steel Bars for Reference to Tables A.1 - A.8.

Table A.1 The Example Output of Stresses, Strains, and Degradation at Each Gauss-point of Concrete Layers which are Located at Different Portions of Beam No. 3 (See Figure A.1) at t = 0 (Calculated by FPPRCM-S).

E = concrete element; L = layer of concrete element;

C+0 = no cracking or crushing; C+1 = one crack;

C+2 = two cracks; C-1 = crushing;

θ = crack angle, see Figure 2.7.

Element No.	Layer No.	Gauss point	Strains $\{\varepsilon_c\}_{xy}$			Stresses $\{\sigma_c\}_{xy}$			Crack or Crush	
			$\varepsilon_{c,x}$ (10^{-4})	$\varepsilon_{c,y}$ (10^{-4})	$\gamma_{c,xy}$ (10^{-4})	$\sigma_{c,x}$ (MPa)	$\sigma_{c,y}$ (MPa)	$\tau_{c,xy}$ (MPa)	Symbols	θ (degree)
E1	L1	1	- 0.175	- 0.293	1.119	- 0.738	- 1.051	1.483	C+0	---
		2	- 0.171	- 1.289	1.655	- 1.258	- 4.123	2.120	C+0	---
		3	0.244	- 0.287	0.349	0.633	- 0.799	0.471	C+0	---
		4	0.249	- 1.282	0.885	0.057	- 3.908	1.146	C+0	---
	L2	1	- 0.175	- 0.293	1.119	- 0.738	- 1.051	1.483	C+0	---
		2	- 0.171	- 1.289	1.655	- 1.258	- 4.123	2.120	C+0	---
		3	0.244	- 0.287	0.349	0.633	- 0.799	0.471	C+0	---
		4	0.249	- 1.282	0.885	0.057	- 3.908	1.146	C+0	---
E2	L1	1	1.711	- 1.190	- 3.380	- 0.679	- 4.194	- 2.385	C+1	- 29.095
		2	1.727	- 0.068	- 1.670	0.382	- 0.835	- 0.571	C+1	- 14.284
		3	2.738	- 1.196	- 2.712	- 0.004	- 4.051	- 1.373	C+1	- 16.650
		4	2.753	- 0.074	- 1.001	0.456	- 0.262	- 0.316	C+1	- 1.398
	L2	1	1.711	- 1.190	- 3.380	- 0.679	- 4.194	- 2.385	C+1	- 29.095
		2	1.727	- 0.068	- 1.670	0.382	- 0.835	- 0.571	C+1	- 14.284
		3	2.738	- 1.196	- 2.712	- 0.004	- 4.051	- 1.373	C+1	- 16.650
		4	2.753	- 0.074	- 1.001	0.456	- 0.262	- 0.316	C+1	- 1.398

Table A.1 (continued)

E3	L1	1	17.430	0.065	2.192	0.033	- 0.020	- 0.095	C+1	4.059
		2	17.430	0.071	- 2.537	0.003	- 0.028	- 0.128	C+1	- 3.566
		3	14.570	0.065	2.196	0.032	- 0.054	- 0.090	C+1	4.845
		4	14.570	0.071	- 2.533	0.062	- 0.121	0.203	C+1	- 6.188
	L2	1	17.430	0.065	2.192	0.033	- 0.020	- 0.095	C+1	4.059
		2	17.430	0.071	- 2.537	0.003	- 0.028	- 0.128	C+1	- 3.566
		3	14.570	0.065	2.196	0.032	- 0.054	- 0.090	C+1	4.845
		4	14.570	0.072	- 2.533	0.062	- 0.121	0.203	C+1	- 6.188
E4	L1	1	- 4.790	1.104	1.665	- 12.420	0.654	1.846	C+0	---
		2	- 4.790	1.024	- 1.576	- 12.500	0.440	- 1.754	C+0	---
		3	- 6.756	1.104	1.617	- 16.540	- 0.283	1.672	C+0	---
		4	- 6.756	1.024	- 1.625	- 16.510	- 0.482	- 1.673	C+0	---
	L2	1	- 4.790	1.104	1.665	- 12.420	0.654	1.846	C+0	---
		2	- 4.790	1.024	- 1.576	- 12.500	0.440	- 1.754	C+0	---
		3	- 6.756	1.104	1.617	- 16.540	- 0.283	1.672	C+0	---
		4	- 6.756	1.024	- 1.625	- 16.510	- 0.482	- 1.673	C+0	---
E5	L1	1	14.500	0.053	1.530	0.064	0.033	- 0.292	C+1	4.683
		2	14.500	- 0.011	- 1.031	0.036	- 0.079	0.181	C+1	- 3.092
		3	12.950	0.053	1.490	0.007	0.043	0.068	C+1	2.851
		4	12.950	- 0.011	- 1.071	0.089	- 0.085	0.417	C+1	- 5.085
	L2	1	14.500	0.053	1.530	0.064	0.033	- 0.292	C+1	4.683
		2	14.500	- 0.011	- 1.031	0.036	- 0.079	0.181	C+1	- 3.092
		3	12.950	0.053	1.490	0.007	0.043	0.068	C+1	2.851
		4	12.950	- 0.011	- 1.071	0.089	- 0.085	0.417	C+1	- 5.085

Table A.1 (continued)

E6	L1	1	- 4.620	0.990	1.770	- 12.120	0.432	1.980	C+0	---
		2	- 4.618	0.971	- 1.479	- 12.170	0.383	- 1.660	C+0	---
		3	- 6.591	0.990	1.758	- 16.220	- 0.497	1.822	C+0	---
		4	- 6.590	0.971	- 1.491	- 16.210	- 0.543	- 1.545	C+0	---
	L2	1	- 4.620	0.990	1.770	- 12.120	0.432	1.980	C+0	---
		2	- 4.618	0.971	- 1.479	- 12.170	0.383	- 1.660	C+0	---
		3	- 6.591	0.990	1.758	- 16.220	- 0.497	1.822	C+0	---
		4	- 6.590	0.971	- 1.491	- 16.210	- 0.543	- 1.545	C+0	---
E7	L1	1	- 5.240	0.867	- 0.796	-13.670	- 0.206	- 0.878	C+0	---
		2	- 5.254	2.171	2.082	-13.600	0.214	2.133	C+1	80.959
		3	- 3.497	0.871	0.000	- 9.612	0.694	0.000	C+0	---
		4	- 3.511	2.174	2.878	- 9.687	- 0.071	2.425	C+1	76.662
	L2	1	- 5.240	0.867	- 0.796	-13.670	- 0.206	- 0.878	C+0	---
		2	- 5.254	2.171	2.082	-13.600	0.214	2.133	C+1	80.959
		3	- 3.497	0.871	0.000	- 9.612	0.694	0.000	C+0	---
		4	- 3.511	2.174	2.878	- 9.687	- 0.071	2.425	C+1	76.662
E8	L1	1	11.680	0.184	1.734	0.579	0.651	- 1.320	C+1	12.794
		2	11.680	- 0.176	2.106	0.202	- 0.687	- 0.515	C+1	9.402
		3	11.910	0.183	1.518	0.232	1.092	1.308	C+1	- 4.968
		4	11.900	- 0.177	1.890	0.030	- 0.400	0.742	C+1	- 0.649
	L2	1	11.680	0.184	1.734	0.579	0.651	- 1.320	C+1	12.794
		2	11.680	- 0.176	2.106	0.202	- 0.687	- 0.515	C+1	9.402
		3	11.910	0.183	1.518	0.232	1.092	1.308	C+1	- 4.968
		4	11.900	- 0.177	1.890	0.030	- 0.400	0.742	C+1	- 0.649

Table A.1 (continued)

E9	L1	1	- 8.814	1.154	1.463	- 19.740	- 0.993	1.376	C+0	---
		2	- 8.844	- 2.880	8.052	-19.540	- 9.334	6.890	C+0	---
		3	- 4.846	1.143	- 0.957	- 12.580	0.735	- 1.063	C+0	---
		4	- 4.873	- 2.889	5.628	- 13.150	- 9.186	5.628	C+0	---
	L2	1	- 8.814	1.154	1.463	- 19.740	- 0.993	1.376	C+0	---
		2	- 8.844	- 2.880	8.052	-19.540	- 9.334	6.890	C+0	---
		3	- 4.846	1.143	- 0.957	- 12.580	0.735	- 1.063	C+0	---
		4	- 4.873	- 2.889	5.628	- 13.150	- 9.186	5.628	C+0	---
E10	L1	1	12.220	- 0.193	- 3.175	0.271	- 1.015	0.505	C+1	- 11.860
		2	12.220	0.188	- 2.140	1.471	0.117	2.077	C+2	- 19.498
		3	12.850	- 0.191	- 2.942	- 0.042	- 0.673	- 0.634	C+1	- 2.604
		4	12.840	0.189	- 1.908	0.368	1.396	- 1.721	C+1	6.136
	L2	1	12.220	- 0.193	- 3.175	0.271	- 1.015	0.505	C+1	- 11.860
		2	12.220	0.188	- 2.140	1.471	0.117	2.077	C+2	- 19.498
		3	12.850	- 0.191	- 2.942	- 0.042	- 0.673	- 0.634	C+1	- 2.604
		4	12.840	0.189	- 1.908	0.368	1.396	- 1.721	C+1	6.136

Table A.2 The Example Output of Stresses, Strains, and Degradation at Each Gauss-point of Concrete Layers which are Located at Different Portions of Beam No. 3 (See Figure A.1) at t = 1 hr (Calculated by FPPRCM-S).

E = concrete element; L = layer of concrete element;

C+0 = no cracking or crushing; C+1 = one crack;

C+2 = two cracks; C-1 = crushing;

θ = crack angle, see Figure 2.7.

Element No.	Layer No.	Gauss point	Strains $\{\varepsilon_c\}_{xy}$			Stresses $\{\sigma_c\}_{xy}$			Crack or Crush	
			$\varepsilon_{c,x}$ (10^{-4})	$\varepsilon_{c,y}$ (10^{-4})	$\gamma_{c,xy}$ (10^{-4})	$\sigma_{c,x}$ (MPa)	$\sigma_{c,y}$ (MPa)	$\tau_{c,xy}$ (MPa)	Symbols	θ (degree)
E1	L1	1	- 1.686	0.286	- 0.555	- 5.111	- 0.056	- 0.711	C+0	---
		2	- 1.675	0.228	4.854	- 4.760	- 3.309	4.635	C+1	45.659
		3	2.410	- 0.039	- 1.486	0.741	0.453	- 0.702	C+2	7.546
		4	2.685	0.141	4.566	- 0.638	- 2.384	1.584	C+1	29.920
	L2	1	- 1.686	0.286	- 0.555	- 5.111	- 0.056	- 0.711	C+0	---
		2	- 1.675	0.228	4.854	- 4.760	- 3.309	4.635	C+1	45.659
		3	2.410	- 0.039	- 1.486	0.741	0.453	- 0.702	C+2	7.546
		4	2.685	0.141	4.566	- 0.638	- 2.384	1.584	C+1	29.920
E2	L1	1	- 6.654	- 6.290	- 8.670	- 2.460	- 2.488	- 1.559	C+2	- 29.095
		2	- 6.937	- 2.918	- 6.317	- 2.603	- 1.248	- 1.043	C+2	- 14.284
		3	- 5.164	- 7.541	0.696	- 2.038	- 2.881	0.098	C+2	- 16.650
		4	- 5.695	- 4.132	3.509	- 2.219	- 1.619	0.584	C+2	- 1.398
	L2	1	- 1.611	- 0.838	- 13.860	- 3.397	- 5.194	- 4.552	C+2	- 29.095
		2	- 6.724	3.865	- 15.190	- 4.344	1.214	- 2.792	C+2	- 14.284
		3	- 2.485	- 4.724	- 4.110	- 2.297	- 5.374	- 1.553	C+2	- 16.650
		4	- 2.621	2.208	- 2.954	- 3.435	0.269	- 0.565	C+2	- 1.398

Table A.2 (continued)

E3	L1	1	- 4.391	- 2.692	8.281	- 1.692	- 1.101	1.373	C+2	4.059
		2	- 3.946	- 2.668	2.761	- 1.560	- 1.048	0.464	C+2	- 3.566
		3	- 5.045	- 2.627	8.809	- 1.934	- 1.085	1.458	C+2	4.845
		4	- 4.525	- 2.673	3.223	- 1.787	- 1.042	0.549	C+2	- 6.188
	L2	1	3.935	8.355	1.052	0.033	0.054	0.344	C+2	4.059
		2	4.753	8.981	- 4.784	- 0.131	0.140	- 1.074	C+2	- 3.566
		3	- 0.270	8.496	1.379	- 0.216	0.103	0.564	C+2	4.845
		4	- 0.047	8.825	- 5.268	0.528	0.325	- 1.504	C+2	- 6.188
E4	L1	1	- 9.418	- 6.365	12.220	- 8.926	- 4.528	3.524	C+2	72.766
		2	- 10.310	- 4.091	8.462	- 8.220	- 4.454	1.471	C+2	99.179
		3	- 10.490	- 6.485	12.420	- 9.655	- 4.663	3.679	C+2	72.307
		4	- 10.980	- 4.437	9.240	- 9.025	- 4.418	1.672	C+2	94.767
	L2	1	- 7.154	12.340	0.660	- 13.76	0.155	0.396	C+1	82.334
		2	- 6.948	13.700	- 5.704	- 13.75	- 0.238	- 1.865	C+1	97.346
		3	- 9.027	12.930	2.881	- 16.900	- 0.057	1.202	C+1	84.282
		4	- 8.990	14.180	- 3.599	- 16.64	- 0.086	- 1.304	C+1	95.054
E5	L1	1	- 4.398	- 2.682	8.300	- 1.690	- 1.102	1.376	C+2	4.683
		2	- 3.942	- 2.564	2.560	- 1.557	- 1.009	0.430	C+2	- 3.092
		3	- 5.002	- 2.726	8.993	- 1.933	- 1.106	1.489	C+2	2.851
		4	- 4.581	- 2.569	3.207	- 1.806	- 1.004	0.544	C+2	- 5.085
	L2	1	3.579	8.311	1.039	0.049	0.066	0.373	C+2	4.683
		2	4.358	9.282	- 4.944	- 0.089	0.126	- 1.114	C+2	- 3.092
		3	- 0.418	8.612	1.984	- 0.444	0.063	0.568	C+2	2.851
		4	- 0.234	9.336	- 4.674	0.259	0.238	- 1.315	C+2	- 5.085

Table A2 (continued)

E6	L1	1	- 9.276	- 6.035	12.310	- 8.811	- 4.281	3.439	C+2	74.313
		2	- 10.140	- 3.945	8.386	- 8.103	- 4.314	1.454	C+2	99.065
		3	- 10.430	- 6.080	12.080	- 9.580	- 4.425	3.396	C+2	75.000
		4	- 11.010	- 4.144	8.733	- 8.932	- 4.310	1.516	C+2	96.660
	L2	1	- 6.907	13.790	0.820	- 13.090	0.206	0.257	C+1	81.933
		2	- 6.631	14.220	- 5.695	- 13.150	- 0.222	- 1.770	C+1	97.231
		3	- 8.861	14.380	2.497	- 16.320	0.000	0.951	C+1	83.824
		4	- 8.718	14.740	- 4.097	- 16.160	- 0.107	- 1.403	C+1	95.054
E7	L1	1	- 6.285	- 2.806	4.943	- 2.412	- 1.143	0.809	C+2	95.799
		2	- 6.018	- 3.184	1.827	- 2.341	- 1.250	0.328	C+2	80.959
		3	- 6.807	- 2.850	3.625	- 2.629	- 1.130	0.600	C+2	90.356
		4	- 6.758	- 2.994	0.846	- 2.599	- 1.199	0.118	C+2	76.662
	L2	1	- 3.448	7.992	- 0.830	- 4.350	0.006	- 0.146	C+2	93.965
		2	- 3.868	4.301	- 4.938	- 4.190	0.502	- 0.797	C+2	80.959
		3	- 4.257	8.410	- 1.689	- 5.324	- 0.007	- 0.349	C+2	91.215
		4	- 5.459	4.446	- 6.600	- 5.256	0.917	- 0.827	C+2	76.662
E8	L1	1	- 3.442	- 5.669	6.575	- 2.612	- 5.546	1.800	C+2	12.794
		2	- 4.149	- 5.249	13.140	- 2.812	- 5.576	3.014	C+2	9.402
		3	- 1.966	- 5.820	4.921	- 2.070	- 4.998	0.858	C+2	- 4.968
		4	- 2.236	- 6.029	11.520	- 2.140	- 5.330	2.276	C+2	- 0.649
	L2	1	20.190	12.780	- 3.280	0.877	- 0.843	- 1.790	C+2	12.794
		2	20.020	10.180	4.236	- 0.067	0.097	0.258	C+2	9.402
		3	24.900	12.380	- 4.682	- 0.111	0.149	- 0.780	C+2	- 4.968
		4	24.630	10.120	2.872	0.048	- 0.013	1.031	C+2	- 0.649

Table A2 (continued)

E9	L1	1	- 11.200	- 5.651	6.827	- 4.198	- 2.154	1.210	C+2	71.391
		2	- 6.574	- 4.133	31.110	- 4.579	- 4.113	4.410	C+1	51.452
		3	- 7.684	- 4.330	3.232	- 2.924	- 1.736	0.522	C+2	100.898
		4	- 4.237	- 5.275	27.070	- 3.623	- 4.129	3.963	C+2	49.315
	L2	1	- 8.862	0.286	13.290	- 12.170	- 1.862	5.091	C+1	72.078
		2	- 3.561	1.013	43.170	- 11.690	- 8.869	10.35	C+1	53.807
		3	- 5.979	- 0.937	- 2.787	- 6.343	- 0.960	- 0.739	C+2	92.877
		4	- 2.732	- 4.578	23.90	- 8.729	- 8.001	8.474	C+1	50.890
E10	L1	1	- 2.483	- 6.147	4.740	-2.875	- 4.960	0.807	C+2	- 11.860
		2	- 1.571	- 7.862	11.080	- 3.383	- 5.137	2.511	C+2	- 19.498
		3	- 1.614	- 5.935	3.025	- 1.585	- 5.240	0.514	C+2	- 2.604
		4	- 2.330	- 6.014	9.387	- 1.696	- 5.760	2.152	C+2	6.136
	L2	1	20.340	8.865	- 6.721	- 0.178	0.208	- 0.456	C+2	- 11.860
		2	20.030	8.429	0.837	1.631	- 1.603	1.990	C+2	- 19.498
		3	25.170	8.938	- 7.003	- 0.135	0.170	- 1.768	C+2	- 2.604
		4	24.980	8.028	0.819	0.217	- 0.184	- 0.881	C+2	6.136

Table A.3 The Example Output of Stresses, Strains, and Degradation at Each Gauss-point of Concrete Layers which are Located at Different Portions of Beam No. 3 (See Figure A.1) at t = 2 hr (Calculated by FPPRCM-S).

E = concrete element; L = layer of concrete element;

C+0 = no cracking or crushing; C+1 = one crack;

C+2 = two cracks; C-1 = crushing;

θ = crack angle, see Figure 2.7.

Element No.	Layer No.	Gauss point	Strains $\{\varepsilon_c\}_{xy}$			Stresses $\{\sigma_c\}_{xy}$			Crack or Crush	
			$\varepsilon_{c,x}$ (10^{-4})	$\varepsilon_{c,y}$ (10^{-4})	$\gamma_{c,xy}$ (10^{-4})	$\sigma_{c,x}$ (MPa)	$\sigma_{c,y}$ (MPa)	$\tau_{c,xy}$ (MPa)	Symbols	θ (degree)
E1	L1	1	- 0.949	0.032	- 0.244	- 3.042	- 0.449	- 0.323	C+0	---
		2	- 0.933	- 3.576	2.753	- 4.233	- 5.965	2.968	C+1	45.695
		3	1.160	- 0.431	- 4.587	2.160	0.215	- 1.470	C+2	7.546
		4	1.536	- 3.678	- 0.620	0.172	- 5.121	1.241	C+1	29.920
	L2	1	- 0.949	0.032	- 0.244	- 3.042	- 0.449	- 0.323	C+0	---
		2	- 0.933	- 3.576	2.753	- 4.233	- 5.965	2.968	C+1	45.695
		3	1.160	- 0.431	- 4.587	2.160	0.215	- 1.470	C+2	7.546
		4	1.536	- 3.678	- 0.620	0.172	- 5.121	1.241	C+1	29.920
E2	L1	1	0.464	- 5.409	- 12.880	- 1.108	- 2.511	- 1.697	C+2	- 29.095
		2	- 3.027	- 0.945	- 8.970	- 0.998	- 0.280	- 1.482	C+2	- 14.284
		3	3.919	- 8.082	- 4.514	- 0.004	- 3.197	- 0.490	C+2	- 16.650
		4	0.284	- 3.621	- 0.680	0.376	- 1.449	- 0.126	C+2	- 1.398
	L2	1	7.317	0.811	- 26.120	- 2.457	- 2.684	- 2.965	C+2	- 29.095
		2	- 2.316	3.194	- 19.39	- 1.691	0.557	-3.372	C+2	- 14.284
		3	6.312	- 3.343	- 13.41	- 0.892	- 3.000	- 1.950	C+2	- 16.650
		4	1.786	- 0.851	- 7.103	0.048	- 0.632	- 1.258	C+2	- 1.398

Table A3 (continued)

E3	L1	1	6.580	- 1.162	6.192	- 0.118	- 0.493	0.871	C+2	4.059
		2	7.780	- 0.540	- 2.279	- 0.022	- 0.229	- 0.219	C+2	- 3.566
		3	2.894	- 1.360	6.390	- 0.160	- 0.583	0.976	C+2	4.845
		4	4.118	- 0.667	- 1.931	- 0.032	- 0.292	- 0.175	C+2	- 6.188
	L2	1	15.630	9.811	3.927	- 0.068	0.082	0.540	C+2	4.059
		2	17.720	11.500	- 5.514	- 0.094	0.110	- 0.830	C+2	- 3.566
		3	7.172	9.649	3.417	- 0.109	0.119	0.664	C+2	4.845
		4	9.474	11.660	- 5.181	- 0.205	0.217	- 0.961	C+2	- 6.188
E4	L1	1	- 8.847	- 5.344	11.280	- 4.707	- 2.441	2.350	C+2	72.766
		2	- 9.038	- 3.111	7.521	- 4.411	- 1.873	1.260	C+2	99.179
		3	- 11.170	- 5.555	8.761	- 5.668	- 2.695	1.900	C+2	72.307
		4	- 10.750	- 3.716	5.995	- 5.325	- 2.052	0.997	C+2	94.767
	L2	1	- 5.644	18.540	- 1.395	- 9.535	0.451	- 0.971	C+1	82.334
		2	- 4.854	19.940	- 12.060	- 9.725	- 0.547	- 2.825	C+1	97.346
		3	- 7.801	19.670	1.926	- 13.160	0.095	0.281	C+1	84.282
		4	- 7.458	20.820	- 8.906	- 12.970	- 0.278	- 2.258	C+1	95.054
E5	L1	1	5.283	- 1.145	6.024	- 0.134	- 0.493	0.853	C+2	4.683
		2	6.367	- 0.491	- 1.837	- 0.017	- 0.206	- 0.192	C+2	- 3.092
		3	2.247	- 1.507	6.121	- 0.089	- 0.625	0.981	C+2	2.851
		4	3.407	- 0.655	- 1.356	- 0.019	- 0.277	- 0.127	C+2	- 5.085
	L2	1	13.930	9.756	3.647	- 0.077	0.090	0.513	C+2	4.683
		2	15.860	11.880	- 4.888	- 0.076	0.091	- 0.784	C+2	- 3.092
		3	6.227	9.630	3.492	- 0.064	0.073	0.675	C+2	2.851
		4	8.164	11.990	- 4.412	- 0.153	0.164	- 0.879	C+2	- 5.085

Table A3 (continued)

E6	L1	1	- 8.358	- 5.510	12.280	- 4.517	- 2.488	2.487	C+2	74.313
		2	- 8.658	- 3.242	7.681	- 4.229	- 1.937	1.300	C+2	99.064
		3	- 10.820	- 5.754	9.120	- 5.540	- 2.774	1.897	C+2	75.000
		4	- 10.540	- 3.753	5.863	- 5.196	- 2.109	0.958	C+2	96.660
	L2	1	- 5.281	19.180	- 1.239	- 8.856	0.501	- 1.072	C+1	81.933
		2	- 4.409	20.100	- 12.32	- 9.046	- 0.556	- 2.845	C+1	97.231
		3	- 7.572	20.250	1.703	-12.720	0.141	0.127	C+1	83.824
		4	- 7.129	20.980	9.525	-12.520	- 0.307	- 2.407	C+1	95.054
E7	L1	1	- 1.485	- 1.552	6.014	- 0.486	- 0.495	0.997	C+2	95.799
		2	- 0.697	- 1.443	- 0.245	- 0.227	- 0.467	- 0.040	C+2	80.959
		3	- 3.238	- 1.276	5.910	- 1.040	- 0.413	0.981	C+2	90.356
		4	- 2.519	- 1.092	- 0.391	- 0.184	- 0.352	- 0.068	C+2	76.662
	L2	1	- 0.402	7.111	- 0.094	- 0.268	0.026	0.150	C+2	93.965
		2	0.634	4.445	- 6.287	- 0.271	0.404	- 1.230	C+2	80.959
		3	- 1.444	7.982	0.045	0.941	0.007	0.058	C+2	91.215
		4	- 2.208	4.602	- 8.147	- 0.832	0.899	- 1.624	C+2	76.662
E8	L1	1	0.186	- 3.041	5.985	- 0.296	- 2.276	1.261	C+2	12.794
		2	- 0.435	- 3.252	13.030	- 0.615	- 2.663	2.489	C+2	9.402
		3	1.732	- 3.575	4.433	0.297	- 2.217	0.730	C+2	- 4.968
		4	1.068	- 4.219	11.190	0.224	- 2.722	1.970	C+2	- 0.649
	L2	1	37.240	23.760	- 1.987	0.991	- 0.935	- 1.999	C+2	12.794
		2	36.660	19.990	6.609	- 0.049	0.101	0.247	C+2	9.402
		3	42.890	22.530	- 4.120	0.012	0.048	- 0.159	C+2	- 4.968
		4	42.190	19.750	4.706	0.073	- 0.016	1.519	C+2	- 0.649

Table A3 (continued)

E9	L1	1	- 15.180	- 5.259	14.360	- 4.449	- 1.664	2.190	C+2	71.391
		2	- 5.416	- 0.398	63.320	- 4.486	- 5.524	5.417	C+1	51.452
		3	- 7.784	- 3.541	11.160	- 2.502	- 1.089	1.852	C+2	100.898
		4	5.162	4.010	67.340	- 3.127	- 5.513	4.570	C+2	49.315
	L2	1	- 6.446	- 0.838	17.010	- 5.057	- 1.734	3.505	C+1	72.078
		2	1.250	7.561	62.860	- 5.810	- 6.488	6.579	C+1	53.807
		3	- 4.918	- 1.819	3.775	- 2.588	- 1.027	0.649	C+2	92.877
		4	6.117	3.999	49.020	- 3.659	- 5.908	5.137	C+1	50.890
E10	L1	1	2.134	- 4.143	1.366	0.296	- 2.521	0.112	C+2	- 11.860
		2	2.332	- 6.592	9.659	0.502	- 2.775	1.666	C+2	- 19.498
		3	4.559	- 3.468	0.036	0.010	- 2.228	0.034	C+2	- 2.604
		4	3.545	- 3.682	9.421	- 0.320	- 2.616	1.641	C+2	6.136
	L2	1	37.920	17.860	- 10.620	- 0.158	0.210	- 0.445	C+2	- 11.860
		2	36.800	17.110	0.613	2.392	- 2.342	2.912	C+2	- 19.498
		3	45.910	18.170	- 10.730	- 0.174	0.232	- 2.372	C+2	- 2.604
		4	45.250	16.140	1.572	0.329	- 0.273	- 1.322	C+2	6.136

Table A.4 The Example Output of Stresses, Strains, and Degradation at Each Gauss-point of Concrete Layers which are Located at Different Portions of Beam No. 3 (See Figure A.1) at t = 3 hr (Calculated by FPPRCM-S).

E = concrete element; L = layer of concrete element;

C+0 = no cracking or crushing; C+1 = one crack:

C+2 = two cracks; C-1 = crushing;

θ = crack angle, see Figure 2.7.

Element No.	Layer No.	Gauss point	Strains $\{\varepsilon_c\}_{xy}$			Stresses $\{\sigma_c\}_{xy}$			Crack or Crush	
			$\varepsilon_{c,x}$ (10^{-4})	$\varepsilon_{c,y}$ (10^{-4})	$\gamma_{c,xy}$ (10^{-4})	$\sigma_{c,x}$ (MPa)	$\sigma_{c,y}$ (MPa)	$\tau_{c,xy}$ (MPa)	Symbols	θ (degree)
E1	L1	1	- 0.711	- 0.036	- 0.150	- 2.339	- 0.535	- 0.200	C+0	---
		2	- 0.392	- 4.309	3.031	- 3.991	- 6.594	3.238	C+1	45.659
		3	1.048	- 0.466	- 5.421	1.535	0.365	- 1.855	C+2	7.546
		4	1.708	- 4.398	- 1.324	- 0.234	- 5.986	0.863	C+1	29.920
	L2	1	- 0.711	- 0.036	- 0.150	- 2.339	- 0.535	- 0.200	C+0	---
		2	- 0.392	- 4.309	3.031	- 3.991	- 6.594	3.238	C+1	45.659
		3	1.048	- 0.466	- 5.421	1.535	0.365	- 1.855	C+2	7.546
		4	1.708	- 4.398	- 1.324	- 0.234	- 5.986	0.863	C+1	29.920
E2	L1	1	9.941	- 3.048	- 27.100	- 1.339	- 2.410	- 1.885	C+2	- 29.095
		2	5.083	0.875	- 16.640	- 1.057	0.058	- 2.078	C+2	- 14.284
		3	16.660	- 6.213	- 17.250	- 0.405	- 2.573	- 1.081	C+2	- 16.650
		4	11.930	- 1.462	- 6.654	- 0.043	- 0.517	- 1.007	C+2	- 1.398
	L2	1	17.390	1.768	- 36.330	- 1.744	- 2.160	- 2.186	C+2	- 29.095
		2	63.260	2.009	- 20.400	- 1.323	0.169	- 2.589	C+2	- 14.284
		3	18.090	- 3.197	- 21.940	- 0.847	- 2.211	- 1.769	C+2	- 16.650
		4	10.270	- 1.627	- 8.423	- 0.058	- 0.754	- 1.319	C+2	- 1.398

Table A4 (continued)

E3	L1	1	41.740	0.123	8.375	- 0.035	- 0.025	0.404	C+2	4.059
		2	43.380	0.612	- 9.616	- 0.063	0.370	- 0.681	C+2	- 3.566
		3	31.460	0.003	8.255	- 0.064	- 0.073	0.479	C+2	4.845
		4	33.100	0.544	- 9.515	- 0.065	0.051	- 0.381	C+2	- 6.188
	L2	1	46.550	6.197	8.194	- 0.032	0.060	0.398	C+2	4.059
		2	49.790	8.783	- 9.247	- 0.058	0.089	- 0.674	C+2	- 3.566
		3	31.540	5.958	7.374	- 0.066	0.086	0.486	C+2	4.845
		4	35.120	8.823	- 9.359	- 0.106	0.129	- 0.570	C+2	- 6.188
E4	L1	1	- 12.040	- 5.607	9.773	- 4.506	- 2.109	1.712	C+2	72.766
		2	- 11.280	- 2.901	3.088	- 4.231	- 1.201	0.471	C+2	99.179
		3	- 16.500	- 5.644	6.934	- 5.974	- 2.180	1.219	C+2	72.307
		4	- 15.210	- 3.294	1.481	- 5.585	- 1.320	2.199	C+2	94.767
	L2	1	- 8.118	15.810	- 0.659	- 13.390	0.253	0.007	C+1	82.334
		2	- 6.828	18.850	- 16.710	- 12.910	- 0.840	- 4.157	C+1	97.346
		3	- 10.920	18.220	6.365	- 17.500	- 0.185	1.874	C+1	84.282
		4	- 10.490	20.490	- 10.460	- 16.770	- 0.336	- 2.740	C+1	95.054
E5	L1	1	32.200	0.162	7.081	- 0.031	- 0.017	0.297	C+2	4.683
		2	33.160	0.483	- 6.739	- 0.038	0.393	- 0.508	C+2	- 3.092
		3	25.200	- 0.331	6.169	- 0.047	- 0.133	0.605	C+2	2.851
		4	26.640	0.400	- 6.291	- 0.031	0.124	- 0.249	C+2	- 5.085
	L2	1	36.560	6.130	6.692	- 0.025	0.048	0.272	C+2	4.683
		2	39.190	9.109	- 5.905	- 0.026	0.052	- 0.435	C+2	- 3.092
		3	24.940	5.610	5.562	- 0.046	0.062	0.598	C+2	2.851
		4	28.070	9.133	- 5.586	- 0.048	0.068	- 0.353	C+2	- 5.085

Table A4 (continued)

E6	L1	1	- 11.700	- 5.254	11.000	- 4.396	- 1.958	1.916	C+2	74.313
		2	- 10.920	- 2.826	3.723	- 4.106	- 1.175	0.578	C+2	99.064
		3	- 16.260	- 5.359	6.904	- 5.903	- 2.067	1.209	C+2	75.000
		4	- 14.920	- 3.162	1.449	- 5.486	- 1.278	0.204	C+2	96.660
	L2	1	- 7.953	17.100	- 0.264	- 12.970	0.282	- 0.022	C+1	81.933
		2	- 6.553	19.120	- 16.740	- 12.480	- 0.826	- 4.116	C+1	97.231
		3	- 10.740	19.500	6.196	- 17.030	- 0.160	1.738	C+1	83.824
		4	- 10.150	20.860	- 10.990	- 16.320	- 0.354	- 2.832	C+1	95.054
E7	L1	1	- 8.108	1.989	3.844	- 2.864	0.243	0.663	C+2	95.799
		2	- 7.301	- 1.139	- 1.700	- 2.113	- 0.311	- 0.322	C+2	80.959
		3	- 8.827	2.825	3.059	- 3.094	0.008	0.513	C+2	90.356
		4	- 8.448	- 8.196	- 3.476	- 2.480	- 0.179	- 0.635	C+2	76.662
	L2	1	- 8.089	6.396	0.742	- 3.558	0.049	0.207	C+2	93.965
		2	- 8.122	- 0.420	- 5.985	- 2.927	- 0.213	- 0.968	C+2	80.959
		3	- 8.358	7.407	- 1.294	- 3.657	- 0.002	- 0.182	C+2	91.215
		4	- 8.975	0.252	- 8.897	- 3.197	- 0.021	- 1.448	C+2	76.662
E8	L1	1	9.126	- 2.445	7.934	- 0.232	- 1.450	0.689	C+2	12.794
		2	8.763	- 3.678	16.220	- 0.675	- 2.069	2.227	C+2	9.402
		3	1.063	- 3.502	3.849	0.173	- 1.613	0.893	C+2	- 4.968
		4	9.588	- 4.871	12.220	0.052	- 2.263	2.056	C+2	- 0.649
	L2	1	47.060	22.820	0.225	1.181	- 1.124	- 2.387	C+2	12.794
		2	45.990	16.270	10.170	0.033	0.018	0.017	C+2	9.402
		3	53.480	20.330	- 4.146	0.116	- 0.056	0.413	C+2	- 4.968
		4	52.460	15.680	6.482	0.085	- 0.030	1.887	C+2	- 0.649

Table A4 (continued)

E9	L1	1	- 27.220	- 3.051	17.410	- 6.974	- 0.771	2.199	C+2	71.391
		2	- 14.110	10.170	88.760	- 7.909	- 3.994	5.681	C+1	51.452
		3	- 17.530	- 3.528	10.360	- 4.982	- 0.884	1.829	C+2	100.898
		4	- 3.699	10.510	80.820	- 5.992	- 3.874	4.852	C+2	49.315
	L2	1	- 21.090	- 4.581	11.960	- 6.981	- 1.620	1.942	C+1	72.078
		2	- 13.380	10.530	66.030	- 8.122	- 3.658	5.490	C+1	53.807
		3	- 15.110	- 3.911	5.372	- 5.260	- 1.465	0.888	C+2	92.877
		4	- 4.520	8.850	58.810	- 5.984	- 3.657	4.699	C+1	50.890
E10	L1	1	11.400	- 4.548	- 2.376	0.203	- 2.224	0.236	C+2	- 11.860
		2	9.321	- 6.860	6.150	1.398	- 2.901	1.455	C+2	- 19.498
		3	17.500	- 4.149	- 2.068	0.004	- 1.892	- 0.102	C+2	- 2.604
		4	15.780	- 3.964	10.200	- 0.220	- 1.952	1.169	C+2	6.136
	L2	1	47.860	13.080	- 16.830	- 0.108	0.158	- 0.341	C+2	- 11.860
		2	45.740	14.500	- 1.626	3.021	- 2.972	3.684	C+2	- 19.498
		3	59.630	13.780	- 15.150	- 0.207	0.267	- 2.810	C+2	- 2.604
		4	58.410	12.790	2.440	0.448	- 0.390	- 1.840	C+2	6.136

Table A.5 The Example Output of Stresses, Strains, and Degradation of Main Reinforcing Steel Bar Elements which are Located at Different Portions of Beam No. 3 (See Figure A.1) at t = 0 (Calculated by FPPRCM-S).

B = steel bar element;

Y+0 = no yielding;

Y+1 = yield.

Element No.	Strain, ε_s (10^{-4})	Stress, σ_s (MPa)	Yield
B1	0.397	7.711	Y+0
B2	3.136	60.920	Y+0
B3	13.520	262.700	Y+0
B4	12.380	240.500	Y+0
B5	- 3.401	- 66.070	Y+0
B6	11.980	220.000	Y+0
B7	- 3.767	- 73.180	Y+0
B8	13.130	241.100	Y+0

Table A.6 The Example Output of Stresses, Strains, and Degradation of Main Reinforcing Steel Bar Elements which are Located at Different Portions of Beam No. 3 (See Figure A.1) at t = 1 hr (Calculated by FPPRCM-S).

B = steel bar element;

Y+0 = no yielding;

Y+1 = yield.

Element No.	Strain, ε_s (10^{-4})	Stress, σ_s (MPa)	Yield
B1	4.103	79.700	Y+0
B2	8.498	158.000	Y+0
B3	16.090	299.200	Y+0
B4	15.580	289.600	Y+0
B5	- 15.690	- 291.700	Y+0
B6	14.670	262.600	Y+0
B7	- 5.001	- 97.150	Y+0
B8	13.400	246.100	Y+0

Table A.7 The Example Output of Stresses, Strains, and Degradation of Main Reinforcing Steel Bar Elements which are Located at Different Portions of Beam No. 3 (See Figure A.1) at t = 2 hr (Calculated by FPPRCM-S).

B = steel bar element;

Y+0 = no yielding;

Y+1 = yield.

Element No.	Strain, ε_s (10^{-4})	Stress, σ_s (MPa)	Yield
B1	2.433	47.260	Y+0
B2	5.412	93.590	Y+0
B3	13.310	230.100	Y+0
B4	12.520	216.500	Y+0
B5	- 26.350	- 386.000	Y+1
B6	15.770	271.600	Y+0
B7	- 7.139	- 138.700	Y+0
B8	13.770	252.800	Y+0

Table A.8 The Example Output of Stresses, Strains, and Degradation of Main Reinforcing Steel Bar Elements which are Located at Different Portions of Beam No. 3 (See Figure A.1) at t = 3 hr (Calculated by FPPRCM-S).

B = steel bar element;

Y+0 = no yielding;

Y+1 = yield.

Element No.	Strain, ε_s (10^{-4})	Stress, σ_s (MPa)	Yield
B1	2.398	46.580	Y+0
B2	5.621	88.590	Y+0
B3	12.340	194.500	Y+0
B4	11.210	176.700	Y+0
B5	- 14.510	- 228.700	Y+1
B6	17.550	290.800	Y+0
B7	- 6.801	- 132.100	Y+0
B8	14.150	259.900	Y+0

APPENDIX B AUTHOR'S PUBLICATIONS

Non-linear Finite Element Model to Predict Temperature Histories within Reinforced Concrete in Fires

Zhaohui Huang, Andrew Platten and John Roberts

Department of Built Environment

University of Central Lancashire

Preston PR1 2HE

United Kingdom

ABSTRACT

A non-linear finite element procedure is proposed to predict the temperature distribution history of cross-sections of structural members, such as beams composed of reinforced concrete in fire conditions. In this model the effect of moisture in concrete has been taken into account, and the thermal properties of concrete have been considered as temperature and moisture dependent. In order to validate the model, a series of proving tests have been carried out through a quantitative verification of the model against known test results and fairly good accuracy is found.

This paper has been accepted for publication by **Building and Environment,** The International Journal of Building Science and its Applications.